



**HAL**  
open science

# Development of amorphous metallic alloys for biomedical applications and understanding of the plasticity phenomena

Oriane Baulin

► **To cite this version:**

Oriane Baulin. Development of amorphous metallic alloys for biomedical applications and understanding of the plasticity phenomena. Materials. Université de Lyon, 2018. English. NNT : 2018LYSEI073 . tel-02063280

**HAL Id: tel-02063280**

**<https://theses.hal.science/tel-02063280>**

Submitted on 11 Mar 2019

**HAL** is a multi-disciplinary open access archive for the deposit and dissemination of scientific research documents, whether they are published or not. The documents may come from teaching and research institutions in France or abroad, or from public or private research centers.

L'archive ouverte pluridisciplinaire **HAL**, est destinée au dépôt et à la diffusion de documents scientifiques de niveau recherche, publiés ou non, émanant des établissements d'enseignement et de recherche français ou étrangers, des laboratoires publics ou privés.



# INSA

N°d'ordre NNT : 2018LYSEI073

**THESE de DOCTORAT DE L'UNIVERSITE DE LYON**  
opérée au sein de  
**L'INSA de Lyon**

**Ecole Doctorale N° ED 34**  
**Matériaux de Lyon**

**Spécialité/ discipline de doctorat :**  
Matériaux

Soutenue publiquement le 12/10/2018, par :  
**Oriane Baulin**

---

**Development of amorphous metallic  
alloys for biomedical applications and  
understanding of the plasticity  
phenomena**

---

Devant le jury composé de :

A. Lindsay Greer	Professeur des Universités	Cambridge	<b>Président</b>
Mariana Calin	Maitre de Conférences	IFW Dresden	<b>Rapporteur</b>
Jean-Jacques Blandin	Directeur de Recherches	Grenoble INP	<b>Rapporteur</b>
Anne Tanguy	Professeur des Universités	INSA Lyon	<b>Examinatrice</b>
Jean-Marc Pelletier	Professeur des Universités	INSA Lyon	<b>Examinateur</b>
Damien Fabrègue	Professeur des Universités	INSA Lyon	<b>Directeur de thèse</b>
Sébastien Gravier	Maitre de Conférences	VULKAM	<b>Invité</b>
David Rodney	Professeur des Universités	Lyon 1	<b>Invité</b>



## Département FEDORA – INSA Lyon - Ecoles Doctorales – Quinquennal 2016-2020

SIGLE	ECOLE DOCTORALE	NOM ET COORDONNEES DU RESPONSABLE
<b>CHIMIE</b>	<b>CHIMIE DE LYON</b> <a href="http://www.edchimie-lyon.fr">http://www.edchimie-lyon.fr</a> Sec. : Renée EL MELHEM Bât. Blaise PASCAL, 3e étage <a href="mailto:secretariat@edchimie-lyon.fr">secretariat@edchimie-lyon.fr</a> INSA : R. GOURDON	<b>M. Stéphane DANIELE</b> Institut de recherches sur la catalyse et l'environnement de Lyon IRCEL YON-UMR 5256 Équipe CDFA 2 Avenue Albert EINSTEIN 69 626 Villeurbanne CEDEX <a href="mailto:directeur@edchimie-lyon.fr">directeur@edchimie-lyon.fr</a>
<b>E.E.A.</b>	<b>ÉLECTRONIQUE, ELECTROTECHNIQUE, AUTOMATIQUE</b> <a href="http://edeea.ec-lyon.fr">http://edeea.ec-lyon.fr</a> Sec. : M.C. HAVGOUDOUKIAN <a href="mailto:ecole-doctorale.eea@ec-lyon.fr">ecole-doctorale.eea@ec-lyon.fr</a>	<b>M. Gérard SCORLETTI</b> École Centrale de Lyon 36 Avenue Guy DE COLLONGUE 69 134 Écully Tél : 04.72.18.60.97 Fax 04.78.43.37.17 <a href="mailto:gerard.scorletti@ec-lyon.fr">gerard.scorletti@ec-lyon.fr</a>
<b>E2M2</b>	<b>ÉVOLUTION, ÉCOSYSTÈME, MICROBIOLOGIE, MODÉLISATION</b> <a href="http://e2m2.universite-lyon.fr">http://e2m2.universite-lyon.fr</a> Sec. : Sylvie ROBERJOT Bât. Atrium, UCB Lyon 1 Tél : 04.72.44.83.62 INSA : H. CHARLES <a href="mailto:secretariat.e2m2@univ-lyon1.fr">secretariat.e2m2@univ-lyon1.fr</a>	<b>M. Philippe NORMAND</b> UMR 5557 Lab. d'Ecologie Microbienne Université Claude Bernard Lyon 1 Bâtiment Mendel 43, boulevard du 11 Novembre 1918 69 622 Villeurbanne CEDEX <a href="mailto:philippe.normand@univ-lyon1.fr">philippe.normand@univ-lyon1.fr</a>
<b>EDISS</b>	<b>INTERDISCIPLINAIRE SCIENCES-SANTÉ</b> <a href="http://www.ediss-lyon.fr">http://www.ediss-lyon.fr</a> Sec. : Sylvie ROBERJOT Bât. Atrium, UCB Lyon 1 Tél : 04.72.44.83.62 INSA : M. LAGARDE <a href="mailto:secretariat.ediss@univ-lyon1.fr">secretariat.ediss@univ-lyon1.fr</a>	<b>Mme Emmanuelle CANET-SOULAS</b> INSERM U1060, CarMeN lab, Univ. Lyon 1 Bâtiment IMBL 11 Avenue Jean CAPELLE INSA de Lyon 69 621 Villeurbanne Tél : 04.72.68.49.09 Fax : 04.72.68.49.16 <a href="mailto:emmanuelle.canet@univ-lyon1.fr">emmanuelle.canet@univ-lyon1.fr</a>
<b>INFOMATHS</b>	<b>INFORMATIQUE ET MATHÉMATIQUES</b> <a href="http://edinfomaths.universite-lyon.fr">http://edinfomaths.universite-lyon.fr</a> Sec. : Renée EL MELHEM Bât. Blaise PASCAL, 3e étage Tél : 04.72.43.80.46 Fax : 04.72.43.16.87 <a href="mailto:infomaths@univ-lyon1.fr">infomaths@univ-lyon1.fr</a>	<b>M. Luca ZAMBONI</b> Bât. Braconnier 43 Boulevard du 11 novembre 1918 69 622 Villeurbanne CEDEX Tél : 04.26.23.45.52 <a href="mailto:zamboni@maths.univ-lyon1.fr">zamboni@maths.univ-lyon1.fr</a>
<b>Matériaux</b>	<b>MATÉRIAUX DE LYON</b> <a href="http://ed34.universite-lyon.fr">http://ed34.universite-lyon.fr</a> Sec. : Marion COMBE Tél : 04.72.43.71.70 Fax : 04.72.43.87.12 Bât. Direction <a href="mailto:ed.materiaux@insa-lyon.fr">ed.materiaux@insa-lyon.fr</a>	<b>M. Jean-Yves BUFFIÈRE</b> INSA de Lyon MATEIS - Bât. Saint-Exupéry 7 Avenue Jean CAPELLE 69 621 Villeurbanne CEDEX Tél : 04.72.43.71.70 Fax : 04.72.43.85.28 <a href="mailto:jean-yves.buffiere@insa-lyon.fr">jean-yves.buffiere@insa-lyon.fr</a>
<b>MEGA</b>	<b>MÉCANIQUE, ÉNERGÉTIQUE, GÉNIE CIVIL, ACOUSTIQUE</b> <a href="http://edmega.universite-lyon.fr">http://edmega.universite-lyon.fr</a> Sec. : Marion COMBE Tél : 04.72.43.71.70 Fax : 04.72.43.87.12 Bât. Direction <a href="mailto:mega@insa-lyon.fr">mega@insa-lyon.fr</a>	<b>M. Jocelyn BONJOUR</b> INSA de Lyon Laboratoire CETHIL Bâtiment Sadi-Carnot 9, rue de la Physique 69 621 Villeurbanne CEDEX <a href="mailto:jocelyn.bonjour@insa-lyon.fr">jocelyn.bonjour@insa-lyon.fr</a>
<b>ScSo</b>	<b>ScSo*</b> <a href="http://ed483.univ-lyon2.fr">http://ed483.univ-lyon2.fr</a> Sec. : Viviane POLSINELLI Brigitte DUBOIS INSA : J.Y. TOUSSAINT Tél : 04.78.69.72.76 <a href="mailto:viviane.polsinelli@univ-lyon2.fr">viviane.polsinelli@univ-lyon2.fr</a>	<b>M. Christian MONTES</b> Université Lyon 2 86 Rue Pasteur 69 365 Lyon CEDEX 07 <a href="mailto:christian.montes@univ-lyon2.fr">christian.montes@univ-lyon2.fr</a>

\*ScSo : Histoire, Géographie, Aménagement, Urbanisme, Archéologie, Science politique, Sociologie, Anthropologie



# Acknowledgement

A mon tour de passer à l'exercice difficile des remerciements après ces trois années. Mon arrivée en thèse le 1<sup>er</sup> octobre 2015 me semble dater d'hier, pourtant il y a eu bon nombre de rires, de larmes, de coups de gueule, de doutes et de joie. A contrario de ce que l'on pourrait penser, la réalisation d'une thèse est très loin d'être un travail solitaire. Sans les collaborations, sans mes collègues, mes amis et mes collègues devenus mes amis, je n'y serai pas parvenu. En ce sens, un grand nombre de personnes ayant contribué à ce projet de près ou de loin, méritent d'être remerciées et de voir leur nom sur ces quelques pages.

First, I want to express my gratitude to Pr. A. LIINDSAY GREER for doing me the honour of presiding my jury, and also for the time dedicated to the reading of the manuscript.

I would like to acknowledge the members of the jury for the time they spent to review carefully my manuscript, and of course, attending my PhD defense: MARIANA CALIN, JEAN-JACQUES BLANDIN, and ANNE TANGUY. Warm thanks also are due to the two invited members for their input in this project: SEBASTIEN GRAVIER, and DAVID RODNEY.

Ensuite je tiens à remercier très chaleureusement mes encadrants, pour m'avoir guidée en m'apportant des visions très complémentaires, avec beaucoup de pédagogie et de bienveillance, sur les plans scientifique qu'humain.

Tout d'abord DAMIEN, hormis de nombreuses discussions scientifiques extrêmement riches, merci pour ta confiance durant ce travail. Merci aussi pour la liberté que tu m'as laissée (promis, il n'y a pas d'ironie) pour construire le sujet comme je le souhaitais, avec enthousiasme, sans freiner mes idées et en calmant mes angoisses!

JEAN-MARC, merci pour m'avoir transmis tes connaissances sur les verres métalliques et t'être rendu disponible dès que j'en avais besoin. J'ai beaucoup apprécié la clarté de tes explications et indications qui m'ont permis plus d'une fois, de sortir de la brume!

Je souhaite remercier chaleureusement, SEBASTIEN GRAVIER, ALEXIS LENAIN, GEORGES KAPELSKI, XAVIER CERUTTI et PAUL HERVIER, du SIMAP à Grenoble, pour m'avoir accueilli au sein de leur laboratoire et laissée utiliser leurs équipements tout en me conseillant et s'impliquant dans mon projet.

I also wish to thank a lot HIDEMI KATO and TAKESHI WADA, from Tohoku University. I had the great opportunity to work in their lab during 2 months. Thank you very much for your expertise and your advice.

Ma reconnaissance va aussi à JONATHAN AMODEO pour avoir grandement contribué à l'étude alliant modélisation et expérimental. J'ai beaucoup appris grâce à cette collaboration tant humainement que scientifiquement. Evidemment je remercie DAVID RODNEY, pour ses précieux conseils et son apport d'expérience sur la modélisation de verres métalliques par MD.

Comment ne pas remercier, MATTHIEU BUGNET, qui m'a tout appris sur le MET, l'EELS et la rédaction d'articles. Tu as passé beaucoup de temps à observer et comprendre mes précipités mais aussi à repasser un nombre de fois incalculables sur mon anglais sommaire, sans jamais perdre patience. Bien sûr j'associe SOPHIE CAZOTTES, à ces remerciements, pour les analyses des précipités

et aussi toutes les relectures. De plus, merci à THIERRY DOUILLARD, pour avoir passé un temps incroyable sur l'analyse FIB et la reconstruction de mes volumes.

Merci à MICHEL PEREZ pour s'être intéressé, (presque autant, voire plus que moi !) à mes « hollow precipitates » et m'avoir aidé à comprendre leur formation, avec dynamisme et optimisme, tout en rendant accessible la diffusion, qui était restée un mystère pour moi.

Mille mercis à BENOIT TER-OVANEISSIAN, pour ses nombreuses discussions et conseils sur la corrosion.

Je remercie aussi chaleureusement DANIEL HARTMANN et SANDRA BALVAY, pour avoir réalisé et analysé les tests de biocompatibilité mais aussi avoir pris du temps pour relire et m'expliquer les points que je ne comprenais pas.

Merci à KADER pour avoir usiné tout ce que j'ai pu demander et toujours avec le sourire.

Bien sûr, je remercie toute ma formidable équipe. Ces trois années ont été formidables. L'ambiance, la gentillesse de toutes ces personnes font que j'ai été heureuse de venir travailler chaque jour en me sentant à ma place. Tout d'abord, les permanents: MERCI FRIDA, la maman du labo, ERIC pour avoir animé l'équipe, JEAN-YVES pour être né en 1903 et toujours aussi jeune, JEROME le roi du tomo, PATRICE pour partager tes belles photos de montagne, FLORIAN pour les séances SPS du vendredi, SYLVAIN pour occuper le micro-onde pendant 10 minutes tous les midis, JOEL L. pour m'embêter des que tu passes dans les couloirs, STEPH pour avoir suivi mon élan « Ballon », XTOF pour tes conseils et nos discussions toujours très sympas (et la cuisine d'Odile), XAVIER, der König des Lichtbogenofens, l'équipe Metal'IN (CAROLE et HUGO pour votre bonne humeur), notre voisin de bureau JOEL C., JULIEN, un très bon professeur de dynamique moléculaire et Véronique, toujours prévenante.

Merci à toute la troupe de doctorants qui ont très largement rendu ces trois années intenses, uniques et inoubliables (mais heureusement quand même, c'est la fin!). Tout d'abord, les filles avec qui j'ai démarré le 1<sup>er</sup> octobre 2015 et avec qui nous formions une super triplète: JUSTINE ET GWEN, merci pour nos pauses, débriefs et discussions, vous me manquerez beaucoup! Il y avait déjà une belle bande d'anciens : SEB évidemment, (on sait très bien que les rillettes du Mans sont les meilleures!) MELANIE, gentillesse et douceur réunie, THIBAUT, mon premier co-bureau qui a subi toutes mes plaintes mais dont j'ai subi toutes les farces. WILLIAM (Wiwi), compagnon de Hard Rock, même au Japon. JOSSELIN, pour ton rire communicateur, MORGANE MA., pour nos discussions de voyage, VICTOR, pour tes recettes originales et le yoga, ALETHEA, pour tes soirées déguisées, et enfin JUAN, merci de m'avoir soutenu ici ou au Japon !

Puis nous avons été rejoints par THEO, mon acolyte cinéophile, partant pour toutes les activités. Puis SIBOULETTE (oui, je souhaite que ce nom soit inscrit noir sur blanc pour qu'il perdure dans le temps) pour me faire découvrir toute la discographie de Jojo. Evidemment merci à ma co-bureau aussi MORGANE MO. pour m'avoir bien aidé au Japon et au cours de la thèse.

Puis sont arrivés, ZACK, JULIE, FRANCOIS, GABRIEL, ALEXIS merci d'avoir contribué à continuer cette belle ambiance de groupe, de partage et de bonne humeur =)

Enfin bon courage aux derniers petits nouveaux qui ont débarqués : LUCILE, ALEX, ARNAUD, MARION, FLORE, QINQIN, merci à vous aussi de toujours faire attention à nous, les vieux, pendant la rédaction.

Evidemment je vais terminer par mes co-bureaux actuels, GABRIEL (Gabichou) et ALEXANDRE, on est devenus inséparables en formant le bureau des « dissipés », même si parfois vous êtes insupportables (Haha moi jamais !), que ferai-je sans vous ? Merci de m'avoir supporté aux pires moments.

Bien sûr l'ambiance ne s'arrête pas à l'équipe METAL, et même si beaucoup sont déjà partis, je tiens à remercier notre belle brochette de doctorants MATEIS : NICO, ETIENNE, CLEMENT, CLAIRE, THOMAS, ERIK, MALGO, JOSE, MALO et FANFAN!

Merci aussi à TIANA, GUILHEM et GUILLAUME parce que vous êtes aussi ma deuxième équipe, et que vous m'avez beaucoup aidé et intégrée. Mais aussi merci à SANDRINE CARDINAL pour ton humour et ta disponibilité.

Enfin je vais finir par ceux qui sont là depuis presque toujours, mes copains d'INSA, qui m'ont énormément soutenue, dans n'importe quels moments : APOLLINE, LAURANE, CHARLOTTE, NICO, VIVIEN, ELODIE et LIONEL. Je ne vous remercierai jamais assez.

Je remercie aussi mes beaux-parents, pour nous avoir donné un beau cadre de départ de vie à Lyon.

Je n'oublie pas, évidemment, ma MAMAN qui a toujours tout fait pour moi et grâce à qui j'en suis arrivée là. Je ne te remercierai jamais assez. Merci aussi à ma MAMY, ma TANTE, mon ONCLE et mes COUSIN(E)S, qui sont présents à la moindre difficulté.

Je dédie cette thèse à DANIEL HUBER. Même si tu n'es plus là pour voir l'achèvement de cette thèse, sans le savoir, tu m'as poussé dans la voie de la vulgarisation scientifique.

Enfin, mon chéri, ETIENNE, d'être dans tous mes projets depuis 4 ans, en supportant mon humeur variable, comme tu le fais si bien.

Et mille mercis à Spotify, d'avoir créé une playlist « Travailler en musique ».

## Résumé de la thèse (Français)

Les alliages métalliques amorphes, appelés aussi verres métalliques (noté BMG dans ce travail), connaissent un intérêt grandissant, de par leurs propriétés remarquables comparées à celles des alliages métalliques cristallins. Nous pouvons citer, par exemple, une haute limite élastique due à l'absence de dislocations, mais aussi une résistance élevée à la corrosion provoquée par l'absence de microstructure, ou encore un faible module de Young. Ce dernier point est particulièrement intéressant pour une application en tant que biomatériaux, dans le but d'éviter les phénomènes d'ostéolyses (destruction du tissu osseux). Cependant, ce type de matériaux possède deux inconvénients majeurs : (i) un manque de déformation plastique, ainsi (ii) qu'une taille critique faible, provoquée par la nécessité d'avoir une vitesse de refroidissement très élevée, lors de l'élaboration. Pour pallier ce problème, l'ajout d'éléments avec un petit rayon atomique, comme le beryllium ou l'aluminium, est fréquemment employé. Cependant, ces éléments ne sont pas biocompatibles et peuvent même être dangereux pour le corps humain, sous forme d'ions relargués. L'objectif de cette thèse est donc, tout d'abord, de développer de nouvelles nuances de verres métalliques complètement biocompatibles, puis de définir des axes d'amélioration pour augmenter la taille critique, ainsi que la ductilité de ces matériaux.

Dans une première partie, deux nouvelles compositions biocompatibles ont été développées, la première a été réalisée dans l'objectif d'obtenir un biomatériau résorbable (Mg-Ca-Au-Yb), où l'influence de l'ajout d'Yb a été traité. La seconde a été développée pour réaliser un biomatériau de renfort (Zr-Co-Ga-(Si)-(Sn)), où le remplacement de Al par Ga a été étudié. Une caractérisation complète de ces alliages a ensuite été réalisée : stabilité thermique, résistance à la corrosion, biocompatibilité ou encore propriétés mécaniques.

S'affranchir d'éléments comme l'aluminium, le nickel ou le beryllium peut se révéler difficile pour obtenir des pièces sous forme massive de quelques millimètres de diamètre. C'est pourquoi, dans un second temps, l'objectif a été de trouver des voies d'amélioration, tant au niveau procédé de fabrication, qu'au niveau de la composition du matériau.

Premièrement, en utilisant un système déjà connu, Cu-Zr-Ti, l'addition de terre-rares et plus particulièrement d'yttrium a été étudiée. En ajoutant 1% atomique d'yttrium au système, la déformation plastique a été augmentée d'environ 2%, ainsi que la résistance à la corrosion et la biocompatibilité. La microstructure de l'alliage a été étudiée plus en détails par la microscopie électronique en transmission (MET). Des précipités d' $Y_2O_3$ , créant des zones cristallisées, ont été mis en évidence. Ce sont ces derniers qui semblent responsables d'une augmentation de la ductilité.

Une autre technique de mise en forme, utilisant la métallurgie des poudres, a pu être abordée. La vitesse de refroidissement pour obtenir une poudre métallique par atomisation est particulièrement élevée et permet d'obtenir une poudre complètement amorphe, même pour des systèmes présentant une faible aptitude à former des verres. En utilisant le Spark Plasma Sintering (SPS) comme technique de densification de poudre, la fabrication de composites alliant poudres amorphe et cristalline est possible.

Enfin, le rôle du pré-cyclage mécanique et de la vitesse de déformation sur la réponse mécanique et les mécanismes de déformation ont été étudiés en associant simulation par dynamique moléculaire et essais de compression quasi-statiques. Un échantillon non pré-cyclé présente une déformation très localisée avec une bande de cisaillement principale favorisée, alors qu'un échantillon pré-cyclé présente un mécanisme de déformation plus homogène avec apparition de bandes de cisaillement secondaires. Cet effet dépend aussi de l'amplitude de la contrainte de pré-cyclage.

## PhD abstract *(English)*

Metallic glasses exhibit improved properties compared to pure crystalline metals, as for example, a high strength and a high corrosion resistance, due to the absence of microstructure and also a low Young modulus. This last feature is interesting for use as biomaterials to prevent bone osteolysis due to stress shielding. However, these materials exhibit two main drawbacks: a lack of ductility and a small critical size. To improve these points, most parts of the glasses for biomedical applications still contain toxic elements, such as Be or Al. This work aims to find new fully biocompatible compositions of metallic glasses and suggest three solutions to remedy some issues, based on micro-alloying, powder metallurgy and deformation mechanisms understanding.

In the first part of the work, two new compositions for metallic glasses were elaborated: a Mg-Ca-Au-Yb system for use as bioresorbable materials and a Zr-Co-Ga-(Si)-(Sn) glassy system for use as reinforcement materials. A complete study on the processing and the characterization of the samples has been conducted: thermal stability, also corrosion properties, cytotoxicity and mechanical properties are also crucial to characterize for a use as biomaterials. Mg-Ca-Au-Yb system deals with the influence of the addition of Yb on this system and the Zr-Co-Ga-(Si)-(Sn), deals with the replacement of Al by Ga and minor additions of Si and Sn to improve the corrosion resistance.

However, trying to use only biocompatible elements considerably reduces the possibility to obtain fully amorphous large diameter samples. In that respect, the other part of the work consists to study the possible ways of increasing the samples size, using an Al-free, Ni-free well-known system: Cu-Zr-Ti.

First, yttrium additions in the Cu-Zr-Ti system has been investigated. The optimum amount of yttrium to add and the characterization of this material was conducted. 1 at. % of Y in the Cu-Zr-Ti leads to an increase of 2% of plastic strain, of the corrosion resistance, and biocompatibility. The microstructure was precisely studied using Transmission Electron Microscopy (TEM) observations and some explanation about this improvement can be discussed. To the author knowledge, for the first time, yttrium nano-precipitates with a core-shell structure were observed. This leads to an improvement of the ductility of the material, due to the nano-crystallized areas induced by the precipitates.

Moreover, a new process using the powders metallurgy with Spark Plasma Sintering (SPS) allows the creation of larger sintered samples. Indeed, the cooling rate of the powder is really high compared to a bulk, and amorphous powder can be obtained for low GFA systems. This process is also a good approach to manufacture ex-situ composites samples, adding some ductile particles in the amorphous matrix.

At last, the role of the mechanical pre-cycling and of the strain rate on the stress response and elementary deformation mechanisms were investigated using both atomistic simulation and compressive mechanical tests. Un-pre-strained samples deform due to a local shear banding process while pre-cycled samples are characterized by a more homogeneous deformation. The deformation mechanisms depends on the stress amplitude. This means the lower the stress amplitude of the pre-cycles, the higher the hotspots proportion, and the ductility. A statistical analysis of the vein pattern after fracture was also developed.

## Résumé du chapitre I

Les verres métalliques possèdent des propriétés uniques grâce à leur structure amorphe. Leur absence de microstructure et de joints de grains leur confère des propriétés mécaniques uniques, comme une grande résistance, une haute limite élastique, une très bonne résistance à la corrosion mais aussi un aspect de surface particulièrement brillant, comparé à leurs homologues cristallins. Leur structure isotrope et homogène est aussi un avantage pour la fabrication de petites pièces, ce qui, ainsi, permet des applications dans les domaines de la micromécanique, du biomédical ou de l'horlogerie.

La composition de ces matériaux peut être ajustée en fonction des applications visées. Le choix des éléments peut affecter grandement les propriétés et le comportement du matériau. Un grand nombre de systèmes basés sur un large panel d'éléments a été réalisé et étudié. Toutefois, s'il est possible de choisir les bons éléments pour obtenir les propriétés attendues, tous les systèmes ne forment pas un alliage amorphe. Certains critères ont été mis en place de manière à augmenter la probabilité de former un échantillon amorphe. Néanmoins, la structure désordonnée dépend d'autres paramètres, comme par exemple, la pureté de l'environnement d'élaboration, la pureté des éléments initiaux ou la manière de procéder.

De nouvelles recherches visent cependant à s'affranchir des deux inconvénients majeurs: le manque de ductilité et le faible diamètre critique. La première solution est d'ajouter un faible élément (microalliage), une seconde méthode consiste à changer le procédé d'élaboration pour réaliser des composites. Enfin, une dernière méthode consiste à pré-déformer l'échantillon (rejouvence). Cette dernière technique sera développée dans le dernier chapitre.

Le microalliage d'éléments appropriés peut changer drastiquement le comportement des systèmes amorphes, en particulier, la résistance à la corrosion, la ductilité ou encore la biocompatibilité. L'ajout d'éléments comme les terres-rares, peut être très intéressant pour obtenir un large diamètre critique, ou des échantillons plus stables, avec de meilleures propriétés mécaniques. En effet, ils présentent souvent un large rayon atomique qui permet de stabiliser la phase liquide, ou encore une grande affinité avec l'oxygène permettant de piéger les dernières impuretés.

L'élaboration de composites permet aussi d'augmenter le diamètre critique ainsi que la ductilité. Dans ce but, deux techniques sont possibles : réaliser des composites in-situ ou ex-situ, utilisant différents procédés pendant la trempe, les traitements thermiques ou encore en utilisant la métallurgie des poudres.

Beaucoup de travaux étudient l'élaboration des verres métalliques, leurs améliorations, ou encore, consistent à comprendre leurs mécanismes de déformation.

Précédemment, il a été précisé que les verres métalliques pouvaient être adaptés aux applications biomédicales. Toutefois, aucune composition n'est à ce jour, complètement biocompatible car les éléments tels que l'aluminium, par exemple, sont très difficiles à remplacer.

Le but de ce travail est d'élaborer deux nouvelles compositions biocompatibles, de verres métalliques, pour un usage en tant que biomatériaux dégradables mais aussi de renfort. Ces deux études sont traitées dans les Chapitres 3 avec un système base Mg et 4, avec un système base Zr, respectivement. Néanmoins, il apparaît que les éléments non désirables pour le corps humain sont difficiles à remplacer et jouent un rôle important sur la ductilité et le diamètre critique. L'usage d'éléments biocompatibles uniquement rend l'élaboration particulièrement complexe. Dans le Chapitre 5, un système sans Ni, ni Be ou Al, a permis d'étudier une voie d'amélioration pour obtenir une meilleure ductilité ou diamètre critique : le microalliage d'yttrium. Cela permet de comprendre les mécanismes ayant lieu lors de l'addition de Y dans un système et son effet bénéfique. Dans le même but, le Chapitre 6, propose l'étude d'un autre procédé d'élaboration en utilisant la métallurgie des poudres, de manière à réaliser des plus larges mais aussi des composites, grâce à l'atomisation par gaz et au SPS (Spark Plasma Sintering). Un dernier Chapitre 7 étudie une autre voie d'amélioration de la ductilité de ces alliages en les pré-déformant. L'étude des mécanismes de déformation a été menée parallèlement avec des essais expérimentaux (essais de compression) mais aussi grâce à la modélisation par dynamique moléculaire.

## Résumé du chapitre II

Dans cette partie, l'ensemble des techniques expérimentales sont expliquées et discutées.

Premièrement, l'importance du choix du moyen d'élaboration dépend de la composition : Fusion à l'arc ou fusion par induction pour les alliages initiaux, de manière à éviter le moins de perte de matière possible, tout en conservant une bonne homogénéité chimique. Ensuite, lors de l'élaboration des échantillons, l'épaisseur va être un paramètre clé pour étudier les propriétés souhaitées : rubans en utilisant la trempe sur roue (Chapitre 3 et 4) ou échantillons massifs par moulage (Chapitre 5).

Un autre mode d'élaboration est aussi décrit : la métallurgie des poudres. Cette méthode est caractérisée et développée durant cette thèse. Le procédé consiste à fritter des poudres de verres métalliques, permettant d'obtenir un large diamètre, voire des échantillons composites. Cette technique est décrite dans le Chapitre 6.

Ensuite, divers appareils ont été utilisés pour étudier plus en détails ces matériaux. De nombreuses propriétés sont d'abord vérifiées, pour ensuite envisager une étude visant une application biomatériaux. En effet, ces derniers doivent respecter des normes très strictes. La première étape est une caractérisation basique : Diffraction par rayons X, mesures de densité, mesures de DSC (Differential Scanning Calorimetry). Ensuite, des recherches plus approfondies sont réalisées : études de la stabilité thermiques en utilisant la DSC et la diffraction des rayons X à hautes températures, des observations de la structure grâce à la microscopie en transmission, des tests mécaniques ou de corrosion avec analyse de surface. De plus, des essais de cytotoxicité, de manière à discuter la biocompatibilité des échantillons, sont réalisés. Enfin, des observations par électrons secondaires (SEM) sont faites sur les faciès de rupture.

Ces techniques permettent d'avoir une image complète des matériaux et de leur perspective pour cette thèse.

## Résumé du chapitre III

Dans cette partie, une nouvelle composition de verre métallique biodégradable a été élaborée, utilisant seulement des éléments biocompatibles. L'approche complète, basée sur les critères de formation d'un verre, a été décrite, notamment pour le choix de ce nouveau système.

L'élaboration de ces nouvelles compositions Mg-Ca-Au-Yb et Mg-Ca-Au a été réalisée par fusion par induction de manière à éviter toute vaporisation du Mg, ce qui changerait la composition et affecterait les propriétés de l'alliage. De nombreuses précautions ont été prises quant à l'utilisation de Ca de manière à éviter la formation d'une couche d'oxyde sur le matériau initial, dû à la forte réactivité du calcium avec l'atmosphère.

Ensuite, les rubans ont été élaborés et caractérisés par différents moyens. Après avoir vérifiés les propriétés basiques de ces alliages concernant leur caractère amorphe, leur GFA (aptitude à former un verre) a été mesurée et définit comme étant trop limitée pour pouvoir obtenir un échantillon amorphe, massif. Ensuite, l'ajout de terre-rares (Yb) a été discuté. L'action de ce type d'élément est très bénéfique pour la stabilité thermique du matériau. Il permet notamment d'éviter la relaxation structurale tout en augmentant la résistance à la cristallisation. Une légère amélioration de la résistance à la corrosion semble aussi apparaître. Un développement plus en profondeur de l'action des terre-rares sur un système amorphe sera traitée dans le Chapitre 5.

Cette nouvelle composition biocompatible a été élaborée avec succès. La stabilité thermique est assez grande pour éviter les risques de cristallisation durant le procédé de stérilisation. Le module de Young de ce nouvel alliage est proche de celui du Mg pur, de manière à éviter les problèmes d'ostéolyse. La GFA est encore insuffisante pour pouvoir obtenir un échantillon massif. Cependant, actuellement, il est possible d'envisager une application de revêtement ou de dépôt.

## Résumé du chapitre IV

Dans ce chapitre, une nouvelle composition base Zr a été réalisée sous forme de rubans. L'aluminium a été remplacé avec succès par du Ga. La GFA est assez faible mais augmente considérablement avec l'ajout de 2 at.% de Sn. De par la nature majoritaire en Zr de cet alliage, il démontre de bonnes propriétés mécaniques. Sn et Si ont été ajoutés en faibles quantités de manière à augmenter la résistance à la corrosion, la stabilité thermiques mais aussi et surtout, la biocompatibilité.

L'ajout de Ti dans le système permet réaliser une substitution entre Ti et Zr, ce qui a pour but d'augmenter le désordre et donc l'épaisseur critique. Dans ce but, un plan d'expérience a été établi de manière à comprendre l'influence de chaque élément pour augmenter la probabilité de former un échantillon massif amorphe et trouver la composition optimale. La caractérisation de la phase cristalline est aussi réalisée pour comprendre la difficulté de former un verre avec ce système. Cependant, aucune raison permettant d'expliquer cette faible GFA n'est mise en valeur. L'ajout d'un élément possédant un important rayon atomique et qui pourrait réagir avec les impuretés d'oxygène, tel que l'yttrium, peut-être envisagé. Ce point sera développé dans le chapitre suivant.

Cependant, même si actuellement aucun échantillon massif amorphe n'a été formé, Cette composition novatrice, avec un faible module de Young et sans élément nocif pour le corps humain a été formée. La température de transition vitreuse étant élevée, de larges perspectives peuvent être proposées grâce au procédé de frittage.

## Résumé du chapitre V

Un système base Cu déjà connu est le sujet d'étude de ce chapitre, pour une utilisation en tant que biomatériau. L'ajout de Y est aussi étudiée de manière à augmenter la GFA et la déformation plastique de l'échantillon, qui sont des paramètres critiques. Le microalliage est une technique très intéressante pour augmenter ces deux propriétés. Cela conduit à une augmentation de la GFA, de la stabilité thermique, la déformation plastique, la résistance à la corrosion ainsi que de la biocompatibilité. Même si les alliages contiennent un large pourcentage de cuivre, en présence de fluides type « corps humain », en présence de protéines, la dégradation est ralentie et le potentiel de corrosion est relativement proche de celui d'un échantillon de TA6V. De plus un palier de passivation apparaît grâce à la présence d'albumine dans le milieu, ce qui reflète un comportement viable en tant que biomatériaux dans des conditions assez proches du corps humain. Cependant, il existe un optimum de 1 at.% au-delà duquel les propriétés semblent diminuer.

Néanmoins, l'yttrium montre une grande affinité avec l'oxygène, ce qui permet l'augmentation des propriétés mécanique et de résistance à la corrosion. En effet, ceci est dû à la présence de précipités d'yttria, observés en transmission et formés durant la fusion et induisant des zones cristallines lors du refroidissement par moulage. Deux types de précipités sont remarqués, des petits pleins et des larges avec une cavité. L'hypothèse de cette formation repose sur l'effet Kirkendall et une différence des coefficients de diffusion entre l'oxygène et le zirconium.

Ce nouveau matériau peut trouver une place pour des applications telles que les dispositifs de contraception intra-utérins. En effet, grâce à l'importante proportion de Cu, l'effet spermicide et la légère irritation de la paroi utérine peuvent avoir lieu, empêchant l'implantation. De plus, le caractère amorphe implique une résistance à la corrosion plus importante que les dispositifs actuels, ce qui permet de s'affranchir de la présence d'argent, initialement prévue pour contrôler la dégradation du Cu.

## Résumé du chapitre VI

Une nouvelle méthode d'élaboration de verres métalliques a été testée, discutée et optimisée : le frittage de poudre. La première étape consiste à étudier l'influence de deux paramètres : la durée de frittage et la température de frittage de manière à obtenir des échantillons bien densifiés pour la caractérisation des diverses propriétés. Les études conduisent à envisager un procédé avec un temps faible, 5 min, à une température un peu plus élevée, 435°C. L'échantillon ainsi élaboré présente un diamètre d'environ 1 cm, ce qui est bien supérieur au diamètre obtenu par moulage. Cependant, les propriétés de résistance à la corrosion, de stabilité thermique ou encore la limite élastique sont toutes diminuées. Pour obtenir des propriétés plus proches d'un échantillon obtenu par coulée et moulage, il faut introduire des particules cristallines et ainsi obtenir un échantillon composite. Dans cette partie, 30 mas.% est la meilleure fraction à ajouter pour obtenir de bonnes propriétés mécaniques. Cette dernière est déjà une fraction conséquente. L'optimisation du procédé peut encore être approfondie pour se rapprocher des propriétés d'un échantillon obtenu grâce à la fusion à l'arc.

Plusieurs voies d'amélioration découlent de ce travail, notamment la réalisation de composites in-situ, permettant d'éviter la présence d'interfaces entre les grains de poudre, ce qui diminue les caractéristiques mécaniques. D'autres essais pourraient être envisagés en utilisant des poudres non sphériques, permettant une meilleure compacité.

## Résumé du chapitre VII

Un des moyens suscitant un intérêt grandissant, depuis quelques années, de la part des scientifiques pour introduire de la déformation plastique dans les verres métalliques, est la technique de rejeuence. Celle-ci s'oppose à la relaxation structurale et permet d'atteindre un état de plus haute énergie avec plus de volume libre et plus de défauts. Cette introduction de défaut conduit à une augmentation de la déformation plastique du matériau et peut-être provoquée par divers moyens, thermiques ou mécaniques.

Dans ce chapitre, une technique consiste à réaliser une pré-déformation d'un système par pre-cyclage en compression. Le nombre de cycles (2, 4 et 6) ainsi que l'influence de l'amplitude de la contrainte (400, 700 and 1200 MPa) sont présentés. Un effet très bénéfique d'un pré-cyclage à 400 MPa est mis en avant, même pour un très faible nombre de cycles. Ces résultats expérimentaux sont associés à des résultats de modélisation par dynamique moléculaire, de manière à comprendre les mécanismes élémentaires à l'échelle atomique. Il apparaît que deux mécanismes de déformation existent : une localisation très forte, pour des échantillons qui n'ont pas subi de pré-cyclage et une déformation plus homogène pour des échantillons cyclés. Le pré-cyclage conduit donc à une augmentation des défauts et donc de site de nucléations des bandes de cisaillement, régissant la déformation.

Une corrélation entre ces résultats et une analyse statistique de la taille des vein-patterns présentés sur le plan de fracture a été réalisée.

Enfin, une transposition de ces résultats à l'effet de vitesse a aussi été conduite.

# List of Contents

LIST OF CONTENTS .....	I
LIST OF FIGURES .....	VII
LIST OF TABLES .....	IX
INTRODUCTION .....	2
CHAPTER I .....	9
STATE OF ART ON METALLIC GLASSES FOR BIOMEDICAL APPLICATIONS .....	9
<b>1-1- Background about metallic glasses .....</b>	<b>9</b>
<b>1-1-1- What is a glass? .....</b>	<b>9</b>
<b>1-1-2- Stability of an amorphous system .....</b>	<b>10</b>
<b>1-1-3- Technique of fast quenching .....</b>	<b>11</b>
<b>1-1-4- Thermal Stability of a glassy system .....</b>	<b>13</b>
<b>1-1-5- Characterization of the glass forming ability .....</b>	<b>14</b>
<b>1-1-6- Mechanical behaviours of a metallic glass .....</b>	<b>15</b>
<b>1-1-6-1- Existence of two distinct behaviours .....</b>	<b>15</b>
<b>1-1-6-2- High temperature behaviour .....</b>	<b>17</b>
<i>1-1-6-2-1- Viscosity of metallic glasses</i> .....	17
<i>1-1-6-2-2- Fragility concept</i> .....	18
<b>1-1-6-3- Low temperature behaviour .....</b>	<b>19</b>
<i>1-1-6-3-1- Structural properties</i> .....	19
<i>1-1-6-3-2- Shear bands</i> .....	21
<i>1-1-6-3-3- Fracture in metallic glasses</i> .....	25
<i>1-1-6-3-4- Fracture modes</i> .....	26
<b>1-2- Criteria for glass formation .....</b>	<b>29</b>
<b>1-3- Attractive properties of the metallic glasses .....</b>	<b>30</b>
<b>1-4- Applications .....</b>	<b>32</b>
<b>1-5- Examples of metallic glasses (biomaterials) .....</b>	<b>33</b>
<b>1-5-1- Reinforcement materials .....</b>	<b>33</b>
<i>1-5-1-2- Zr-based BMGs</i> .....	33
<i>1-5-1-3- Ti-based BMGs</i> .....	34
<b>1-5-2- Biodegradable Materials .....</b>	<b>35</b>
<i>1-5-2-1- Mg-Based BMGs</i> .....	35
<i>1-5-2-2- Ca-based BMGs</i> .....	36
<i>1-5-2-3- Zn-based BMGs</i> .....	36
<i>1-5-2-4- Sr-based BMGs</i> .....	37
<b>1-6- Improvements of the bulk metallic glasses systems .....</b>	<b>37</b>
<b>1-6-1- Microalloying .....</b>	<b>37</b>

1-6-1-1- <i>Kinds of minor addition</i>	37
1-6-1-2- <i>Effects on the GFA</i>	42
1-6-1-3- <i>Enhancement of the properties</i>	45
1-6-1-4- <i>Empirical rules</i>	47
<b>1-6-2- Composites manufacturing</b>	47
<b>1-6-3- Porous metallic glasses</b>	49
<b>1-7- Conclusion</b>	<b>50</b>
<b>1-8- References</b>	<b>52</b>
<b>CHAPTER II</b>	<b>69</b>
<b>EXPERIMENTAL TECHNIQUES</b>	<b>69</b>
<b>2-1- Materials Processing</b>	<b>69</b>
<b>2-1-1- Master alloys processing</b>	69
<b>2-1-2- Samples processing</b>	71
2-1-2-1- <i>Bulk metallic glass samples</i>	71
2-1-2-2- <i>Ribbon metallic glass samples</i>	73
2-1-2-3- <i>Sintered Samples</i>	73
<b>2-1-3- Samples studied</b>	74
<b>2-2- Characterization of the samples</b>	<b>75</b>
<b>2-2-1- Structural Characterization</b>	75
2-2-1-1- <i>Density</i>	75
2-2-1-2- <i>X-Ray Diffraction (XRD)</i>	75
2-2-1-3- <i>Transmission Electron Microscopy (TEM)</i>	76
2-2-1-4- <i>Energy Dispersive X-Ray Spectroscopy (EDX)</i>	77
<b>2-2-2- Thermal Characterization</b>	77
2-2-2-1- <i>Differential Scanning Calorimetry (DSC)</i>	78
2-2-2-2- <i>High Temperature XRD</i>	79
<b>2-2-3- Mechanical Characterization</b>	80
2-2-3-1- <i>Compressive tests</i>	80
2-2-3-2- <i>Nanoindentation tests</i>	81
2-2-3-3- <i>Hardness measurements</i>	81
<b>2-2-4- Biocompatibility Characterization</b>	82
2-2-4-1- <i>Corrosion resistance</i>	82
2-2-4-2- <i>XPS analysis</i>	83
2-2-4-3- <i>Cytotoxicity tests</i>	83
<b>2-3- Conclusion</b>	<b>84</b>
<b>2-4- References</b>	<b>85</b>
<b>CHAPTER III</b>	<b>88</b>
<b>ROLE OF YTTERBIUM ON THE PROPERTIES OF A NEW BIODEGRADABLE METALLIC GLASS SYSTEM</b>	<b>88</b>
<b>3-1- The reason for a new Mg-based composition</b>	<b>88</b>
<b>3-2- Development of a new alloy and study of the influence of Ytterbium on the properties of a Mg-based metallic glass</b>	<b>90</b>

3-3-	Outlooks on this new processed alloy .....	96
3-4-	Conclusion .....	98
3-5-	References.....	98
CHAPTER IV .....		102
AL SUBSTITUTION BY GA TO PROCESS BIOCOMPATIBLE ZR-BASED METALLIC GLASS .....		102
4-1-	The need for a new Zr-based composition .....	102
4-2-	Processing and characterization of a new biocompatible Zr-based composition.....	103
4-3-	From the ribbons to the bulk samples: Experimental Design .....	109
4-3-1-	Increase of the glass forming ability and critical diameter .....	109
4-3-2-	Experimental Design.....	110
4-3-3-	Results and Discussion .....	112
4-4-	Further investigations about promising non-fully amorphous samples.....	117
4-4-1-	Mechanical properties.....	117
4-4-2-	Investigation about the crystalline phase .....	118
4-4-2-	Potential applications.....	120
4-5-	Conclusion .....	120
4-6-	References.....	121
CHAPTER V .....		124
SUGGESTED IMPROVEMENT OF THE CRITICAL DIAMETER AND OF THE LACK OF DUCTILITY ON A WELL-KNOWN CAST SYSTEM FOR BIOMEDICAL USE .....		124
5-1-	Improvement of mechanical, thermal, and corrosion properties of Ni- and Al-free Cu–Zr–Ti metallic glass with yttrium addition .....	124
5-2-	Corrosion resistance in RPMI medium .....	145
5-3-	Structural investigations on the Y <sub>2</sub> O <sub>3</sub> precipitates.....	147
5-3-1-	Experimental methods .....	147
5-3-2-	Structural and chemical analysis of the precipitates surroundings .....	148
5-3-3-	3D distribution of the precipitates and crystallized phases in the volume .....	149
5-3-4-	Discussion about hollow Y <sub>2</sub> O <sub>3</sub> precipitate formation.....	152
5-3-5-1-	Formation of the precipitate and the crystallised areas	152
5-3-5-2-	Determination of the second phase inside the precipitate	153
5-3-5-2-	Hypothesis of Kirkendall effect	154
5-5-	References.....	158
CHAPTER VI .....		162
SINTERED METALLIC GLASSES AND COMPOSITES BY PLASMA SINTERING.....		162

<b>6-1- Reminders of powder metallurgy .....</b>	<b>162</b>
6-1-1- Powders processing .....	163
6-1-2- Densification of the samples .....	164
<b>6-2- Sintered samples and optimization of the process .....</b>	<b>168</b>
6-2-1- Manufacturing and characteristics of the powders .....	168
6-2-2- Optimization of the sintering process .....	170
6-2-2-1- Processing of sintered samples .....	170
6-2-2-2- Characterization of the sintered samples .....	175
<b>6-3- Improvement of the system by composite samples processing .....</b>	<b>179</b>
6-3-1- Processing of the composites samples .....	179
6-3-2- Characterization of the composites samples .....	182
6-3-2-1- Thermal Stability .....	182
6-3-2-2- Corrosion resistance .....	183
6-3-2-3- Mechanical Tests .....	183
<b>6-4- Conclusion .....</b>	<b>189</b>
<b>6-5- References .....</b>	<b>190</b>
<b>CHAPTER VII .....</b>	<b>197</b>
<b>INFLUENCE OF THE REJUVENATION MECHANISMS ON THE DUCTILITY OF BMGS .....</b>	<b>197</b>
<b>7-1- Rejuvenation in metallic glasses .....</b>	<b>197</b>
7-1-1- What is rejuvenation? .....	197
7-1-1- How to obtain rejuvenation? .....	198
<b>7-2- Methods .....</b>	<b>202</b>
7-2-1- Experimental compressive tests .....	202
7-2-2- Simulation methods .....	204
<b>7-3- Results .....</b>	<b>205</b>
7-3-1- Mechanical properties of pre-cycled Cu-Zr metallic glass: experimental results .....	206
7-3-2- Mechanical properties of pre-cycled Cu-Zr metallic glass: molecular dynamics simulations .....	207
<b>7-4- Discussion about elementary deformation processes responsible for the ductility increase .....</b>	<b>209</b>
7-4-1- Fracture plane topology analysis .....	210
7-4-1-1- Vein pattern size analysis .....	210
7-4-1-2- Discussion about the toughness evaluation .....	212
7-4-1-3- Differences on the pre-cycling amplitude .....	213
7-4-2- Verification using molecular dynamics and complementary experimental analysis .....	214
7-4-2-1- Complete study of $N$ and $\sigma_c$ using molecular dynamic .....	214
7-4-2-1- Adaptation to the strain rates influence .....	215
<b>7-5- Conclusion .....</b>	<b>217</b>
<b>7-6- References .....</b>	<b>217</b>
<b>CONCLUSION .....</b>	<b>222</b>



# List of Figures

## CHAPTER 1

Figure 1-1 : Variations of the specific volume or enthalpy versus temperature of pure substance. $T_g$ and $T_m$ correspond to the glass transition temperature and melting temperature respectively <sup>2</sup> .....	10
Figure 1-2 : Evolution of the atomic compactness due to the structural relaxation or crystallization mechanisms .....	11
Figure 1-3: Conventional DSC curves obtained for a metallic glass <sup>61</sup> .....	13
Figure 1-4: Compressive Stress-Strain curves of a metallic glass (Vitreloy 1) <sup>74</sup> .....	16
Figure 1-5: Map of the deformation of metallic glasses by Spaepen <sup>76</sup> .....	17
Figure 1-6: Comparison of the data for several glass-forming liquids and the universal curve <sup>78</sup> .....	18
Figure 1-7: Angell classification of the different alloys from the most fragile to the strongest <sup>79</sup> .....	19
Figure 1-8: Atomic jump description <sup>76</sup> .....	20
Figure 1-9: Atomic cluster of Miracle : a) 2D clusters; b) 3D clusters <sup>92</sup> .....	21
Figure 1-10: Schematic representation of the different steps in the shear banding phenomenon <sup>96</sup> .....	22
Figure 1-11 : Schematic representation of STZ <sup>73</sup> .....	23
Figure 1-12: Schematic representation of the Quasi-Point Defect model <sup>102</sup> .....	23
Figure 1-13: Propagation front of a shear band according to the model by Shimizu and Ogata <sup>103</sup> .....	24
Figure 1-14: Schematic representation showing of the shear band formation under compressive load.....	24
Figure 1-15: Side view of the sample fractured at the strain rate of $1 \times 10^{-3} \text{ s}^{-1}$ in tension a), in compression b) <sup>114</sup> .....	26
Figure 1-16: Typical cleavage mode under compression of $\text{Fe}_{65.5}\text{Cr}_4\text{Mo}_4\text{P}_{12}\text{C}_5\text{B}_{5.5}$ with a fracture stress about 3000 MPa <sup>115</sup> .....	27
Figure 1-17: Fragmentation of Co-based BMG. Surface fracture during fragmentation <sup>117</sup> .....	27
Figure 1-18: SEM picture of the vein pattern on the fracture plane on a Cu-based BMG .....	28
Figure 1-19: a) SEM micrograph of the fracture surface overview of the typical brittle BMG showing mist and mirror regions. b) Typical periodic striped patterns in the mirror region on the fracture plane of Mg-based BMG. c and d) show a higher magnification of the periodic corrugations <sup>126</sup> .....	29
Figure 1-20: Compressive stress-strain curves of a crystalline Ti-alloy and $(\text{Cu}_{60}\text{Zr}_{30}\text{Ti}_{10})_{99}\text{Y}_1$ .....	30
Figure 1-21: Ashby Map of metallic glasses <sup>132</sup> .....	31
Figure 1-22 : Examples of applications using metallic glasses <sup>141</sup> .....	33
Figure 1-23: a) 2D and b) 3D representative mouse femur with an intramedullary CMZSY HE-BMG for 4 weeks.. .....	35
Figure 1-24: Surface topology of the Ca-based samples after different surface treatments, a) 15 min water etching .....	36
Figure 1-25: Potentiodynamic polarization curves of $\text{Zr}_{65-x}\text{Hf}_x\text{Cu}_{17.5}\text{Ni}_{10}\text{Al}_{7.5}$ ( $x=0, 1$ and $2$ at.%) alloys in 3% NaCl solution <sup>235</sup> .....	46
Figure 1-26: Two different kinds of composite samples.....	48
Figure 1-27: Summary of the composites samples process .....	49
Figure 1-28: Image of 88%-porosity $\text{Pd}_{43}\text{Ni}_{10}\text{Cu}_{27}\text{P}_{20}$ foam <sup>251</sup> .....	50

## CHAPTER 2

Figure 2-1: Induction melting device picture <sup>1</sup> .....	70
Figure 2-2: Arc melting device in SIMAP Laboratory, Grenoble.....	71
Figure 2-3: Principle of the tilt-casting experiment <sup>2</sup> .....	72

Figure 2-4: Schematic representation of the suction casting experiment <sup>3</sup> .....	73
Figure 2-5: Principle of the melt-spinning device picture <sup>4</sup> .....	74
Figure 2-6: Principle of XRD measurement <sup>5</sup> .....	76
Figure 2-7: Examples of XRD diffractograms for amorphous alloys and crystalline peaks <sup>6</sup> .....	76
Figure 2-8: Example of a typical DSC curve for metallic glasses of Al-Ni-Y system .....	79
Figure 2-9: Schematic representation of the heating during the high-temperature XRD experiments. ....	80
Figure 2-10: a) 3D picture of the evolution of the crystallization in the Cu-based BMG sample, b) Graph showing the evolution of the intensity of the peaks depending on the time .....	80
Figure 2-11: Optical micrograph of indent; the induced crack allows the determination of the toughness <sup>14</sup> ....	82
Figure 2-12: Three electrodes assembly for the evaluation of the corrosion resistance.....	83

### CHAPTER 3

Figure 3-1: Mixing enthalpy, atomic radius difference for alloying with titanium to evaluate the GFA, with biological safety information <sup>15</sup> .....	89
Figure 3-2: Mixing enthalpy and atomic radius difference for alloying with magnesium to evaluate GFA, with biocompatibility data .....	89
Figure 3-3: Mixing enthalpy and atomic radius difference of the system Mg-Ca-Au .....	90
Figure 3-4: Immersion tests in SBF of the samples without Yb a) and with Yb b).....	97

### CHAPTER 4

Figure 4-1: Comparison of the properties between Al and Ga based on th data of Takeuchi and Inoue's work <sup>9</sup> .....	103
Figure 4-2: Micrograph of the samples with the border line between the amorphous area and the crystalline area .....	112
Figure 4-3: Intensity of the crystalline peak appearing on the XRD diffractogram for the different Zr/Ti ratio of the experimental design: $Zr_{56+y-x}Ti_xCo_{28-y}Ga_{16}$ with $x=0, 5, 10$ and $46$ and $y=-5, 0, 5, 10$ .....	113
Figure 4-4: Coloured map of the $Zr_{56+y-x}Ti_xCo_{28-y}Ga_{16}$ experimental design summarizing the evolution of the size of the amorphous area with $x$ , the Ti content and $y$ , the cobalt content .....	114
Figure 4-5: Coloured map of the $(Ti_{82} Zr_{18})_{56+x+y}Co_{28-x}Ga_{16-y}$ experimental design summarizing the size of the amorphous areas .....	115
Figure 4-6: Representation of the $(Zr_{55}Ti_{12}Co_{33})_{84+x}Ga_{16-x}$ experimental design .....	116
Figure 4-7: XRD diffractograms data of all the processed samples of the experimental design .....	116
Figure 4-8: Stress-strain curves of the compressive tests of the non-fully amorphous samples.....	117
Figure 4-9: DSC curves of the three samples to evaluate the melting temperatures.....	18
Figure 4-10: SEM micrographs and EDX analysis of the dendritic phase .....	119

### CHAPTER 5

Figure 5-1: Polarization curves for the Cu-Zr-Ti-Y system in different electrolyte solutions: NaCl, NaCl+Albumin, RPMI .....	146
Figure 5-2: Schematic representation of the FIB experiment .....	148
Figure 5-3: a), b) TEM micrograph of the two kinds of precipitates, with and without the surrounding crystalline areas.....	149
Figure 5-4: EDX maps of the precipitate and the surrounding crystallized area.....	149
Figure 5-5: (A) Distribution of the large crystalline areas (In-Lens low voltage, SE imaging), (B) Visualization of a few crystalline areas with a few Y2O3 precipitates (In-Lens low voltage SE imaging). The triangular shape is induced by the random cross-section. Insert is a standard Everhart-Thornley SE imaging of a selected area which shows more punctual elements (small dark contrasts) within the dendrite (C)Low loss in-Lens BS imaging of crystalline area. (D) ISI-SIM imaging of a few crystalline area and a precipitate .....	150

Figure 5-6: 3D FIB/SEM reconstructed views of (A) Crystallized area in the volume (red and green) and yttria precipitates (yellow), (B) Extracted dendrite-like structures detected in 2D by surface observations in SEM (7.6%vol here). Within a significant crystallized area, a cuboid precipitate (220nm x 140 nm x 215nm) in yellow contain a nanometric pore. (C) Extracted small crystallized volumes and cuboid precipitates less than 50 $\mu\text{m}$ width. (D) Reconstructed view of a crystalline area with a large precipitate .....	152
Figure 5-7: Analyse of the second phase in the middle of the precipitates, using different acceleration voltage or detector .....	153
Figure 5-8: Low voltage Everhart-Thornley SE imaging of 4 hollow yttria precipitates. Several morphologies are visible from spherical to cubical. (White particules are colloidal silica particles used for polishing) .....	154
Figure 5-9: Schematic representation of Kirkendall effect in these samples.....	155
Figure 5-10: Evolution of the concentration in Y and O in the oxide layer .....	156
Figure 5-11: Evolution of $r_1$ and $r_2$ depending on the time .....	157

## CHAPTER 6

Figure 6-1: Schematic representation of the gas atomization technique <sup>15</sup> .....	163
Figure 6-2: Principle of the milling/grinding technique <sup>19</sup> .....	164
Figure 6-3: Processing of powder by electrolysis <sup>20</sup> .....	164
Figure 6-4: Current and heat repartition in the metallic powder and in the die during the SPS <sup>7</sup> .....	165
Figure 6-5: Schematic representation of the device used for the sintering of the sample <sup>21</sup> .....	165
Figure 6-6: Hot Pressing schematic representation <sup>25</sup> .....	166
Figure 6-7: Picture of the Hot Isostatic Pressing (HIP) <sup>28</sup> .....	166
Figure 6-8: Picture of the Powder Rolling process to obtain consolidated samples <sup>29</sup> .....	167
Figure 6-9: Picture of the extrusion process <sup>25</sup> .....	167
Figure 6-10: Amorphous powder $\text{Cu}_{60}\text{Zr}_{30}\text{Ti}_{10}$ before calibration .....	169
Figure 6-11: a) XRD spectrum of the Cu-Zr-Ti powder, b) DSC curve of the elaborated powder, with the black arrow for $T_g$ .....	170
Figure 6-12: Schematic representation of the sintering process .....	171
Figure 6-13: XRD diffractograms of the samples sintered at different temperatures .....	171
Figure 6-14: Influence of the sintering time on the amorphous characteristic of the sintered samples .....	172
Figure 6-15: High load hardness measurements. The black points noticed on the picture of the 435 °C-5min sample are due to the polishing. It doesn't correspond to porosities. ....	174
Figure 6-16: SEM micrographs after sintering process a) 435°C during 5 min, b) 440°C during 3 min.....	174
Figure 6-17: DSC curves of the sintered sample $\text{Cu}_{60}\text{Zr}_{30}\text{Ti}_{10}$ (20 K/min).....	175
Figure 6-18: Non-isothermal high temperature XRD experiments a), c) sintered sample b), d) cast sample ....	176
Figure 6-19: Isothermal high temperature XRD measurements a, c) sintered sample, b, d) cast sample.....	176
Figure 6-20: Evolution of the crystallized fraction in the cast and the sintered samples .....	177
Figure 6-21: a) Polarization curves comparing two samples: sintered and cast. b) Photograph of the sample surface after the corrosion test. ....	178
Figure 6-22: Compressive tests of the cast sample (green) and sintered sample (red) at $1.2 \times 10^{-4} \text{ s}^{-1}$ .....	179
Figure 6-23: SEM Micrograph of the Ti-6Al-4V powder .....	180
Figure 6-24: SEM micrographs of the crystalline particles distribution and surface observations.....	181
Figure 6-25: (Left) XRD diffractograms of the three samples: 0%, 10% and 30% Ti-6Al-4V, (Right) Comparison with the powder before sintering process.....	182
Figure 6-26: High temperature XRD 3D-spectra for the sample with 10% Ti-6Al-4V, a) isochronal measurement, b) isothermal measurement at $T=460 \text{ }^\circ\text{C}$ .....	182
Figure 6-27: Polarization curves of all the samples: cast, 0%, 10% and 30% Ti-6Al-4V .....	183
Figure 6-28: Compression tests of all the elaborated sintered composite samples compared to the cast sample .....	184
Figure 6-29: SEM micrographs of the fracture pieces of the sintered samples: a) 0% particles, b) 10% particles, c) 30% particles .....	185

Figure 6-30: Higher magnification on the fracture topology a) 0% of crystalline particles, b) 10% and c) 30% Ti-6Al-4V.....	186
Figure 6-31: SEM micrographs of vein patterns of the composites fracture topology samples a) 10% and b) 30% .....	187
Figure 6-32: SEM picture of the bad quality of densification at the bottom of the 30% Ti-6Al-4V sample.....	188
Figure 6-33: EDX map analysis of the fracture topology of the 30% sample .....	188

## CHAPTER 7

Figure 7-1: Schematic representation amorphous structures differences between structural relaxation and rejuvenation <sup>4</sup> .....	198
Figure 7-2: Schematic representation of the High-Pressure Torsion (HPT) technique <sup>10</sup> .....	199
Figure 7-3: a) Picture of the compressive apparatus, b) schematic representation of the sample setting up.....	203
Figure 7-4: Picture of the measurement method to determine the vein pattern area in order to study the pre-cycling influence. The measurement number increases to 3000 for the strain rate influence study. ....	204
Figure 7-5: Picture of the Cu-Zr sample before and after replication .....	205
Figure 7-6: Stress-Strain curve for pre-cycled samples, at 400 MPa, 700 MPa and 1200 MPa, 2,4 and 6 cycles.....	206
Figure 7-7: Yield strength values a) and plastic strain values b) obtained from the stress-strain curves of the pre-cycled samples .....	207
Figure 7-8: a) Illustration of the deformation mechanisms for different cooling rates, b) for different strain rates. Only atoms with $D^2 > 100$ are shown with yellow atoms corresponding to higher values of $D^2$ . ....	208
Figure 7-9: a) Compressive tests of an as-quenched sample, b) compressive test of a pre-cycled sample, $N=4$ , $\sigma_c = 200$ MPa .....	209
Figure 7-10: a) Distribution of the vein pattern areas for an as-cast sample, a pre-cycled sample at 400 MPa and another one at 1200 MPa (1000 measurements for each sample), b) Box-plot of the distribution of the vein pattern areas.....	211
Figure 7-11: $K_c$ distribution calculated from the size of the vein pattern measured for the three samples: pre-cycled at 400 MPa, 1200 MPa and no pre-cycled .....	213
Figure 7-12: SEM pictures of the samples $N=4$ , $\sigma_c = 1200$ MPa (left), and the sample $N=4$ , $\sigma_c = 400$ MPa (right) .....	214
Figure 7-13: Schematic representation of the three steps mechanisms observed during experimental tests and atomistic simulation.....	215
Figure 7-14: a) Distribution of the vein pattern area for different strain rates, b) Box-plot analysis of the distribution.....	216
Figure 7-15: Evolution of the deformation mechanisms depending on the compressive strain rate .....	217



# List of Tables

## CHAPTER 1

Table 1: Description of the metallic glasses system with critical size > 10 mm <sup>38</sup> .....	12
Table 2 : Values of K <sub>c</sub> for different BMGs .....	26
Table 3 : Summary of the effects of minor additions of metalloid elements in different bulk metallic glasses <sup>159</sup> .....	38
Table 4: Summary of the effects of minor additions of metallic elements in different bulk metallic glasses <sup>185</sup> ..	37
Table 5: Summary of the effects of minor additions of rare-earth elements in different bulk metallic glasses <sup>185</sup> .....	38

## CHAPTER 2

Table 1: Table indicating the different samples used during this PhD .....	74
--	----

## CHAPTER 4

Table 1: Presentation of the different compositions of the Zr-Co-Ga-Ti system, according to the experimental design Zr <sub>56+y-x</sub> Ti <sub>x</sub> Co <sub>28-y</sub> Ga <sub>16</sub> .....	110
Table 2: All the compositions of the three experimental design .....	111
Table 3: Composition of the first experimental design .....	113
Table 4: Summarizing of the melting temperature of the three samples .....	118

## CHAPTER 6

Table 1: Summarizing of the advantages/drawbacks of the densification techniques .....	167
Table 2: EDX Results of the processed sample .....	169
Table 3: Characteristics of the sintered samples depending on the time .....	173
Table 4: Characteristics of the elaborated composites samples .....	180

## CHAPTER 7

Table 1: Variability of K <sub>c</sub> depending on the chosen size of the vein patterns .....	213
--	-----



# Introduction

---

# Introduction

Biomaterials are synthetic or natural substances used for a period in the human body to treat or replace any organ, tissue or part of the body. As biomaterials are not inert and interact with the body, they cause a biological response. For this reason, they have to respect strict specifications. Several materials are used for a long time for this purpose, as for example metals, polymers or ceramics. The first traces of the metallic alloys as biomaterials date back the seventh century B.C., with the use of gold by Etruscan people to fix tooth crown. Then, metallic alloys for biomedical applications have been widely developed since the 16<sup>th</sup> century, as they are very interesting due to their ductility and malleability, their high resistance to fracture, good conductivity and also shininess. The most commonly used are gold, Ti-6Al-4V or Cr-Co alloys. However, their lifetime is limited by the degradation and current research shows a potential toxicity from the Al or Cr, as released ions. Bioceramics or bioglasses have been developed as dental or bone implants since the beginning of the twentieth century, after discovering that these kinds of materials can create bonds with the body. They also exhibit good resistance to abrasion and corrosion. Moreover, they have the properties of being quasi-inert in the body but also exhibit a large brittleness.

For the past few decades, a new type of materials became an issue of growing importance for the biomaterials community: the metallic glasses. They are processed using the fast-quench technique. The first one was processed under ribbons form by Duwez et al. in Caltech in 1960, using the melt spinning technique. Because of the very high cooling rates, only limited thicknesses are reachable to obtain a fully amorphous samples.

Their structure exhibits a disordered feature composed of randomly placed atoms. The amorphous structure gives them two main interesting properties: First, they experience a glass transition and a supercooled liquid state. In this range of temperature, the viscosity is well-controlled, which is an advantage for the machining of the materials. They also exhibit an absence of microstructure and crystalline defects, as dislocation, governing the mechanical properties. Thus, metallic glasses are stronger than their crystalline counterparts. They also show an absence of grain boundaries, which increases the corrosion resistance.

Thanks to all these promising properties, metallic glasses find an interest in the wide range of areas: sport equipment, jewellery, biomaterials as dental implants or even in electronics.

The composition can be chosen and controlled depending on the targeted applications. According to the movements, a wide range of systems have been developed over the years, as shown in Fig. i. Mg, Ca, Sr and Zn-based systems can be used, especially for the biodegradable materials. In the opposite, Zr- and Ti-based BMGs are used for reinforcement applications.

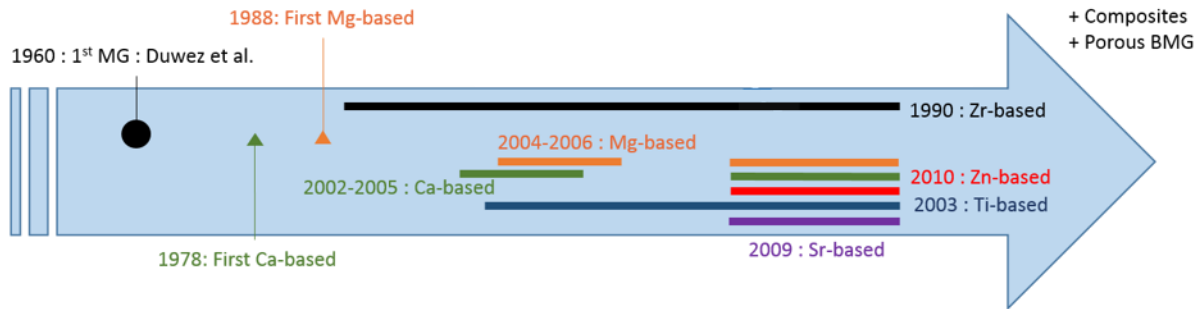


Figure i: History of the metallic glasses developments (biomaterials)

However, this kind of material exhibits two main drawbacks. First, during mechanical tests at room temperature, metallic glasses show a lack of ductility: even if their compression failure is not as catastrophic as in tension, the ductility is still very low. Secondly, due to the high cooling rate of the processing, the diameter of the fully amorphous samples is limited to few millimetres. The critical size strongly depends on the composition and some records have been established with centimetres samples (Pd- or Zr-based) but the most part of the systems are smaller than one centimetre diameter.

To prevent these two drawbacks, small atoms, such as Be or Al are often added. However, they are not fully biocompatible with the human body. At this time, no real fully biocompatible composition has been processed yet.

Thus, the purpose of this PhD work is to process and characterize new fully biocompatible metallic glass compositions and understand the deformation mechanisms. First of all, the development of new biocompatible compositions is explained and discussed. However, as these new compositions exhibit a small glass forming ability, some techniques to improve the small critical diameter and the lack of ductility have been performed on a well-known Ni-, Al- free Cu-based system. These improvements rely on a change of composition and of the process but also on a deformation mechanisms understanding, to increase the ductility.

In order to secure this objective, this PhD work is composed of seven chapters organized as follows:

Starting with **the bibliography chapter**, general properties and attractive features of the bulk metallic glasses compared to other crystalline materials are developed. All the potential systems used in the biomedical field are described. Then, the deformation mechanisms are discussed to understand the distinctive characteristics of the metallic glasses. Eventually, a description of the current findings to improve the metallic glasses properties is performed.

In **the second chapter**, the different materials used in this work and the experimental technique to process and characterize the amorphous alloys are described.

The first new biocompatible composition is described in **Chapter 3**. The system used is a ribbon form Mg-based system, for a potential application as biodegradable material. The choice of the elements and their proportions is explained. Then, the processing, the results of

the characterization as biomaterials and the influence of Yb addition in the initial system are developed.

**Chapter 4** deals with the processing and a complete characterization of the second new biocompatible composition. This system matches with reinforcement biomaterials, as it is a Zr-based system. The characterizations of the thermal stability, the mechanical properties and the biocompatibility of this new alloy have been conducted, and the replacement of Al by Ga is proposed and discussed

The **fifth chapter** concerns the improvement of the ductility and of the critical diameter using the rare-earth microalloying technique. Additions of yttrium were tried in a well-known system: Cu-Zr-Ti. The thermal stability, corrosion resistance, biocompatibility and ductility are also investigated. A complete study of the microstructure is conducted using TEM (Transmission Electronic Microscopy) and FIB (Focused-ion Beam) experiments in order to determine the cause of the ductility increase.

In the **sixth chapter**, another kind of improvement is approached using the powder metallurgy on the same Cu-Zr-Ti system to compare the results with the cast ones. Indeed, based on the cooling rate, fully amorphous small particles of a composition with a small glass forming ability are easy to obtain, using gas atomization. The densification of the sample using SPS (Spark Plasma Sintering) is a technique allowing high diameter samples, keeping a good control of the temperature to avoid the crystallization. Then, ex-situ composites processing, reinforced with crystalline particles to increase the ductility, is also tried.

Finally, **the last chapter** proposed an understanding of a deformation mechanism in the metallic glass, inducing more ductility in the macroscopic behaviour. This mechanism is called "rejuvenation" and is conducted by pre-cycling the sample. A statistical approach based on the compressive results and fractography analyses associated with atomistic simulation using molecular dynamics are employed to determine the elementary deformation mechanisms.



# Chapter 1

## State of Art on Bulk Metallic Glasses

<b>STATE OF ART ON METALLIC GLASSES FOR BIOMEDICAL APPLICATIONS.....</b>	<b>9</b>
<b>1-1- Background about metallic glasses .....</b>	<b>9</b>
<b>1-1-1- What is a glass? .....</b>	<b>9</b>
<b>1-1-2- Stability of an amorphous system .....</b>	<b>10</b>
<b>1-1-3- Technique of fast quenching .....</b>	<b>11</b>
<b>1-1-4- Thermal Stability of a glassy system .....</b>	<b>13</b>
<b>1-1-5- Characterization of the glass forming ability.....</b>	<b>14</b>
<b>1-1-6- Mechanical behaviours of a metallic glass .....</b>	<b>15</b>
<b>1-1-6-1 Existence of two distinct behaviours.....</b>	<b>15</b>
<b>1-1-6-2 High temperature behaviour .....</b>	<b>17</b>
1-1-6-2-1- Viscosity of metallic glasses	17
1-1-6-2-2- Fragility concept	18
<b>1-1-6-3- Low temperature behaviour .....</b>	<b>19</b>
1-1-6-3-1- Structural properties	19
1-1-6-3-2- Shear bands	21
1-1-6-3-3- Fracture in metallic glasses	25
1-1-6-3-4- Fracture modes	26
<b>1-2- Criteria for glass formation .....</b>	<b>29</b>
<b>1-3- Attractive properties of the metallic glasses .....</b>	<b>30</b>
<b>1-4- Applications.....</b>	<b>32</b>

<b>1-5- Examples of metallic glasses</b> .....	<b>33</b>
<b>1-5-1- Reinforcement materials</b> .....	33
1-5-1-2- Zr-based BMGs	33
1-5-1-3- Ti-based BMGs	34
<b>1-5-2- Biodegradable Materials</b> .....	35
1-5-2-1- Mg-Based BMGs	35
1-5-2-2- Ca-based BMGs	36
1-5-2-3- Zn-based BMGs	36
1-5-2-4- Sr-based BMGs	37
<b>1-6- Improvements of the bulk metallic glasses systems</b> .....	<b>37</b>
<b>1-6-1- Microalloying</b> .....	37
1-6-1-1- Kinds of minor addition	37
1-6-1-2- Effects on the GFA	42
1-6-1-3 Enhancement of the properties	45
1-6-1-4- Empirical rules	47
<b>1-6-2- Composites manufacturing</b> .....	47
<b>1-6-3- Porous metallic glasses</b> .....	49
<b>1-7- Conclusion</b> .....	<b>50</b>
<b>1-8- References</b> .....	<b>52</b>

---

# Chapter I

## State of art on metallic glasses for biomedical applications

### 1-1- Background about metallic glasses

Most part of time the term “glass” is used for mineral materials containing silicon and oxygen. Because of its high resistance, this is a major material in our society existing for a very long time. However, a new kind of glass knows an increasing interest for the past decades, called metallic glasses. Compared to the silica glasses, metallic glasses exhibit the same amorphous structure and absence of long-range order. Nevertheless, they are mainly composed of metallic atoms but also of metalloid elements (Si, C, P, B), usually introduced to increase the ability to form a glass in Fe-based systems. The combination of metallic bonds and amorphous structure contribute to their unique properties. Johnson’s team in CalTech processed the most well-known metallic glass, under the commercialized name Vitreloy 1<sup>1</sup>. Then, it has been declined under several compositions: Vitreloy 105, Vitreloy 1b, Vitreloy 106a...

#### 1-1-1- What is a glass?

Fig. 1-1 explains how to obtain an amorphous material, whether it be mineral, oxide or polymer. Once the material is molten, the alloy is cooled using fast quench technique. In classic crystalline alloys, the cooling causes atoms movements around given positions, which generates crystal formation. A very high cooling rate prevents the germination of the crystals and atoms from ordering. The structure exhibits a short or medium topological or chemical range order instead of a long-range order like in their metallic crystalline counterparts. It is a competition between the crystallization kinetic and the quenching kinetic (Fig. 1-1). The system will become a supercooled liquid (temperature below  $T_l$  or  $T_m$  without becoming a solid) and then a glass, more or less relaxed depending on the cooling rate. The obtained structure is out of equilibrium, and called metastable.

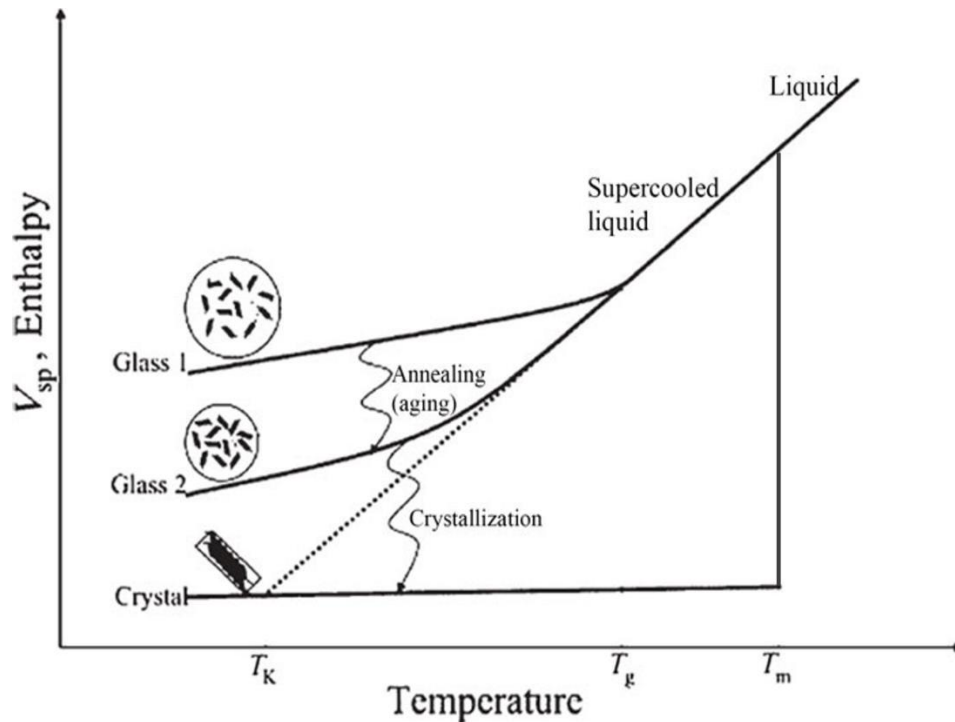


Figure 1-1 : Variations of the specific volume or enthalpy versus temperature of pure substance.  $T_g$  and  $T_m$  correspond to the glass transition temperature and melting temperature respectively<sup>2</sup>.

### 1-1-2- Stability of an amorphous system

Because of this feature, there are two possible evolutions: (i) the system remains amorphous but reaches a lower energy state and the free volume decreases. This phenomenon is called structural relaxation (Fig. 1-2)<sup>3</sup>. This contributes to eliminate the spaces between atoms due to the liquid-state disorder. It is also called physical ageing. These empty spaces, called free volume, act like internal defects in the system and describe the structure of metallic glasses. The opposite of structural relaxation is the rejuvenation, where defects are introduced for instance by plastic deformation, inducing a higher energy state. This process allows a higher ductility. Rejuvenation can also be conducted by thermal experiments<sup>4</sup>. A further study will be developed in Chapter 7 on the rejuvenation to improve ductility. (ii) The other possibility is to change from an amorphous state to a crystalline one. If the material is exposed to a too elevated temperature or a low temperature during a too long duration, atoms have enough energy and time to reorganize themselves and evolve into a crystalline system.

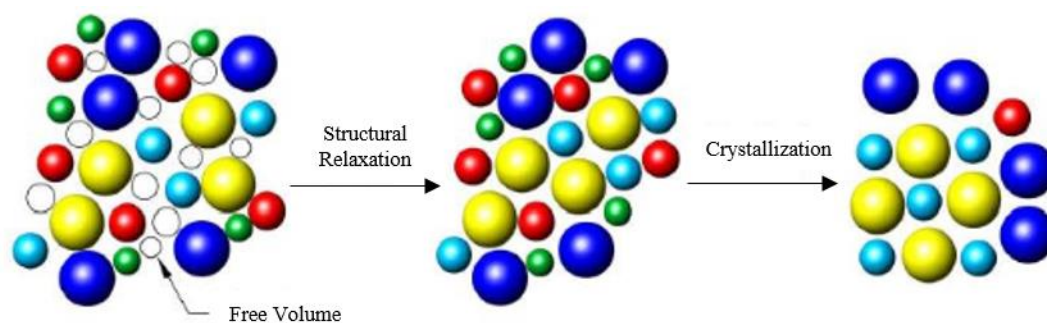


Figure 1-2 : Evolution of the atomic compactness due to the structural relaxation or crystallization mechanisms

### 1-1-3- Technique of fast quenching

The first implemented experimental technique to process metallic glasses, known as melt spinning, offers the possibility to obtain very low thickness alloy. The first amorphous metallic alloy was obtained using this technique. It consists of quenching the molten alloy on a rotating cold copper wheel, leading to the production of ribbons form. As a matter of fact, the higher thickness, the slower the quench. The cooling rate reached with this technique is about  $10^6 \text{ K}\cdot\text{s}^{-1}$  and the first system used by Duwez et al. had the composition  $\text{Au}_{75}\text{Si}_{25}$ <sup>5</sup>.

High cooling rates were necessary during few years to process glassy alloys except for some noble materials, which exhibit a high glass forming ability: Pd-Cu-Si and Pd-Ni-P<sup>6,7,8</sup>. For the twenty past years, techniques and chemical compositions evolved and the formation of bulk samples became easier, using cooling rates of about only 1 K/s. The range of the cooling rate is now between  $10^{-1}$  and  $10^7 \text{ K}\cdot\text{s}^{-1}$ . The thickness of the bulk samples can go from 1 mm to few centimetres with a first record obtained by Inoue's group with the alloy Pd-Cu-P-Ni in 1997, reaching a diameter of about 72 mm<sup>8</sup>. Nowadays the record continues to belong to Nishiyama et al., from the same group with 80 mm with Pd-Cu-Ni-P system<sup>9</sup>.

From 1990, different systems were elaborated with a wide range of main elements : Zr<sup>10,11,12,13</sup>, Ti<sup>14,15-19</sup>, Cu<sup>20-24</sup>, precious metal-based<sup>25-28</sup>. Since 2004, a strong trend emerged to conduct researches to improve the biodegradable amorphous alloys using Mg<sup>29-33</sup>, Ca<sup>14,29,34,35</sup> or Sr-based systems<sup>36,37</sup>. The table below shows the metallic glasses formed with a size over 10 mm.

Table 1: Description of the metallic glasses system with critical size > 10 mm <sup>38</sup>

<b>System</b>	<b>Alloys</b>	<b>Critical Size (mm)</b>	<b>Method</b>	<b>Year</b>	<b>Ref</b>
<i>Pd-based</i>	Pd <sub>40</sub> Ni <sub>40</sub> P <sub>20</sub>	10	Fluxing	1984	7
	P <sub>40</sub> Cu <sub>30</sub> Ni <sub>7.5</sub> P <sub>20</sub>	72	Water Quenching	1997	8
	P <sub>42.5</sub> Cu <sub>30</sub> Ni <sub>7.5</sub> P <sub>20</sub>	80	Copper mould casting	2012	9
<i>Zr-based</i>	Zr <sub>65</sub> Al <sub>7.5</sub> Ni <sub>10</sub> Cu <sub>7.5</sub>	16	Water Quenching	1993	39
	Zr <sub>41.2</sub> Ti <sub>13.8</sub> Cu <sub>12.5</sub> Ni <sub>10</sub> Be <sub>22.5</sub>	25	Copper mould casting	1993	1
	Zr <sub>46</sub> Cu <sub>30.14</sub> Ag <sub>8.36</sub> Al <sub>8</sub> Be <sub>7.5</sub>	73	Copper mould casting	2011	40
<i>Cu-based</i>	Cu <sub>46</sub> Zr <sub>42</sub> Al <sub>7</sub> Y <sub>5</sub>	10	Copper mould casting	2004	41
	Cu <sub>49</sub> Hf <sub>42</sub> Al <sub>9</sub>	10	Copper mould casting	2006	42
	Y <sub>36</sub> Sc <sub>20</sub> Al <sub>24</sub> Co <sub>20</sub>	25	Water Quenching	2003	43
<i>REE-based</i>	La <sub>62</sub> Al <sub>14</sub> Cu <sub>12</sub> Ni <sub>12</sub>	12	Copper mould casting	2004	44
	(La <sub>0.7</sub> Ce <sub>0.3</sub> ) <sub>65</sub> Al <sub>10</sub> Co <sub>5</sub>	25	Tilt-pour casting	2007	45
	La <sub>65</sub> Al <sub>14</sub> (Cu <sub>5/6</sub> Ag <sub>1/6</sub> ) <sub>11</sub> Ni <sub>5</sub> Co <sub>5</sub>	30	Copper mould casting	2007	46
	Nd <sub>70</sub> Al <sub>10</sub> Fe <sub>20</sub> Nd <sub>60</sub> Al <sub>10</sub> Fe <sub>30</sub>	12	Copper mould casting	1997	47
<i>Mg-based</i>	Mg <sub>54</sub> Cu <sub>26.5</sub> Ag <sub>8.5</sub> Gd <sub>11</sub>	25	Copper mould casting	2005	48
	Mg <sub>59.5</sub> Cu <sub>22.9</sub> Ag <sub>6.6</sub> Gd <sub>11</sub>	27	Copper mould casting	2007	49
<i>Fe-based</i>	Fe <sub>48</sub> Cr <sub>15</sub> Mo <sub>14</sub> Er <sub>2</sub> C <sub>15</sub> B <sub>6</sub>	12	Copper mould casting	2004	50
	(Fe <sub>44.3</sub> Cr <sub>5</sub> Co <sub>5</sub> Mo <sub>12.5</sub> Mn <sub>11.2</sub> C <sub>15.8</sub> B <sub>5.9</sub> ) <sub>98.5</sub> Y <sub>1.5</sub>	12	Copper mould casting	2004	51
	Fe <sub>41</sub> Co <sub>7</sub> Cr <sub>15</sub> Mo <sub>14</sub> C <sub>15</sub> B <sub>6</sub> Er <sub>2</sub>	16	Copper mould casting	2005	52
<i>Co-based</i>	Co <sub>48</sub> Cr <sub>15</sub> Mo <sub>14</sub> C <sub>15</sub> B <sub>6</sub> Er <sub>2</sub>	10	Copper mould casting	2006	53
<i>Ti-based</i>	Ti <sub>40</sub> Zr <sub>25</sub> Cu <sub>12</sub> Ni <sub>3</sub> Be <sub>20</sub>	14	Copper mould casting	2005	54
	Ti <sub>40</sub> Zr <sub>26</sub> Be <sub>28</sub> Fe <sub>6</sub>	10	Copper mould casting	2013	55
	Ti <sub>32.8</sub> Zr <sub>30.2</sub> Be <sub>26.6</sub> Ni <sub>5.3</sub> Cu <sub>9</sub>	50	Water Quenching	2010	56
<i>Ca-based</i>	Ca <sub>65</sub> Mg <sub>15</sub> Zn <sub>20</sub>	15	Copper mould casting	2004	57
	Ca <sub>50</sub> Mg <sub>22.5</sub> Cu <sub>27.5</sub>	10	Copper mould casting	2006	58
<i>Pt-based</i>	Pt <sub>42.5</sub> Cu <sub>27</sub> Ni <sub>9.5</sub> P <sub>21</sub>	20	Water Quenching	2004	59
<i>Ni-based</i>	Ni <sub>50</sub> Pd <sub>30</sub> P <sub>20</sub>	21	Water Quenching	2009	60

### 1-1-4- Thermal Stability of a glassy system

As in other amorphous materials, for example in polymers, the metallic glasses show the same structure, meaning that the same phenomena are expected. They exhibit a crystallization temperature  $T_x$ , and a glass transition temperature  $T_g$ . These temperatures are key features for these materials and usually determined using DSC (Differential Scanning Calorimetry) measurements, as it is shown in Fig. 1-3.

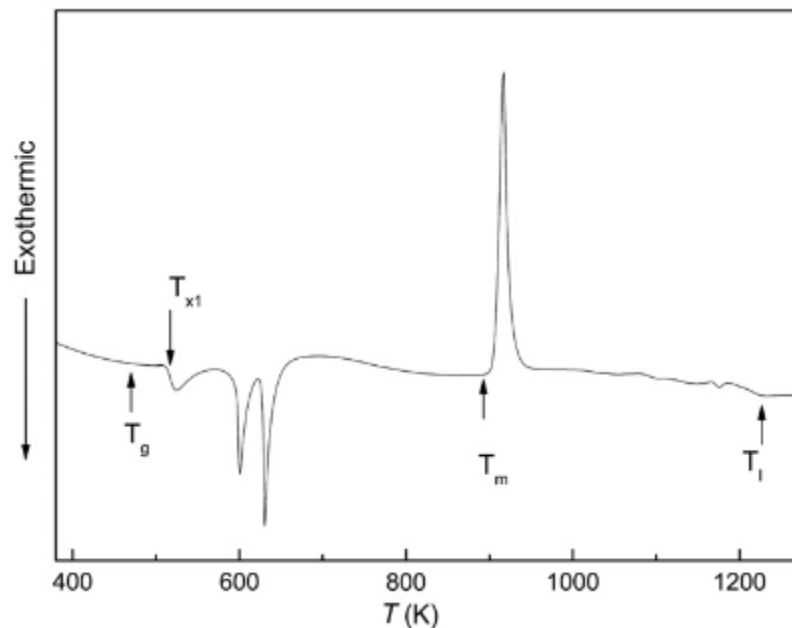


Figure 1-3: Conventional DSC curves obtained for a metallic glass <sup>61</sup>

Because it is a metastable system, the range of temperature in which the material is usable without crystallization, is critical to be defined. To obtain this information, DSC measurements or Differential Thermal Analysis (DTA) experiments can be conducted. The curve in Figure 1-3 is commonly obtained from the DSC experiments, with  $T_g$  the glass transition,  $T_x$  the crystallization,  $T_m$  the melting temperature, and  $T_l$  the liquidus temperature. Depending on the system, the crystallization can happen in several steps, indicating the evolution of the first phase or the presence of several phases. The glass transition is a key temperature to reach for a metallic glass because it causes a state change in the system. The alloy becomes a viscous liquid. Below the glass transition, atoms show very low mobility. When the glass transition is reached, the mobility becomes higher and the sample can be deformed. The mechanical properties are drastically changed.

Two kinds of measurements are also used: isothermal and non-isothermal (isochronal) measurements, depending on the targeted information. For example, crystallization kinetic will be investigated using isothermal measurements and characteristic temperatures, using isochronal measurements.

Employing several heating rates during non-isothermal treatments can bring key information. For example, using the Kissinger's law <sup>62</sup> or the Flynn-Wall-Ozawa (FWO) law <sup>63,64</sup>,

it is possible to obtain the different activation energies (of glass transition, primary crystallization...) and the crystallization rate.

The Johnson-Mehl-Avrami (JMA) law can be used <sup>65</sup>, using isothermal measurements to investigate the mechanisms of two-step crystallization process (nucleation of crystallites and their growth).

$$\alpha(t) = 1 - \exp(-K(t - \tau))^n \quad (1)$$

With  $\tau$ , incubation time and  $n$ , the Avrami coefficient, and  $K$  a parameter taking into account the kinetic parts.

$$\ln(-\ln(1 - \alpha(t))) = n \ln K + n \ln(t - \tau) \quad (2)$$

Using the Avrami coefficient from Eq. 1 and 2, information about crystallization modes can be available. Their interpretations can be found in the work of Wei et al. <sup>66</sup>.

### 1-1-5- Characterization of the glass forming ability

The ability to obtain an amorphous alloy is called “glass forming ability” and noted GFA. This parameter is evaluated using different criteria which evolved over the years because of the varied new compositions.

From 1970 to 2000, only two criteria were used <sup>67</sup>: the first one is the width of the supercooled liquid region  $\Delta T$ , used by Inoue et al.

$$\Delta T = T_x - T_g \quad (3)$$

The second parameter is the “reduced glass transition temperature”

$$T_{rg} = \frac{T_g}{T_l} \quad (4)$$

With  $T_l$ , the liquidus temperature. The larger  $T_{rg}$  and  $\Delta T$  are, the higher the GFA. These two criteria were the firsts to be used in metallic glasses. However, because of the numerous new compositions, correlation of these parameters with the evaluation of the GFA was not accurate. Other parameters were implemented to evaluate the GFA of the new compositions. The two main parameters, based on the characteristic temperatures of the materials, makes the evaluation of the glass forming ability and the thermal stability possible <sup>68,69</sup>.

$$\gamma = \frac{T_x}{T_g + T_l} \quad (5)$$

$$\delta = \frac{T_x}{T_l - T_g} \quad (6)$$

For all those criteria the same trend is observed, i.e. the higher  $\Delta T$ ,  $T_{rg}$ ,  $\gamma$ , and  $\delta$  the higher the GFA.

However, all these definitions are only based on calculations. The real relevant parameter, which makes sense is the experimental critical diameter, noted  $D_c$ . It is related to the minimum cooling rate needed to cool a supercooled liquid without crystallization.

The higher the critical diameter ( $D_c$  in millimetres) of the piece, the higher the GFA. Zhu et al. proposed the following relationship <sup>70</sup>:

$$\log(D_c) = -2,57 + 6,16 \frac{T_g}{T_l} \quad (7)$$

Models were also implemented to understand the ability to form a glass, as the Egami and Waseda Criterion <sup>71</sup> based on the strain of the crystalline lattice, or the Nagel and Tauc criterion <sup>72</sup>, stating that a glass is formed if the electronic energy is in a metastable minimum.

Calin et al. <sup>18</sup> investigated the composition range to obtain glassy alloys, depending on the nature of the element. For example, for a system metal-metalloid, 75 to 85% of metal and 15 to 25% of metalloid are needed to be close to a deep eutectic.

Thus, the first characterization of the metallic glasses is based on the knowledge of the characteristics temperatures in order to predict the amorphous character or the GFA. Moreover, because they are metastable and out of equilibrium, the range of temperatures where crystallization is avoided is crucial to be determined, using a thermal stability analysis.

## **1-1-6- Mechanical behaviours of a metallic glass**

### **1-1-6-1 Existence of two distinct behaviours**

The characterization of a system goes through a number of tested properties after the basic testing of the thermal features. In this part, we developed the mechanical behaviour of a system, which can be very different depending on the temperature and applied stresses <sup>73</sup>.

Two mechanical behaviours are highlighted on a metallic amorphous system. These two regimes are shown in Figure 1-4, where the difference is a temperature matter. The first behaviour occurs at low temperatures, usually  $T < 0.8T_g$ . Atoms exhibit a very low mobility and the observed macroscopic behaviour is mainly brittle with a very high yield strength. This range of temperature corresponds to the usable temperature range. For this reason, it is crucial to conduct the characterization of this system at this range of temperatures. In opposite to this, at high temperature,  $T > 0.8T_g$ , a more important atomic mobility is induced, which allows a higher ductility. This range of temperatures corresponds to shaping process temperature of the system. Because of a state change, the mobility increases and complex shapes are easier to process.

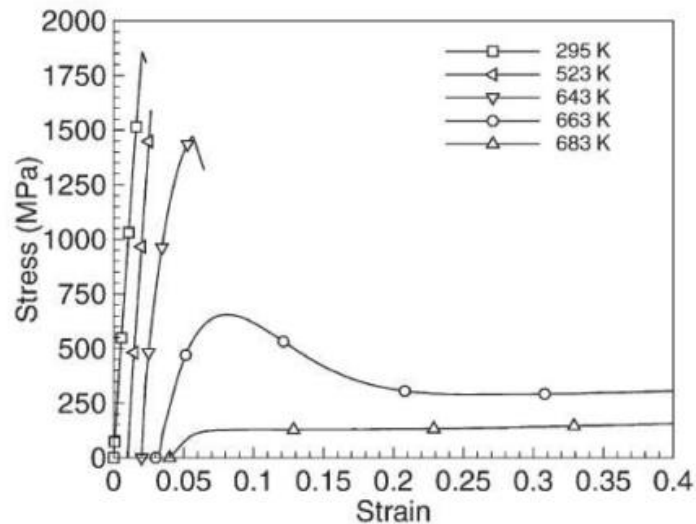


Figure 1-4: Compressive Stress-Strain curves of a metallic glass (Vitroloy 1) <sup>74</sup>

Since the metallic glasses exhibit two distinct domains, the relevant parameters to characterize it, are different. For the low temperature behaviour, we will test the most critical properties for the use, as for example the fracture and the deformation, while for the high temperature behaviour, we will test the shaping features, such as the viscosity and fragility.

Spaepen <sup>75</sup> built a map to predict the homogeneity of the behaviour depending on the temperature and the applied stresses. The two different behaviours are represented in Fig1-5.

At high temperature ( $T > T_g$ ), the deformation uses a homogeneous flow mechanism; the material is described as Newtonian viscous.

At low temperature ( $T < 0.8T_g$ ), the deformation uses an inhomogeneous flow mechanism, it is almost a plastic flow and the strain is localized in a few very thin shear bands perpendicular or at  $45^\circ$  from the solicitation direction. The localized deformation in shear bands requires a faster deformation in the layer of the materials in shear bands. Thus, the viscosity in this area becomes lower. The shear bands characteristics will be developed later.

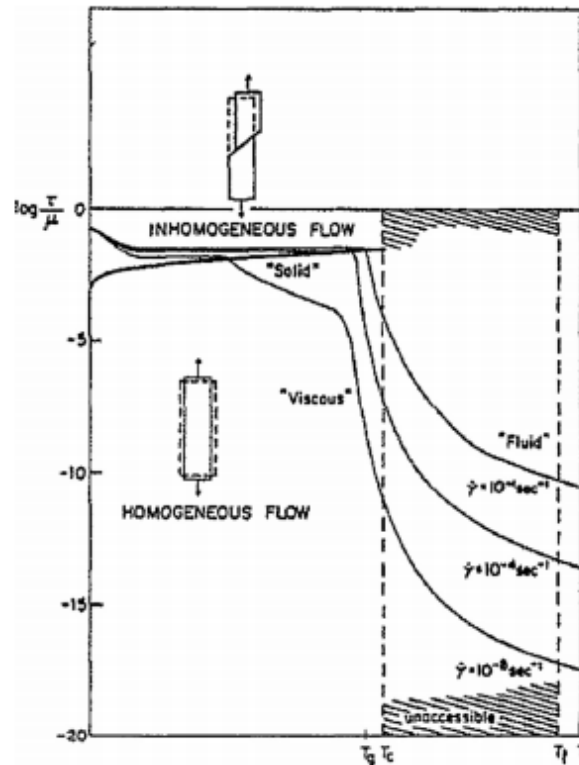


Figure 1-5: Map of the deformation of metallic glasses by Spaepen <sup>76</sup>

## 1-1-6-2 High temperature behaviour

### 1-1-6-2-1- Viscosity of metallic glasses

The shear viscosity is a temperature-sensitive property for the glass-forming liquids, showing a change of 17 orders of magnitude upon cooling from high-temperature to  $T_g$ . The change of the viscosity with the temperature is presented in the work of Angell <sup>77</sup>, as it is described in the next part. Recently, Blodgett et al. highlight the universality of the dynamical behaviour of a metallic liquid when the temperature is scaled by a high-temperature universal scaling temperature,  $T_A$ , predicted by molecular dynamics simulations <sup>78</sup>. This temperature corresponds to the onset of cooperative motion in a liquid leading to the glass transition. The curve of  $\log(\eta/\eta_0)$ , the viscosity scaled by the viscosity at the extrapolated value at an infinite temperature, as a function of  $T_A/T$ , reproduces all liquid metals behaviours (shown in Fig. 1-6).

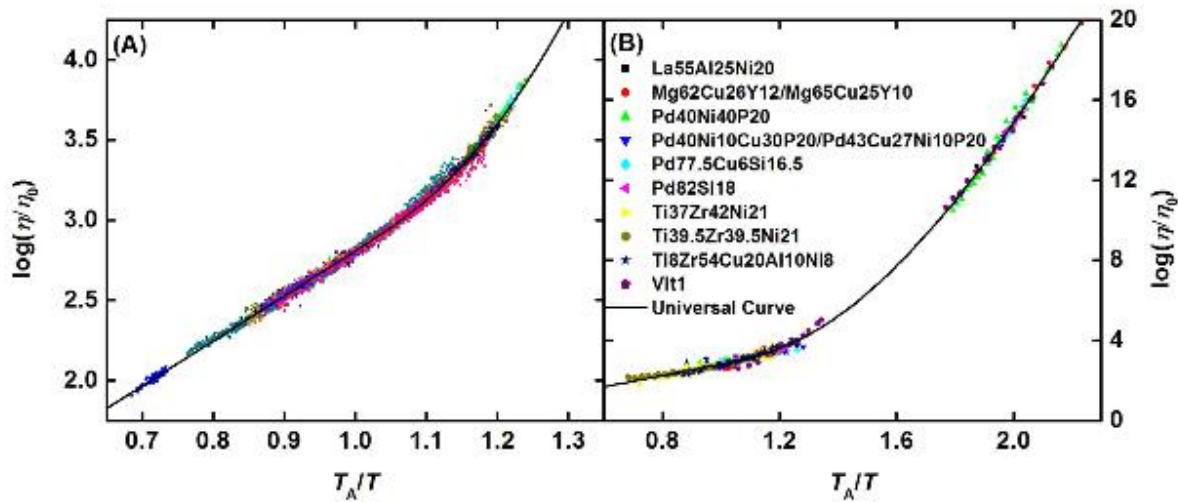


Figure 1-6: Comparison of the data for several glass-forming liquids and the universal curve <sup>78</sup>

### 1-1-6-2-2- Fragility concept

The glass transition is influenced by the heating rate, so an objective way to compare the systems between each other should be found. Moreover, a way to predict the glass-forming ability could be implemented. For these purposes, Angell introduced a parameter called the fragility ( $m$ ) <sup>79,80</sup>, based on the viscosity measurements and defined as follows:

$$m = \left. \frac{d(\ln\tau(T))}{d\left(\frac{T_g}{T}\right)} \right|_{T_g} \quad (9)$$

With  $T$ , the temperature,  $\tau$ , the temperature-dependant relaxation time. According to the classification of Angell, the good glass forming alloys are strong liquids with high viscosity, while the fragile liquids are called “marginal glass formers”. Indeed, a change in the viscosity allows to investigate a change in the atoms mobility during the supercooling and to classify the different systems.

Mukherjee et al. <sup>81</sup> introduced the fragility parameter ( $D$ ):

$$\eta = \eta_0 \exp\left(\frac{DT_0}{T-T_0}\right) \quad (10)$$

With  $D$ , the fragility parameter,  $\eta_0$ , the high temperature limit of viscosity and  $T_0$ , the Vogel-Fulchter-Tammann <sup>82,83</sup> temperature. The two parameters can also be linked as the following relationship:

$$m=f(D) \quad (10)$$

The fragility parameter indicates how closely the system obeys to an Arrhenius behaviour. The values are from 5 to 100 with 5 for fragile liquids and 100 for the strong ones, for example  $\text{SiO}_2$  (Fig 1-6). This parameter offers a direct evaluation of the GFA. For strong liquids, the behaviour of the viscosity depending on the ratio  $T_g/T$  is linear which means a small difference with Arrhenius law. However, for fragile liquids, the viscosity evolution is the

opposite, like the red curve in Fig. 1-7. The metallic glasses exhibit intermediate values with a large difference between the different systems.

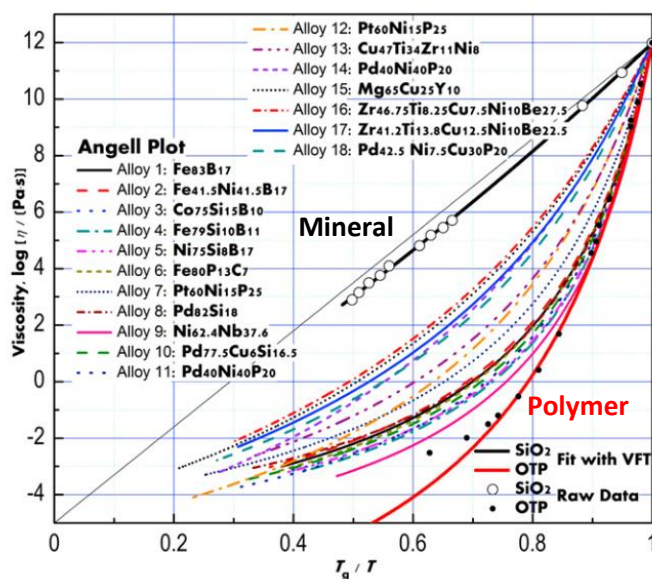


Figure 1-7: Angell classification of the different alloys from the most fragile polymer to the strongest mineral<sup>79</sup>

### 1-1-6-3- Low temperature behaviour

#### 1-1-6-3-1- Structural properties

First, because the structure of metallic glasses is unique and determines the deformation at low temperature, the structural models will be described.

Several models were elaborated to describe the structure of the BMGs. A complete review has been published by Yue et al. in 2017<sup>84</sup>. They develop the state of art of all the existing structural models used to describe the atomic structure of the amorphous alloys. Two categories of models exist. The first models aim at describing the global structure. Bernal in 1959<sup>85</sup> proposed a model called the Hard Sphere Random Dense Packing model, describing the structure of a liquid. Three assertions constitute this model: (i) the liquid is homogeneous, coherent and irregular. (ii) The second is that, all atoms are like rigid balls stacking randomly and (iii) finally, atoms are incompressible.

Another very important model is the Free Volume model developed initially by Turnbull and Cohen<sup>86,87</sup>. It describes molecular transport in glass forming liquids, explaining the phenomenon of self-diffusion in Van der Waals liquids and liquid metals. Later, Spaepen used the free volume to explain the plastic flow, the deformation, the fracture in metallic glasses, and to model the shear banding process<sup>76</sup>. In this model, the basic flow event is seen as an individual atomic jump driven by shear stress, as described in Fig.1-8, and plasticity in metallic glasses results of an atomic jump series assisted by thermal fluctuations. However, the limit of this model is the behaviour at low temperatures which is not well described<sup>88</sup>.

Nevertheless, this model has been extensively developed to fit better with the experimental results.

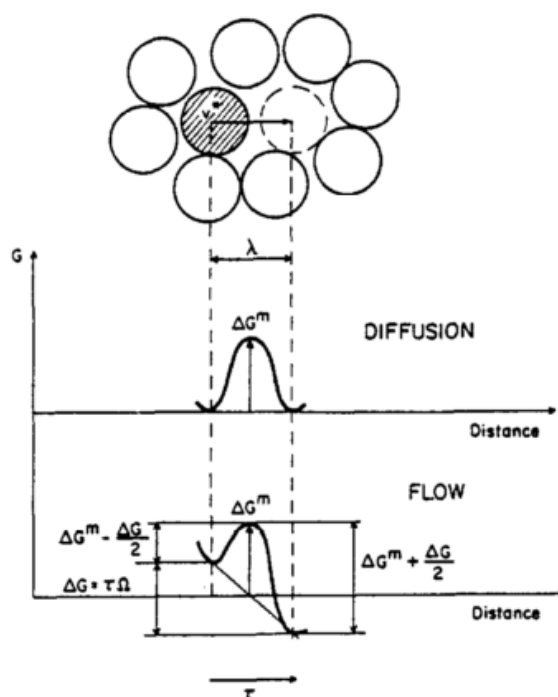


Figure 1-8: Atomic jump description <sup>76</sup>

The second category of models is based on a description of the metallic glasses atomic structure. In crystalline alloys, defects are defined as the deviations from the standard order (dislocations, vacancies...). However, in amorphous materials there is no long-range order so the defects are more difficult to define.

The first model is the Quasi-Point Defect (QPD) model, first implemented by Perez et al. <sup>89</sup> in polymers, but also used in metallic glasses. This model enlarges the free-volume concept and proposes that the micro-density fluctuations in metallic glasses could be considered as quasi-point defects in the supercooled liquid <sup>90</sup>. It discusses the existence of areas with a strong concentration of defects and some with low concentration of defects. Thus, it is possible to define the defect in metallic glass as the difference from the average volume. The work of Perez et al. also determined the consequences of applying a stress and heating a glass which is the percolation of shear-microdomains resulting in a liquid behaviour.

Granato et al. <sup>91</sup> describe the interstitialcies (interstitial defects similar to dumbbell configuration) as the basic structural defect. Because of their high shear susceptibility and large entropy, these defects play an important role in the phenomena in condensed matter. Liquids are considered as lattice containing few percents of interstitialcies. Moreover, glasses are considered as frozen liquids and could exhibit the same structure. Nevertheless, interstitialcies are defects in simple metal but in more complex system, the structural defects should be more like dumbbells shape with an analogous to the one of interstitialcies. The irreversible character of the structural relaxation results from the irreversible decrease of the defects number.

The last model was first defined in 1970, using the fact that amorphous alloys exhibit a crystal like short range structure, stacking various types of polyhedra, which are the basic

unit of metallic glasses. Thus, in the structure there are two kinds of areas: a solid-like area with high modulus and liquid-like area with low Young's modulus, responsible of the deformation. Miracle<sup>92</sup> developed his model following this description (Fig. 1-9).

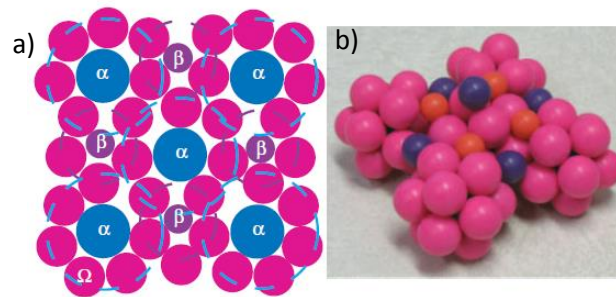


Figure 1-9 : Atomic cluster of Miracle : a) 2D clusters; b) 3D clusters<sup>92</sup>

Many other models are also based on the evolution of energy during structural relaxation or on materials internal defects. For example, Adam and Gibbs also developed a model based on the theory of entropy fluctuations and atoms rearrangement<sup>93</sup>. However, all the other models are not widely accepted, so they won't be presented here.

### 1-1-6-3-2- Shear bands

As it has been said concerning the low temperature behaviour, the deformation is heterogeneous, and the structural description of the materials helps to understand their deformation. The plastic deformation is very localized, at nano-scale, and rules by the small zones called shear bands<sup>94</sup>. These areas measure about 10 to 20 nm thick and their speed is about 10% of the transversal sound waves speed. Their mechanisms occur in several stage shown on the Fig. 1-10. The shearing nature of the shear bands has been demonstrated by Leamy et al. in 1972<sup>95</sup>, then studied by Greer et al.<sup>94</sup> and more recently by Maaß and Löffler<sup>96-98</sup>.

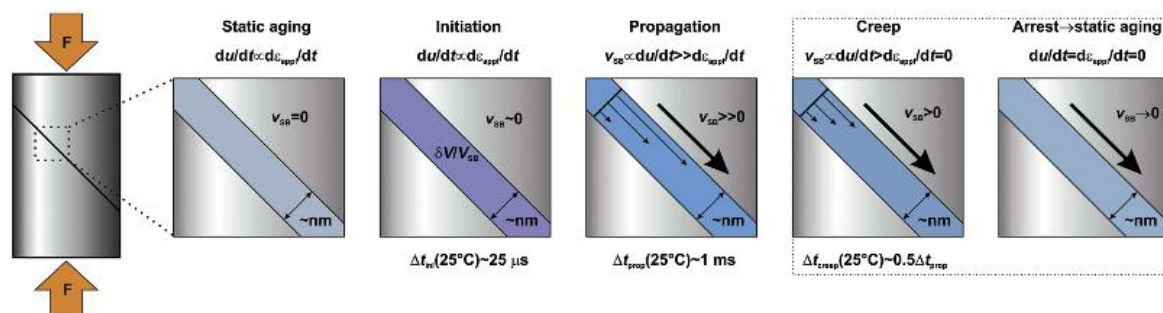


Figure 1-10: Schematic representation of the different steps in the shear banding phenomenon<sup>96</sup>

According to the models describing the structure of the sample, several theories were developed to understand the deformation mechanisms in metallic glasses under applied stress, especially to understand the formation of the shear bands. It is worth noting the growing interest on that topic during the past few years. However, the physical origin of the shear bands is not completely resolved yet. Several hypotheses have been introduced:

- The first one is that the behaviour is analogous to the action of dislocations in crystalline materials, meaning that plasticity is ruled by the displacement of shear bands. If two shear bands meet, their displacement is blocked and this phenomenon contributes to hardening.
- Based on the density fluctuations defined previously, during solicitations the strain induces dilatation and the free volume around atoms is modified. There are differences of deformation between several areas which induces non-homogenous deformation. This is the strain softening mechanism. The apparent causes of this mechanism are first, the dilatation induced by the strain and secondly the temperature rise. This last one is controversial because the range of temperature rise was evaluated between from few tens to few thousands of Kelvin <sup>99</sup> from direct measurements and it is not well accepted if it is the cause of the strain softening or the consequence. Greer et al. conducted a very interesting experiment to evaluate the local heating. They observed the very local melting of a tin coating on the metallic glass surface. <sup>100</sup> Thus, they conclude to a local heating in some areas over the melting point of tin (231°C).
- Argon implemented a model based on the shear transformation zones (STZ) (shown in Fig. 1-11) <sup>73,101</sup>. This is a thermally activated phenomenon in which the displacement of a cluster, containing few to 100 atoms, is larger than the surrounding atoms, which causes dilatation in the material. First the calculations of this model were based on the Eshelby type inclusion calculations. Contrarily to the dislocations in the crystalline alloys, STZs are immobile. It is considered as a flow event and not as a defect. According to simulations, the structure in STZs becomes more disordered but it doesn't migrate.

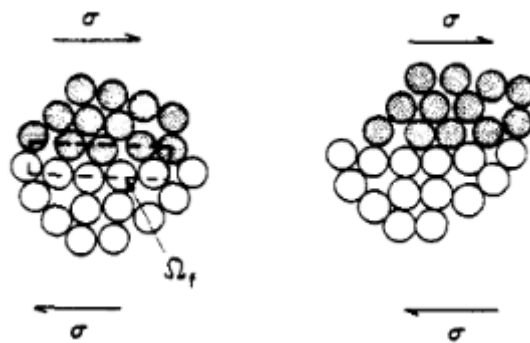


Figure 1-11 : Schematic representation of STZ <sup>73</sup>

- The Quasi-Point Defect of Perez <sup>89</sup> can also explain the Shear Micro Domains (SMD) creation under a mechanical solicitation. When a stress is applied, shear micro domains are created around the QPD, and the elastic energy is stored at the contour of the area. If the solicitation disappears, the domain can come back to the initial state. But if the stress is higher, several domains can be created and coalesce, as it is presented in Fig. 1-12. The deformation is visco-plastic and the shear band can be formed.

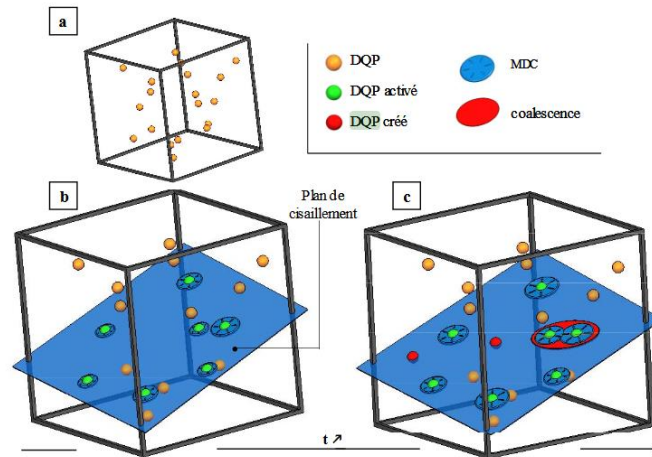


Figure 1-12: Schematic representation of the Quasi-Point Defect model <sup>102</sup>

- The shear bands can also be induced because of the internal defects and are preferentially formed on these heterogeneous nucleation sites. The shear bands appear where the stress is higher to become a mature shear band, then to cross the sample. Their propagation mechanism is presented in Fig. 1-13

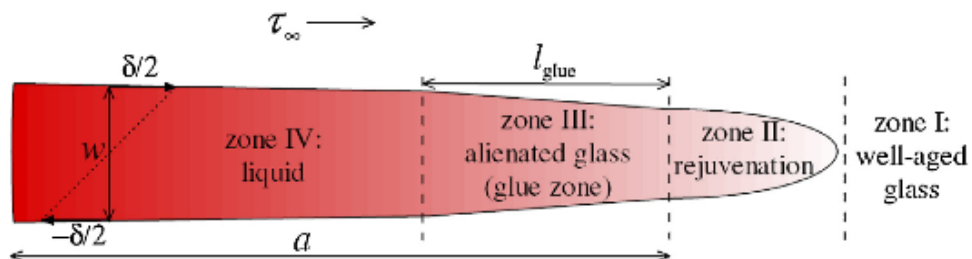


Figure 1-13: Propagation front of a shear band according to the model by Shimizu and Ogata <sup>103</sup>

- A last model on this question corresponds to a two-stage mechanism, the first stage, lasting only few  $\mu\text{s}$ , during which the shear offset and the local heating are limited, is shear band creation and the shearing by structural rejuvenation is initiated. The STZs will be activated along the shear band and the structure inside is disordered and causes the softening of the material. The rejuvenation propagates from stress concentrators to cross the entire sample but there is no significant increase of the shear strain or temperature. The second stage is once the creation of this softened plane take place, the synchronized sliding and shear off along the rejuvenated plane occur. The shear offset increases and the plastic strain and local heating become more important. The shear band becomes thicker and thicker <sup>94</sup>. All the whole shear band propagation is described in Fig. 1-14.

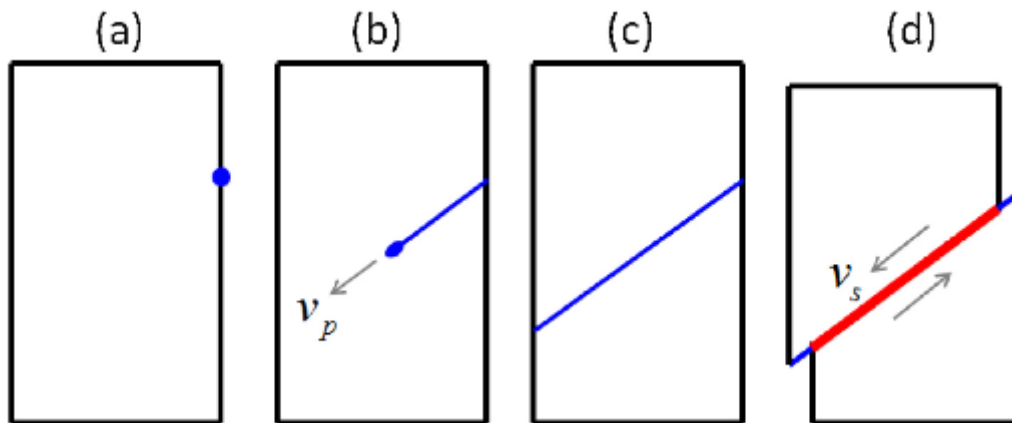


Figure 1-14: Schematic representation showing of the shear band formation under compressive load. a) First, a higher stress is located on an area of the sample surface, b) Propagation of the structural disordering (rejuvenation) at a velocity ( $v_p$ ), this velocity is the same order of magnitude as the shear wave speed ( $10^{-3} \text{ s}^{-1}$ ). c) The propagating front crosses the entire sample, resulting in a rejuvenated plane (at this time, the strain is small and the temperature in the band is cold). d) Shearing and sliding movements ( $v_s$  is the velocity of one part of the sample relative to the other) <sup>94</sup>

The propagation of the shear bands is the motion of the band along the shear plane. The operation of the shear band is the progressive motion of the shear front before the propagation. The shear bands are complicated to study with experimental data, because of the small size and the lack of information provided on this phenomenon. However, the viscosity of a propagating shear band could be calculated with the load drop, displacement and elapsed time during one serrated event.

In any case, according to all the models, the deformation in metallic glasses comes from a local atomic scale rearrangement.

### 1-1-6-3-3- Fracture in metallic glasses

Elastic and plastic deformation mechanisms were widely studied for crystalline materials. However, in amorphous materials without any microstructure, grain boundaries or dislocations, the mechanisms are very different. Despite the large interest for the past few years on this topic <sup>94,104–107</sup>, numerous questions still remain. Hu et al. <sup>108</sup> highlight the relationship between the strain, the fracture and the shear bands.

Because of the short-range order and the shear bands presence, there exists an asymmetric behaviour between tensile and compressive tests. If the fracture in tension is catastrophic, the fracture during compressive tests can exhibit limited plasticity. In some BMGs, during the plastic regime, serrated flow can appear <sup>109–111</sup>. This serrated flow is composed of two main events: sudden stress drop just before elastic reloading part. The sudden stress drop is caused by the rapid shear band operating process, where the propagation rate of the shear band is much higher than the loading rate. This is the opposite of the elastic reloading part.

The serrated flow is compared to a stick-slip instability of the shear banding process and it suggests that the plasticity of a metallic glass also depends on the extrinsic parameters,

as the machine stiffness, dimensions of the shape and not only intrinsic parameters as the Young modulus, etc.

Wright et al.<sup>112</sup> measured the propagation rate of a shear band, they acquired strain and load data at time-resolved up to 400 kHz with four gauges on the sides of the sample and piezoelectric cell near the BMG. The propagation rate was evaluated to be 0,002 m/s, if the entire plane is moving simultaneously. If the motion is located on the propagating front, the displacement rate is about 2 to 8 m/s. These values are lower than the shear wave speed which is about 2000 m/s. The velocity is too low to increase the temperature enough to melt the glass as in catastrophic failure.

When the sample is loaded up to the yield stress, a major shear band rules the deformation. Its sliding causes a release of elastic energy.

#### 1-1-6-3-4- Fracture modes

There are different fracture modes in the metallic glasses, indicating the fully amorphous character of the sample or if it is brittle or not.

- The first mode is the “Shear fracture Mode”. This mode occurs during tensile tests or compressive tests for metallic glasses. The angle between the fracture plane and the tensile direction is between  $45^\circ < \theta < 90^\circ$ . During compressive tests, this angle is between  $0^\circ < \theta < 45^\circ$ <sup>113</sup>, as it is shown in Fig. 1-15. During the observation of the fracture plane under SEM, melt areas are noticed.

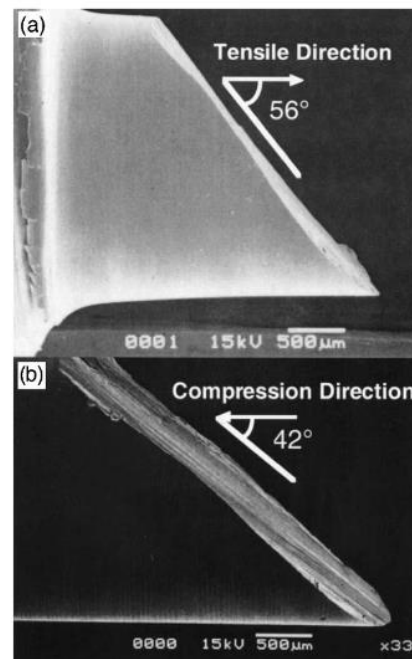


Figure 1-15: Side view of the sample fractured at the strain rate of  $1 \times 10^{-3} \text{ s}^{-1}$  in tension a), in compression b) <sup>114</sup>.

- The second fracture mode is called “the Cleavage mode”. The fracture plane is perpendicular to the direction of the tension or bending. It mostly concerns the very brittle BMGs as for example, Mg, Rare-earth elements (REE) or Fe-based BMGs <sup>115,116</sup> (Fig. 1-16).

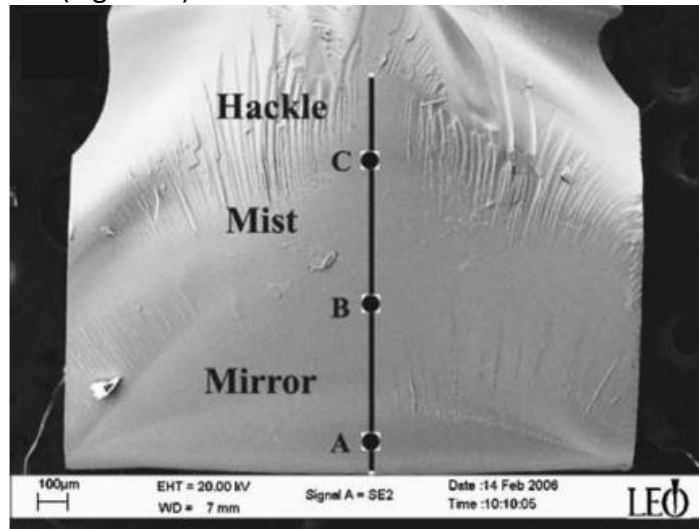


Figure 1-16: Typical cleavage mode under compression of  $\text{Fe}_{65.5}\text{Cr}_4\text{Mo}_4\text{P}_{12}\text{C}_5\text{B}_{5.5}$  with a fracture stress about 3000 MPa <sup>115</sup>

- The last mode is called “The fragmentation mode”, which takes place during the compression of very brittle metallic glasses, Mg or Co-based, for example. The fracture does not induce the presence of two pieces, but numerous small particles are visible after fracture <sup>117</sup>, as it is shown in Fig. 1-17.

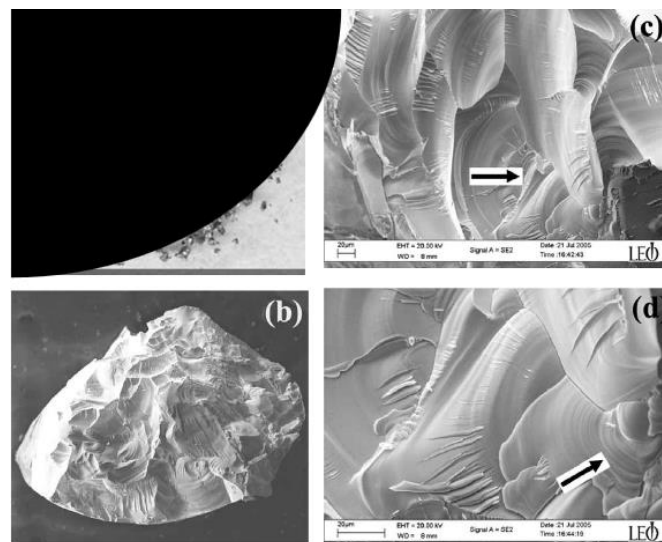


Figure 1-17: Fragmentation of Co-based BMG. Surface fracture during fragmentation <sup>117</sup>

The size of the sample has a strong influence on the results of the mechanical tests, as it has been noticed a transition between an inhomogeneous and homogenous behaviour depending on the sample size. The properties of the fracture in metallic glasses, not only depend on intrinsic parameters, as the material properties, but also on extrinsic parameters, as for example, the size of the samples or the experimental conditions. <sup>118</sup>

The observation of the fracture plane is also necessary to obtain information about the plasticity of the materials, especially for the first fracture mode. The Figure 1-18 presents the fracture plane of a Cu-Zr-Ti sample, showing a typical topology of a ductile fracture.

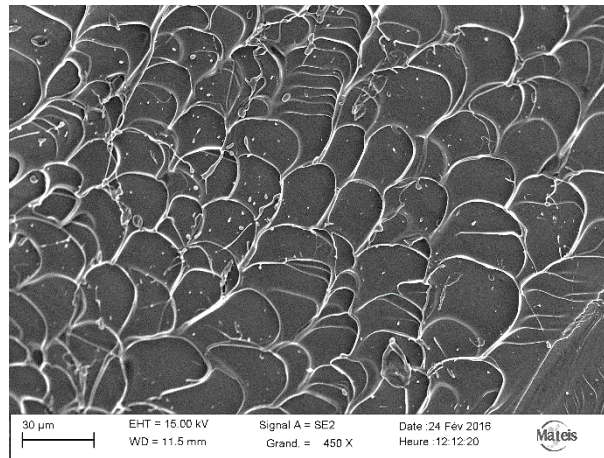


Figure 1-18: SEM picture of the vein pattern on the fracture plane on a Cu-based BMG

The most appropriate model to explain the aspect of this fracture plane is the comparison with two solid plates separated by a viscous layer <sup>119</sup>. The pattern noticed on the Figure 1-18, called “vein pattern”, comes from the melting areas in the samples. Indeed some areas exhibit a high stress concentration, due to the disordered structure associated with inhomogeneous stress.

From the diameter evaluation of the vein pattern, it is possible to evaluate the toughness ( $K_C$ ). To obtain this result, the following equation was implemented in the work of Xi et al. <sup>120</sup> using the work on polyester resins of Christiansen et al. <sup>121</sup>. It relates the size of the vein pattern ( $\omega$ ), the yield strength ( $\sigma_y$ ), and the  $K_C$ .

$$\omega = \frac{1}{6\pi} \left( \frac{K_C}{\sigma_y} \right)^2 \quad (11)$$

Table 2 shows few results for  $K_C$  in different metallic glasses.

Table 2 : Values of  $K_C$  for different BMGs

BMGs	$K_C$	References
Zr-based	86-200 MPa.m <sup>1/2</sup>	122
Pd-based	45 MPa.m <sup>1/2</sup>	123
Fe-based	4 MPa.m <sup>1/2</sup>	124

It should be noted that Pampillo et al. <sup>125</sup> proposed a theory about the vein pattern formation which could potentially come from the grouping of two fractures in the same plane.

A second kind of feature is less common but it can be observed for glasses with brittle fracture: “Nanoscale Corrugations”. Usually, two regions are distinguishable: The called “mist areas”, containing mainly nanoscale dimple structure, and “mirror areas”. This topology is shown on Fig. 1-19.

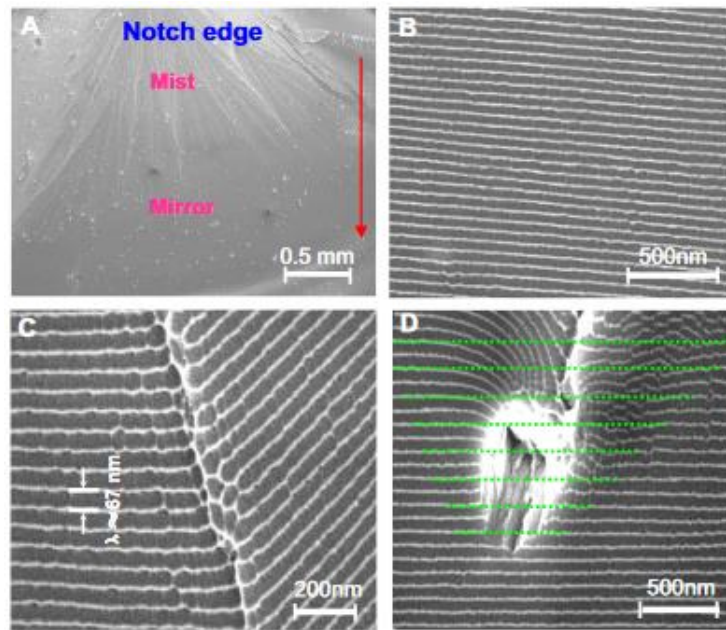


Figure 1-19: a) SEM micrograph of the fracture surface overview of the typical brittle BMG showing mist and mirror regions. b) Typical periodic striped patterns in the mirror region on the fracture plane of Mg-based BMG. c and d) show a higher magnification of the periodic corrugations <sup>126</sup>

## 1-2- Criteria for glass formation

The properties of metallic glasses are very different depending on the system, and the system is chosen depending on the targeted application. In order to optimize the manufacturing of new compositions, researchers tried to define several criteria. Following these, the possibilities of a potential success in elaboration of a fully amorphous structure for a given system are increased.

In 2000, Inoue established three main rules to respect, in order to obtain a metallic glass <sup>127</sup>:

- Use of at least three different components
- The atomic radius difference needs to be at least 12% to obtain a high compactness.
- The mixing enthalpy needs to be highly negative to have an amorphous and disordered phase during the cooling from a temperature higher than the liquidus down to a temperature below the glass transition temperature.

The implementation of these criteria leads the researchers to be interested in the eutectics and quasi eutectics, and also in having different atomic radii to increase the density and the viscosity of the liquid. New methods are also implemented concerning the processing, trying to threshold impurities concentration during the melting, which is susceptible to act as preferential sites of heterogeneous nucleation and formation of crystals.

### 1-3- Attractive properties of the metallic glasses

Because of their unique structure and mechanical properties, metallic glasses are now very attractive. Due to their amorphous character and their lack of microstructure (absence of grain boundaries and dislocations), metallic glasses exhibit higher elastic mechanical properties (as shown in Fig. 1-20) than their crystalline counterparts, as for example, a high yield strength, and an important elastic strain. However, there exists a broad dispersion concerning the plastic properties, depending on the composition. For example, Mg-based alloys are very brittle while Zr- and Cu- based show higher plastic strain.

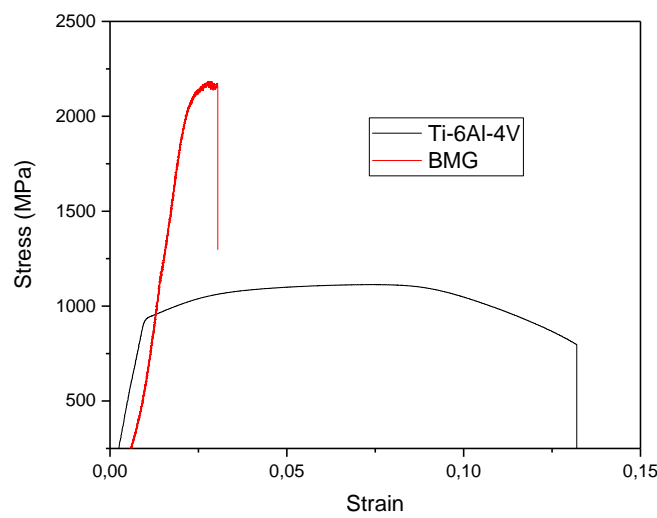


Figure 1-20: Compressive stress-strain curves of a crystalline Ti-alloy and  $(\text{Cu}_{60}\text{Zr}_{30}\text{Ti}_{10})_{99}\text{Y}_1$

Concerning the toughness, the range of values is from 2 MPa $\cdot$ m to 200 MPa $\cdot$ m. Usually for Zr-based BMGs and Ti-based BMGs the toughness is about 40 – 50 MPa $\cdot$ m<sup>1/2</sup> and about 22 MPa $\cdot$ m<sup>1/2</sup>, respectively<sup>128</sup>.

Without any grain boundaries, corrosion sites are limited and corrosion resistance is also improved. These general properties can vary according to the chosen elements.

Moreover, due to the presence of a disordered structure, the electron diffusion is more difficult and the resistivity of this kind of material is also increased. The electrical resistivity of the metallic glasses is high, more than 1  $\mu\Omega\cdot$ m and the temperature coefficient of resistivity is small and negative<sup>129</sup>. Based on this result, methods have been implemented to assembly two parts using Joule effect<sup>130</sup>.

Concerning the magnetic properties, only concerning the Fe-based metallic glasses or Co-based systems, who show high permeability, low coercivity, and low magnetic anisotropy due to the absence of microstructure and precipitates. These are good properties to process magnetic yokes, like linear actuators. Moreover, as the trend in electronic field is to reduce the size of components, keeping multifunctionality, bulk metallic glasses are promising. Another application as cores for choke coils is also proposed in the work of Inoue et al.<sup>131</sup>. However, the main drawbacks of these materials are the lack of ductility and the small critical size, due to the high cooling rates needed.

Compiling data and characteristics, Ashby and Greer have been able to integrate metallic glasses into the selection materials map to compare the properties and the performances, for example in this case, the elastic limit and the Young's modulus. <sup>132</sup>

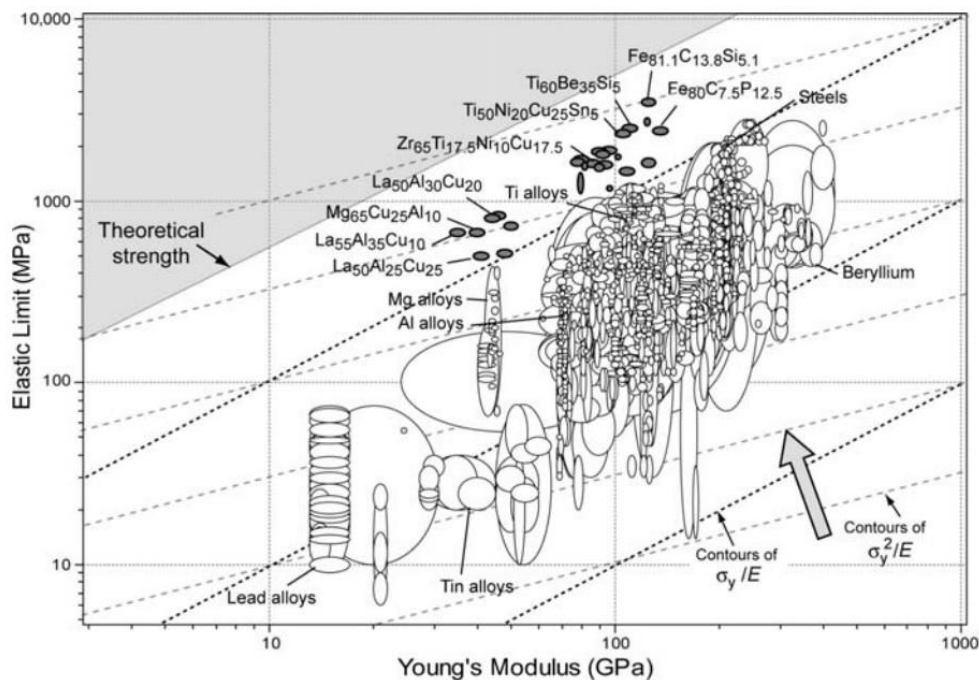


Figure 1-21: Ashby Map of metallic glasses <sup>132</sup>

On this map, it is possible to compare the metallic glasses to other metallic alloys according to their elastic limit and their Young's modulus. It is clear from Figure 1-21 that the metallic glasses exhibit very high elastic limit, above all the other materials. They also show high Young's modulus but lower than that for the steels.

The results about the behaviour of the metallic glasses should be considered cautiously because it is highly influenced by different parameters: extrinsic and experimental conditions (temperature, geometry of the sample, machine stiffness...) and also intrinsic (free volume, elastic limit...)

They also exhibit attractive shaping properties: since their viscosity decreases with the increasing temperature and this is an important result in order to improve the processing of the metallic glasses. This constitutes an important advantage to obtain complex shapes.

## 1-4- Applications

It has been said that metallic glasses show very unusual properties and it can be useful in a wide range of applications <sup>133</sup>. Their high yield strength is an important advantage in the sports field, where they can find a use as golf clubs or tennis rackets. For the same reasons, they can also be used in the aeronautic field where this kind of material is very interesting in order to decrease the weight of the planes.

Moreover, it is possible to control the biocompatibility of the system playing with the composition or on the surface topology. For example, Zr-, Ti- based systems are developed to replace some of the actual used alloy containing Ni or Al. Ni-free Zr-based systems are promising to replace actual stents. Mg, Ca or Zn can also be used as biodegradable alloys, with as an example, the Ca-Mg-Zn system which is promising for skeletal implants<sup>134–137</sup>. Thanks to their resistance to corrosion and the flexible Young modulus with the composition, they can be used for biomedical applications. This point will be detailed at the end of this chapter.

BMGs also exhibit thermoplastic formability in a specific range of temperature above  $T_g$ , it is easy to print micro-patterns with a high precision, which is interesting for MEMS or NEMS applications<sup>132</sup>. Advanced Si-based fuel cell demands expensive cost of the process and complex processing, but newly developed BMGs are promising to replace it<sup>138–140</sup>. Catalysis is also a field where BMGs can find a place because of the complex electronic structure due to the atomic disorder.

Finally, thanks to their smooth, shiny surface aspect, and wear resistance, BMGs are also interesting for watchmaking or jewellery.



Figure 1-22 : Examples of applications using metallic glasses<sup>141</sup>

## 1-5- Examples of metallic glasses (biomaterials)

Metallic glasses can be divided into several categories, according to the targeted applications, especially in the biomedical field. The properties are very different between reinforcement materials, as prosthesis or dental implants where mechanical strength have to be significant, and bones void fillers where perfect biocompatibility is necessary. In the following parts, different materials and base constituents with their main properties are summarized.

### 1-5-1- Reinforcement materials

Even if the contact with the organism is not direct, for this kind of material, a good biocompatibility is necessary. High mechanical properties are required for these materials, especially concerning the fatigue resistance. The corrosion should have poor action on this amorphous alloy, as they have to resist in the environment.

#### 1-5-1-2- Zr-based BMGs

These alloys exhibit very good advantages like a good glass forming ability, a low Young Modulus (50 GPa to 100 GPa), a high yield strength (1700-1800 MPa) and elastic strain (2%)<sup>142</sup>.

These systems were the first to be processed with high dimensions. However, thanks to their unique properties, a miniaturization is possible to obtain small objects for cardiovascular applications, like stents. The corrosion resistance of these alloys is also better than the resistance of their crystalline counterparts.

Moreover, to increase further their resistance to corrosion, alloying elements can be added. For example, niobium is a good addition element<sup>143</sup> because Nb atoms substitute to Zr atoms and increase the alloy resistance. Ti is also an addition element used to substitute Zr atoms because these two kinds of atoms are very similar. Ti allows to increase the atomic radius difference and thus obtain a better glass forming ability. Nowadays, there is no fully biocompatible system. Among all the compositions close to the targeted systems, the following systems, which could be interesting: Zr-Ti-Cu-Al<sup>144</sup>, Zr-Co-Al<sup>145,146</sup>, or Zr-Cu-Al-Nb-Pd<sup>147</sup>. For this last one, the corrosion behaviour has been studied in SBF (simulated body fluid) and the formation of a passive layer ZrO<sub>2</sub> has been proved. Moreover, the sample exhibits a good wettability surface and a good biocompatibility because the cells have good proliferation and adhesion on the surface.

#### 1-5-1-3- Ti-based BMGs

Ti based amorphous alloys are lighter and exhibit a better corrosion resistance than Zr-based ones. Their crystalline counterparts have always been among the most used materials in the biomedical applications, as for example Ti-6Al-4V. For the Ti-BMGs, the Young modulus is low compared to crystalline Ti-alloy (80 to 120 GPa) and they exhibit a very high yield strength (1,6 GPa). These alloys also show the formation of a passive film on the surface when they are immersed in an electrolyte solution for corrosion tests. Thus, the corrosion rate is very low. They show better corrosion resistance than the crystalline Ti-alloys<sup>148</sup>. When immersed for 15 days in a simulated body fluid (SBF), hydroxy-apatite layer is formed, which means they have a very good biocompatibility.

Moreover, during cytotoxicity tests, cells are numerous and the adhesion to the material is really good. There is no inflammation during in-vivo tests.

Among all the studied compositions for biomedical applications, there are several main systems, such as Ti-Zr-Cu-Pd<sup>149,19</sup>, Ti-Zr-Cu-Pd-Sn<sup>150</sup> or Ti-Zr-Cu-Fe-Si-Ag-Sn<sup>16</sup>. However, the presence of iron, copper even silver can be disputable. There are also several systems with a better biocompatibility but a worse glass forming ability like Ti-Zr-Si or Ti-Zr-Nb-Si<sup>18</sup>. A compromise between these two properties should be found.

## 1-5-2- Biodegradable Materials

### 1-5-2-1- Mg-Based BMGs

Magnesium is a very important element in biomedical applications for a long time. A lot of crystalline alloys are already used as biomaterials: Mg-Zn, Mg-Sr or Mg-Ca. The mechanical properties of the Mg-BMGs are more interesting than for Mg-crystalline alloys, keeping good degradation properties. The Young modulus is also very low, which is a good advantage for materials in contact with bones to avoid osteolysis issues. Several biocompatible bulk systems have been studied: Mg-Zn-Yb, Mg-Zn-Ca-Yb<sup>151</sup> or Mg-Zn-Ca<sup>30,32,152</sup>, Mg-Zn-Ca-Sr<sup>29</sup>, Ca-Mg-Zn-Sr-Yb<sup>33</sup>. During the corrosion studies, the corrosion mechanism found corresponds to uniform corrosion with a lower corrosion rate and a better biocompatibility than for the crystalline Mg-alloys.

It was also noticed that in all BMG systems rare-earth elements alloying in small amount could help to increase the ductility in bending or in tension. Yb for example is biocompatible and then, a high entropy system very interesting for biomaterials was elaborated: Ca<sub>20</sub>Mg<sub>20</sub>Zn<sub>20</sub>Sr<sub>20</sub>Yb<sub>20</sub><sup>33</sup>. The mechanical properties are increased and addition of strontium helps the bone's creation. During in vitro and in vivo tests, no inflammation was observed. The cell proliferation was also better than other metallic glasses (Fig. 1-23). However it still contains Zn element.

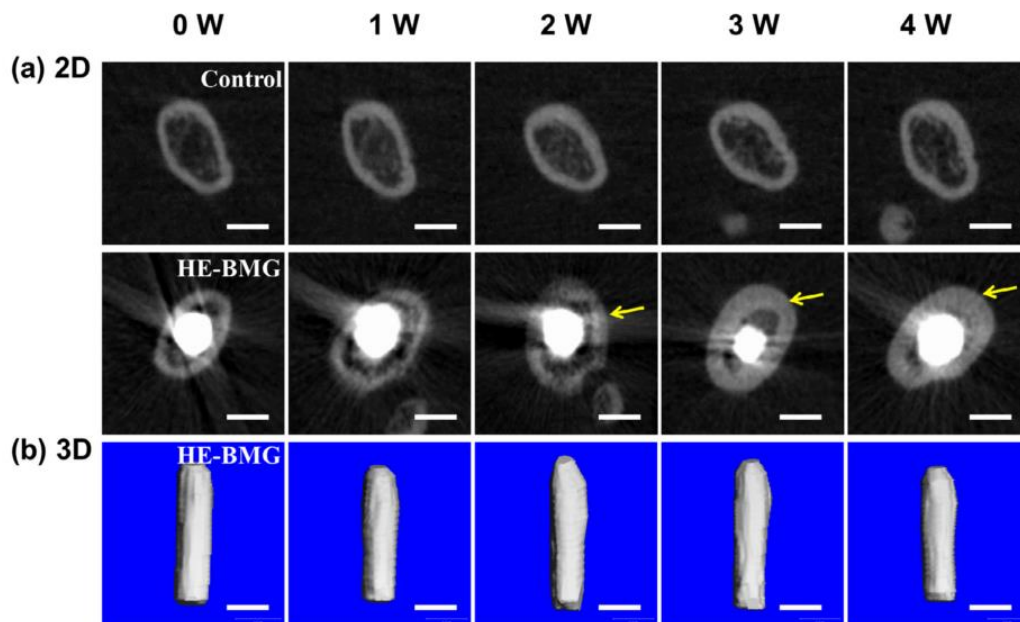


Figure 1-23: a) 2D and b) 3D representative mouse femur with an intramedullary CMZSY HE-BMG for 4 weeks. No degradation and no debris around the implant appear, the cortical bone thickness is higher than the non-implanted bone, indicating new bone formation of the peri-implant cortical bone <sup>33</sup>.

#### 1-5-2-2- Ca-based BMGs

Ca-BMGs are similar to the Mg-based BMGs. However, their main drawback is to be much more reactive due to the instability of calcium. They can be used for biomedical applications needing high corrosion rates. To control their reactivity, surface treatments or micro alloying are possible, as it is shown in Fig. 1-24.

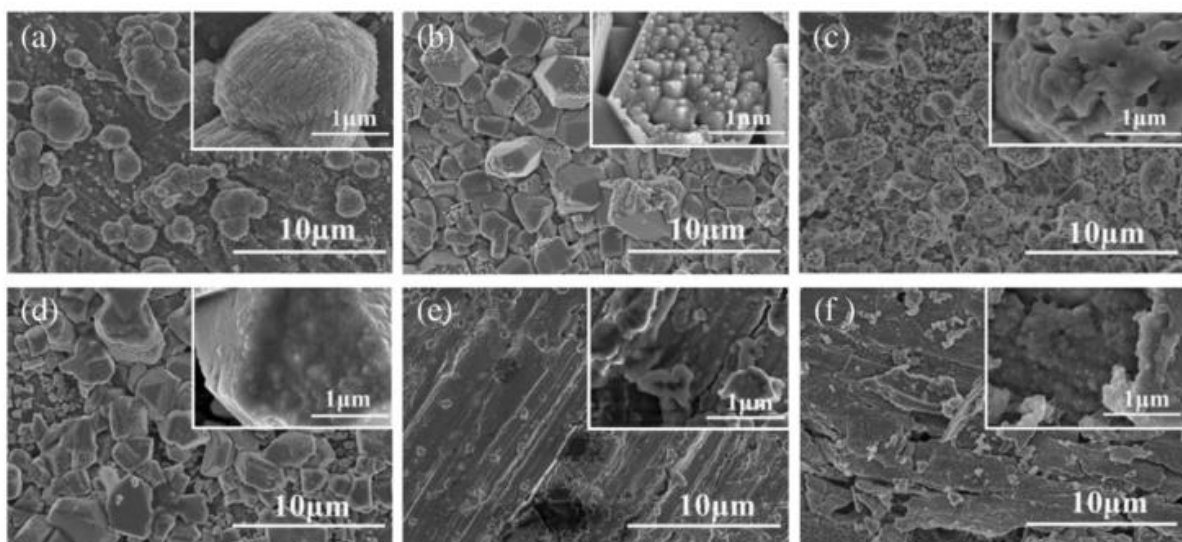


Figure 1-24: Surface topology of the Ca-based samples after different surface treatments, a) 15 min water etching, b) 30 min of water etching, c) 15 min water etching + fluoroalkylsilane coating, d) 30 min water etching + fluoroalkylsilane, e) Fe coating, f) Fe+ fluoroalkylsilane <sup>153</sup>

Concerning the studied systems, it is almost the same as Mg-based BMGs, but with a richer composition in calcium than magnesium<sup>34,152,154–156</sup>.

Because of their absence of microstructure, no intergranular corrosion like in other crystalline structures can be observed as in the case of Mg-based alloys.

#### *1-5-2-3- Zn-based BMGs*

Zn is a main metallic element in the human body and this is also a main element of enzymes and proteins. The mechanical properties of Zn-based BMGs are higher than for crystalline alloys. There is no hydrogen emissions during its immersion and dissolution<sup>157</sup>. Moreover, after 30 days immersion, mechanical properties are not decreased.

Only few studies have been considered on this system and the only one interesting studied system is : Zn-Ca-Mg-Yb<sup>157</sup>.

#### *1-5-2-4- Sr-based BMGs*

These metallic glasses have few specific applications because their glass transition temperature is very low and limit the usable temperature range. They can quickly degrade but the degradation can be readily tuned by changing the composition and using the minor addition principle. This element fits well with the demand of the biomedical applications. Strontium is also a good element for bones and it is an element used in osteoporosis treatment. This element allows to decrease the bones reduction and stimulate the bones formation, as shown in the work of Zhao et al.<sup>158</sup>.

## **1-6- Improvements of the bulk metallic glasses systems**

There is a wide range of metallic glass systems, adapted to the targeted applications. Depending on the compositions, the glass forming ability, the critical diameter and the properties could be very different. However, the main drawbacks of this kind of alloys still remain the lack of ductility and the small critical diameter. During this work, new biocompatible discovered compositions are processed under ribbon forms so investigations on potential improvements to obtain bulk samples are conducted in four ways: micro-alloying, sintered and composites processing, and rejuvenation, which will be developed in the Chapter 7.

## 1-6-1- Microalloying

### 1-6-1-1- Kinds of minor addition

What is called minor addition is the intentional introduction of impurities in an alloy. The purpose of the minor additions is to improve properties of the alloys: manufacturability, thermal stability, mechanical properties and corrosion properties. At the beginning the minor addition was used in a lot of fields of metallurgy and for a long time. For example, in 3000-1000 B.C. in China, the properties of the alloy Cu-Sn were improved with the minor addition of lead <sup>159</sup>. It has also been found that iron can be mechanically improved with the addition of carbon, leading to steels. Concerning the crystalline alloys, this concept has been really developed during the second half of the 20<sup>th</sup> century, especially in Al-based alloys and Mg-based alloys <sup>160</sup>. In the steel industry, addition of rare earth elements is used in the casting process because the reactions between Rare-Earth Element (REE) and impurities are thermodynamically favoured compared to the reactions between impurities and other elements. The result is that adding a small amount of REE can scavenge and deoxidize the alloy.

The main advantages of minor additions are the variety and the amount of the added element. This is crucial for the alloy properties. Minor additions are used in metallic glasses for two purposes: the increase of the GFA and the improvement of the mechanical and chemical properties. All the kinds of minor additions will be developed in this part.

#### 1-6-1-1-1- Metalloid elements

Si, B, and C <sup>161</sup> are metalloid elements very often used for this purpose. All these elements have very strong affinity with the common elements in BMG alloys, such as Zr, Ti, Cu, Fe, Mg and REE (very negative mixing enthalpy) <sup>162,163-165</sup>. If this type of element amount is too high, intermetallic compounds can be formed and a detrimental effect on GFA can be induced. However, because of their very small atomic radius, adding these elements can improve the compactness of the alloy, and the resistance to crystallization is improved.

It should be noted that, usually metalloid element addition is very effective in Zr-based BMG but could also have negative effects in some particular cases (Si in Zr-based BMG).

Si has the particularity to lower the liquidus temperature and thus allows to adjust the composition quite easily close to a eutectic. The addition of Si in Ti-based or Cu-based BMG can drastically increase the GFA.

Table 3 summarizes the effects of metalloid additions.

Table 3 : Summary of the effects of minor additions of metalloid elements in different bulk metallic glasses <sup>159</sup>

<i>Alloying Element</i>	<b>Optimum content (at. %)</b>	<b>Base alloy (at. %)</b>	<b>Effect on GFA</b>	<b>References</b>
<i>C</i>	<1	Zr <sub>52.5</sub> Al <sub>10</sub> Cu <sub>17.9</sub> Ni <sub>14.6</sub>	No appreciable difference	166
	<2	Zr <sub>41</sub> Ti <sub>14</sub> Cu <sub>12.5</sub> Ni <sub>10</sub> Be <sub>22.5</sub>	Enhance GFA	167
	<5	FeGaPCB	Enhance GFA	168
	<5	Fe-based BMG	Enhance GFA	169
	<5	La <sub>55</sub> Al <sub>25</sub> Ni <sub>20</sub>	No appreciable difference	170
<i>Si</i>	1	Ti-Zr-Hf-Cu-Ni	Enhance GFA	171
	<1	Zr <sub>52.5</sub> Al <sub>10</sub> Cu <sub>17.9</sub> Ni <sub>14.6</sub>	No appreciable difference	166
	2	Fe-Ga-P-C-B	Enhance GFA	168
	2	Ni <sub>59</sub> Zr <sub>20</sub> Ti <sub>16</sub> Si <sub>2</sub> Sn <sub>3</sub>	Enhance GFA	172
	<5	Cu <sub>47</sub> Ti <sub>34</sub> Zr <sub>11</sub> Ni <sub>8</sub>	Enhance GFA	173
	<5	Ni-Ti-Zr-Si	Enhance GFA	174
	<5	Fe-Al-Ga-P-C-B-Si	Enhance GFA	175
<i>B</i>	<5	FeGaPCB	Enhance GFA	168
	<5	Fe-based BMG	Enhance GFA	169
	<5	La <sub>55</sub> Al <sub>25</sub> Ni <sub>20</sub>	No appreciable difference	170
	2	Ni-Nb-Sn	Enhance GFA	176

### 1-6-1-1-2- Metallic elements

Transition metallic elements are also often used for microalloying in BMGs. The amount is different from the metalloid elements because the risk to form intermetallic compounds is less important. Thus, the amount of minor additions can be larger.

Since metallic atoms have a large atomic size, as Zr and Sn, they also are very helpful to increase the GFA and can stabilize the supercooled liquid phase. However, some large metallic atoms as Ca, Sb have a negative effect on Zr- and Ti- based alloys.

The intermediate atoms, such as Fe <sup>177,178</sup>, Ni<sup>15,179</sup>, Co <sup>177</sup>, Cu, Mo<sup>180</sup>, Zn, Nb <sup>181,182</sup>, Ta <sup>183</sup> or Ti <sup>184,185</sup>, are often used in minor additions but a beneficial effect on the bulk glass formation is observed only with an amount higher than 5% <sup>182</sup>. Nevertheless, it should be noted that for REE-based, Ti- and Cu-based BMGs, intermediate atoms can have detrimental effects on GFA with addition fewer than 2 at. %.

Table 4 shows the effects of the metallic elements minor additions:

Table 4: Summary of the effects of minor additions of metallic elements in different bulk metallic glasses <sup>159</sup>

<b>Alloying element</b>	<b>Optimum content (at. %)</b>	<b>Base alloy (at. %)</b>	<b>Effect on GFA</b>	<b>References</b>
<i>Fe</i>	2	Zr <sub>41</sub> Ti <sub>14</sub> Cu <sub>12.5</sub> Ni <sub>10-x</sub> Fe <sub>x</sub> Be <sub>22.5</sub>	No difference	186
	1	(Cu <sub>60</sub> Zr <sub>30</sub> Ti <sub>10</sub> ) <sub>100-x</sub> Fe <sub>x</sub>	Deteriorated	187
	1-2	Ce <sub>70-x</sub> Al <sub>10</sub> Cu <sub>20</sub> Fe <sub>x</sub>	Enhanced	188
	1-5	(Pr <sub>60</sub> Al <sub>10</sub> Ni <sub>10</sub> Cu <sub>20</sub> ) <sub>100-x</sub> Fe <sub>x</sub>	Deteriorated	189
<i>Ni</i>	1-3	(Cu <sub>60</sub> Zr <sub>30</sub> Ti <sub>10</sub> ) <sub>100-x</sub> Ni <sub>x</sub>	Deteriorated	187
	3	Ti <sub>40</sub> Zr <sub>25</sub> Ni <sub>3</sub> Cu <sub>12</sub> Be <sub>20</sub>	Enhanced	54
<i>Al</i>	1-5	(Cu <sub>50</sub> Zr <sub>50</sub> ) <sub>100-x</sub> Al <sub>x</sub>	Enhanced	190
	1-2	Fe <sub>61</sub> Co <sub>7</sub> Zr <sub>10</sub> Mo <sub>5</sub> W <sub>2</sub> Al <sub>x</sub>	Enhanced	191
<i>Co</i>	1	(Cu <sub>60</sub> Zr <sub>30</sub> Ti <sub>10</sub> ) <sub>100-x</sub> Co <sub>x</sub>	Deteriorated	187
	1	Ce <sub>70-x</sub> Al <sub>10</sub> Cu <sub>20</sub> Co <sub>x</sub>	Enhanced	188
<i>Cu</i>	1-2	Nd <sub>60-x</sub> Fe <sub>20</sub> Al <sub>10</sub> Co <sub>10</sub> Cu <sub>x</sub>	Deteriorated	192
	<10	Ce <sub>70-x</sub> Al <sub>10</sub> Cu <sub>20</sub> Cu <sub>x</sub>	Enhanced	188
<i>Mo</i>	2	(Cu <sub>60</sub> Hf <sub>25</sub> Ti <sub>15</sub> ) <sub>100-x</sub> Mo <sub>x</sub>	Deteriorated	193
	2-4	(Fe <sub>0.7</sub> Mn <sub>0.3</sub> ) <sub>65</sub> Zr <sub>4</sub> Nb <sub>4</sub> Mo <sub>x</sub> B <sub>24</sub>	Enhanced	194
	0.5	(Cu <sub>47</sub> Zr <sub>11</sub> Ti <sub>34</sub> Ni <sub>8</sub> ) <sub>99.5</sub> Mo <sub>0.5</sub>	No difference	195
	<3	(Cu <sub>0.64</sub> Zr <sub>0.36</sub> ) <sub>1-x</sub> Mo <sub>x</sub>	Enhanced	196
<i>Zn</i>	2	Fe-Ga-P-C-B	Enhanced	197
	5	Mg <sub>65</sub> Cu <sub>25-x</sub> Y <sub>10</sub> Zn <sub>x</sub>	Enhanced	198
	5	Ce <sub>70-x</sub> Al <sub>10</sub> Co <sub>20</sub> Zn <sub>x</sub>	Enhanced	189
<i>Nb</i>	1	Ce <sub>70-x</sub> Al <sub>10</sub> Cu <sub>20</sub> Nb <sub>x</sub>	No difference	188
	1-5	Zr <sub>41</sub> Ti <sub>14</sub> Cu <sub>12.5</sub> Ni <sub>10-x</sub> Nb <sub>x</sub> Be <sub>22.5</sub>	Enhanced	199
	2.5	(Zr <sub>65</sub> Al <sub>10</sub> Cu <sub>15</sub> Ni <sub>10</sub> ) <sub>100-x</sub> Nb <sub>x</sub>	Enhanced	200
	2	Fe <sub>72-x</sub> Al <sub>5</sub> Ga <sub>2</sub> P <sub>11</sub> C <sub>6</sub> B <sub>4</sub> Nb <sub>x</sub>	Deteriorated	180
	4	(Co <sub>70.5</sub> Fe <sub>4.5</sub> Si <sub>10</sub> B <sub>15</sub> ) <sub>100-x</sub> Nb <sub>x</sub>	Enhanced	201
	2	(Cu <sub>60</sub> Hf <sub>25</sub> Ti <sub>15</sub> ) <sub>100-x</sub> Nb <sub>x</sub>	No difference	202
<i>Ta</i>	<3	(Cu <sub>0.64</sub> Zr <sub>0.36</sub> ) <sub>1-x</sub> Nb <sub>x</sub>	Enhanced	194
	2	(Cu <sub>60</sub> Hf <sub>25</sub> Ti <sub>15</sub> ) <sub>100-x</sub> Ta <sub>x</sub>	Deteriorated	193
	<3	(Cu <sub>0.64</sub> Zr <sub>0.36</sub> ) <sub>1-x</sub> Ta <sub>x</sub>	Enhanced	196
<i>Ti</i>	1-5%	(Cu <sub>50</sub> Zr <sub>50</sub> ) <sub>100-x</sub> Ti <sub>x</sub>	Enhanced	176
	1-5%	Zr <sub>56.2-x</sub> Ti <sub>x</sub> Cu <sub>31.3</sub> Ni <sub>4.0</sub> Al <sub>8.5</sub>	Enhanced	203
<i>Zr</i>	2	Co <sub>40</sub> Fe <sub>22</sub> Nb <sub>8-x</sub> B <sub>30</sub> Zr <sub>x</sub>	Enhanced	204
	2	(Y <sub>56</sub> Al <sub>24</sub> Co <sub>20</sub> ) <sub>100-x</sub> Zr <sub>x</sub>	Enhanced	43
	<3	Ce <sub>70-x</sub> Al <sub>10</sub> Cu <sub>20</sub> Zr <sub>x</sub>	No difference	189
	3	Ni <sub>60</sub> Nb <sub>40-x</sub> Sn	Enhanced	176
<i>Sn</i>	<3	Ti-based	Enhanced	205
	1	(Cu <sub>60</sub> Zr <sub>30</sub> Ti <sub>10</sub> ) <sub>100-x</sub> Sn <sub>x</sub>	Enhanced	163
	1	Ti <sub>44</sub> Cu <sub>40</sub> Ni <sub>8</sub> Zr <sub>8-x</sub> Sn <sub>x</sub>	Enhanced	195, 31
	<3	(Cu <sub>0.64</sub> Zr <sub>0.36</sub> ) <sub>1-x</sub> Sn <sub>x</sub>	Enhanced	196

### 1-6-1-1-3- Rare-earth elements

Rare earth elements (REE) have been used in the metallic glass formation, as minor additions and also BMG-forming base. They are often used in glassy alloys because they can

react with impurities preferentially and play a role of scavenging the impurities. They exhibit plentiful of unique properties, which can also lead to functional materials applications.

Table 5 below summarizes the systems containing rare earth elements.

Table 5: Summary of the effects of minor additions of rare-earth elements in different bulk metallic glasses <sup>159</sup>

<i>Alloying elements</i>	<b>Optimum content (at. %)</b>	<b>Base alloy</b>	<b>Effect on GFA</b>	<b>References</b>
Y	2	FeCoCrMoCBy	Enhanced	52
	5	ZrTiCuNi	Enhanced	206
	<5	Fe-based BMG	Enhanced	207
	<3	CuZrAl	Enhanced	41
Gd	<15	REE based BMG	Enhanced	208
	<5	CuZr based	Enhanced	209
Sc	<0.1	Zr <sub>52.5</sub> Al <sub>10</sub> Ti <sub>5</sub> Cu <sub>17.9</sub> Ni <sub>14.6</sub>	Markedly enhanced	166
	<1	Zr <sub>55</sub> Al <sub>10</sub> Cu <sub>30</sub> Ni <sub>5</sub>	Enhanced	210
	<5	Co <sub>60</sub> Cr <sub>15</sub> Mo <sub>14</sub> C <sub>15</sub> B <sub>5</sub>	Enhanced	53
Er	<15	Mg-Cu based	Enhanced	208
	<2	FeMoCBEr	No appreciable difference	211

Yttrium is the most “magic” REE to improve GFA and BMGs manufacturability of the BMG-forming alloys, especially in Cu- and Fe- based alloys. In the system Cu-Zr-Al, only 1 or 2 at.% <sup>212–214</sup> is necessary to improve the manufacturability of the system, thanks to the suppression of the eutectic clusters growth and the primary phase precipitation.

Yttrium in Fe-based <sup>207</sup> alloys at 2 at.% allows to increase the thermal stability by adjusting the composition and lowering the liquidus temperature. It also increases the manufacturability in scavenging oxygen impurities and creates innocuous Yttrium oxides <sup>51,191,194</sup>. As it is one of the biggest atoms, it induces the most important sequential change in the chemical order. The diffusivity is lowered and the topological and chemical short range orders increase, as the density of the undercooled liquid. It favours the glass formation thermodynamically and kinetically.

In Ti-based alloys, additions of only between 0.2 at. % and 1 at.% Y is necessary to improve the GFA <sup>215</sup>. Concerning the Zr-based BMGs <sup>216</sup>, it depends on the purity of Zr. For low purity Zr, the amount to be added is at least 0.5 at % and for a high purity Zr, it has to be less than 0.4 at. %. It is also very helpful for low purity raw materials in order to increase the critical diameter. Yttrium is not only able to scavenge the oxygen from the undercooled liquid but also to lower the liquidus temperature in Fe-based alloys. Y-based BMGs, can be formed directly from the liquid and reach diameters over 2 cm by water quenching. In the Zr-Cu-Ni-Al system, additions of only 0.5 at.% of Y increases the critical diameter from 3 mm to 10 mm <sup>181</sup>.

REE have very similar properties, as atomic size, or other chemical properties and have the same effect as micro alloying, except Y which reacts very easily with oxygen.

As BMGs are very sensitive to the manufacturing conditions, and also to the purity of the raw materials, the oxygen content should be limited. Otherwise, it will be detrimental to the glass formation. Oxygen triggers the formation of metastable crystalline phase. REEs seem

to have drastic and not fully explained effects on manufacturability of some BMGs. For example, the addition of REE in Mg-based allows to improve the GFA and to withstand a low vacuum during the process. Large REEs elements as Y, Sc, Gd, Er... have a beneficial effect on GFA, even in minute addition <sup>217-219</sup>.

Other additions were conducted in the system Cu-Zr-Al (Ce, Nd, Gd, Y, Dy, Ly) <sup>220</sup> and it appears that with 0.4 at. % the  $T_g$  is lowered as the GFA is increased and over 4% the plastic strain decreases as the yield strength.

In the Al-Ca-Ni system, several REEs additions were tried: Ce, La, Y, and Yb <sup>221</sup>. For all these four components, the optimal amount added was about 1% and the best element to add to this system is Yb. It impedes the formation of competing  $\alpha$ -Al clusters and enhances the stability of the liquid phase. Because it is the smallest atomic mismatch with Ca, the Yb atoms can substitute with Ca atoms. So the formation of crystallites is delayed and the crystallization resistance of the supercooled liquid is enhanced <sup>222</sup>.

Y, Ce and La additions also delay the  $\alpha$ -Al clusters precipitation but because they have a large atomic mismatch with Ca, the original liquid phase is strongly destabilized and the liquidus temperature is increased. This is the opposite of the intended effect of stabilizing the liquid phase and decreasing the liquidus temperature to be as close as possible to a eutectic temperature.

The influence on mechanical properties of Y additions in a Cu-Zr-Ti system will be the topic of Chapter 5.

### *1-6-1-2- Effects on the GFA*

The GFA of a BMG depends on two parameters: (i) The liquid structural features and properties and (ii) the stability of the competing crystalline phases. A small change in the composition of the liquid phase can cause the destabilization of the competing crystalline phases, and have an influence on the GFA. This is an important influence of minor additions. In this part, these mechanisms will be discussed.

#### 1-6-1-2-1- Influence on the liquid phase

The influence on the GFA comes from a change in the liquid behaviour. The viscosity, noted  $\eta$ , of glass forming liquids near  $T_g$  is compared using the fragility concept and the  $m$  values. Remember  $m$  corresponds to the fragility parameter introduced by Angell <sup>80</sup>. To keep in mind an idea of the value's orders, " $m$ " is between 16 (for strong liquid) and 200 (for fragile liquid). The evaluation of  $m$  is an indicator of how fast the viscosity evolves near  $T_g$ . The fragility of a glass forming liquid is related to the macroscopic properties and the GFA of the final glass because the structure and the properties of a glass depend on the properties of a frozen liquid <sup>223</sup>. Minor additions can change the liquid phase behaviour, modifying the properties of the final metallic glass GFA.

For example, in the Cu-Zr system, the addition of 8 at.% of Al and 1 at.% of Gd induces a decrease of  $m$  for the compositions :  $\text{Cu}_{50}\text{Zr}_{50}$ ,  $(\text{Cu}_{50}\text{Zr}_{50})_{92}\text{Al}_8$  and  $(\text{Cu}_{50}\text{Zr}_{50})_{92}\text{Al}_7\text{Gd}_1$  from 62, then 43, then 29 respectively <sup>209</sup>. The higher the concentration of alloying elements, the more  $m$  decreases. This indicates a favourable change in the liquid behaviour.

The GFA could also be determined by the evaluation of the heat capacity  $\Delta C_p$ , near  $T_g$ . It is possible to see a change in the liquid behaviour by the highlight of a distinct fragile-strong transition by a jump in  $\Delta C_p$ . It suggests a strong resistance to structural degradation in a liquid. Concerning the fragile liquid, the jump of heat capacity is closer to a sharp peak. Minor additions can convert “fragile” liquids into intermediate “strong” liquids, and increases the GFA.

#### 1-6-1-2-2- Influence of the topological and chemical ordering

From a microstructure point of view, there is a correlation between the short-range order and the fragility. The strongest glasses exhibit a strong tendency to short range order <sup>224</sup>, which enhances the glass forming ability. The short-range order degree rules the fragility. A decrease of  $m$  induced by minor additions leads to a strong tendency of short range order. According to the Adam-Gibbs theory <sup>93</sup>, the liquid becomes more viscous and denser, which slows down the crystallization.

Another change in microstructure comes from electronegativity difference between the additional element and the constituents. Indeed, the GFA can be increased if the electronegativity mismatch between the added element and the main constituents of the alloy is optimal <sup>205</sup>. In this case, quasi covalence between the additional element and the components will be formed. According to the work of Inoue <sup>127</sup>, strong liquids contain quasi covalent four-coordinated network. As the metallic bond is weaker than a covalent bond, these last ones are the first bonds responsible for the packing in BMGs. The ordering of this kind of bonds plays a crucial role in the glass formation.

#### 1-6-1-2-3- Liquid phase stabilization

It has been already mentioned that some minor additions thermodynamically and kinetically stabilize the liquid phase. First, additional elements and the main component should exhibit a high mixing enthalpy to form preferentially new local atomic pairs of crystalline compounds. The result of this action is the formation of new clusters in the undercooled liquid, increasing the short range order. To initiate new crystalline structures, the short range has to be disturbed and the bonds in the clusters have to be broken upon cooling to create new strong bonds with other constituents, which contributes to the liquid phase stabilization. Thus, the competition between short-range order and long range order of crystalline structures control the GFA of undercooled liquid <sup>225-227</sup>. The local clusters induced by alloying additions increase the energy barrier for the supercooled liquid region to overcome in order to create a crystalline phase. Adding other elements will first strengthen the liquid phase stability and secondly, delay the crystallization process. Moreover, in some cases using

proper additions and proper amounts, the new atoms can occupy some interstitial sites in the structure which increases the packing density of the liquid.

It also can lower the liquidus temperature and adjust the composition close to a eutectic<sup>68,209,228</sup>, which also contributes to the liquid phase stabilization.

#### 1-6-1-2-4- Suppression of the competing crystalline phase

Glass formation is a competition process between molten liquid and crystalline phases. If the proper atoms are added, the suppression of the competing crystalline phase can occur and the glass formation is favoured. For instance, in the Cu-Zr system, the diagram shows a lot of eutectics far below melting temperatures of the system (which is associated with the GFA). The major competitor to the glass formation in Cu<sub>50</sub>Zr<sub>50</sub> is the hexagonal phase Cu<sub>51</sub>Zr<sub>14</sub>. When 2 at. % of Al are added, the primary phase on cooling changes to Al<sub>2</sub>Zr and then adding 6 at. % of Al changes the primary phase to Al<sub>2</sub>Zr<sub>3</sub> while the GFA is enhanced for the same amount. The increase of the GFA is linked to the suppression of the competing crystalline phase. This can be interpreted because the composition gets closer to deep metastable eutectic. Additions inhibit the nucleation and the growth of the primary phase Cu<sub>51</sub>Zr<sub>14</sub> and the relevant phase diagram is then a very deep metastable eutectic. The alloy composition has been adjusted to a deeper eutectic system.

#### *1-6-1-3 Enhancement of the properties*

The other main action of the minor additions is the enhancement of the properties: corrosion resistance, thermal stability or mechanical properties.

#### 1-6-1-3-1- Thermal stability

The most critical point is that trying to enhance the thermal stability, the effect on the GFA can be detrimental. A good compromise has to be found to improve both properties. Additions of some elements stabilize the original system, as for example with Ni-Ti system, Ta and Nb in a Zr-based system, can stabilize the system. For example, they have similarities with Ni and Ti from a structural point of view but higher melting temperatures<sup>229</sup>. If Ti and Ni substitute with Nb and Ta the thermal stability is higher without modifying the GFA.

Nb can improve the thermal stability especially in Zr-based alloys but in some cases, the GFA can also be impacted which is not the case of Ta replacing Ti<sup>230</sup>.

So the addition of metals with similar structural aspect and higher melting temperatures is a good way to increase the thermal stability.

### 1-6-1-3-2- Mechanical properties

Because of the particular structure and atomic scale in homogeneities due to the minor additions, we observed a “work hardening” phenomenon. The strain and stress concentrations in these areas are very different from the other parts of the samples, which create preferential sites for the shear bands nucleation and also as a barrier to cross. It leads to the ability of extensive shear bands and multiplications of the shear bands. It has been proved with the addition of Al in Cu-Zr system. Al is a very helpful element for the plasticity enhancement and the same phenomenon was also observed with the addition of Ti in Cu-Zr<sup>231</sup> or Ta in Zr-Cu-Ni-Al<sup>232</sup>. Some elements can improve the fatigue resistance as Ni<sup>233</sup>.

The compressive strength of the amorphous alloys Fe-TM-B (with TM: transition metals) has been increased up to 3800 MPa and the Vickers hardness has been evaluated about 1000 Hv for the Fe<sub>60</sub>Co<sub>8</sub>Zr<sub>10</sub>Mo<sub>5</sub>W<sub>2</sub>B<sub>1</sub> composition<sup>234</sup>.

### 1-6-1-3-3- Corrosion resistance

Corrosion resistance is usually investigated using the electrochemical polarization, weight loss measurements, corrosion rates and XPS analyses. Some elements are very well-known to improve the corrosion resistance, as for example, Cr, Mo, Nb, W, Hf<sup>193</sup>. Between Mo, Cr, and W, Mo addition is probably the best because of the difference ionizing energy of out shell electrons. However, all these elements lead to a decrease of T<sub>g</sub> and T<sub>x</sub>.

The corrosion resistance and the influence of the minor additions depend on the studied system. In this part, small examples are given for several systems and the main additional elements.

Cu-based amorphous alloys are not resistant against corrosion but they exhibit a drastic change with Mo or Cr additions, even better than stainless steel. The corrosion potential and the pitting potential are increased. Concerning the Zr-based systems, additions of Nb and Hf atoms increase their corrosion resistance thanks to the formation of a passive film after anodic polarization enriched of aluminium oxides and depleted in phosphate ions, as it is shown in Fig. 1-25.

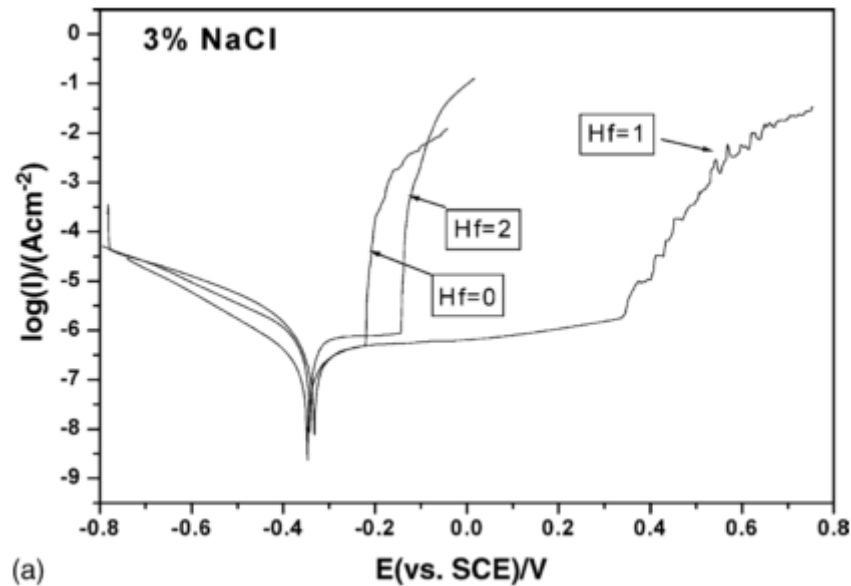


Figure 1-25: Potentiodynamic polarization curves of  $Zr_{65-x}Hf_xCu_{17.5}Ni_{10}Al_{7.5}$  ( $x=0, 1$  and  $2$  at.%) alloys in 3% NaCl solution <sup>235</sup>

Concerning Mo, Ta and Nb, in all the systems they lead to an enrichment in the passivation film. Because they are the most corrosion resistant elements and often depleted in copper oxides, the corrosion potential or the pitting potential is increased. These elements contribute to quickly form a passive film on the surface of the sample.

From tests in 37°C for 20 days, the minor additions allow to reduce considerably the ion release of all kinds of metals because the minor addition induces a rapid formation of a highly protective film <sup>236,207</sup>. This result is very interesting for biomedical applications.

#### 1-6-1-4- Empirical rules

##### 1-6-1-4-1- Improvement of the thermal stability

A compromise between good GFA and good thermal stability is often needed, as the GFA and the thermal stability are different properties. Depending on the targeted influence, minor additions can show contrary results on GFA and thermal stability. In order to enhance the thermal stability, several recommendations are made in the review paper of Wang et al. <sup>159</sup>, as shown below:

- Small atoms have to be chosen to be added in the system to increase the density packing of the liquid structure.
- Other constituents have to be selected to stabilize the liquid phase and lower the melting point.
- For the purpose of suppressing the nucleation and crystal growth of the competing crystalline phases, proper elements have to be added.

- Oxygen and other harmful impurities need to be scavenged by other chemical species (as Y) to form innocuous oxides.

#### 1-6-1-4-2- Enhancement of the mechanical properties

There exists a correlation between linear elastic constants and mechanical properties, plastic yielding of the glass, thermal stability and rheological properties of glass-forming liquid<sup>204,237,238</sup>. Thus, controlling the elastic moduli of the alloy can be used to control the properties of the glass. The properties can be tailored by an appropriate selection of adding components depending on the targeted elastic moduli.

### **1-6-2- Composites manufacturing**

From 1990, researchers noticed that the addition of ductile crystalline particles can reduce the brittle fracture and increase the ductility<sup>239</sup>. Thus, the different ways to process composite samples with an amorphous matrix containing crystalline particles were investigated. The principle is that the second crystalline phase acts, first, as nucleation sites for shear bands and secondly, as a barrier trapping these bands. Thus, the number of defects and the ductility are increased.

There are two kinds of composite materials, shown on the Fig. 1-26.

- In-situ composites<sup>240,241</sup>:

The first way to process in-situ composite is to form crystalline dendrites phase during the quench. The quantity and the distribution of crystalline phases are difficult to control<sup>242</sup>.

The other way is to conduct a proper thermal treatment after quenching in order to induce nano-crystallization. Once again, it is complicated to control the distribution and the quantity of the crystalline phase in the sample but in both cases, the interfaces between the crystalline and amorphous phase are strong.

- Ex-situ composites<sup>243,244</sup>:

For this kind of material, powder metallurgy can be used. Crystalline particles are employed and mixed to the processed amorphous powder, then the densification step is conducted. All the ways to process powder and densify it will be developed in Chapter 6. The advantages are the good control of the volume fraction, the nature, the size of the crystalline phase. However, the particle interfaces are weak.

The other process is to use very high melting point elements particles, as WC or Ta during the process. The melting point will not be reached for these particles, which will remain unchanged in the sample after the quench. The drawback is the difficulty to control the distribution of the particles in the sample and the choice of the particles nature is limited.

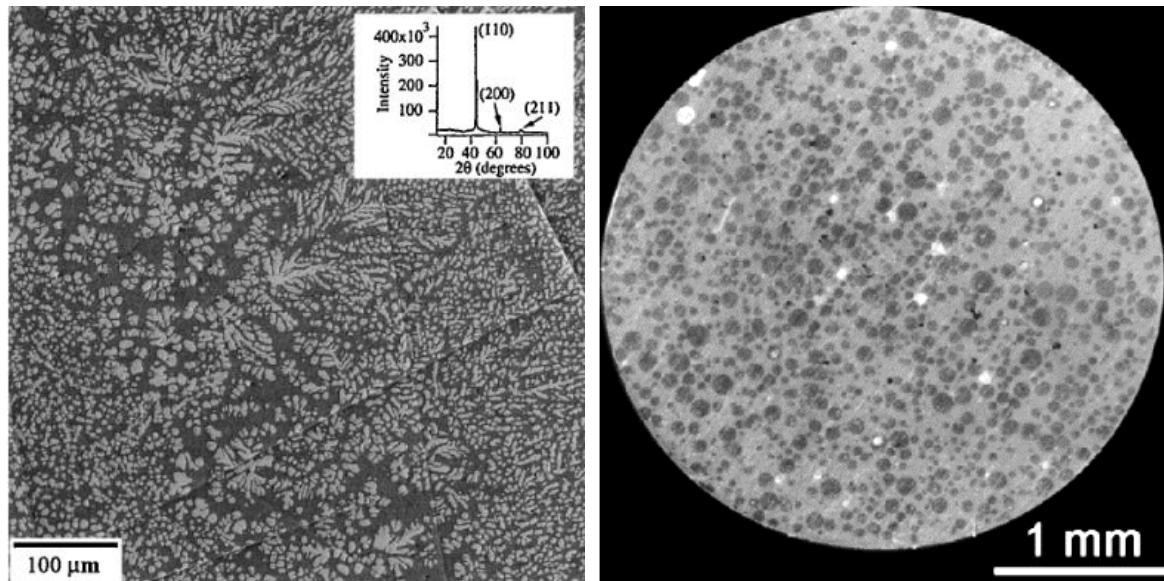


Figure 1-26: Two different kinds of composite samples, a) SEM micrograph of an in-situ composite microstructure of the  $(Zr_{75}Ti_{18.34}Nb_{6.66})_{75}X_{25}^{230}$ , b) SEM micrograph of the cross section of an ex-situ composite containing 40 vol.% Ti powders of  $Mg_{65}Cu_{25}Gd_{10}$  metallic glass<sup>245</sup>

The Figure 1-27 shows summarized the different ways to process composite samples.

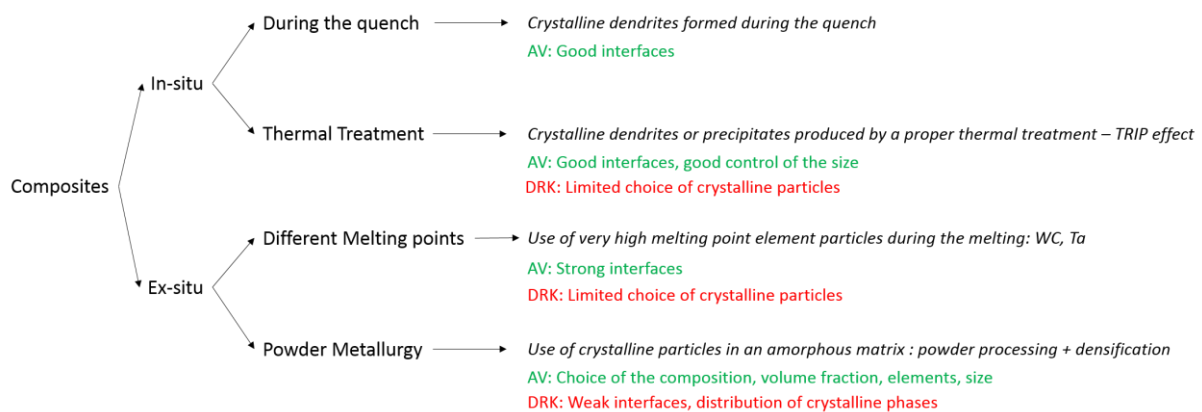


Figure 1-27: Summary of the composites samples process.

The Chapter 6 will discuss about the powder metallurgy technique to process bulk metallic glasses, associating powder obtained by atomization and densification by Spark Plasma Sintering (SPS). This technique is not only applied for the ductility enhancement by composites processing but also for the critical diameter improvement without using any crystalline particles. The amorphous powders start to arouse interest from 1970 and then the technique to densify the samples were developed. This process offers technological advances and it is easy to obtain powder less than 100  $\mu\text{m}$  diameter at least because the cooling rate of the powder is close to  $10^6 \text{ K}\cdot\text{s}^{-1}$  for atomization process. Thus, amorphous powder can be processed even for compositions with not a high glass forming ability. It is a relevant technique to overcome the small critical diameter issues and also to improve the plasticity of the samples. The use of powder metallurgy technique is also interesting to process complex shapes.

With a proper temperature above  $T_g$ , the glassy powder can be easily deformed, using the benefit of the uniaxial pressure and the pulsed direct current. With a reasonable temperature above  $T_g$ , it is easy to reach full consolidation <sup>246,247</sup>.

### 1-6-3- Porous metallic glasses

The idea to use porous structure for biomedical applications is very interesting because cells have better adhesion and a better growth in porous support. One supplementary advantage: it is possible to adjust the pores quantity and modify the Young modulus of the material and other mechanical characteristics.

In 1996, Apfel and Qiu <sup>248</sup> had the idea to elaborate porous structures before Schroers et al. did it in 2003 <sup>249</sup>. The first foam metallic glass was:  $\text{Pd}_{43}\text{Ni}_{10}\text{Cu}_{27}\text{P}_{20}$ . At least, Brothers and Dunand <sup>250</sup>, implemented the first experimental method to process of Zr-metallic glass foams to be commercialized. Demetriou et al. established the fact that with low medium porosities, the mechanical properties and plasticity are increased whereas with important porosities, mechanical properties drops catastrophically <sup>251,252</sup>.

For the metallic glasses foam, the Young modulus is depending on the density of the foam and the shape of the original bulk as <sup>253</sup>:

$$E_{\text{foam}} \propto \left( \frac{\rho_{\text{foam}}}{\rho_{\text{bulk}}} \right)^2 \quad (11)$$



Figure 1-28: Image of 88%-porosity  $\text{Pd}_{43}\text{Ni}_{10}\text{Cu}_{27}\text{P}_{20}$  foam <sup>251</sup>

## 1-7- Conclusion

Metallic glasses are unique systems with promising properties. Because of their amorphous nature, they can reach high mechanical properties, especially yield strength, high

corrosion resistance, good wear resistance and a very shiny and smooth surface aspect compared to their crystalline counterparts. The structure is also isotropic and homogeneous, which is a very interesting advantage, especially for small devices. This kind of material is particularly promising for the micromechanics samples, especially in the medical field, jewellery or in watchmaking.

These materials are also adjustable depending on the target applications. The choice of the base elements can drastically change the behaviour of the sample and affect the properties. A large number of studies focus on almost all the elements as base of the systems. If we can choose the proper elements to add in order to obtain the intended properties, all the systems and all the elements are not able to form an amorphous alloy. In order to increase the possibilities to obtain an amorphous bulk sample, some criteria to follow were implemented. Nevertheless, the glassy structure is dependent on other parameters, as for example, the purity of the processing environment, the purity of the raw materials, or the way to process.

New fields of interest concern the metallic glasses improvement trying to avoid the main drawbacks: the lack of ductility and the critical diameter. The first solution is to add a small amount of elements, the second one is to find other kinds of processes to get composites samples. A last one consists to conduct rejuvenation on the sample, but it will be developed in the last chapter.

Micro-additions of appropriate elements can drastically influence the behaviour of the glassy systems, especially the corrosion behaviour, the ductility and the biocompatibility. Additions of some elements, like rare-earth elements, could be very interesting to obtain a higher critical diameter, more stable systems and better mechanical properties, using different mechanisms (scavenge impurities, increase of the compactness because of the high atomic radius...).

Composites processing allows the increase of the critical diameter or ductility. For this purpose, two techniques are possible: in-situ composites and ex-situ composites, using different processes during quenching, thermal treatment, or powder metallurgy.

There is a lot of works about the processing of the metallic glasses, their improvement and also to understand the deformation mechanisms. It has been mentioned that BMGs are very promising in the biomedical field. However, no real composition is fully biocompatible because some elements are difficult to replace, as for example, aluminium.

The aim of this work is to process new fully biocompatible compositions of metallic glasses, for a use as biodegradable materials and as reinforcing materials. These two studies will be handled in Chapter 3, on a Mg-based system and in Chapter 4, on a Zr-based system. Nevertheless, it appears that some harmful elements as Be or Al are difficult to replace and play an important role on the critical size and ductility. Using only biocompatible elements makes the manufactory of bulk samples more difficult. Thus in Chapter 5, we choose a Ni-free, Be-free, Al-free system (Cu-Zr-Ti) and study the influence of Y addition to precisely understand the mechanism of this microalloying and the beneficial effect on the size and on the ductility. With the same purpose, we also studied a different process, using gas atomization powder

and SPS, in order to manufacture composite samples to increase the critical size and the ductility. This study is given in the same system than Chapter 6 to compare. A last Chapter 7 proposes an understanding of the deformation mechanisms using experimental compressive tests and molecular dynamic simulations. The strain rate influence and rejuvenation on the mechanical properties are discussed.

## 1-8- References

1. Peker, A. & Johnson, W. L. A highly processable metallic glass:  $Zr_{41.2}Ti_{13.8}Cu_{12.5}Ni_{10.0}Be_{22.5}$ . *Appl. Phys. Lett.* **63**, 2342–2344 (1993).
2. Bhugra, C., Pikal M.J. Role of thermodynamic, molecular, and kinetic factors in crystallization from the amorphous state. *J. Pharm. Sci.* **97**, 1329–1349 (2008)
3. Pelletier, J. M. Influence of structural relaxation on atomic mobility in a  $Zr_{41.2}Ti_{13.8}Cu_{12.5}Ni_{10.0}Be_{22.5}$  (Vit1) bulk metallic glass. *J. Non-Cryst. Solids* **354**, 3666–3670 (2008).
4. Saida, J., Yamada, R., Wakeda, M. & Ogata, S. Thermal rejuvenation in metallic glasses. *Sci. Technol. Adv. Mater.* **18**, 152–162 (2017).
5. Klement, W., Willens, R. H., Duwez, P. « Non-crystalline structure in solidified Gold-Silicon alloys », *Nature*, vol. 187, n° 4740, p. 869–870, 1960
6. Drehman, A. J., Greer, A. L. & Turnbull, D. Bulk formation of a metallic glass:  $Pd_{40}Ni_{40}P_{20}$ . *Appl. Phys. Lett.* **41**, 716–717 (1982).
7. Kui, H. W., Greer, A. L. & Turnbull, D. Formation of bulk metallic glass by fluxing. *Appl. Phys. Lett.* **45**, 615–616 (1984).
8. Inoue, A., Nishiyama, N. & Kimura, H. Preparation and Thermal Stability of Bulk Amorphous  $Pd_{40}Cu_{30}Ni_{10}P_{20}$  Alloy Cylinder of 72 mm in Diameter. *Mater. Trans. JIM* **38**, 179–183 (1997).
9. Nishiyama, N., Takenaka, K., Miura, H. *et al.* The world's biggest glassy alloy ever made. *Intermetallics* **30**, 19–24 (2012).
10. Buzzi, S., Jin, K., Uggowitzer, P. *et al.* Cytotoxicity of Zr-based bulk metallic glasses. *Intermetallics* **14**, 729–734 (2006).
11. Qiu, C. L., Chen, Q., Liu, L. *et al.* A novel Ni-free Zr-based bulk metallic glass with enhanced plasticity and good biocompatibility. *Scr. Mater.* **55**, 605–608 (2006).
12. Zhao, G.-H., Aune, R. E., Mao, H. & Espallargas, N. Degradation of Zr-based bulk metallic glasses used in load-bearing implants: A tribocorrosion appraisal. *J. Mech. Behav. Biomed. Mater.* **60**, 56–67 (2016).
13. Horton, J. A. & Parsell, D. E. Biomedical Potential of a Zirconium-Based Bulk Metallic Glass. *MRS Proc.* **754**, CC1.5 (2002).
14. Amiya, K. & Inoue, A. Formation and Thermal Stability of Ca-Mg-Ag-Cu Bulk Glassy Alloys. *Mater. Trans.* **43**, 2578–2581 (2002).
15. Men, H., Pang, S., Inoue, A. & Zhang, T. New Ti-Based Bulk Metallic Glasses with Significant Plasticity. *Mater. Trans.* **46**, 2218–2220 (2005).
16. Pang, S., Liu, Y., Li, H. *et al.* New Ti-based Ti-Cu-Zr-Fe-Sn-Si-Ag bulk metallic glass for biomedical applications. *J. Alloys Compd.* **625**, 323–327 (2015).
17. Xie, G., Qin, F. & Zhu, S. Recent Progress in Ti-Based Metallic Glasses for Application as Biomaterials. *Mater. Trans.* **54**, 1314–1323 (2013).
18. Calin, M., Gebvert, M., Cosmina, A. *et al.* Designing biocompatible Ti-based metallic glasses for implant applications. *Mater. Sci. Eng. C* **33**, 875–883 (2013).
19. Zhu, S., Wang, X., Qin, F. & Inoue, A. Glass-forming ability and thermal stability of Ti-Zr-Cu-Pd-Si bulk glassy alloys for biomedical applications. *Mater. Trans.* **48**, 163–166 (2007).

20. Zhang, W. & Inoue, A. Cu-based bulk glass formation in the Cu-Zr-Ga alloy system and their mechanical properties. *Mater. Trans.* **45**, 532–535 (2004).
21. Qin, B. & Lai, W. S. Metallic glass-forming composition range of the Cu–Zr–Ti ternary system determined by molecular dynamics simulations with many-body potentials. *J. Mater. Res.* **26**, 547–560 (2011).
22. Inoue, A., Zhang, W., Zhang, T. & Kurosaka, K. High-strength Cu-based bulk glassy alloys in Cu–Zr–Ti and Cu–Hf–Ti ternary systems. *Acta Mater.* **49**, 2645–2652 (2001).
23. Desré, P. J., Lin, C. K., Chen, G. S., Louh, R. F. & Chen, K. C. Formation of Cu-Zr-Ti Amorphous Alloys with Significant Supercooled Liquid Region by Mechanical Alloying. *J. Metastable Nanocrystalline Mater.* **2–6**, 67–72 (1999).
24. Zhang, T., Kurosaka, K. & Inoue, A. Thermal and Mechanical Properties of Cu-Based Cu-Zr-Ti-Y Bulk Glassy Alloys. *Mater. Trans.* **42**, 2042–2045 (2001).
25. Wada, T., Takenaka, K., Nishiyama, N. & Inoue, A. Formation and Mechanical Properties of Porous Pd-Pt-Cu-P Bulk Glassy Alloys. *Mater. Trans.* **46**, 2777–2780 (2005).
26. Nishiyama, N., Takenaka, K., Wada, T., Kimura, H. & Inoue, A. Undercooling Behavior and Critical Cooling Rate of Pd-Pt-Cu-P Alloy. *Mater. Trans.* **46**, 2807–2810 (2005).
27. Takenaka, K., Wada, T., Nishiyama, N., Kimura, H. & Inoue, A. New Pd-based bulk glassy alloys with high glass-forming ability and large supercooled liquid region. *Mater. Trans.* **46**, 1720–1724 (2005).
28. Cardinal, S., Qiao, J., Pelletier, J. M. & Kato, H. Bulk metallic glasses based on precious metals: Thermal treatments and mechanical properties. *Intermetallics* **63**, 73–79 (2015).
29. Li, H.F., Pang, S.J., Liu, Y. *et al.* Biodegradable Mg–Zn–Ca–Sr bulk metallic glasses with enhanced corrosion performance for biomedical applications. *Mater. Des.* **67**, 9–19 (2015).
30. Gu, X., Shiflet, G. J., Guo, F. Q. & Poon, S. J. Mg–Ca–Zn Bulk Metallic Glasses with High Strength and Significant Ductility. *J. Mater. Res.* **20**, 1935–1938 (2005).
31. Inoue, A. & Masumoto, T. Mg-based amorphous alloys. *Mater. Sci. Eng. A* **173**, 1–8 (1993).
32. Guo, F., Joseph Poon, S., Gu, X. & Shiflet, G. J. Low-density Mg-rich metallic glasses with bending ductility. *Scr. Mater.* **56**, 689–692 (2007).
33. Li, H. F., Xie, X., Zhao, K., *et al.* In vitro and in vivo studies on biodegradable CaMgZnSrYb high-entropy bulk metallic glass. *Acta Biomater.* **9**, 8561–8573 (2013).
34. Senkov, O. N., Miracle, D., Barney, E. *et al.* Local atomic structure of Ca-Mg-Zn metallic glasses. *Phys. Rev. B* **82**, 104206 (2010).
35. Senkov, O. N., Miracle, D. B., Keppens, V. & Liaw, P. K. Development and Characterization of Low-Density Ca-Based Bulk Metallic Glasses: An Overview. *Metall. Mater. Trans. A* **39**, 1888–1900 (2008).
36. Zhao, K., Li, J. F., Zhao, D. Q., Pan, M. X. & Wang, W. H. Degradable Sr-based bulk metallic glasses. *Scr. Mater.* **61**, 1091–1094 (2009).
37. Li, H. F., Zhao, K., Wang, Y. B., Zheng, Y. F. & Wang, W. H. Study on bio-corrosion and cytotoxicity of a Sr-based bulk metallic glass as potential biodegradable metal. *J. Biomed. Mater. Res. B Appl. Biomater.* **100B**, 368–377 (2012).
38. Qiao, J., Jia, H. & Liaw, P. K. Metallic glass matrix composites. *Mater. Sci. Eng. R Rep.* **100**, 1–69 (2016).
39. Inoue, A., Zhang, T., Nishiyama, N., Ohba, K. & Masumoto, T. Preparation of 16 mm Diameter Rod of Amorphous  $Zr_{65}Al_{7.5}Ni_{10}Cu_{17.5}$  Alloy. *Mater. Trans. JIM* **34**, 1234–1237 (1993).
40. Lou, H. B., Wang, X., Xu, F. *et al.* 73 mm-diameter bulk metallic glass rod by copper mould casting. *Appl. Phys. Lett.* **99**, 051910 (2011).
41. Xu, D., Duan, G. & Johnson, W. L. Unusual Glass-Forming Ability of Bulk Amorphous Alloys Based on Ordinary Metal Copper. *Phys. Rev. Lett.* **92**, 245504 (2004).
42. Jia, P., Guo, H., Li, Y., Xu, J. & Ma, E. A new Cu–Hf–Al ternary bulk metallic glass with high glass forming ability and ductility. *Scr. Mater.* **54**, 2165–2168 (2006).
43. Guo, F., Poon, S. J. & Shiflet, G. J. Metallic glass ingots based on yttrium. *Appl. Phys. Lett.* **83**, 2575–2577 (2003).

44. Zhang, Y., Tan, H. & Li, Y. Bulk Glass Formation of 12 mm Rod in La–Cu–Ni–Al Alloys. *Mater. Sci. Eng. A* **375–377**, 436–439 (2004).
45. Li, R., Pang, S., Ma, C. & Zhang, T. Influence of similar atom substitution on glass formation in (La–Ce)–Al–Co bulk metallic glasses. *Acta Mater.* **55**, 3719–3726 (2007).
46. Jiang, Q. K., Zhang, G.Q., Yang, L. *et al.* La-based bulk metallic glasses with critical diameter up to 30mm. *Acta Mater.* **55**, 4409–4418 (2007).
47. Inoue, A. & Zhang, T. Thermal stability and glass-forming ability of amorphous Nd–Al–TM (TM = Fe, Co, Ni or Cu) alloys. *Mater. Sci. Eng. A* **226–228**, 393–396 (1997).
48. Ma, H., Shi, L. L., Xu, J., Li, Y. & Ma, E. Discovering inch-diameter metallic glasses in three-dimensional composition space. *Appl. Phys. Lett.* **87**, 181915 (2005).
49. Zheng, Q., Xu, J. & Ma, E. High glass-forming ability correlated with fragility of Mg–Cu(Ag)–Gd alloys. *J. Appl. Phys.* **102**, 113519 (2007).
50. Ponnambalam, V., Poon, S. J. & Shiflet, G. J. Fe-based bulk metallic glasses with diameter thickness larger than one centimeter. *J. Mater. Res.* **19**, 1320–1323 (2004).
51. Lu, Z. P., Liu, C. T., Thompson, J. R. & Porter, W. D. Structural Amorphous Steels. *Phys. Rev. Lett.* **92**, 245503 (2004).
52. Shen, J., Chen, Q., Sun, J., Fan, H. & Wang, G. Exceptionally high glass-forming ability of an FeCoCrMoCBy alloy. *Appl. Phys. Lett.* **86**, 151907 (2005).
53. Men, H., Pang, S. J. & Zhang, T. Effect of Er doping on glass-forming ability of Co<sub>50</sub>Cr<sub>15</sub>Mo<sub>14</sub>C<sub>15</sub>B<sub>6</sub> alloy. *J. Mater. Res.* **21**, 958–961 (2006).
54. Guo, F., Wang, H., Poon, S. J. & Shiflet, G. J. Ductile titanium-based glassy alloy ingots. *Appl. Phys. Lett.* **86**, 091907 (2005).
55. Gong, P., Yao, K., Wang, X. & Shao, Y. A New Centimeter-Sized Ti-Based Quaternary Bulk Metallic Glass with Good Mechanical Properties. *Adv. Eng. Mater.* **15**, 691–696 (2013).
56. Tang, M. Q., Zhang, H., Zhu, Z. *et al.* TiZr-base Bulk Metallic Glass with over 50 mm in Diameter. *J. Mater. Sci. Technol.* **26**, 481–486 (2010).
57. Park, E. S. & Kim, D. H. Formation of Ca–Mg–Zn bulk glassy alloy by casting into cone-shaped copper mold. *J. Mater. Res.* **19**, 685–688 (2004).
58. Senkov, O. N., Scott, J. M. & Miracle, D. B. Composition range and glass forming ability of ternary Ca–Mg–Cu bulk metallic glasses. *J. Alloys Compd.* **424**, 394–399 (2006).
59. Schroers, J. & Johnson, W. L. Highly processable bulk metallic glass-forming alloys in the Pt–Co–Ni–Cu–P system. *Appl. Phys. Lett.* **84**, 3666–3668 (2004).
60. Zeng, Y., Nishiyama, N., Yamamoto, T. & Inoue, A. Ni-Rich Bulk Metallic Glasses with High Glass-Forming Ability and Good Metallic Properties. *Mater. Trans.* **50**, 2441–2445 (2009).
61. Fu, H. M., Mu, J., Wang, A. *et al.* Synthesis and compressive properties of Al–Ni–Y metallic glass. *Philos. Mag. Lett.* **89**, 711–716 (2009).
62. Kissinger, H. E. Reaction Kinetics in Differential Thermal Analysis. *Anal. Chem.* **29**, 1702–1706 (1957).
63. Flynn, J. H. & Wall, L. A. A quick, direct method for the determination of activation energy from thermogravimetric data. *J. Polym. Sci. [B]* **4**, 323–328 (1966).
64. Flynn, J. H. & Wall, L. A. General treatment of the thermogravimetry of polymers. *J. Res. Natl. Bur. Stand. Sect. Phys. Chem.* **70A**, 487 (1966).
65. Savalia, R. T., Lad, K. N., Pratap, A., Dey, G. K. & Banerjee, S. Study of formation of nano-quasicrystals and crystallization kinetics of Zr–Al–Ni–Cu metallic glass. *J. Therm. Anal. Calorim.* **78**, 745–751 (2004).
66. Wei, S., Ding, B., Lei, T. & Hu, Z. Crystallization of amorphous Zr Cu Al alloy with wide supercooled liquid region. *Mater. Lett.* **37**, 263–267 (1998).
67. Turnbull, D. Under what conditions can a glass be formed? *Contemp. Phys.* **10**, 473–488 (1969).
68. Lu, Z. P. & Liu, C. T. A new glass-forming ability criterion for bulk metallic glasses. *Acta Mater.* **50**, 3501–3512 (2002).
69. Chen, Q. *et al.* A new criterion for evaluating the glass-forming ability of bulk metallic glasses. *Mater. Sci. Eng. A* **433**, 155–160 (2006).

70. Zhu, S. L., Wang, X. M., Qin., F. X. & Inoue, A. A new Ti-based bulk glassy alloy with potential for biomedical application. *Mater. Sci. Eng. A* **459**, 233–237 (2007).
71. Egami, T. & Waseda, Y. Atomic size effect on the formability of metallic glasses. *J. Non-Cryst. Solids* **64**, 113–134 (1984).
72. Nagel, S. R. & Tauc, J. Nearly-Free-Electron Approach to the Theory of Metallic Glass Alloys. *Phys. Rev. Lett.* **35**, 380–383 (1975).
73. Argon, A. S. Plastic deformation in metallic glasses. *Acta Met. Mater* **27**, 47–58 (1979).
74. Trexler, M. M. & Thadhani, N. N. Mechanical properties of bulk metallic glasses. *Prog. Mater. Sci.* **55**, 759–839 (2010).
75. Spaepen, F. Homogeneous flow of metallic glasses: A free volume perspective. (2005).
76. Spaepen, F. A microscopic mechanism for steady state inhomogeneous flow in metallic glasses. *Acta Metall.* **25**, 407–415 (1977).
77. Angell, C. A. Glass-Formers and Viscous Liquid Slowdown since David Turnbull: Enduring Puzzles and New Twists. *MRS Bull.* **33**, 544–555 (2008).
78. Blodgett, M. E., Egami, T., Nussinov, Z. & Kelton, K. F. Proposal for universality in the viscosity of metallic liquids. *Scientific Reports* **5**, 13837 (2015).
79. Angell, C. Relaxation in liquids, polymers and plastic crystals — strong/fragile patterns and problems. *J. Non-Cryst. Solids* **131–133**, 13–31 (1991).
80. Angell, C. A. Formation of Glasses from Liquids and Biopolymers. *Science* **267**, 1924–1935 (1995).
81. Mukherjee, S., Schroers, J., Zhou, Z., Johnson, W. . & Rhim, W.-K. Viscosity and specific volume of bulk metallic glass-forming alloys and their correlation with glass forming ability. *Acta Mater.* **52**, 3689–3695 (2004).
82. Raghavan, R., Murali, P. & Ramamurty, U. Influence of Cooling Rate on the Enthalpy Relaxation and Fragility of a Metallic Glass. *Metall. Mater. Trans. A* **39**, 1573–1577 (2008).
83. Wen, P., Zhao, D., Pan, M. *et al.* Relaxation of metallic  $Zr_{46.75}Ti_{8.25}Cu_{7.5}Ni_{10}Be_{27.5}$  bulk glass-forming supercooled liquid. *Appl. Phys. Lett.* **84**, 2790–2792 (2004).
84. Yue, X., Inoue, A., Liu, C., *et al.*, The development of structure model in metallic glasses. *Materials Research* **20**, 326-338 (2017).
85. Bernal, J. D. A Geometrical Approach to the structure of Liquids. *Nature* **183**, 141–147 (1959).
86. Turnbull, D., Under what conditions can a glass be formed ?, *Contemp. Phys.* **10**, 473-488 (1969).
87. Cohen, M. H. & Turnbull, D. Molecular Transport in Liquids and Glasses. *J. Chem. Phys.* **31**, 1164–214514 (1959).
88. Schuh, C., Hufnagel, T. & Ramamurty, U. Mechanical behavior of amorphous alloys. *Acta Mater.* **55**, 4067–4109 (2007).
89. Perez, J. Quasi-punctual defects in vitreous solids and liquid-glass transition. *Solid State Ion.* **39**, 69–79 (1990).
90. Qiao, J. C. & Pelletier, J. M. Enthalpy relaxation in  $Cu_{46}Zr_{45}Al_7Y_2$  and  $Zr_{55}Cu_{30}Ni_5Al_{10}$  bulk metallic glasses by differential scanning calorimetry (DSC). *Intermetallics* **19**, 9–18 (2011).
91. Granato, A. V. & Khonik, V. A. An Interstitialcy Theory of Structural Relaxation and Related Viscous Flow of Glasses. *Phys. Rev. Lett.* **93**, 155502 (2004).
92. Miracle, D. B. A structural model for metallic glasses. *Nat. Mater.* **3**, 697–702 (2004).
93. Adam, G. & Gibbs, J. H. On the Temperature Dependence of Cooperative Relaxation Properties in Glass-Forming Liquids. *J. Chem. Phys.* **43**, 139–146 (1965).
94. Greer, A. L., Cheng, Y. Q. & Ma, E. Shear bands in metallic glasses. *Mater. Sci. Eng. R Rep.* **74**, 71–132 (2013).
95. Leamy, H. J., Wang, T. T. & Chen, H. S. Plastic flow and fracture of metallic glass. *Metall. Mater. Trans. B* **3**, 699 (1972).
96. Maaß, R. & Löffler, J. F. Shear-Band Dynamics in Metallic Glasses. *Adv. Funct. Mater.* **25**, 2353–2368 (2015).
97. Daub, E. G., Klaumünzer, D. & Löffler, J. F. Effective temperature dynamics of shear bands in metallic glasses. *Phys. Rev. E* **90**, 062405 (2014).

98. Klaumünzer, D., Lazarev, R., Maaß, R. *et al.* Probing Shear-Band Initiation in Metallic Glasses. *Phys. Rev. Lett.* **107**, 185502 (2011).
99. Liu, F. X., Gao, Y. F. & Liaw, P. K. Rate-Dependent Deformation Behavior of Zr-Based Metallic-Glass Coatings Examined by Nanoindentation. *Metall. Mater. Trans. A* **39**, 1862–1867 (2008).
100. Lewandowski, J. J. & Greer, A. L. Temperature rise at shear bands in metallic glasses. *Nat. Mater.* **5**, 15–18 (2006).
101. Argon, A. S. & Shi, L. T. Development of visco-plastic deformation in metallic glasses. *Acta Metall.* **31**, 499–507 (1983).
102. Renaud, R. Loi physique de comportement des polymères amorphes et intégration dans un code éléments finis. (INSA Lyon, 2006).
103. Shimizu, F., Ogata, S. & Li, J. Yield point of metallic glass. *Acta Mater.* **54**, 4293–4298 (2006).
104. Li, F., Xie, Y., Gu, J. *et al.* Inhomogeneous creep deformation in metallic glasses. *Mater. Sci. Eng. A* **648**, 57–60 (2015).
105. Cui, J., Li, J., Wang, J., Li, L. & Kou, H. Deformation behavior of a Ti-based bulk metallic glass composite in the supercooled liquid region. *Mater. Des.* **90**, 595–600 (2016).
106. Huang, R., Suo, Z., Prevost, J. H. & Nix, W. D. Inhomogeneous deformation in metallic glasses. *J. Mech. Phys. Solids* **50**, 1011–1027 (2002).
107. Sun, B. A. & Wang, W. H. The fracture of bulk metallic glasses. *Prog. Mater. Sci.* **74**, 211–307 (2015).
108. Hu, N. Shear bands in dense metallic granular materials. *J. Mech. Phys. Solids* **52**, 499–531 (2004).
109. Wright, W. J., Schwarz, R. B. & Nix, W. D. Localized heating during serrated plastic flow in bulk metallic glasses. *Mater. Sci. Eng. A* **319–321**, 229–232 (2001).
110. Jiang, W. H. & Atzmon, M. Rate dependence of serrated flow in a metallic glass. *J. Mater. Res.* **18**, 755–757 (2003).
111. Hu, J., Sun, B., Yang, Y. *et al.* Intrinsic versus extrinsic effects on serrated flow of bulk metallic glasses. *Intermetallics* **66**, 31–39 (2015).
112. Wright, W. J., Samale, M. W., Hufnagel, T. C., Leblanc, M. M. & Florando, J. N. Studies of shear band velocity using spatially and temporally resolved measurements of strain during quasistatic compression of a bulk metallic glass. *Acta Mater.* **57**, 4639–4648 (2009).
113. Chen, Y., Jiang, M. Q., Wei, Y. J. & Dai, L. H. Failure criterion for metallic glasses. *Philos. Mag.* **91**, 4536–4554 (2011).
114. Mukai, T., Nieh, T. ., Kawamura, Y., Inoue, A. & Higashi, K. Effect of strain rate on compressive behavior of a Pd<sub>40</sub>Ni<sub>40</sub>P<sub>20</sub> bulk metallic glass. *Intermetallics* **10**, 1071–1077 (2002).
115. Zhang, Z. F., Wu, F., Gao, W. *et al.* Wavy cleavage fracture of bulk metallic glass. *Appl. Phys. Lett.* **89**, 251917 (2006).
116. Wang, G., Chan, K. C., Xu, X. H. & Wang, W. H. Instability of crack propagation in brittle bulk metallic glass. *Acta Mater.* **56**, 5845–5860 (2008).
117. Zhang, Z. F., Zhangy, H., Shenz, B. L., Inouez, A. & Eckertx, J. Shear fracture and fragmentation mechanisms of bulk metallic glasses. *Philos. Mag. Lett.* **86**, 643–650 (2006).
118. Greer, J. R. & De Hosson, J. T. M. Plasticity in small-sized metallic systems: Intrinsic versus extrinsic size effect. *Prog. Mater. Sci.* **56**, 654–724 (2011).
119. Deibler, L. A. & Lewandowski, J. J. Model experiments to mimic fracture surface features in metallic glasses. *Mater. Sci. Eng. A* **527**, 2207–2213 (2010).
120. Xi, X. K., Zhao, D., Pan, M. *et al.* Fracture of Brittle Metallic Glasses : Brittleness or Plasticity. *Physical Review Letters* **94**, 125510 (2005)
121. Christiansen, A. & Shortall, J. B. The fracture toughness and fracture morphology of polyester resins. *J. Mater. Sci.* **11**, 1113–124 (1976).
122. Lewandowski \*, J. J., Wang, W. H. & Greer, A. L. Intrinsic plasticity or brittleness of metallic glasses. *Philos. Mag. Lett.* **85**, 77–87 (2005).
123. Kimura, H. & Masumoto, T. Deformation and fracture of an amorphous Pd-Cu-Si alloy in V-notch bending tests—II. *Acta Metall.* **28**, 1677–1693 (1980).

124. Shek, C. H., Lin, G. M., Lee, K. L. & Lai, J. K. L. Fractal fracture of amorphous Fe Ni V Si B alloy. *J. Non-Cryst. Solids* **224**, 244–248 (1998).
125. Pampillo A.C., R. A. C. The fracture topography of metallic glasses. *J. Mater. Sci.* **9**, 718–724 (1974).
126. Wang, Y. T., Xi, X. K., Wang, G., Xia, X. X. & Wang, W. H. Understanding of nanoscale periodic stripes on fracture surface of metallic glasses. *J. Appl. Phys.* **106**, 113528 (2009).
127. Inoue, A. Stabilization of metallic supercooled liquid. *Acta Mater.* **48**, 279–306 (2000).
128. Inoue, A., Shen, B. & Nishiyama, N. Development and Applications of Late Transition Metal Bulk Metallic Glasses. in *Bulk Metallic Glasses* **18**, 1–25 (Springer US, 2008).
129. Suryanarayana, C. & Inoue, A. *Bulk Metallic Glasses*. (CRC press, 2010).
130. Yavari, A. R., de Oliveira, M. F. & Botta Filho, W. J. Shaping of Bulk Metallic Glasses by Simultaneous Application of Electrical Current and Low Stress. *Supercooled Liq. Bulk Glas. Nanocrystalline States Alloys* **644**, L12.20.1-6 (2000).
131. Inoue, A. & Nishiyama, N. New Bulk Metallic Glasses for Applications as Magnetic-Sensing, Chemical, and Structural Materials. *MRS Bull.* **32**, 651–658 (2007).
132. Ashby, M. & Greer, A. Metallic glasses as structural materials. *Scr. Mater.* **54**, 321–326 (2006).
133. Khan, M. M., Nemati, A., Rahman, Z. *et al.* Recent Advancements in Bulk Metallic Glasses and Their Applications: A Review. *Crit. Rev. Solid State Mater. Si.* **43**, 233-268 (2017).
134. Zheng, Y., Wang, J. & Wang, W. Corrosion of and cellular response to Mg-Zn- Ca bulk metallic glasses. *Biomaterials* **31**, 1093–1103 (2009).
135. Cao, J. D., Kirkland, N. T., Laws, K. J., Birbilis, N. & Ferry, M. Ca–Mg–Zn bulk metallic glasses as bioresorbable metals. *Acta Biomater.* **8**, 2375–2383 (2012).
136. Fu, X. L., Tan, M., Chen, Y. *et al.* High temperature deformation behavior of Mg<sub>67</sub>Zn<sub>28</sub>Ca<sub>5</sub> metallic glass and its composites. **621**, 1–7 (2015).
137. Nowosielski, R., Cezarz-Andracke, K. Impact of Zn and Ca on dissolution rate, mechanical properties and GFA of resorbable Mg–Zn–Ca metallic glasses. *Arch. Civ. Mech. Eng.* **67**, 9–19 (2015).
138. Jayaraj, J., Kim, Y. C., Kim, K. B., Seok, H. K. & Fleury, E. Corrosion studies on Fe-based amorphous alloys in simulated PEM fuel cell environment. *Sci. Technol. Adv. Mater.* **6**, 282–289 (2005).
139. Inoue, A. & Takeuchi, A. Recent development and application products of bulk glassy alloys☆. *Acta Mater.* **59**, 2243–2267 (2011).
140. Chen, M. A brief overview of bulk metallic glasses. *NPG Asia Mater.* **3**, 82–90 (2011).
141. Schroers, J., Hodges, T., Kumar, G. *et al.* Thermoplastic blow molding of metals. *Mater. Today* **14**, 14–19 (2011).
142. Liu, L., Qiu, C., Huang, C. *et al.* Biocompatibility of Ni-free Zr-based bulk metallic glasses. *Intermetallics* **17**, 235–240 (2008).
143. Liu, L., Qiu, C. L., Chen, Q. & Zhang, S. M. Corrosion behavior of Zr-based bulk metallic glasses in different artificial body fluids. *J. Alloys Compd.* **425**, 268–273 (2006).
144. Li, J., Shi, L., Zhu, Z. *et al.* Zr<sub>61</sub>Ti<sub>2</sub>Cu<sub>25</sub>Al<sub>12</sub> metallic glass for potential use in dental implants: Biocompatibility assessment by in vitro cellular responses. *Mater. Sci. Eng. C* **33**, 2113–2121 (2013).
145. Wada, T., Qin, F., Wang, X. *et al.* Formation and bioactivation of Zr-Al-Co bulk metallic glasses. *J. Mater. Res.* **24**, 2941–2948 (2009).
146. Liu, L., Qiu, C. L., Chen, Q., Chan, K. C. & Zhang, S. M. Deformation behavior, corrosion resistance, and cytotoxicity of Ni-free Zr-based bulk metallic glasses. *J. Biomed. Mater. Res. A* **86A**, 160–169 (2008).
147. Huang, L., Yokoyama, Y., Wu, W. *et al.* Ni-free Zr-Cu-Al-Nb-Pd bulk metallic glasses with different Zr/Cu ratios for biomedical applications. *J. Biomed. Mater. Res. B Appl. Biomater.* **100B**, 1472–1482 (2012).
148. Qin, F., Yoshimura, M., Wang, X. *et al.* Corrosion Behavior of a Ti-Based Bulk Metallic Glass and Its Crystalline Alloys. *Mater. Trans.* **48**, 1855–1858 (2007).

149. Zhu, S. L., Wang, X. M., Qin, F. X. & Inoue, A. A new Ti-based bulk glassy alloy with potential for biomedical application. *Mater. Sci. Eng. A* **459**, 233–237 (2007).
150. Oak, J.-J., Louzguine-Luzgin, D. V. & Inoue, A. Fabrication of Ni-free Ti-based bulk-metallic glassy alloy having potential for application as biomaterial, and investigation of its mechanical properties, corrosion, and crystallization behavior. *J. Mater. Res.* **22**, 1346–1353 (2007).
151. Yu, H.J., Wang, J.Q., Shi, X.T. *et al.* Ductile Biodegradable Mg-Based Metallic Glasses with Excellent Biocompatibility. *Adv. Funct. Mater.* **23**, 4793-4800 (2013).
152. Zberg, B., Uggowitzer, P. J. & Löffler, J. F. MgZnCa glasses without clinically observable hydrogen evolution for biodegradable implants. *Nat. Mater.* **8**, 887–891 (2009).
153. Li, H. F., Wang, Y. B., Cheng, Y. & Zheng, Y. F. Surface modification of Ca<sub>60</sub>Mg<sub>15</sub>Zn<sub>25</sub> bulk metallic glass for slowing down its biodegradation rate in water solution. *Mater. Lett.* **64**, 1462–1464 (2010).
154. Wang, Y. B., Xie, X., Li, H. *et al.* Biodegradable CaMgZn bulk metallic glass for potential skeletal application. *Acta Biomater.* **7**, 3196–3208 (2011).
155. Cao, J. D., Kirkland, N. T., Laws, K. J., Birbilis, N. & Ferry, M. Ca–Mg–Zn bulk metallic glasses as bioresorbable metals. *Acta Biomater.* **8**, 2375–2383 (2012).
156. Jiao, W., Zhao, K., Xi, X. *et al.* Development of CaZn based glassy alloys as potential biodegradable bone graft substitute. *J. Non-Cryst. Solids* **357**, 3830–3840 (2011).
157. Jiao, W. *et al.* Zinc-based bulk metallic glasses. *J. Non-Cryst. Solids* **356**, 1867–1870 (2010).
158. Zhao, K., Li, J. F., Zhao, D. Q., Pan, M. X. & Wang, W. H. Degradable Sr-based bulk metallic glasses. *Scr. Mater.* **61**, 1091–1094 (2009).
159. Wang, W. Roles of minor additions in formation and properties of bulk metallic glasses. *Prog. Mater. Sci.* **52**, 540–596 (2007).
160. Liu, C. T. & Lu, Z. P. Effect of minor alloying additions on glass formation in bulk metallic glasses. *Intermetallics* **13**, 415–418 (2005).
161. Wang, W.-H. & Bai, H. Y. Role of small atoms in the formation and properties of Zr–Ti–Cu–Ni–Be bulk amorphous alloys. *J. Appl. Phys.* **84**, 5961–5968 (1998).
162. Zhang, T., Men, H., Pang, S. *et al.* Effects of a minor addition of Si and/or Sn on formation and mechanical properties of Cu–Zr–Ti bulk metallic glass. *Mater. Sci. Eng. A* **449–451**, 295–298 (2007).
163. Choi-Yim, H., Busch, R. & Johnson, W. L. The effect of silicon on the glass forming ability of the Cu<sub>47</sub>Ti<sub>34</sub>Zr<sub>11</sub>Ni<sub>8</sub> bulk metallic glass forming alloy during processing of composites. *J. Appl. Phys.* **83**, 7993–7997 (1998).
164. Zeng, Y., Inoue, A., Nishiyama, N. & Chen, M. Remarkable effect of minor boron doping on the formation of the largest size Ni-rich bulk metallic glasses. *Scr. Mater.* **60**, 925–928 (2009).
165. Chen, N., Louzguine-Luzgin, D. V., Xie, G. Q., Wada, T. & Inoue, A. Influence of minor Si addition on the glass-forming ability and mechanical properties of Pd 40 Ni 40 P 20 alloy. *Acta Mater.* **57**, 2775–2780 (2009).
166. Kundig, A., Lepori, D., Perry, A. *et al.* Influence of Low Oxygen Contents and Alloy Refinement on the Glass Forming Ability of Zr<sub>52.5</sub>Cu<sub>17.9</sub>Ni<sub>14.6</sub>Al<sub>10</sub>Ti<sub>5</sub>. *Mater. Trans.* **43**, 3206–3210 (2002).
167. Wang, W.-H., Wei, Q. & Bai, H. Y. Enhanced thermal stability and microhardness in Zr–Ti–Cu–Ni–Be bulk amorphous alloy by carbon addition. *Appl. Phys. Lett.* **71**, 58–60 (1997).
168. Shen, B., Akiba, M. & Inoue, A. Effects of Si and Mo additions on glass-forming in FeGaPCB bulk glassy alloys with high saturation magnetization. *Phys. Rev. B* **73**, 104204 (2006).
169. Hu, Y., Pan, M., Liu, L. *et al.* Synthesis of Fe-based bulk metallic glasses with low purity materials by multi-metalloids addition. *Mater. Lett.* **57**, 2698–2701 (2003).
170. Ozaki K., Kobayashi K., Nishio, T. Effect of Boron or Carbon on Amorphous Formation of La<sub>55</sub>Al<sub>25</sub>Ni<sub>20</sub> Alloy. *Mater. Trans. JIM* **39**, 499–503 (1998).
171. Ma, C., Soejima, H., Ishihara, S. *et al.* New Ti-Based Bulk Glassy Alloys with High Glass-Forming Ability and Superior Mechanical Properties. *Mater. Trans.* **45**, 3223–3227 (2004).

172. Bae, D. H., Lee, M. H., Kim, D. H. & Sordelet, D. J. Plasticity in Ni<sub>59</sub>Zr<sub>20</sub>Ti<sub>16</sub>Si<sub>2</sub>Sn<sub>3</sub> metallic glass matrix composites containing brass fibers synthesized by warm extrusion of powders. *Appl. Phys. Lett.* **83**, 2312–2314 (2003).
173. Inoue, A., Negishi, T., Kimura, H., Aoki, T. Effect of B Addition of Supercooled Liquid Region in Zr-Cu-Al Base Amorphous Alloys. *Mater. Trans. JIM* **38**, 185–188 (1997).
174. Yi, S., Lee, J. K., Kim, W. T. & Kim, D. H. Ni-based bulk amorphous alloys in the Ni-Ti-Zr-Si system. *J. Non-Cryst. Solids* **291**, 132–136 (2001).
175. Inoue Akihisa, Murakami Akira, Zhang Tao, T. A. Thermal Stability and Magnetic properties of Bulk Amorphous Fe-Al-Ga-P-C-B-Si Alloys. *Mater. Trans. JIM* **38**, 189–196 (1997).
176. Choi-Yim, H., Xu, D. & Johnson, W. L. Ni-based bulk metallic glass formation in the Ni-Nb-Sn and Ni-Nb-Sn-X (X=B,Fe,Cu) alloy systems. *Appl. Phys. Lett.* **82**, 1030–1032 (2003).
177. Nollmann, N., Binkowski, I., Schmidt, V., Rösner, H. & Wilde, G. Impact of micro-alloying on the plasticity of Pd-based bulk metallic glasses. *Scr. Mater.* **111**, 119–122 (2016).
178. Pan, J., Liu, L. & Chan, K. C. Enhanced plasticity by phase separation in CuZrAl bulk metallic glass with micro-addition of Fe. *Scr. Mater.* **60**, 822–825 (2009).
179. Zhang, B., Zhao, D., Pan, M. Formation of cerium-based bulk metallic glasses. *Acta Materialia*. **54**, 3025-3032 (2006).
180. Inoue, A., Shibata, T. & Zhang, T. Effect of Additional Elements on Glass Transition Behavior and Glass Formation Tendency of Zr-Al-Cu-Ni Alloys. *Mater. Trans. JIM* **36**, 1420–1426 (1995).
181. Liu, L., Qiu, C., Sun, M. *et al.* Improvements in the plasticity and biocompatibility of Zr-Cu-Ni-Al bulk metallic glass by the microalloying of Nb. *Mater. Sci. Eng. A* **449–451**, 193–197 (2007).
182. Zhang, C. M., Hui, X., Li, Z. G. & Chen, G. L. Improving the strength and the toughness of Mg-Cu-(Y, Gd) bulk metallic glass by minor addition of Nb. *J. Alloys Compd.* **467**, 241–245 (2009).
183. Pan, J., Chan, K., Chen, Q. *et al.* The effect of microalloying on mechanical properties in CuZrAl bulk metallic glass. *J. Alloys Compd.* **504**, S74–S77 (2010).
184. Li, X., Bian, X., Hu, L., Wu, Y. & Zhang, J. Effect of microalloying on glass formation and thermal stability of Cu-Pr-based amorphous alloys. *J. Alloys Compd.* **439**, 87–90 (2007).
185. Shi, B., Xu, Y., Ma, W. *et al.* Effect of Ti addition on the glass forming ability, crystallization and plasticity of (Zr<sub>64.13</sub>Cu<sub>15.75</sub>Ni<sub>10.72</sub>Al<sub>10</sub>)<sub>100-x</sub>Ti<sub>x</sub> bulk metallic glasses *Mat. Sci. Eng. A* **639**, 345-349 (2015).
186. Zhao, Q. Zhang, Yong, P., Ming Z., Wang, W. H. The Effects of Iron Addition on the Glass-Forming Ability and Properties of Zr-Ti-Cu-Ni-Be-Fe Bulk Metallic Glass. *Mater Trans JIM* **41**, 1427–1431 (2000).
187. Zhang, T., Yamamoto, T. & Inoue, A. Formation, Thermal Stability and Mechanical Properties of (Cu<sub>0.6</sub>Zr<sub>0.3</sub>Ti<sub>0.1</sub>)<sub>100-x</sub>M<sub>x</sub> (M=Fe, Co, Ni) Bulk Glassy Alloys. *Mater. Trans.* **43**, 3222–3226 (2002).
188. Zhang, B., Zhao, D. Q., Pan, M. X., Wang, W. H. & Greer, A. L. Amorphous Metallic Plastic. *Phys. Rev. Lett.* **94**, 205502 (2005).
189. Wang, Y. T., Pang, Z. Y. *et al.* Doping-induced formation of bulk nanocrystalline alloy from metallic glass with controllable microstructure and properties. *J. Non-Cryst. Solids* **352**, 444–449 (2006).
190. Yu, P., Bai, H. Y., Tang, M. B. & Wang, W. L. Excellent glass-forming ability in simple Cu<sub>50</sub>Zr<sub>50</sub>-based alloys. *J. Non-Cryst. Solids* **351**, 1328–1332 (2005).
191. Wang, W. H., Pan, M. X., Zhao, D. Q., Hu, Y. & Bai, H. Y. Enhancement of the soft magnetic properties of FeCoZrMoWB bulk metallic glass by microalloying. *J. Phys. Condens. Matter* **16**, 3719–3723 (2004).
192. Fan, G. J., Löser, W., Roth, S., Eckert, J. & Schultz, L. Magnetic properties of cast Nd<sub>60-x</sub>Fe<sub>20</sub>Al<sub>10</sub>Co<sub>10</sub>Cu<sub>x</sub> alloys. *Appl. Phys. Lett.* **75**, 2984–2986 (1999).
193. Qin, C., Asami, K., Zhang, T., Zhang, W. & Inoue, A. Effects of Additional Elements on the Glass Formation and Corrosion Behavior of Bulk Glassy Cu-Hf-Ti Alloys. *Mater. Trans.* **44**, 1042–1045 (2003).
194. Ponnambalam, V., Poon, S. J., Shiflet, G. *et al.* Synthesis of iron-based bulk metallic glasses as nonferromagnetic amorphous steel alloys. *Appl. Phys. Lett.* **83**, 1131–1133 (2003).

195. Zhang, Z., Wu, Y., Zhou, J. et al. Effects of a minor addition of Si and/or Sn on formation and mechanical properties of Cu–Zr–Ti bulk metallic glass. *Intermetallics* **42**, 68–76 (2013).
196. Xia, J., Qiang, J., Wang, Y., Wang, Q. & Dong, C. Ternary bulk metallic glasses formed by minor alloying of Cu<sub>8</sub>Zr<sub>5</sub> icosahedron. *Appl. Phys. Lett.* **88**, 101907 (2006).
197. Shen, B., Akiba, M. & Inoue, A. Effects of Si and Mo additions on glass-forming in FeGaPCB bulk glassy alloys with high saturation magnetization. *Phys. Rev. B* **73**, 104204 (2006).
198. Men, H., Hu, Z. Q. & Xu, J. Bulk metallic glass formation in the Mg–Cu–Zn–Y system. *Scr. Mater.* **46**, 699–703 (2002).
199. Zhu, S. L., Wang, X. M. & Inoue, A. Glass-forming ability and mechanical properties of Ti-based bulk glassy alloys with large diameters of up to 1cm. *Intermetallics* **16**, 1031–1035 (2008).
200. Zhang, Y., Ji, Y., Zhao, D. et al. Glass forming and properties of Zr/Nb-based bulk metallic glasses. *Scr. Mater.* **44**, 1107–1112 (2001).
201. Mitrovic, N., Roth, S. & Eckert, J. Kinetics of the glass-transition and crystallization process of Fe<sub>72-x</sub>Nb<sub>x</sub>Al<sub>5</sub>Ga<sub>2</sub>P<sub>11</sub>C<sub>6</sub>B<sub>4</sub> (x=0,2) metallic glasses. *Appl. Phys. Lett.* **78**, 2145–2147 (2001).
202. Inoue, A. & Shen, B. Formation and Soft Magnetic Properties of Co–Fe–Si–B–Nb Bulk Glassy Alloys. *Mater. Trans.* **43**, 1230–1234 (2002).
203. Ma, D., Cao, H., Ding, L. et al. Bulkier glass formability enhanced by minor alloying additions. *Appl. Phys. Lett.* **87**, 171914 (2005).
204. Itoi, T. & Inoue, A. Thermal Stability and Soft Magnetic Properties of Co-Fe-M-B (M=Nb, Zr) Amorphous Alloys with Large Supercooled Liquid Region. *Mater. Trans. JIM* **41**, 1256–1262 (2000).
205. Louzguine, D. V. & Inoue, A. Electronegativity of the constituent rare-earth metals as a factor stabilizing the supercooled liquid region in Al-based metallic glasses. *Appl. Phys. Lett.* **79**, 3410–3412 (2001).
206. Zhang, Y., Pan, M.X. et al. Formation of Zr-based Bulk Metallic Glasses from Low Purity of Materials by Yttrium Addition. *Mater Trans JIM* **41**, 1410–1414 (2000).
207. Lu, Z. P., Liu, C. T. & Porter, W. D. Role of yttrium in glass formation of Fe-based bulk metallic glasses. *Appl. Phys. Lett.* **83**, 2581–2583 (2003).
208. Xi, X. K., Wang, R. J., Zhao, D. Q., Pan, M. X. & Wang, W. H. Glass-forming Mg–Cu–RE (RE=Gd, Pr, Nd, Tb, Y, and Dy) alloys with strong oxygen resistance in manufacturability. *J. Non-Cryst. Solids* **344**, 105–109 (2004).
209. Yu, P., Bai, H. Y. & Wang, W. H. Superior glass-forming ability of CuZr alloys from minor additions. *J. Mater. Res.* **21**, 1674–1679 (2006).
210. Jiang, F., Wang, Z. J., Zhang, Z. B. & Sun, J. Formation of Zr-based bulk metallic glasses from low purity materials by scandium addition. *Scr. Mater.* **53**, 487–491 (2005).
211. Gu, X. J., McDermott, A. G., Poon, S. J. & Shiflet, G. J. Critical Poisson's ratio for plasticity in Fe–Mo–C–B–Ln bulk amorphous steel. *Appl. Phys. Lett.* **88**, 211905 (2006).
212. Bing, L., Yanhong, L., Ke, Y., Jinshan, L. & Xinhui, F. Effect of yttrium addition on the non-isothermal crystallization kinetics and fragility of Cu-Zr-Al bulk metallic glass. *Thermochim. Acta* **642**, 105–110 (2016).
213. Zhang, Y., Chen, J., Chen, G. L. & Liu, X. J. Glass formation mechanism of minor yttrium addition in CuZrAl alloys. *Appl. Phys. Lett.* **89**, 131904 (2006).
214. Wang, Y. F., Li, L., Sun, C., Lu, Q. L. & Shi, Z. Q. Rare Earth Elements on Glass-Forming Ability and Thermal Stability of Cu-Zr-Al Metallic Glass. *Mater. Sci. Forum* **688**, 426–430 (2011).
215. Hao, G., Ren, F., Zhang, Y. & Lin, J. Role of yttrium in glass formation of Ti-based bulk metallic glasses. *Rare Met.* **28**, 68–71 (2009).
216. Yan, M., Shen, J., Zhang, T. & Zou, J. Enhanced glass-forming ability of a Zr-based bulk metallic glass with yttrium doping. *J. Non-Cryst. Solids* **352**, 3109–3112 (2006).
217. Willbold, E., Gu, X., Albert, D. et al. Effect of the addition of low rare earth elements (lanthanum, neodymium, cerium) on the biodegradation and biocompatibility of magnesium. *Acta Biomater.* **11**, 554–562 (2015).

218. Sun, Y. D., Chen, Q. R. & Li, G. Z. Enhanced glass forming ability and plasticity of Mg-based bulk metallic glass by minor addition of Cd. *J. Alloys Compd.* **584**, 273–278 (2014).
219. Hu, Q., Zeng, X. R., Fu, M. W., Chen, S. S. & Jiang, J. Improvement of the thermoplastic formability of  $Zr_{65}Cu_{17.5}Ni_{10}Al_{7.5}$  bulk metallic glass by minor addition of Erbium. *Phys. B Condens. Matter* **502**, 68–72 (2016).
220. Xie, Z., Zhang, Y., Yang, Y., Chen, X. & Tao, P. Effects of rare-earth elements on the glass-forming ability and mechanical properties of  $Cu_{46}Zr_{47-x}Al_7M_x$  (M = Ce, Pr, Tb, and Gd) bulk metallic glasses. *Rare Met.* **29**, 444–450 (2010).
221. Chen, Z. P., Gao, J.E., Wu, Y. *et al.* Role of rare-earth elements in glass formation of Al–Ca–Ni amorphous alloys. *J. Alloys Compd.* **513**, 387–392 (2012).
222. Baulin, O., Fabregue, D., Kato, H. *et al.* A new, toxic element-free Mg-based metallic glass for biomedical applications. *J. Non-Cryst. Solids* **481**, (2018).
223. Novikov, V. N. & Sokolov, A. P. Poisson's ratio and the fragility of glass-forming liquids. *Nature* **431**, 961–963 (2004).
224. Tanaka, H. Relation between Thermodynamics and Kinetics of Glass-Forming Liquids. *Phys. Rev. Lett.* **90**, 055701 (2003).
225. Johnson, W. L. Bulk Glass-Forming Metallic Alloys: Science and Technology. *MRS Bull.* **24**, 42–56 (1999).
226. Greer, A. L. Metallic Glasses. *Science* **267**, 1947–1953 (1995).
227. Sheng, H. W., Luo, W. K., Alamgir, F. M., Bai, J. M. & Ma, E. Atomic packing and short-to-medium-range order in metallic glasses. *Nature* **439**, 419–425 (2006).
228. Shen, J., Chen, Q., Sun, J., Fan, H. & Wang, G. Exceptionally high glass-forming ability of an FeCoCrMoCBy alloy. *Appl. Phys. Lett.* **86**, 151907 (2005).
229. Fan, C., Ott, R. T. & Hufnagel, T. C. Metallic glass matrix composite with precipitated ductile reinforcement. *Appl. Phys. Lett.* **81**, 1020–1022 (2002).
230. Hays, C. C., Kim, C. P. & Johnson, W. L. Microstructure Controlled Shear Band Pattern Formation and Enhanced Plasticity of Bulk Metallic Glasses Containing in situ Formed Ductile Phase Dendrite Dispersions. *Phys. Rev. Lett.* **84**, 2901–2904 (2000).
231. Lee, S.-W., Huh, M.-Y., Fleury, E. & Lee, J.-C. Crystallization - induced plasticity of Cu – Zr containing bulk amorphous alloys. (2005).
232. Xing, L.-Q., Li, Y., Ramesh, K. T., Li, J. & Hufnagel, T. C. Enhanced plastic strain in Zr-based bulk amorphous alloys. *Phys. Rev. B* **64**, 180201 (2001).
233. Yokoyama, Y., Fukaura, K. & Inoue, A. Effect of Ni Addition on Fatigue Properties of Bulk Glassy  $Zr_{50}Cu_{40}Al_{10}$  Alloys. *Mater. Trans.* **45**, 1672–1678 (2004).
234. Inoue, A., Zhang, T., Takeuchi, A. Bulk amorphous alloys with high mechanical strength and good soft magnetic properties in Fe–TM–B (TM=IV–VIII group transition metal) system. *Appl. Phys. Lett.* **71**, 464-466 (1997).
235. Liu, L., Qiu, C. L., Zou, H. & Chan, K. C. The effect of the microalloying of Hf on the corrosion behavior of ZrCuNiAl bulk metallic glass. *J. Alloys Compd.* **399**, 144–148 (2005).
236. Qiu, C. L., Liu, L., Sun, M. & Zhang, S. M. The effect of Nb addition on mechanical properties, corrosion behavior, and metal-ion release of ZrAlCuNi bulk metallic glasses in artificial body fluid. *J. Biomed. Mater. Res. A* **75A**, 950–956 (2005).
237. Kulp, D. T., Egami, T., Luzzi, D. E. & Vitek, V. A Universal Criterion for Amortization in Metallic Systems. *MRS Proc.* **279**, 505 (1992).
238. Johnson, W. L. & Samwer, K. A Universal Criterion for Plastic Yielding of Metallic Glasses with a  $(T/T_g)^{2/3}$  Temperature Dependence. *Phys. Rev. Lett.* **95**, 195501 (2005).
239. Li, Y., Poon, S.J., Shiflet, G. *et al.* Formation of Bulk Metallic Glasses and Their Composites. *MRS Bull.* **32**, 624–628 (2007).
240. Jang, J. S. C., Ciou, J. Y., Hung, T. H., Huang, J. C. & Du, X. H. Enhanced mechanical performance of Mg metallic glass with porous Mo particles. *Appl. Phys. Lett.* **92**, 011930 (2008).
241. Kim, Y. C., Na, J., Park, J. *et al.* Role of nanometer-scale quasicrystals in improving the mechanical behavior of Ti-based bulk metallic glasses. *Appl. Phys. Lett.* **83**, 3093–3095 (2003).

242. Hofmann, D. C., Suh, J., Wiest, A. *et al.* Designing metallic glass matrix composites with high toughness and tensile ductility. *Nature* **451**, 1085–1089 (2008).
243. Schroers, J., Nguyen, T. & Croopnick, G. A. A novel metallic glass composite synthesis method. *Scr. Mater.* **56**, 177–180 (2007).
244. Cardinal, S., Pelletier, J. M., Xie, G. Q. & Mercier, F. Manufacturing of Cu-based metallic glasses matrix composites by spark plasma sintering. *Mater. Sci. Eng. A* **711**, 405–414 (2018).
245. Kinaka, M., Kato, H., Hasegawa, M. & Inoue, A. High specific strength Mg-based bulk metallic glass matrix composite highly ductilized by Ti dispersoid. *Mater. Sci. Eng. A* **494**, 299–303 (2008).
246. Xie, G., Zhang, W., Louzguine-Luzgin, D. V., Kimura, H. & Inoue, A. Fabrication of porous Zr–Cu–Al–Ni bulk metallic glass by spark plasma sintering process. *Scr. Mater.* **55**, 687–690 (2006).
247. Xie, Guoqiang; Louzguine-Luzgin, Dmitri; Fukuhara, Mikio; Kimura, Hisamichi; Inoue, A. Cu particulate dispersed  $\text{Cu}_{50}\text{Zr}_{50}\text{Al}_5$  bulk metallic glass composite with enhances electrical conductivity. *Intermetallics* **18**, 1973–1977 (2010).
248. Apfel, R. E. & Qiu, N. Principle of dynamic decompression and cooling for materials processing. *J. Mater. Res.* **11**, 2916–2920 (1996).
249. Schroers, J., Veazey, C. & Johnson, W. L. Amorphous metallic foam. *Appl. Phys. Lett.* **82**, 370–372 (2003).
250. Brothers, A. H. & Dunand, D. C. Ductile bulk metallic glass foams. *Adv. Mater.* **17**, 484–486 (2005).
251. Demetriou, M. D., Veazey, C., Harmon, J. S., Schramm, J. P. & Johnson, W. L. Stochastic Metallic-Glass Cellular Structures Exhibiting Benchmark Strength. *Phys. Rev. Lett.* **101**, 145702 (2008).
252. Demetriou, M. D., Schramm, C., Veazey, C. *et al.* High porosity metallic glass foam: A powder metallurgy route. *Appl. Phys. Lett.* **91**, 161903 (2007).
253. Schroers, J., Kumar, G., Hodges, T. M., Chan, S. & Kyriakides, T. R. Bulk metallic glasses for biomedical applications. *JOM* **61**, 21–29 (2009).



# Chapter 2

## Experimental Techniques

---

<b>EXPERIMENTAL TECHNIQUES.....</b>	<b>69</b>
<b>2-1- Materials Processing.....</b>	<b>69</b>
2-1-1- Master alloys processing	69
2-1-2- Samples processing	71
2-1-2-1- Bulk metallic glass samples	71
2-1-2-2- Ribbon metallic glass samples	73
2-1-2-3- Sintered Samples	73
2-1-3- Samples studied	74
<b>2-2- Characterization of the samples.....</b>	<b>75</b>
2-2-1- Structural Characterization	75
2-2-1-1- Density	75
2-2-1-2- X-Ray Diffraction (XRD)	75
2-2-1-3- Transmission Electron Microscopy (TEM)	76
2-2-1-4- Energy Dispersive X-Ray Spectroscopy (EDX)	77
2-2-2- Thermal Characterization	77
2-2-2-1- Differential Scanning Calorimetry (DSC)	78

2-2-2-2- <i>High Temperature XRD</i>	79
2-2-3- Mechanical Characterization	80
2-2-3-1- <i>Compressive tests</i>	80
2-2-3-2- <i>Nanoindentation tests</i>	81
2-2-3-3- <i>Hardness measurements</i>	81
2-2-4- Biocompatibility Characterization	82
2-2-4-1- <i>Corrosion resistance</i>	82
2-2-4-2- <i>XPS analysis</i>	83
2-2-4-3- <i>Cytotoxicity tests</i>	83
<b>2-3- Conclusion.....</b>	<b>84</b>
<b>2-4- References .....</b>	<b>85</b>

---

# Chapter II

## Experimental Techniques

In this part, the experimental methods to elaborate and characterize the materials used in this work will be developed. Depending on the particular topics addressed in this project, several kinds of sample shapes are relevant. For the characterization of new compositions, ribbon samples are the best in order to investigate basic properties of the newly developed BMG, as well as to evaluate the Glass Forming Ability (GFA). This last parameter allows the estimation of the critical diameter reachable for bulk samples. However, if the purpose is the improvement, in terms of size, density, or mechanical properties, cast bulk samples are more relevant.

After processing of the samples, basic characterizations have to be conducted to confirm, for example, the amorphous feature using XRD (X-Ray Diffraction) measurements. Transmission Electron Microscope (TEM) can also be used to analyse more precisely the microstructure. EDX analysis and density measurements permit to check the homogeneity of the composition and of the matter distribution. Then thermal properties are investigated using Differential Scanning Calorimetry (DSC) or High Temperature XRD measurements, to evaluate the temperature range available without crystallization. Afterwards, a wide range of specific experiments are conducted for a more detailed characterization of the sample such as: mechanical properties, corrosion tests, or biocompatibility analysis, to assure that the new elaborated samples meet the requirements of the targeted applications.

### 2-1- Materials Processing

#### 2-1-1- Master alloys processing

A wide variety of techniques to process metallic glasses are available, depending on the constituents of the system, of their melting point, and also of the targeted applications. The first step of the metallic glasses processing is the elaboration of a homogeneous master alloy, which will be used in the next step. All the constituents have been precisely weighted to the nearest milligram and placed into the furnace. Two kinds of furnaces can be used, depending the composition:

- The first one is called “induction melting” furnace. It is often used for low melting temperature elements, such as magnesium. Thus, the vaporization of sensitive elements can be avoided, which could cause a change in the composition and prevent the amorphous phase formation. In this work, this technique has been used for the Mg-based metallic glass ribbons samples.

Since the low melting point elements are often very reactive with oxygen, the requirement is to elaborate the alloy under argon atmosphere, which limits the oxygen impurities. Several argon flushes have been needed in order to get a pure atmosphere. This technique also allows the processing of the samples under vacuum.

The principle of this method corresponds to a conventional induction heating using a coil around the crucible containing the different elements to melt, as it is shown in Fig. 2-1. Induction currents are generated and heat the materials until it melts. This process is less violent than the arc melting because the temperature is precisely controlled and adjusted to the melting temperature of the system. Moreover, once the alloy is melted, the metallic ball starts levitating and this movement allows a better homogeneity.

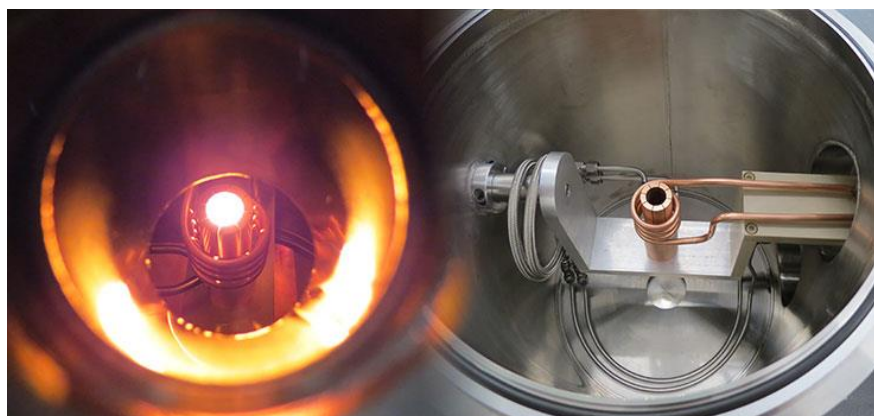


Figure 2-1: Induction melting device picture <sup>1</sup>

- The second kind of furnace is called “arc melting furnace”. The atmosphere during processing is also composed of argon gas and flushes are also necessary to evacuate the last oxygen impurities. First, Ti or Zr-trap called “Zr-getter” has been melted to confine the remaining oxygen molecules before starting the sample processing. The principle is simple: the samples are in crucibles on a cold copper plate placed in order to have the elements with the lowest melting point closer to the copper plate and far from the arc to level the melting of all the elements. Using a power-regulated generator, an arc is created between the tungsten tip and the samples to melt. The melting lasts about 30 seconds, first at 110 A, then 160 A. It is necessary to turn over the sample several times and melt it again (about 6 times) while controlling the intensity of the arc to obtain the best homogeneity.

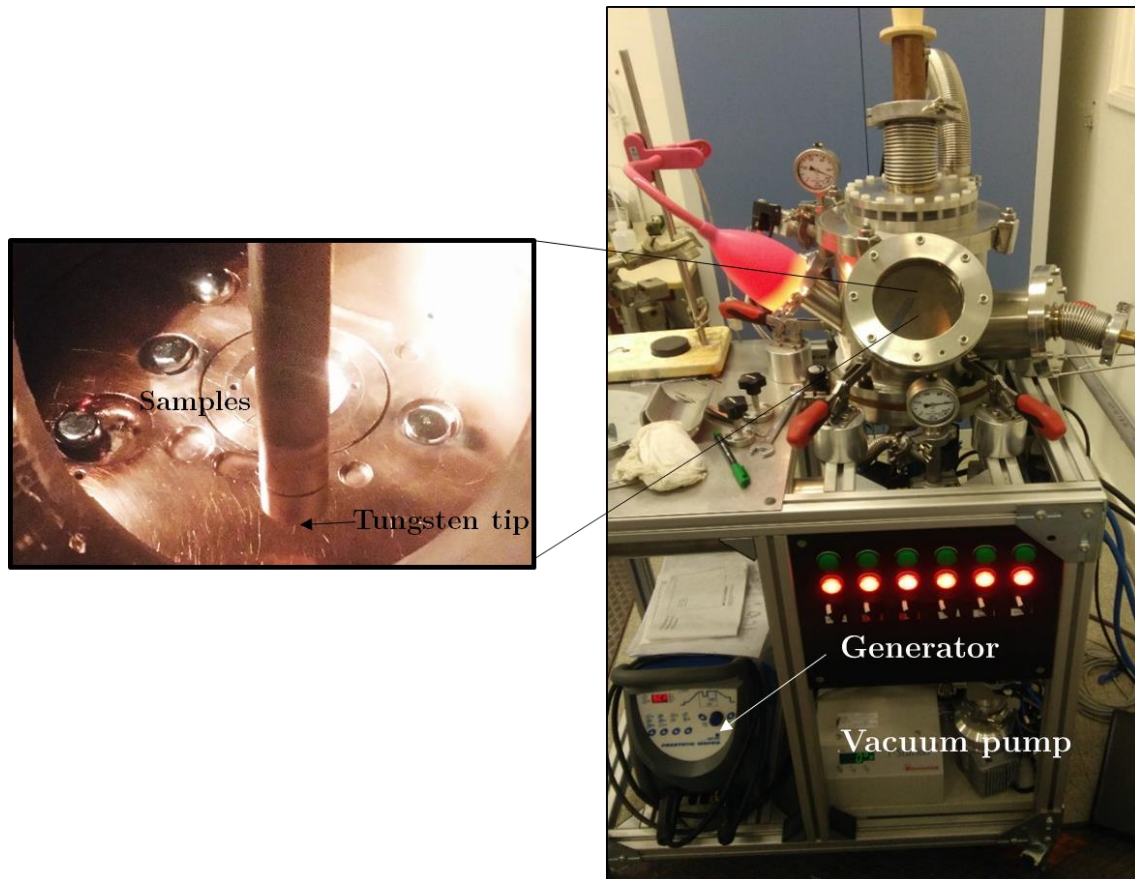


Figure 2-2: Arc melting device in SIMAP Laboratory, Grenoble

## 2-1-2- Samples processing

Once the master ingots have been processed, the samples have to be shaped. As it has been already mentioned, the choice of the shape and dimension depends on the composition and the intended characterization. In this part, all the techniques used in this work will be presented. Two main shapes can be processed: bulk samples and ribbons samples, depending on the GFA of the studied system.

### 2-1-2-1- Bulk metallic glass samples

Two main methods have been used to obtain cylindrical bulk samples, called rods:

- The first one is called “Tilt casting”. The principle is the following: the alloy is molten to reach the fully liquid state and poured in a cold copper crucible. The alloy drop into the mould under gravity and the cooling is performed instantly in contact with the cold mould. This technique is easy to use for the samples with diameters at least 3 mm or 4 mm. If it is smaller, the liquid cannot reach the end of the crucible by the only simple effect of gravity. A part will start to solidify in the mould and then the alloy cannot fill

the entire volume. In this case, the sample does not exhibit a cylindrical shape and the cooling is homogeneous. In order to increase the chance to obtain good surface quality samples, the liquid alloy should exhibit a good viscosity.

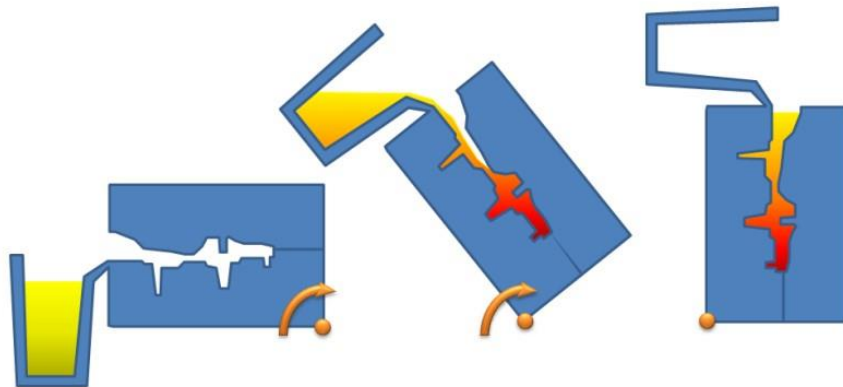


Figure 2-3: Principle of the tilt-casting experiment <sup>2</sup>

- The second method is called “Suction casting”. The principle is to place a mould below the cold copper plate and a tank with a lower pressure under the mould. When the alloy is melted, the valve between the melting enclosure and the tank is opened and the alloy is sucked into the mould and cooled instantly. Using the difference of applied pressure between the tanks and the enclosure, it is possible to fill in small-diameter moulds. However, the pressure difference plays a key role in the final state of the sample. On the other hand, if the difference is too high, argon gas can be trapped in the sample and if it is too low or if the valve is opened too late, the alloy starts dropping.

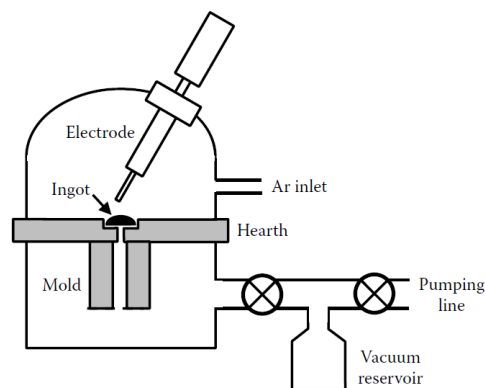


Figure 2-4: Schematic representation of the suction casting experiment <sup>3</sup>

### 2-1-2-2- Ribbon metallic glass samples

In opposite to bulk samples, only one technique exists to elaborate ribbon samples, called “Melt Spinning”. This technique allows to reach the highest cooling rate ( $10^6$  K/s) but also to get very thin samples. The master alloy is heated by induction in a quartz crucible with a 0.5 mm diameter hole at the bottom. A cold copper wheel is under the crucible and rotates at a speed of 2500 rpm. All the enclosure is placed under argon gas atmosphere during the

process. When the alloy is completely melted and homogeneous, the tube gets close enough to the wheel (a distance of two millimetres). Then applying pressure, the liquid is pushed down on the rotating wheel. Ribbons of few tens of micrometres thick are formed. The hole of the crucible controls the width of the ribbon samples and can be adjusted.

Ribbons are a good means to obtain samples with low glass forming ability and to characterize them. It is also the first step to process new compositions to evaluate the GFA and to have an idea of the possible critical diameter for bulk samples. Ribbons samples can be used to determine the glass transition temperature,  $T_g$ , and the crystallization temperature,  $T_x$ .

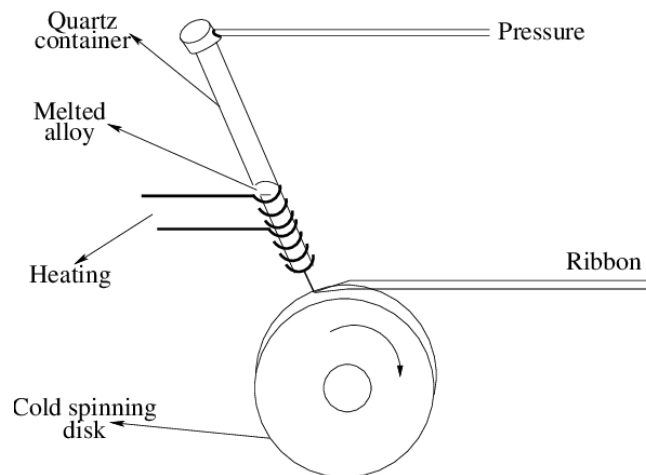


Figure 2-5: Principle of the melt-spinning device picture <sup>4</sup>

### 2-1-2-3- Sintered Samples

After the development of new ribbon compositions, the study of metallic glasses processing is achieved through a phase of improvements concerning the size and ductility of the samples. For this purpose, a new process has been studied in this work, in order to increase the maximum diameter of the sample and to manufacture composite parts samples to overpass the lack of ductility of bulk metallic glass. Spark Plasma Sintering (SPS) was chosen to take benefit of the long experience of MATEIS Lab with this technique. The entire process will be described in Chapter 6. Once the amorphous powder has been processed, the different parameters influencing the SPS were optimized, such as sintering time, sintering temperature or pressure. Crystalline particles can also be added in the amorphous matrix in order to form composite samples and add some ductility. This point will be further developed in Chapter 6.

The master ingots with nominal composition  $\text{Cu}_{60}\text{Zr}_{30}\text{Ti}_{10}$  have been prepared using an arc melting device and high purity raw materials: Cu (99, 9%), Ti (99, 9%) and Zr (99, 9%) in Tohoku University, in Sendai (Japan). Then, powders have been elaborated using gas atomization method. The alloys have been melted by induction in a crucible with a hole at the bottom. Then the melted alloy has been ejected from the crucible and a high pressure of argon

gas (10 MPa) has been applied to atomize the liquid alloy in fine powder. The particles were collected and calibrated to keep only the grain less than 75  $\mu\text{m}$  diameter.

Then the process of the sintered sample has been conducted using SPS system (FCT System HPD 25). The optimal conditions and the SPS process are described and developed in Chapter 6.

### 2-1-3- Samples studied

In this work, several compositions have been investigated depending on the purposes. Table 1 shows the different alloys, their shape, and the laboratory in which they have been produced.

Table 1: Table giving the different samples used during this PhD

<b>System</b>	<b>Laboratory for manufacturing</b>	<b>Shape</b>
<i>Mg-Ca-Au-(Yb)</i>	Tohoku University, Sendai, Japan	Ribbons
<i>Zr-Co-Ga-(Sn)-(Si)</i>	Tohoku University, Sendai, Japan	Ribbons
<i>Zr-Co-Ga-(Ti)</i>	SIMAP, Grenoble, France	/
<i>Cu-Ti-Zr-(Y)</i>	SIMAP, Grenoble, France	Bulk
<i>Cu-Ti-Zr (sintered)</i>	<ul style="list-style-type: none"> <li>• Powders: Tohoku University, Sendai, Japan</li> <li>• SPS: MATEIS, Lyon, France</li> </ul>	Bulk

## 2-2- Characterization of the samples

### 2-2-1- Structural Characterization

#### 2-2-1-1- Density

First of all, density measurement is an easy and quick method to obtain information about crystallinity and potential porosities or trapped bubbles inside the sample. This is a key step before doing any mechanical characterization. The density of a crystalline sample is higher than that of an amorphous alloy but a porous sample exhibits a lower density. However, except for these two cases, the density measurement alone is not enough to conclude and has to be used on the side of hardness analyses or XRD measurements. The results have been obtained on cast bulks samples using simple geometrical measurements and weight of the samples, if the sample fits a perfect cylindrical shape. Otherwise, it is necessary to use the Archimedes method.

## 2-2-1-2- X-Ray Diffraction (XRD)

This is a key technique and a crucial step in the metallic glasses characterization. An X-Rays beam is sent to the sample with an angle  $\theta$ , which causes the dispersion of the beam in several specific directions. The detector rotates around the sample to measure the intensity depending on the directions with an angle  $2\theta$  (see Figure 2-6).

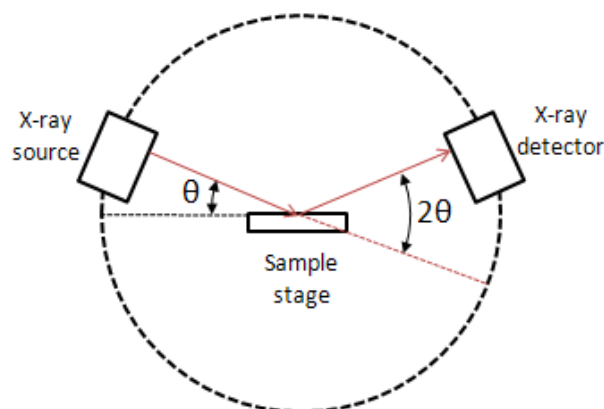


Figure 2-6: Principle of XRD measurement <sup>5</sup>

Using this technique, the possible presence of crystalline phases can be detected because of the appearance of sharp crystalline peaks. It is also possible to obtain the ratio of amorphous phase in case of semi-crystalline materials. For example, in the figure below, the sample is amorphous until a diameter of 7-8 mm. Beyond this value, crystalline peaks appear.

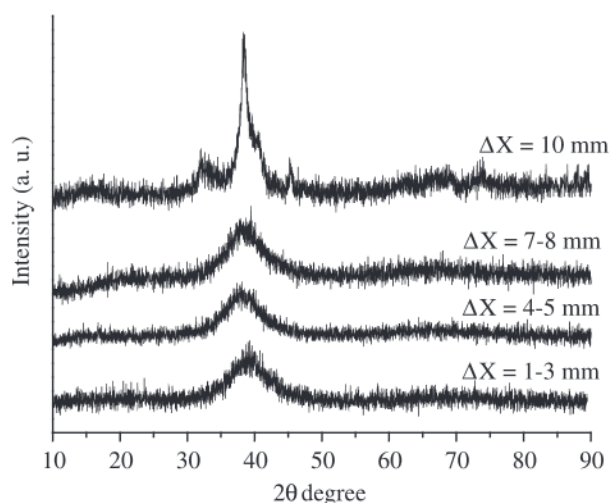


Figure 2-7: Examples of XRD diffractograms for amorphous alloys and crystalline peaks <sup>6</sup>

In this work, experiments have been conducted using a commercial device D8 Advance, Bruker. The working conditions have been set to 40 mA and 40 kV for the X-Rays tube. The detector was a Lynx Eyes detector. The increment was  $0.049^\circ$  for a scan rate equal to 0, 8 sec/step with Cu K $\alpha$  tube. In order to obtain good signal even for small diameter samples or ribbon samples, these last ones were cut into small squares of 5 x 5 mm and put

on a monocrystalline (100) Si-support X-Ray transparent, next to one another. The same process has been followed for the small diameter cylindrical samples, where small slices of 1 mm were cut and put on the Si-support in the same way.

### *2-2-1-3- Transmission Electron Microscopy (TEM)*

Transmission electron microscopy is a powerful microscopy technique to understand the structure of the samples with high resolutions. The principle of this analysis is to send a beam of electrons through a very thin sample (thickness about 100 nm) and detect the transmitted electrons to obtain an image of the structure. To prepare such a thin sample, a dimple technique has been used as pre-thinning experiment. Then a Gatan Precision Ion Polishing System (PIPS) has been used, for 4 hours, 4 kV, with angles of  $-10^\circ$  and  $+10^\circ$ . Finally, a step using Plasma Cleaner can be interesting to avoid carbon deposition on the sample.

A wide range of modes giving different images is available depending on the required information. It is possible to obtain different contrast images or diffraction patterns of a sample, but also obtain very high resolution images close to the atomic scale. In order to do this, the STEM mode has been used with a finer and highly focused electron beam, scanned over the specimen.

In this work, two different devices have been employed. Scanning TEM – high angle annular dark field (STEM-HAADF), providing a Z-contrast, has been used in a JEOL 2010F, at an accelerating voltage of 200 kV. Further chemical analyses have been carried out using electron energy-loss spectroscopy (EELS) and energy dispersive X-ray spectroscopy (EDX) in a FEI Titan ETEM G2 80-300 kV, operating at 300 kV. This technique consists in exposing the materials to a well-known range of kinetic energies, the electrons will undergo an inelastic scattering and their path will be deflected depending on an energy loss. Then this phenomenon is measured and interpreted. These techniques allow to obtain atomic compositions or information about chemical bonding. This experimental device will be further developed in Chapter 5.

### *2-2-1-4- Energy Dispersive X-Ray Spectroscopy (EDX)*

A beam of charged particles such as electrons, or uncharged particles, such as photons or X-rays, interacts with a sample. Some inner electrons of the structure are excited and can be ejected from the shell. An electron from a higher energetic level fills the hole releasing the difference of energy, producing characteristic X-rays. These X-rays are received and measured to obtain the composition of the samples, based on the principle that each element has unique atomic structure. The device used for this analysis was a ZEISS Supra 55VP, with an acceleration voltage of 10 kV, SEM-EDX detector. The same SEM detector with these parameters has also been used to observe fracture topology.

## 2-2-2- Thermal Characterization

Since the metallic glasses are very sensitive to temperature because they are metastable alloys, a precise thermal characterization has to be conducted.

### 2-2-2-1- Differential Scanning Calorimetry (DSC)

This technique allows the heat exchanges evaluation between a sample and a reference. It is used to measure the glass transition temperatures, crystallization or melting temperatures. To avoid oxidation issues, the experiment should be conducted under argon gas. A lot of investigations can be performed, and a lot of information can be obtained using this simple experiment.

In this work, two kinds of measurements have been carried out: isochronal (also called non-isothermal) and isothermal treatment. For example, non-isothermal treatment, using different heating rates can indicate the evolution of the crystallized fraction in the sample. It can also help to determine the activation energy of primary crystallization using Kissinger<sup>7</sup> law and Flynn-Wall-Ozawa<sup>8,9</sup> law and compare it between different systems.

Isothermal experiments are useful to obtain the time available before crystallization. Information about the crystallization can also be available using the areas under the DSC curves and the Avrami equation:

$$\alpha(t) = 1 - \exp(-k(t - \tau)^n) \quad (1)$$

With  $\alpha$ , the crystallized fraction depending on time,  $k$ , a kinetic parameter which takes into account the crystallized areas,  $\tau$ , incubation time and  $n$ , the Avrami coefficient.

A commercial device Netzsch DSC 204 F1, under argon atmosphere has been used for the isothermal measurement of the Mg-based system. The heating rates before the isothermal step has been set to 100K/min and a slower rate, 10K/min, has been used for the last ten degrees to prevent an eventual overshoot from occurring. Then, the temperature has been maintained during a long duration (1 hour). For non-isothermal characterizations of all the systems, a Perkin Elmer DSC 7, under high purity dry nitrogen at a flow rate of 20 ml/min, was used. To get a better accuracy, the weighed mass is always the same (about 14 mg).

Figure 2-8 shows a typical DSC curve example for an isochronal measurement with the characteristics temperatures, indicated by the black arrows.

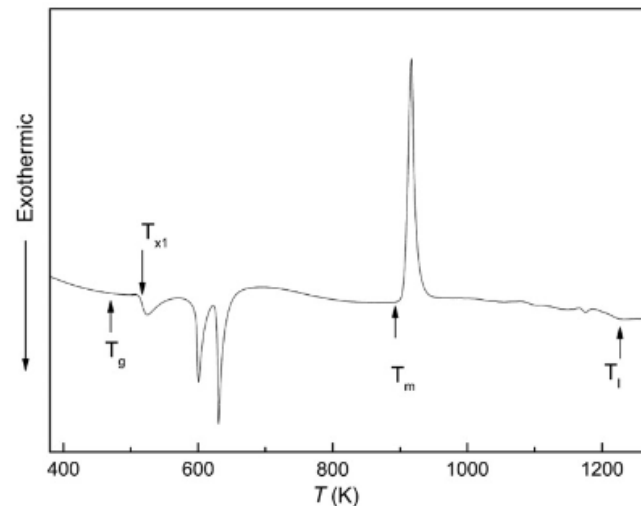


Figure 2-8: Example of a typical DSC curve for metallic glasses of Al-Ni-Y system with  $T_g$ : the glass transition temperature,  $T_x$ : the crystallization temperature,  $T_m$ : the melting temperature,  $T_l$ : the liquidus temperature <sup>10</sup>

### 2-2-2-2- High Temperature XRD

In addition to the DSC experiments, high temperature XRD measurements can be performed in order to follow the evolution of the crystallization of the sample depending on time or temperature. First, non-isothermal measurements have been conducted to evaluate the characteristic temperatures with this device, which can be a little bit different from the results of the DSC. Then, isothermal experiments can be carried out to determine the time available before crystallization at a given temperature. This experiment has been conducted under vacuum and the onset of the crystallization kinetic can be investigated. The two typical heat-treatment during this analysis, namely non-isothermal and isothermal, are presented in the picture below.

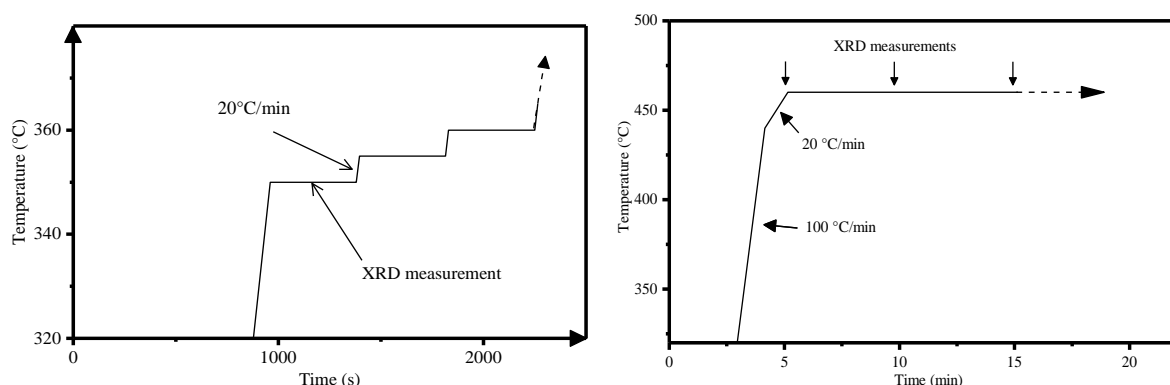


Figure 2-9: Schematic representation of the heating during the high-temperature XRD experiments: (Left) Non-isothermal analysis (Right) Isothermal analysis.

Figure 2-10 shows an example of the results obtained during an isothermal treatment.

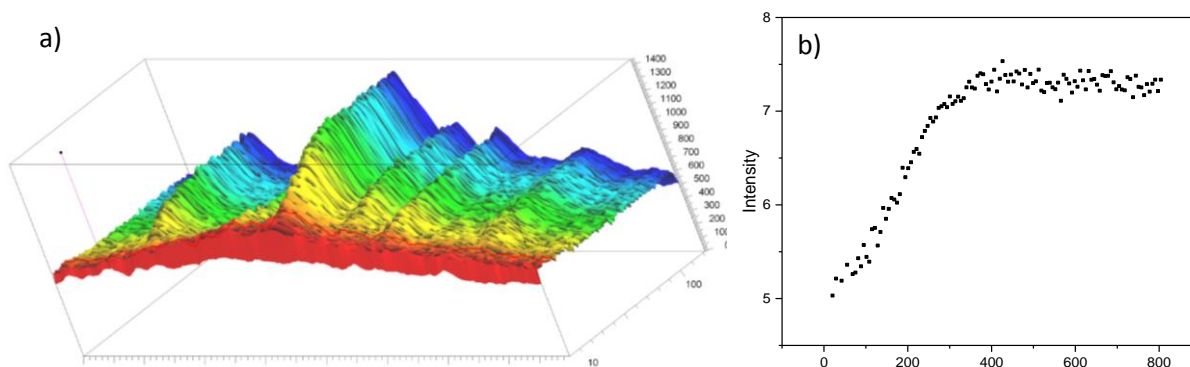


Figure 2-10: a) 3D picture of the evolution of the crystallization in the Cu-based BMG sample, b) Graph showing the evolution of the intensity of the peaks depending on the time

## 2-2-3- Mechanical Characterization

### 2-2-3-1- Compressive tests

To investigate the mechanical behaviour of the samples, mechanical tests have been conducted, especially compressive tests. Indeed, the fracture during tensile tests is often catastrophic and the tensile tests samples are much more complicated to process.

Samples used for the compressive tests of this work are cylinders with 3 mm diameter and about 4 mm high. The samples have been cut using a micro saw or a wire saw. Then the two surfaces have been polished with 1200 SiC paper in order to obtain parallel surfaces and perpendicular to the compressive axis.

The temperature during the tests was the room temperature one.

The device used is an INSTRON 5667 traction and compression device. Deformation has been measured using a video extensometer (Advances Video Extensometer) for non-contacting strain measurement. A small home-made assembly have been developed in order to adapt the machine to the small size of the samples and a Plexiglas protection was also put to protect the extensometer during the fracture.

This kind of test was used for the only system to reach bulk form, the Cu-based system. For ribbons samples, another way to obtain mechanical properties is discussed.

### 2-2-3-2- Nanoindentation tests

Because the ribbon samples are too thin to conduct compressive mechanical tests, nano-indentation tests has been realized to evaluate the Young Modulus after load-unload measurements. The device used is an Agilent G200 Nanoindenter from Agilent Technologies, with Berkovich tip. The ribbons have been glued on a cold mounting resin substrate, using conductive silver paint. The method to indent has been the G-serie CSM Thin Film Method <sup>11,12</sup>

for the Mg-based and the Zr-based amorphous alloy and with the depth limit equal to 500 nm and the surface approach velocity equal to 10 nm/s.

### 2-2-3-3- Hardness measurements

Other classical experiments permitting to get a lot of information about the quality and the toughness of the sample are micro-hardness measurements and high-load hardness measurements. Micro-hardness measurements have been done using a Buehler MicroMet 5104 over the range 10g to 1 kg. The high-load hardness measurements have been done using a Future Tech FV-700 device, over the range of loads from 1 to 30 kg.

The micro-hardness is very useful to obtain information about the hardness of the sample. The high-load measurements also allow to get details about the toughness and the residual stress intensity factor, using the length of the potential crack through the application of the load (Fig 2-11), thanks to the following relationship <sup>13</sup>:

$$K_r = 0.016 \sqrt{\frac{E}{H}} \frac{P}{c^{3/2}} \quad (2)$$

With E, the Young's Modulus, P, the indentation load, c, the half-crack length, H, hardness (MPa).

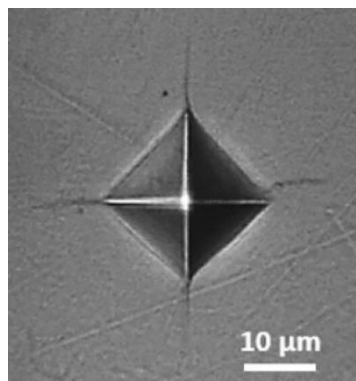


Figure 2-11: Optical micrograph of indent; the induced crack allows the determination of the toughness <sup>14</sup>

### 2-2-4- Biocompatibility Characterization

Since the target applications are for biomedical use, several experiments should be conducted in this goal like cytotoxicity tests, corrosion tests, then X-Ray electron spectroscopy (XPS) analysis. This last analysis allows the investigation of the surface after immersion and resistance tests in conditions as close as possible as that in the human body.

### 2-2-4-1-Corrosion resistance

The corrosion tests have been performed on the Cu-based alloy, using a temperature controlled, three electrodes glass-cell, and a Gamry Ref 600 + potentiostat. The working electrode was composed of metallic glass, the auxiliary electrode and the reference electrode were graphite pin and AgAgCl electrode respectively. Two different electrolyte solutions have been used: the first one was a classical saline solution composed of 0,9 M NaCl and the other one was composed of 0,9 M NaCl and 4g/L of bovine serum (BSA > 98.5%, fraction V, lyophilized, Sigma Aldrich). The two media have been used to compare the positive or negative influence of the proteins on the corrosion of a based copper alloy. The exposed area was circular and measured to be 0.0314 cm<sup>2</sup>. All the tests have been performed in naturally aerated solution at 37°C. A first Open-Circuit Potential (OCP) has been done for one hour for the samples immersed in the NaCl and three hours for the one in NaCl with albumin before the acquisition of the polarization curve. The addition of albumin revealed some difficulties to stabilize the potential and that is why the time of OCP was longer for this sample. Before the acquisition of the polarization curves, the stabilized values of the potential were -0.396 V without albumin and -0.339 V with albumin. The polarization curves have been registered during the scanning of a range of potential with and without albumin, between -6V and 2V and between -6V and -2V respectively. The scan rate was  $1.6 \times 10^{-1}$  mV/s.

The samples have been prepared by polishing with grain size of 1200 SiC and a heat shrinkable tube was applied around the sample in order to investigate the reaction only on the circular cross section.

The OCP analysis permits the study about the stability and thus the deterioration of the surface after several hours in immersion without being crossed by any current. The polarization curve allows the measurement of the corrosion potential, the passive level, the current density and the pitting potential. Then the corrosion resistance can be evaluated.

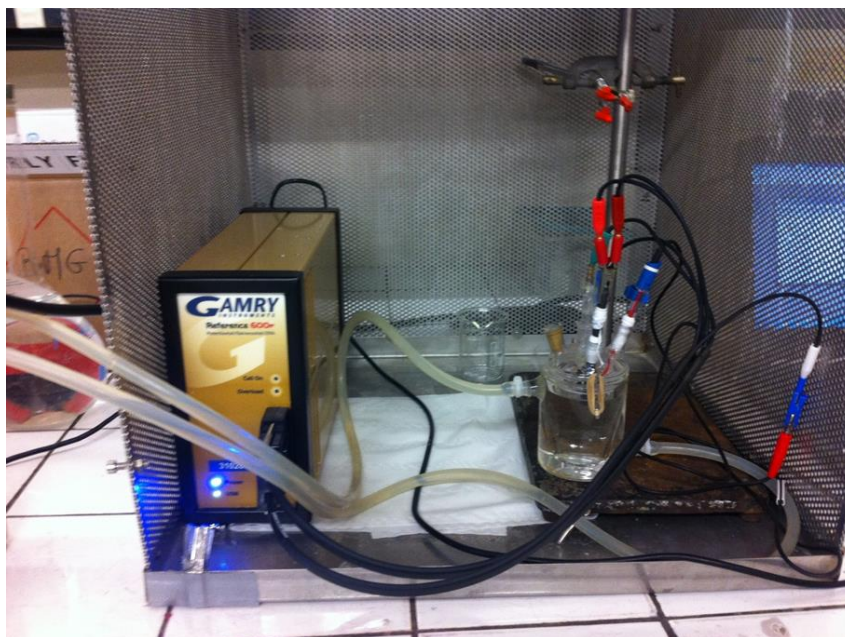


Figure 2-12: Three electrodes assembly for the evaluation of the corrosion resistance

#### 2-2-4-2 XPS analysis

The XPS analysis has been done after five hours of OCP on both samples. A cylindrical sample has been cut in small slices of 1 mm thick and then immersed in the solution either containing only NaCl or NaCl and albumin. After the immersion, the samples have been rinsed with distilled water and dried at the ambient atmosphere. The analysis has been conducted using a Thermo-Fischer K-Alpha in the centre of the samples. The purpose is to determine the elements present on the surface, from a quantitative point of view and the bonding and chemical forms present.

#### 2-2-4-3 Cytotoxicity tests

The cytotoxicity tests have been conducted to evaluate the effect of the material on the cell adhesion and proliferation. In order to control the biocompatibility of a newly developed alloy, cytotoxicity tests have to be done. This is highly important during the development of a new composition, especially when one of the elements is not well-known as a biocompatible one.

In our case, gallium and yttrium were important to test. Cytotoxicity tests were conducted on the Cu-based samples (Chapter 4) and the Zr-based samples (Chapter 5). For the Zr-based system, the cells used were osteoblast-like MG-63 (Corning, NY, USA, ref 3524) and for the Cu-based system, SaOS-2 cultured in 24-well cell culture plates. The initial batch of cells has been lost and new one more efficient have been used. The tests have been conducted in RPMI 1640 medium (Dutscher, France, ref L0498-500) (containing stable L-

glutamine and phenol red) supplemented with 10% fetal bovine serum (Dutscher, ref P040637100) and 5% antibiotic/antimycotic solution (Dutscher, Ref SV30079.01) at 37 °C in a humidified atmosphere of 5% CO<sub>2</sub> to make cell adhesion possible. The samples were disk of 1 mm thick. They have been sterilized by UV for 20 min. A cellular suspension containing 5000 cells has been prepared using a cell counter (Millipore Scepter purchased at Dutscher, ref: 053750). The Scepter cell counter uses the Coulter principle of impedance-based particle detection to reliably and accurately count every cell in the sample. The samples have been placed in the 24-well cell culture plates (one sample in each well). Then, 50 µL of the cellular suspension containing 5000 cells have been deposited in the well, and cell culture plates were incubated 2 h at 37°C. After the addition of 2 mL of culture medium, cells have been incubated for 22 hours. The cell viability was evaluated by the PRESTOBLUE technique (Invitrogen, Carlsbad, CA, USA). The resazurin, which is blue and non-fluorescent, is reduced by the mitochondrial metabolic activity of the cells in resorufin, a pink and fluorescent product, detectable by fluorometry.

The cellular proliferation has been evaluated after 24 hours for the Cu-based metallic glass system and after 4 days, 7 days and 10 days for the Zr-based metallic glass system. The culture medium has been discarded and replaced by 1 mL of the culture medium without FBS, antibiotics and phenol red, but with 10% PrestoBlue put on each well. The samples have been incubated 1.5 h at 37°C under a humidified atmosphere of 5% CO<sub>2</sub>. Then, the plate has been stirred, and 100 µL of each well have been transferred in a 96 black-well plate and the fluorescence measured using an Infinite Pro 200 fluorimeter (Tecan) with a wavelength of 535 nm for excitation and 615 nm for emission. After each measurement, cells have been rinsed twice with RPMI, then 2 mL of medium has been added and the plate incubated until the next measure. Each assay has been done in triplicate. For each sample, a plastic control (cell culture treated polystyrene) has been included to verify the normal behaviour of cells, and it was referred to as "Plastic telltale".

## 2-3- Conclusion

In this part, all the experimental techniques used in this work have been explained and discussed.

First, the importance to choose the proper processing technique is crucial depending on the target composition: Arc melting or Induction Melting to process the master ingots, avoiding mass loss and allowing good homogeneity. Then, the elaboration way and the samples shape are key parameters to investigate the sample properties depending on the purpose of the study: ribbons sample using melt spinning (Chapters 3 and 4) or bulk samples using tilt casting or suction casting (Chapter 5).

Another way to process the metallic glasses involving the powder metallurgy is explained and characterized during this PhD. This process, consisting in sintering powders,

permits to obtain larger diameter bulk samples as well as composite samples. This technique will be described and developed in Chapter 6.

Then various devices to explore in details the samples were described. A lot of properties have to be checked first and then investigated because of the biomaterial purpose and the very strict criteria to respect. First of all, the complete basic characterization of an amorphous alloy has to be done: XRD measurements, density tests, DSC experiments. Then, more detailed investigations are conducted: study of the thermal stability using DSC and high temperature XRD experiments, TEM observations to investigate the structure, mechanical and corrosion tests with surface analysis to test the resistance of all the samples. Moreover, further investigations as cytotoxicity tests to discuss the biocompatibility of the sample, mechanical tests and SEM observations to evaluate  $E$ ,  $\sigma_y$  and the toughness have been conducted.

These techniques give quite a complete picture of the materials and their perspectives of this PhD.

## 2-4- References

1. Arcast Inc. Ind CC 20 Induction Cold Crucible Furnace and Casting Module. (2010). Available at: <http://www.arcastinc.com/indcc20.htm>. (Accessed: 13th April 2018)
2. Lexicon, F. Tilting gravity die casting process. Available at: <https://www.giessereilexikon.com/en/foundry-lexikon/Encyclopedia/show/tilting-gravity-die-casting-process-4367/>. (Accessed: 13th April 2018)
3. Tucker, C. Metallic Glasses. 9 (2016). Available at: <http://slideplayer.com/slide/7581277/>. (Accessed: 13th April 2018)
4. Gonzalez-Vinas, W. & Mancini, H. *Science of Materials : An Introduction (Pre-print)*. (2003).
5. Grebenkemper, J. Powder X-ray Diffraction. (2017). Available at: [https://chem.libretexts.org/Core/Analytical\\_Chemistry/Instrumental\\_Analysis/Diffraction\\_Scattering\\_Techniques/Powder\\_X-ray\\_Diffraction](https://chem.libretexts.org/Core/Analytical_Chemistry/Instrumental_Analysis/Diffraction_Scattering_Techniques/Powder_X-ray_Diffraction). (Accessed: 14th April 2018)
6. César, L. *et al.* New Zr-based Glass-Forming Alloys Containing Gd and Sm. *Materials Research* **15**, 723–727 (2012).
7. Kissinger, H. E. Reaction Kinetics in Differential Thermal Analysis. *Analytical Chemistry* **29**, 1702–1706 (1957).
8. Flynn, J. H. & Wall, L. A. General treatment of the thermogravimetry of polymers. *Journal of Research of the National Bureau of Standards Section A: Physics and Chemistry* **70A**, 487 (1966).
9. Flynn, J. H. & Wall, L. A. A quick, direct method for the determination of activation energy from thermogravimetric data. *Journal of Polymer Science Part B: Polymer Letters* **4**, 323–328 (1966).
10. Fu, H. M. *et al.* Synthesis and compressive properties of Al–Ni–Y metallic glass. *Philosophical Magazine Letters* **89**, 711–716 (2009).
11. Hays, C. C., Kim, C. P. & Johnson, W. L. Microstructure Controlled Shear Band Pattern Formation and Enhanced Plasticity of Bulk Metallic Glasses Containing in situ Formed Ductile Phase Dendrite Dispersions. *Physical Review Letters* **84**, 2901–2904 (2000).

12. Hay, J., Agee, P. & Herbert, E. Continuous stiffness measurement during instrumented indentation testing. *Experimental Techniques* **34**, 86–94 (2010).
13. Hess, P. A., Poon, S. J., Shiflet, G. J. & Dauskardt, R. H. Indentation fracture toughness of amorphous steel. *Journal of Materials Research* **20**, 783–786 (2005).
14. Dulnee, S., Kiminami, C. S., Gargarella, P. & Kaufman, M. J. Microstructural Evolution and Mechanical Properties of Ni<sub>57</sub>Nb<sub>33</sub>Zr<sub>5</sub>Co<sub>5</sub> Metallic Glass. *Materials Research* **20**, 244-247 (2017).

# Chapter 3

## Role of Ytterbium on the properties of a new Mg-based biodegradable metallic glass system

---

<b>ROLE OF YTTERBIUM ON THE PROPERTIES OF A NEW BIODEGRADABLE METALLIC GLASS SYSTEM.....</b>	<b>88</b>
<b>3-1- The reason for a new Mg-based composition.....</b>	<b>88</b>
<b>3-2- Development of a new alloy and study of the influence of Ytterbium on the properties of a Mg-based metallic glass.....</b>	<b>90</b>
<b>3-3- Outlooks on this new processed alloy .....</b>	<b>96</b>
<b>3-4- Conclusion.....</b>	<b>98</b>
<b>3-5- References .....</b>	<b>98</b>

---

## Chapter III

# Role of Ytterbium on the properties of a new biodegradable metallic glass system

To fulfil the purpose of this PhD in finding new biocompatible metallic glasses, two new biocompatible compositions have been proposed. The first one is detailed in this chapter and concerns the processing of a new biodegradable material. The chosen system is a Mg-based metallic glass system containing only fully biocompatible elements. In this part, the classical characterization of this new processed alloy is carried out to evaluate its characteristic fetures. As a potential use as biomaterials, the respect of strict specifications is needed and investigations about the thermal stability during the sterilization process, the biocompatibility or the mechanical properties are conducted.

Moreover, in order to increase the GFA or the crystallization resistance of the system, the role of ytterbium additions on this system is investigated and described.

### 3-1- The reason for a new Mg-based composition

As it was underlined in Chapter 1, a wide range of compositions for use as bioresorbable materials have been already processed. Examples of Ca-based<sup>1,2</sup>, Sr-based<sup>3,4</sup> and Mg-based BMGs<sup>5-7</sup> were given. As a matter of facts, most part of the studied compositions are Mg-based systems and more precisely, many studies concern the system Mg-Ca-Zn<sup>8-14</sup>. However, based on the work of Calin et al.<sup>15</sup>, zinc does not appear in the fully biocompatible elements category, as it is presented in Figure 3-1.

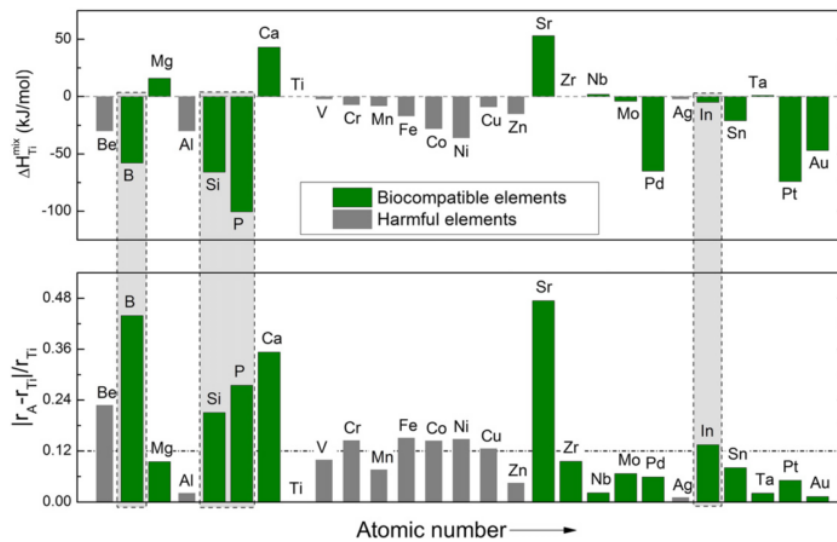


Figure 3-1: Mixing enthalpy, atomic radius difference for alloying with titanium to evaluate the GFA, with biological safety information <sup>15</sup>

The challenge of this work is to process a new composition containing only fully biocompatible elements. However, it is very difficult to replace zinc because it controls the kinetic degradation of Mg-Ca system. To remove zinc and find another element to add, the choice was made using two of the Inoue's criteria to get a good GFA: (i) a negative mixing enthalpy and (ii) a atomic radius difference larger than 12%. Therefore, we used the reported data by Takeuchi and Inoue <sup>16</sup> to choose an element corresponding to these two criteria.

The same table as in the work of Calin et al. has been done for the magnesium. The results are shown in Fig. 3-2.

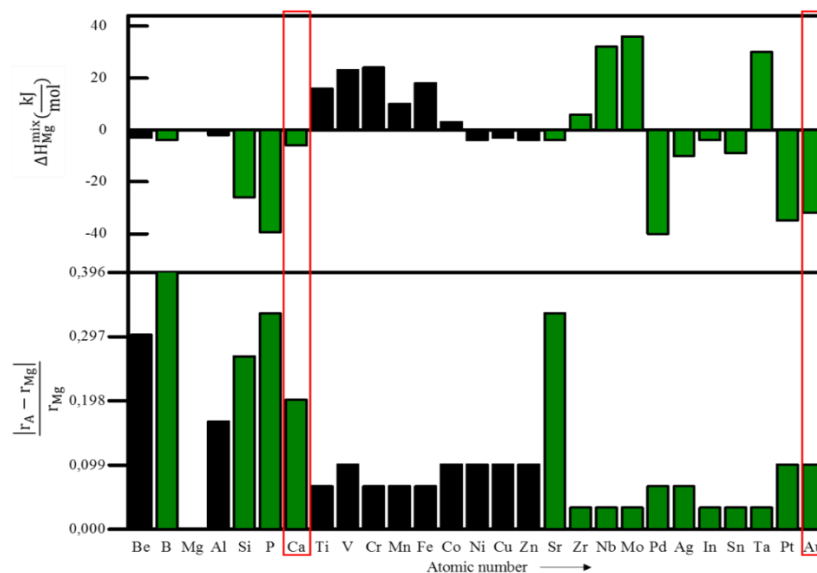


Figure 3-2: Mixing enthalpy and atomic radius difference for alloying with magnesium to evaluate GFA, with biocompatibility data

According to these results, P, Si and Au show a very negative mixing enthalpy with Mg and a large atomic radius difference (values in Fig. 3-3). However, P and Si are metalloid elements and Au is much easier to use during the processing, compared to P and Si. Thus, gold has been chosen.

Gold is also a close element to the Zn in the periodic table, so their properties should be similar. At least, it is also a fully biocompatible element according to Calin et al. <sup>15</sup> and gold exhibits a low Young modulus.

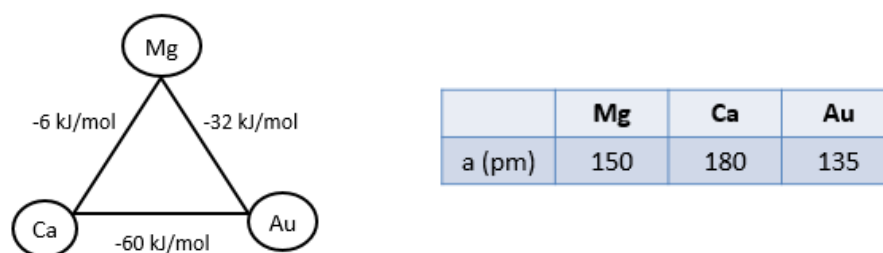


Figure 3-3: Mixing enthalpy and atomic radius difference of the system Mg-Ca-Au

Using the phase diagram corresponding to this system, the choice was to use the deep eutectic compositions.

Then, regarding the first results, Yb additions were tested in order to increase the critical diameter of the sample, enhancing the stability of the liquid phase and improving the resistance to crystallization. As it has been presented in Chapter 1, about the role of minor additions, the REE elements additions are especially very helpful. Consequently, five compositions were processed in Japan, at IMR, in Tohoku University:  $Mg_{(85-x)}Ca_{(8+x)}Au_7$  (with  $x=0, 2, 4$ ) and  $Mg_{(81-x)}Ca_{10}Au_7Yb_{(2+x)}$  (with  $x=0, 8$ ).

### 3-2- Development of a new alloy and study of the influence of Ytterbium on the properties of a Mg-based metallic glass

This part will be presented using a scientific paper published in Journal of Non-Crystalline Solids.

#### Article 1: A new, toxic element-free Mg-based metallic glass for biomedical applications

(Published in Journal of Non-Crystalline Solids, 2018, 481, pp 397-4

### 3-3- Outlooks on this new processed alloy

These new  $Mg_{81}Ca_{10}Au_7Yb_2$  and  $Mg_{85}Ca_8Au_7$  alloys are promising because of the presence of only non-harmful elements. However, the composition does not allow bulk shape samples yet, even with the microalloying of ytterbium. Other biocompatible elements should be added in order to increase the critical diameter, for example Sr, which is also biocompatible. This element could also be very interesting because it can help the bone cell formation as it is the main constituent of the osteoporosis treatment. Moreover, substitution between Sr atoms and Ca atoms is likely possible, which contributes to the maximum disorder theory and helps the GFA to be increased.

Several properties of  $Mg_{85}Ca_8Au_7$  have been characterized in the previous publication. However, as it is supposed to become a biomaterial, corrosion resistance is crucial to be evaluated and this point is missing in the previous work. Since corrosion resistance of this alloy is still low and needs improvements, this point is developed in this part.

Due to the reactivity of this alloy, long corrosion tests with polarization curves acquisition are impossible to conduct. The easiest way to obtain information on the corrosion resistance is to conduct immersion tests in simulated body fluids (SBF).

The results of the immersion tests are presented in the Figure 3-4. As it is shown, the sample is observed during almost one hour and the degradation of the sample is complete in 45 minutes. Because the zinc was the element allowing the control of the degradation of a Mg-Ca alloy and was removed, the kinetic of Mg-Ca degradation is not controlled any longer. The degradation happen too quickly and too early to be usable as biomaterials yet. The addition of new elements with a similar action than the zinc should be investigated.

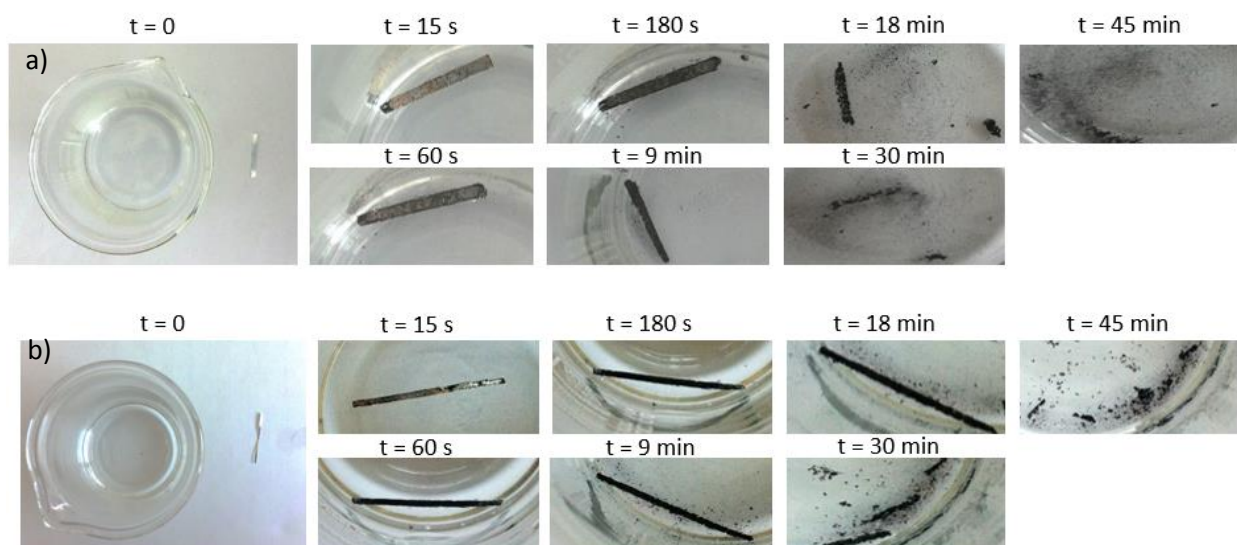


Figure 3-4: Immersion tests in SBF of the samples without Yb a) and with Yb b)

Ytterbium seems to cause a small improvement of the corrosion resistance, regarding the larger size of the degradation debris. For example, after 18 minutes, the initial sample shape still remains. Despite this, the samples suffer from a very quick degradation, which needs to be well controlled.

The Mg/Ca ratio may not be optimum for the corrosion resistance kinetic. Addition of another element to regulate the dissolution of the material or a surface treatment can also be tried to control and reduce the degradation.

Due to this quick degradation, no cytotoxicity test evaluation can be done. Further studies need to be conducted on this point to improve this material for use as biomaterials.

### 3-4- Conclusion

In this part, a new biodegradable metallic glass composition has been processed using only fully biocompatible elements. The complete approach to choose a new system has been described, using the proposed criteria to help the formation of a glassy alloy.

Processing of these new compositions, Mg-Ca-Au-Yb and Mg-Ca-Au, have been developed because Mg-based alloys can suffer from a potential evaporation of the Mg and create a change in the composition of the alloy. Induction melting is required and melting time is significant. Ca has been used carefully handled to avoid the oxides layer on the raw material, due to the strong reactivity of Ca in ambient atmosphere.

Then ribbons samples are processed and characterized in different ways. After checking the basic properties of the alloys concerning the amorphous feature, the GFA is shown to be too limited to obtain a bulk sample. Then, addition of a rare earth element (Yb) has been discussed. The action of this element is significantly beneficial on the thermal stability of the system. The structural relaxation is avoided thanks to Yb action, and the crystallization resistance is enhanced. A small improvement on the corrosion behaviour using this addition seems to appear. Further development of rare-earth elements action in glassy systems will be discussed in Chapter 5.

Eventually, a new biocompatible sample has been successfully processed. The thermal stability is high enough to avoid risks of crystallization during the sterilization process. The Young modulus of this new alloy is close to the one of pure Mg to avoid osteolysis issues. The GFA is still insufficient to get a bulk sample. However, at this time it is possible to mention only potential coating applications or metallic glass deposits on biomaterials.

### 3-5- References

1. Dahlman, J., Senkov, O. N., Scott, J. M. & Miracle, D. B. Corrosion Properties of Ca-Based Bulk Metallic Glasses. **48**, 1850–1854 (2007).
2. Senkov, O. N., Miracle, D. B., Keppens, V. & Liaw, P. K. Development and Characterization of Low-Density Ca-Based Bulk Metallic Glasses: An Overview. *Metallurgical and Materials Transactions A* **39**, 1888–1900 (2008).
3. Li, H. F., Zhao, K., Wang, Y. B., Zheng, Y. F. & Wang, W. H. Study on bio-corrosion and cytotoxicity of a Sr-based bulk metallic glass as potential biodegradable metal. *Journal of Biomedical Materials Research Part B: Applied Biomaterials* **100B**, 368–377 (2012).
4. Zhao, K., Li, J. F., Zhao, D. Q., Pan, M. X. & Wang, W. H. Degradable Sr-based bulk metallic glasses. *Scripta Materialia* **61**, 1091–1094 (2009).
5. Li, H., Pang, S., Liu, Y., Liaw, P. K. & Zhang, T. In vitro investigation of Mg–Zn–Ca–Ag bulk metallic glasses for biomedical applications. *Journal of Non-Crystalline Solids* **427**, 134–138 (2015).
6. Baulin, O., Fabregue, D., Kato, H. *et al.* A new, toxic element-free Mg-based metallic glass for biomedical applications. *Journal of Non-Crystalline Solids* **481**, (2018).
7. Gu, X.N., Li, S.-S., Li, X.-M. & Fan, Y.-B. Magnesium based degradable biomaterials: A review. *Frontiers of Materials Science* **8**, 200–218 (2014).
8. Gu, X., Shiflet, G. J., Guo, F. Q. & Poon, S. J. Mg–Ca–Zn Bulk Metallic Glasses with High Strength and Significant Ductility. *Journal of Materials Research* **20**, 1935–1938 (2005).
9. Cao, J. D., Kirkland, N. T., Laws, K. J., Birbilis, N. & Ferry, M. Acta Biomaterialia Ca – Mg – Zn bulk metallic glasses as bioresorbable metals. *Acta Biomaterialia* **8**, 2375–2383 (2012).
10. Datta, M. K., Chou, D. T., Hong, D. *et al.* Structure and thermal stability of biodegradable Mg–Zn–Ca based amorphous alloys synthesized by mechanical alloying. *Materials Science and Engineering: B* **176**, 1637–1643 (2011).
11. Li, H., Pang S., Liu, Y. *et al.* Biodegradable Mg–Zn–Ca–Sr bulk metallic glasses with enhanced corrosion performance for biomedical applications. *Materials & Design* **67**, 9–19 (2015).
12. Zheng, Y., Wang, J. & Wang, W. Corrosion of and cellular response to Mg-Zn- Ca bulk metallic glasses. *Biomaterials* **31**, 1093–1103 (2009).
13. Nowosielski, R., Borowski, A., Guwer, A. & Babilas, R. Fabrication of ternary Ca-Mg-Zn bulk metallic glasses. *Journal of Achievements in Materials and Manufacturing Engineering* **56**, 67–74 (2013).
14. Li, H., Liu, Y., Pang, S., Liaw, P. K. & Zhang, T. Corrosion fatigue behavior of a Mg-based bulk metallic glass in a simulated physiological environment. *Intermetallics* **73**, 31–39 (2016).
15. Calin, M., Gebert, A., Cosmina, A. *et al.* Designing biocompatible Ti-based metallic glasses for implant applications. *Materials Science & Engineering C* **33**, 875–883 (2013).

16. Takeuchi, A. & Inoue, A. Classification of bulk metallic glasses by atomic size difference, heat of mixing and period of constituent elements and its application to characterization of the main alloying element. *Materials Transaction* **46**, 2817–2829 (2005).

# Chapter 4

## Al substitution by Ga to process a new biocompatible Zr-based metallic glass

---

<b>AL SUBSTITUTION BY GA TO PROCESS BIOCOMPATIBLE ZR-BASED METALLIC GLASS .....</b>	<b>102</b>
<b>4-1- The need for a new Zr-based composition .....</b>	<b>102</b>
<b>4-2- Processing and characterization of a new biocompatible Zr-based composition .....</b>	<b>103</b>
<b>4-3- From the ribbons to the bulk samples: Experimental Design.....</b>	<b>109</b>
<b>4-3-1- Increase of the glass forming ability and critical diameter .....</b>	<b>109</b>
<b>4-3-2- Experimental Design.....</b>	<b>110</b>
<b>4-3-3- Results and Discussion .....</b>	<b>112</b>
<b>4-4- Further investigations about promising non-fully amorphous samples .....</b>	<b>117</b>
<b>4-4-1- Mechanical properties.....</b>	<b>117</b>
<b>4-4-2- Investigation about the crystalline phase .....</b>	<b>118</b>
<b>4-4-2- Potential applications.....</b>	<b>120</b>
<b>4-5- Conclusions .....</b>	<b>120</b>
<b>4-6- References .....</b>	<b>121</b>

---

## Chapter IV

# Al substitution by Ga to process biocompatible Zr-based metallic glass

A new biodegradable and fully biocompatible composition of resorbable metallic glass has been processed in the previous chapter. In this one, we focus on the processing of a new biocompatible composition with high mechanical properties for a use as reinforcement material. This new elaborated composition is also under the form of ribbon samples and needs to be characterized. The chosen system is a Zr-based metallic glass and contains only biocompatible elements. The main challenge of this part is the replacement of Al by Ga. Indeed, Al is a very helpful element to increase GFA and ductility but could be toxic.

Moreover, in order to enhance the GFA and the resistance to corrosion, small additions of Sn and Si were tested and discussed.

### 4-1- The need for a new Zr-based composition

Zr-based bulk metallic glasses are among the most studied systems with Ti-based bulk metallic glasses. This kind of material was studied from 1990 and the interest has never stopped. This type of alloy is very interesting, especially for biomaterials. However, none of the existing system exhibit an absence of non-desirable elements, as small atoms as Be<sup>1,2</sup>, Ni<sup>3,4</sup> or Fe<sup>5</sup> are very helpful to increase the GFA and the ductility. Nevertheless, they are supposed to become toxic, once dissolved, and released in the body under ions form.

One of the most interesting systems for biomaterials is Zr-Co-Al, studied by Wada and Inoue in 2002 <sup>6</sup>.

However, aluminium seems to be recognized as a potential cause of Alzheimer's disease and inhibits the bone's growth, as released ions <sup>7,8</sup>. For this reason, it is important nowadays to process new compositions avoiding aluminium.

Thus, we decided to use an element close to Al in the periodic table which should exhibit close properties. The choice was the gallium, which exhibit a small atomic radius and a very negative mixing enthalpy with the other constituents.

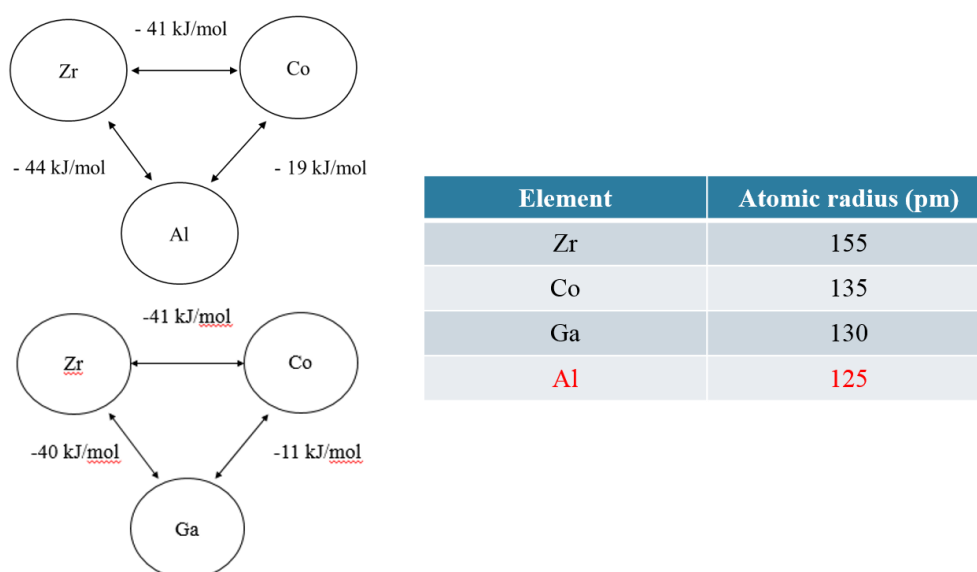


Figure 4-1: Comparison of the properties between Al and Ga based on the data of Takeuchi and Inoue's work<sup>9</sup>

Gallium is often used in semiconductor industry as AsGa or GaN form. However, since 1956, alloys containing gallium were studied in order to replace dental amalgams. This element is also used for medical diagnosis. This is the reason why the gallium could show a good biocompatibility. Despite its very low melting temperature at 29.8°C, its vaporization point is very high at 2024°C, which indicates that no evaporation during arc melting process can happen, and then, no change of composition.

## 4-2- Processing and characterization of a new biocompatible Zr-based composition

This part will be presented under the form of a publication accepted in Journal of Non-Crystalline Solids.

### Article 2: A Ni-, Al-, Be-free Zr-based metallic glass for biomedical applications

Oriane Baulin<sup>1\*</sup>, Damien Fabrègue<sup>1</sup>, Hidemi Kato<sup>2</sup>, Takeshi Wada<sup>2</sup>, Sandra Balvay<sup>3</sup>, Daniel Hartmann<sup>3</sup>, Jean-Marc Pelletier<sup>1</sup>

(Accepted in JNOC, June 2018)

## 4-3- From the ribbons to the bulk samples: Experimental Design

### 4-3-1- Increase of the glass forming ability and critical diameter

As the purpose is to increase the critical diameter of the sample in order to obtain bulk samples, the atomic disorder should be increased. This last feature is helpful to increase the compactness of the liquid phase and then stabilize the system against the crystallization. First, one of the solutions is to add very small or very large biocompatible atoms. The second possibility is to create substitutions between different atoms with close atomic radius. Thus, the second possibility was the easiest way to be implemented in this work and titanium atoms have been chosen to be added in the system and create a potential substitution between Ti and Zr atoms. This mechanism should increase the disorder and delays the crystallization. Taking a look to the different phase diagrams, two compositions seem to be interesting because they exhibit a low temperature eutectic: one in the Ti-rich part and the other one, in the Zr-rich part of the diagram. Moreover, the GFA of this kind of alloy seems to be mostly ruled by the Zr/Ti or Ti/Zr ratio, which is an easy lever to adjust.

Because the system is not well known and contains four different elements, it becomes complicated to study. In order to investigate the influence of each element to find the best glass former, an experimental design has been established, testing different compositions with these four elements to obtain the real influence of each and define the compositions with the best chance to form a fully amorphous sample.

### 4-3-2- Experimental Design

First of all, the ratio Zr/Ti or Ti/Zr, which seems to rule the glass forming ability according to the literature <sup>10,11</sup>, was investigated to find the optimum one. To answer this question, the first compositions to be tested were  $Zr_{56+y-x}Ti_xCo_{28-y}Ga_{16}$  with  $x=0, 5, 10$  and  $46$  and  $y=-5, 0, 5, 10$ , which gives the following processed compositions, presented in Table 1:

Table 1: Presentation of the different compositions of the Zr-Co-Ga-Ti system, according to the experimental design  $Zr_{56+y-x}Ti_xCo_{28-y}Ga_{16}$ 

<b>x</b>	<b>y</b>	<b>Compositions</b>
0	0	$Zr_{56}Co_{28}Ga_{16}$
10	0	$Zr_{46}Co_{28}Ga_{16}Ti_{10}$
10	5	$Zr_{51}Co_{28}Ga_{16}Ti_5$
10	10	$Zr_{51}Co_{23}Ga_{16}Ti_{10}$
5	0	$Zr_{56}Co_{18}Ga_{16}Ti_{10}$
5	5	$Zr_{56}Co_{23}Ga_{16}Ti_5$
5	-5	$Zr_{46}Co_{33}Ga_{16}Ti_5$
5	10	$Zr_{61}Co_{18}Ga_{16}Ti_5$
5	5	$Zr_{56}Co_{23}Ga_{16}Ti_5$
46	0	$Zr_{10}Co_{28}Ga_{16}Ti_{46}$

The processing of 2 millimetres rods has been done using suction casting under argon and Zr-gettered atmosphere; this size is the minimum diameter of the available moulds.

Then, after determining the best ratio Zr/Ti or Ti/Zr, the influence of cobalt or gallium amount has been investigated using these two kinds of composition: firstly,  $(Ti_{82}Zr_{18})_{56+x+y}Co_{28-x}Ga_{16-y}$  with  $x=10$  and  $y=7$ ,  $x=10$  and  $y=0$ . It is worth noting that a trial has been done with  $x=0$  and  $y=7$ , but this it was not injectable in the mould because of its too high viscosity. Then the second kind of composition is  $(Zr_{55}Ti_{12}Co_{33})_{84+x}Ga_{16-x}$  with  $x=5, 8$  and  $11$ . All the compositions are summarized in Table 2:

Table 2: all the compositions of the three experimental design

<b>x</b>	<b>y</b>	<b>Compositions</b>	<b>Experimental Design</b>
0	0	$Zr_{56}Co_{28}Ga_{16}$	$Zr_{56+y-x}Ti_xCo_{28-y}Ga_{16}$
10	0	$Zr_{46}Co_{28}Ga_{16}Ti_{10}$	
10	5	$Zr_{51}Co_{28}Ga_{16}Ti_5$	
10	10	$Zr_{51}Co_{23}Ga_{16}Ti_{10}$	
5	0	$Zr_{56}Co_{18}Ga_{16}Ti_{10}$	
5	5	$Zr_{56}Co_{23}Ga_{16}Ti_5$	
5	-5	$Zr_{46}Co_{33}Ga_{16}Ti_5$	
5	10	$Zr_{61}Co_{18}Ga_{16}Ti_5$	
46	0	$Zr_{10}Co_{28}Ga_{16}Ti_{46}$	
10	7	$(Ti_{82}Zr_{18})_{73}Co_{18}Ga_9$	
10	0	$(Ti_{82}Zr_{18})_{66}Co_{18}Ga_{16}$	
5	/	$(Zr_{55}Ti_{12}Co_{33})_{89}Ga_{11}$	
8	/	$(Zr_{55}Ti_{12}Co_{33})_{92}Ga_8$	$(Zr_{55}Ti_{12}Co_{33})_{84+x}Ga_{16-x}$
11	/	$(Zr_{55}Ti_{12}Co_{33})_{95}Ga_5$	

To compare the different compositions and effects, and because the samples are not fully amorphous, the conventional GFA criteria are not relevant in this part. Thus, we need to implement an objective criterion. We chose to evaluate the GFA with the size of the

amorphous area after casting, before crystallites appear in the bulk. Figure 4-2 shows the micrograph obtained with the boundary between the crystalline area and the amorphous area. After processing and polishing the sample, the amorphous area length is measured and the data is compared for all the compositions.

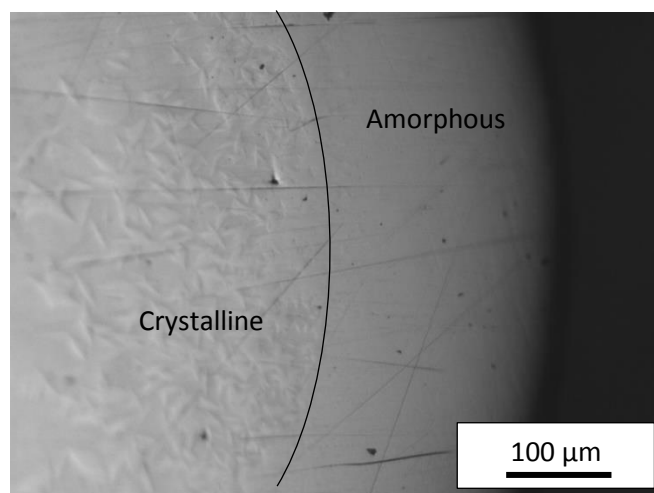


Figure 4-2: Micrograph of the samples with the border line between the amorphous area and the crystalline area

In addition to this criterion, XRD measurements have been conducted. The diffractograms for all these compositions have been performed and compared in order to determine if a composition change produces a more amorphous sample, or if the full width at half maximum is higher, permitting thus, to evaluate the crystallites size.

### 4-3-3- Results and Discussion

In this part, all the results of this analysis are presented based on two types of representations: the coloured maps to show the size of the amorphous area depending on the amount of the studied element and also the data based on XRD diffractograms (intensity of the peaks, beginning of amorphous hump..) to compare the amorphous character.

In the first analysis, the purpose is to find the optimal Zr/Ti ratio in order to vary element by element in a second step. This experimental design concerns compositions, given in the table below.

Several Ti/Zr or Zr/Ti ratio have been tested and the variation of cobalt has also been investigated. The only parameter in this part which is not tested is the amount of gallium, which is constant equal to 16.

Table 3: Composition of the first experimental design

$x$ (at.%)	$y$ (at.%)	Compositions	Experimental Design
0	0	$Zr_{56}Co_{28}Ga_{16}$	$Zr_{56+y-x}Ti_xCo_{28-y}Ga_{16}$
10	0	$Zr_{46}Co_{28}Ga_{16}Ti_{10}$	
10	5	$Zr_{51}Co_{28}Ga_{16}Ti_5$	
10	10	$Zr_{51}Co_{23}Ga_{16}Ti_{10}$	
5	0	$Zr_{56}Co_{18}Ga_{16}Ti_{10}$	
5	5	$Zr_{56}Co_{23}Ga_{16}Ti_5$	
5	-5	$Zr_{46}Co_{33}Ga_{16}Ti_5$	
5	10	$Zr_{61}Co_{18}Ga_{16}Ti_5$	
5	5	$Zr_{56}Co_{23}Ga_{16}Ti_5$	
46	0	$Zr_{10}Co_{28}Ga_{16}Ti_{46}$	

As first observation during processing, elaboration of an amorphous alloy in the Ti-rich part (the sample with  $x = 46$ ) seems to be easier for this system than a Zr-rich glass. It seems to be due to a lower viscosity for a Ti-rich alloy compared to the Zr-rich. The suction casting and the cooling are thus, easier and more homogeneous. The results, based on the XRD diffractograms are shown in the Figure 4-3. It shows the intensity of the crystalline peaks and the potential presence of an amorphous hump.

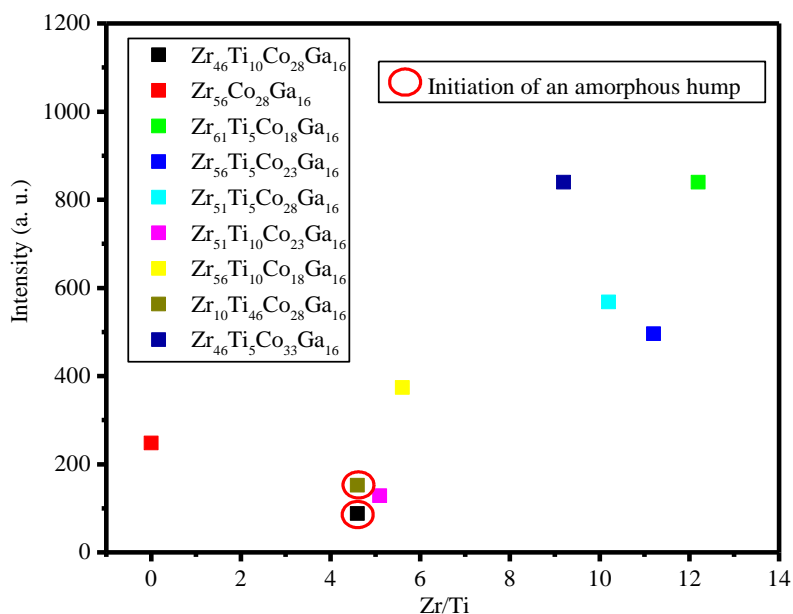


Figure 4-3: Intensity of the crystalline peak appearing on the XRD diffractogram for the different Zr/Ti ratio of the experimental design:  $Zr_{56+y-x}Ti_xCo_{28-y}Ga_{16}$  with  $x=0, 5, 10$  and  $46$  and  $y=-5, 0, 5, 10$ .

Using Figure 4-3 the best glass formers (i.e. smallest intensity and potential beginning of an amorphous hump) seem to be  $Zr_{46}Ti_{10}Co_{28}Ga_{16}$ ,  $Zr_{51}Ti_{10}Co_{23}Ga_{16}$  or  $Zr_{10}Ti_{46}Co_{28}Ga_{16}$ , exhibiting a Zr/Ti or Ti/Zr ratio of 4.6, 5.1 and 4.6 respectively. In opposite, the worst are  $Zr_{46}Ti_5Co_{33}Ga_{16}$ ,  $Zr_{61}Ti_5Co_{18}Ga_{16}$  or  $Zr_{51}Ti_5Co_{28}Ga_{16}$ , which show a Zr/Ti ratio equal to 9.2, 12.2 and 10.2 respectively. According to these results, it seems that there is an optimal ratio

between Zr and Ti which increases the glass forming ability. In this study it is about 4.6, possibly less. If the Zr/Ti or Ti/Zr ratio is too high compared to this value, the alloy is mostly crystalline.

Moreover, it is difficult to conclude on the cobalt amount influence, as it seems to be linked to another element. Indeed, for the three worst compositions, the amount of cobalt is very different. The range of cobalt amount to add seems to be small.

Figure 4-4 shows the size of the amorphous area depending on  $x$ , amount of Ti and  $y$ , amount of Co. The evolution of the parameter has been approximated to be linear in the upper limit of the graph.

From the results of the Figure 4-4, a Ti-based system seems to exhibit a higher GFA. It also appears that addition of cobalt ( $y$ ) is beneficial for Ti-rich system. Indeed, the amorphous area size seems to increase with  $y$ , when the main element of the system is Ti. However, in the Zr-rich part of the map, a too high cobalt amount as well as a too small ( $y$ ) seems to be detrimental.

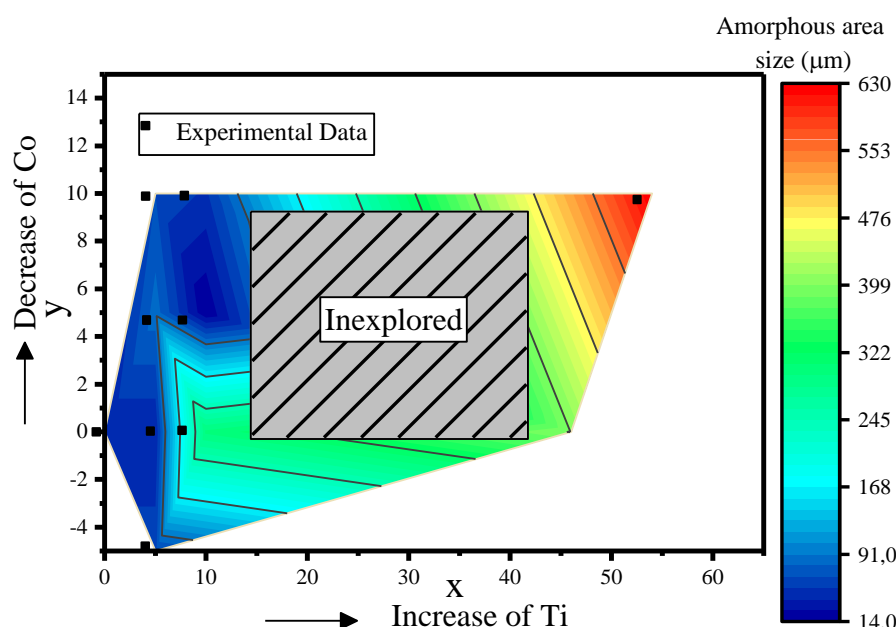


Figure 4-4: Coloured map of the  $Zr_{56+y-x}Ti_xCo_{28-y}Ga_{16}$  experimental design summarizing the evolution of the size of the amorphous area with  $x$ , the Ti content and  $y$ , the cobalt content.

The first results on the map in the Figure 4-4 and the intensity of the XRD diffractogram, allow us to determine the best Ti/Zr or Zr/Ti ratio to obtain a bulk samples. The influence of cobalt composition has also been highlighted. It exhibits an asymmetric behaviour between a Zr-rich and a Ti-rich part of the composition. The range of cobalt amount to add in Zr-rich part seems to be small as the increase of Co is beneficial for Ti-rich part.

Now the other two experimental designs were investigated in the same way, separating the two types of alloys: Zr-rich and Ti-rich, so  $(Zr_{55}Ti_{12}Co_{33})_{84+x}Ga_{16-x}$  with  $x=0, 5, 11$  and  $(Ti_{82}Zr_{18})_{56+x+y}Co_{28-x}Ga_{16-y}$ , with the compositions,  $x=10$  and  $y=7$ ,  $x=10$  and  $y=0$ . The purpose is to get more information about the influence of Co or Ga in the two kinds of systems.

- **$(\text{Ti}_{82}\text{Zr}_{18})_{56+x+y}\text{Co}_{28-x}\text{Ga}_{16-y}$  with  $x=10$  et  $y=0$  ;  $x=10$  et  $y=7$  ;**

According to Figure 4-5, which shows the amorphous area size depending on the Co and Ga content, the effect of a too high cobalt content leads to a highly viscous alloy which is not processable. However, a high content of Co, coupled to a large decrease of Ga could be beneficial. There is a compromise to find in the amount of Co and the amount of Ga. Reducing the gallium seems to conduct to a higher size of the amorphous area, which is very interesting for the processing of bulk samples.

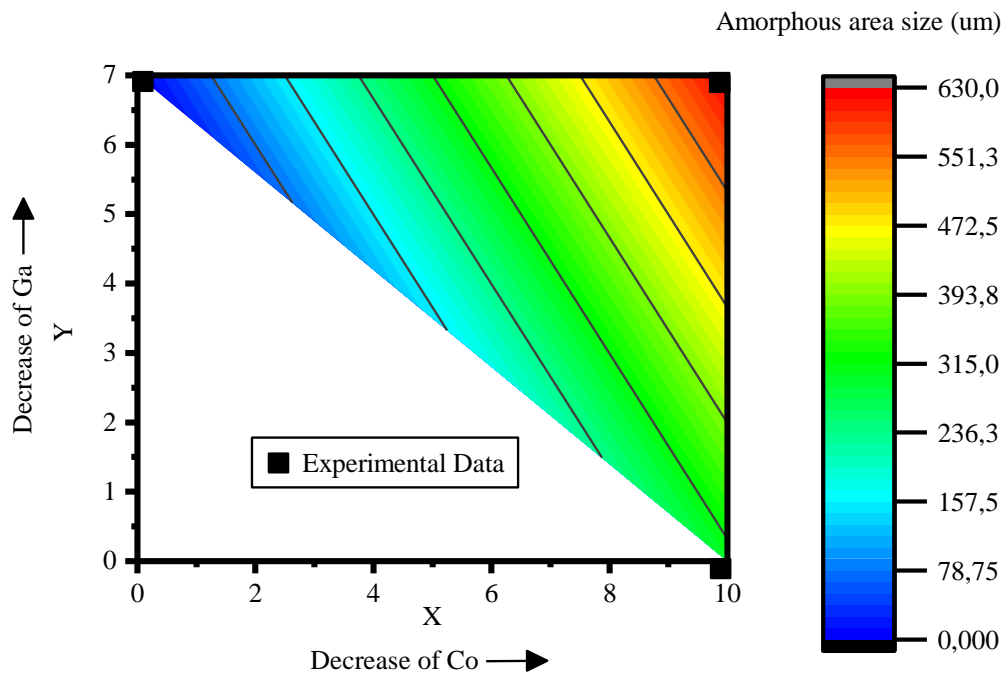


Figure 4-5: Coloured map of the  $(\text{Ti}_{82}\text{Zr}_{18})_{56+x+y}\text{Co}_{28-x}\text{Ga}_{16-y}$  experimental design summarizing the size of the amorphous areas

- **$(\text{Zr}_{55}\text{Ti}_{12}\text{Co}_{33})_{84+x}\text{Ga}_{16-x}$  with  $x=5, 8, 11$**

Using the previous results, cobalt amount was fixed. According to the results presented in Figure 4-6 in the Zr-based system, the same conclusion is also possible: the alloy has a better potential to be amorphous if the gallium content is decreased, especially if the cobalt amount is high.

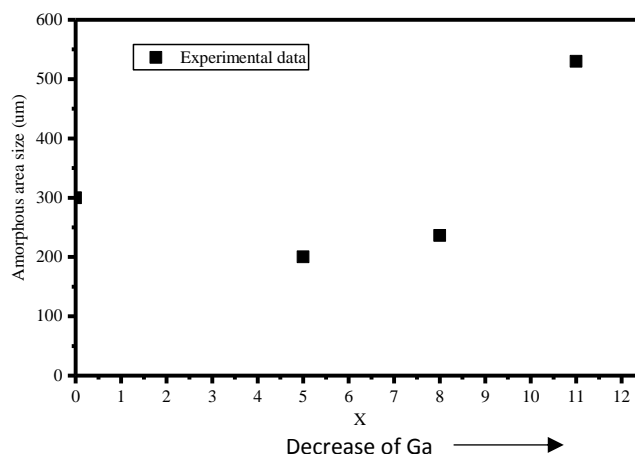


Figure 4-6: Representation of the  $(\text{Zr}_{55}\text{Ti}_{12}\text{Co}_{33})_{84+x}\text{Ga}_{16-x}$  experimental design

In Figure 4-7, data based on the XRD diffractograms are presented. Some of them exhibit an initiation of an amorphous hump, which is marked with the red circles.

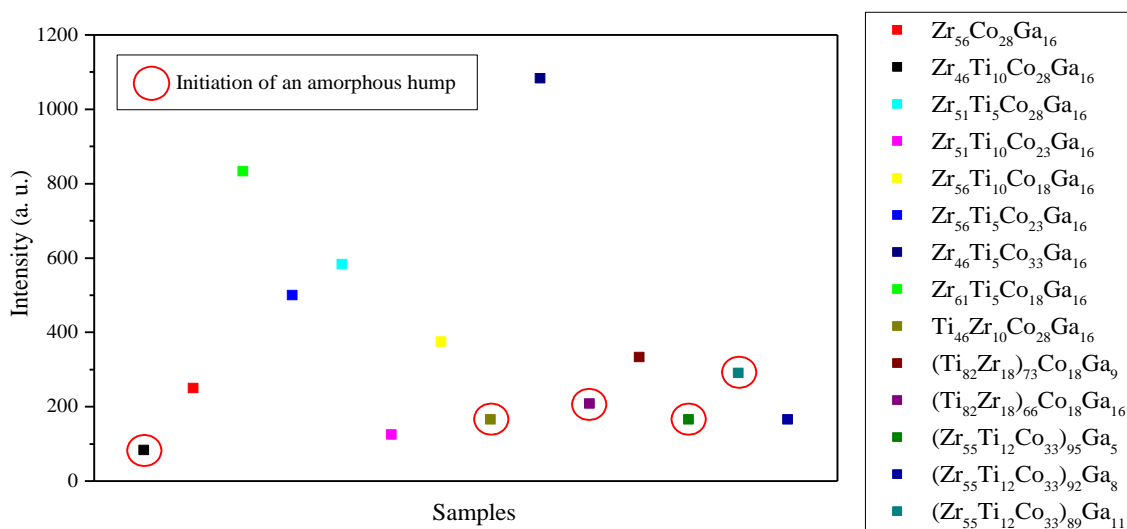


Figure 4-7: XRD diffractograms data of all the processed samples of the experimental design

It appears that several parameters should be taken into account to obtain a bulk metallic glass sample with this system: (i) The first one is to have a ratio between Zr and Ti of 4.6 maximum (ii) then the second one is to reduce Ga if the Co is high. The three following compositions:  $\text{Zr}_{46}\text{Ti}_{10}\text{Co}_{28}\text{Ga}_{16}$ ,  $\text{Zr}_{10}\text{Ti}_{46}\text{Co}_{28}\text{Ga}_{16}$  and  $(\text{Zr}_{55}\text{Ti}_{12}\text{Co}_{33})_{95}\text{Ga}_5$  are mostly amorphous. The worst compositions are  $\text{Zr}_{61}\text{Ti}_5\text{Co}_{18}\text{Ga}_{16}$  and  $\text{Zr}_{46}\text{Ti}_5\text{Co}_{33}\text{Ga}_{16}$ .

## 4-4- Further investigations about promising non-fully amorphous samples

In this part, even if no fully amorphous bulk samples have been processed yet, the most promising samples have been studied to obtain information about their mechanical behaviour. In the second part, the crystalline phase has been analysed to find the reason of the bulk processing difficulties. Lastly, the applications of this system at this stage are discussed.

### 4-4-1- Mechanical properties

Nowadays, no bulk samples have been processed. However, even if the samples are not fully amorphous, the purpose is to obtain good materials for a biomedical use, so compressive tests have been carried out, in order to get information on the mechanical behaviour of these materials, especially the yield strength and the plasticity. Figure 4-8 shows the stress-strain curves of compressive tests for the four best samples, two Ti-based and two Zr-based.

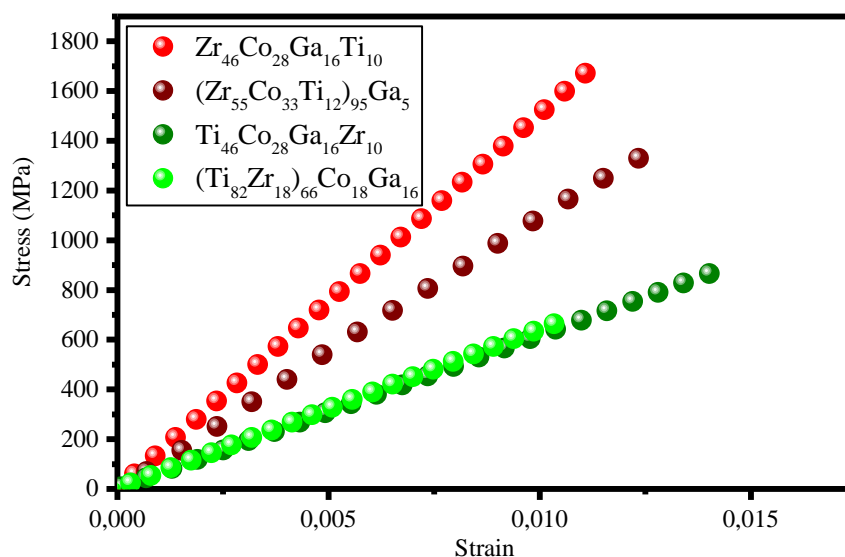


Figure 4-8: Stress-strain curves of the compressive tests of the non-fully amorphous samples

The two Zr-based alloys exhibit very high fracture strength (about 1700 MPa for  $Zr_{46}Ti_{10}Co_{28}Ga_{16}$ ) compared to Ti-6Al-4V (about 1000 MPa), which constitutes a clear advantage but they don't exhibit any ductility. The fracture strength of the Ti-based alloys is lower. Thus, the presence of the crystalline phase is detrimental to the ductility of samples, and should be avoided.

### 4-4-2- Investigation about the crystalline phase

In order to understand the potential causes of the crystalline phase presence, DSC experiments were conducted to measure the melting temperature. The results are shown in Figure 4-9.

The melting temperature decreases as titanium content increases. However, the temperature is still low compared to the temperature reached with arc melting, so there should be no difficulty to reach the melting temperature.

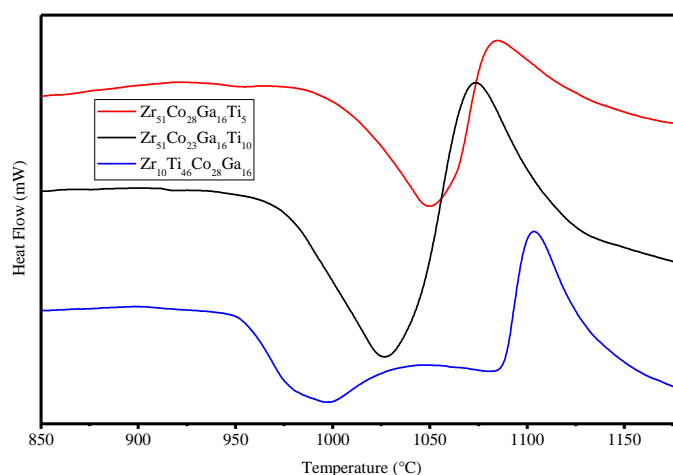


Figure 4-9: DSC curves of the three samples to evaluate the melting temperatures

The temperatures have been measured for different samples and summarized in Table 4.

Table 4: Summarizing of the melting temperature of the three samples

<b>Alloys</b>	<b>Melting Temperatures (°C)</b>
$Zr_{51}Co_{28}Ga_{16}Ti_5$	1106
$Zr_{51}Co_{23}Ga_{16}Ti_{10}$	972
$Zr_{10}Ti_{46}Co_{28}Ga_{16}$	954

The issue of the glass forming ability should come from the lack of another element with a real difference in the atomic mismatch or a remarkable viscosity.

Indeed, during the process, some of the alloys seemed to be very viscous and difficult to introduce into the mould with suction casting increasing the risk to obtain a crystallized alloy.

Because these quaternary alloys are not well-known systems, crystallized phases present have to be studied in order to get information which allows to avoid it during the process. Crystallized dendrites were then analysed using SEM and EDX analysis (Figure 4-10).

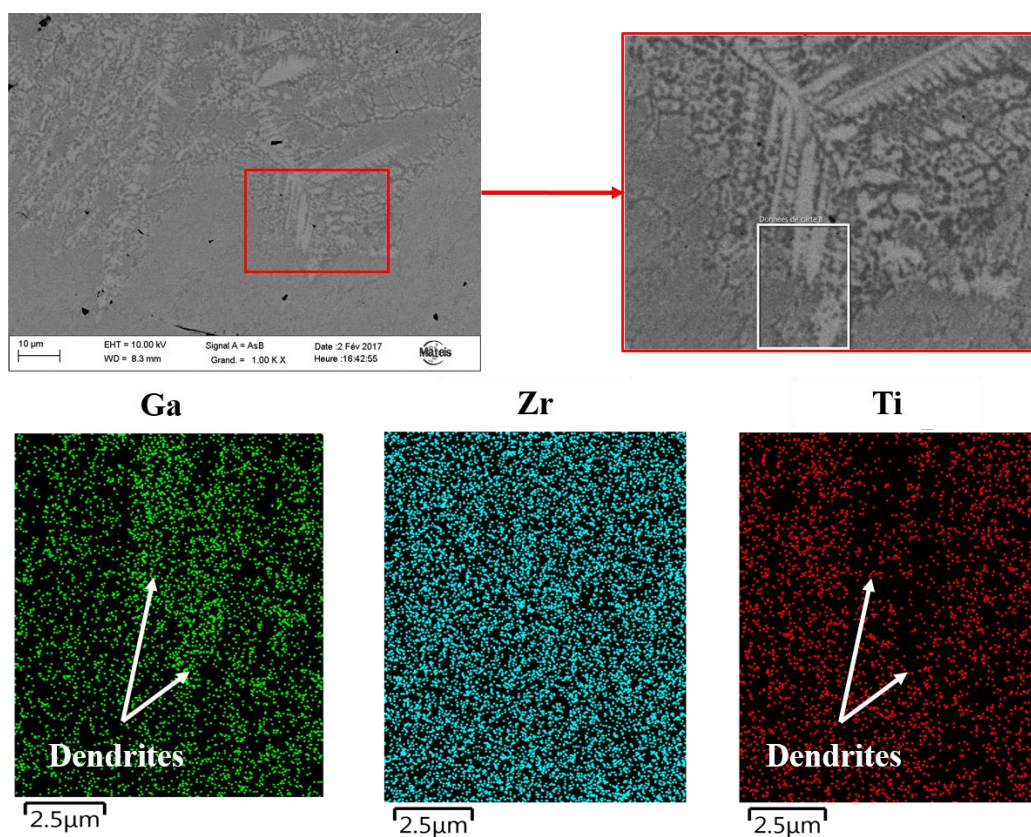


Figure 4-10: SEM micrographs and EDX analysis of the dendritic phase

The matrix seems to be homogeneous without any piece of pure Ga or oxide compounds. The dendrites analysis lead to the conclusion that the crystallized phase is Ga-rich and contains Zr. The concentration of Co is lower than in the amorphous matrix.

In order to increase the GFA of this system, additions of other element should be tried or maybe decrease the Ga content and step by step, replace aluminium. The atomic radius difference seems to be a little bit too low between the different elements. Using a big atom like yttrium which reacts very easily with oxygen contained in the Zr, and prevent the  $ZrO_2$  and  $TiO_2$  formation, could be a very interesting point (cf Chapter 5). Moreover, yttrium exhibits a high atomic radius of 180 pm compared to Ti (140 pm), Zr (155 pm), and Co (135 pm).

#### 4-4-2- Potential applications

Because no bulk sample was successfully processed at this stage, the newly developed metallic glass in this part could be used only as coating, for now. Another possible application to obtain bulk samples from this system is to use powder metallurgy and Spark Plasma Sintering (SPS) process. In that case, an amorphous powder can be obtained due to very high cooling rate during atomization. Then, rapid sintering should be possible as the  $T_g$  temperature of this system is very high. Then with a proper temperature and applied pressure, it is possible to process the densification to obtain centimetre bulk samples (see Chapter 6). Moreover, a control of the remaining porosity could be promising for future for biomedical applications.

## 4-5- Conclusions

In this chapter, a new Zr-based biocompatible metallic glass has been successfully processed under ribbons form. The Al was successfully replaced by Ga. The GFA is low except with 2 at. % of Sn in the system, composition for which the GFA became higher. Because of the Zr-based nature of the material, it exhibits also good mechanical properties. Sn and Si small additions are also very helpful to enhance the corrosion resistance, the thermal stability and above all, the biocompatibility.

Adding Ti in the system to substitute to the Zr atoms, an experimental design has been conducted in order to understand the different action of each element in the system and increase the chance to get as close as possible to the optimum composition to process a fully amorphous bulk sample. Then a characterization of the crystalline phase was conducted to understand the difficulties of forming a bulk metallic glass sample. However, no clear reason has been found yet to explain the small GFA. Adding a high atomic radius element could be a good solution to increase the disorder in the system. Yttrium is high atomic radius size, in addition to be an oxygen pump to prevent from forming oxides, which could be detrimental to the GFA. This point will be investigated in the next chapter.

However, even for now, a new biocompatible composition has been elaborated, with low Young modulus and no harmful elements. Moreover, the high  $T_g$  opens large perspectives in processing by sintering.

## 4-6- References

1. Wang, W.-H. & Bai, H. Y. Role of small atoms in the formation and properties of Zr–Ti–Cu–Ni–Be bulk amorphous alloys. *Journal of Applied Physics* **84**, 5961–5968 (1998).
2. Kim, C. P., Suh, J. Y., Wiest, A. *et al.* Fracture toughness study of new Zr-based Be-bearing bulk metallic glasses. *Scripta Materialia* **60**, 80–83 (2009).
3. Yokoyama, Y., Fukaura, K. & Inoue, A. Effect of Ni Addition on Fatigue Properties of Bulk Glassy  $Zr_{50}Cu_{40}Al_{10}$  Alloys. *Materials Transactions* **45**, 1672–1678 (2004).
4. Zhao, S. F., Gong, P., Li, J. F., Chen, N. & Yao, K. F. Quaternary Ti–Zr–Be–Ni bulk metallic glasses with large glass-forming ability. *Materials & Design* **85**, 564–573 (2015).
5. Wang, S., Wang, Y., Wu, Y., Wang, T. & Hui, X. High plastic Zr–Cu–Fe–Al–Nb bulk metallic glasses for biomedical applications. *International Journal of Minerals, Metallurgy, and Materials* **22**, 648–653 (2015).
6. Wada, T., Qin, F., Wang, X. *et al.* Formation and bioactivation of Zr–Al–Co bulk metallic glasses. *Journal of Materials Research* **24**, 2941–2948 (2009).
7. Reis, A. P., Patinha, C., Noack, Y., Robert, S. & Dias, A. C. Assessing human exposure to aluminium, chromium and vanadium through outdoor dust ingestion in the Bassin Minier de Provence, France. *Environmental Geochemistry and Health* **36**, 303–317 (2014).

8. Kawahara, M. & Kato-Negishi, M. Link between Aluminum and the Pathogenesis of Alzheimer's Disease: The Integration of the Aluminum and Amyloid Cascade Hypotheses. *International Journal of Alzheimer's Disease* (2011).
9. Takeuchi, A. & Inoue, A. Classification of bulk metallic glasses by atomic size difference, heat of mixing and period of constituent elements and its application to characterization of the main alloying element. *Materials Transactions* **46**, 2817–2829 (2005).
10. Wang, L., Ma, L. & Inoue, A. Formation and Mechanical Properties of Ti–Zr–Ni–Cu Amorphous Alloy Containing Icosahedral Nanoscale Quasicrystalline Phase. *Materials Transactions* **43**, 2346–2349 (2002).
11. Wang, Y. L. & Xu, J. Ti (Zr)-Cu-Ni bulk metallic glasses with optimal glass-forming ability and their compressive properties. *Metallurgical and Materials Transactions A: Physical Metallurgy and Materials Science* **39**, 2990–2997 (2008).

# Chapter 5

## Suggested improvement of size effect and lack of ductility on a well-known system for biomedical use

---

<b>SUGGESTED IMPROVEMENT OF THE CRITICAL DIAMETER AND OF THE LACK OF DUCTILITY ON A WELL-KNOWN CAST SYSTEM FOR BIOMEDICAL USE .....</b>	<b>124</b>
<b>5-1- Role of Yttrium addition on the Cu-Zr-Ti system.....</b>	<b>124</b>
<b>5-2- Corrosion resistance in RPMI medium.....</b>	<b>145</b>
<b>5-3- Structural investigations into the Y<sub>2</sub>O<sub>3</sub> precipitates.....</b>	<b>147</b>
<b>5-3-1- Experimental methods .....</b>	<b>147</b>
<b>5-3-2- Structural and chemical analysis of the precipitates surroundings .....</b>	<b>148</b>
<b>5-3-3- 3D distribution of the precipitates and crystallized phases in the volume .....</b>	<b>149</b>
<b>5-3-4- Discussion about hollow Y<sub>2</sub>O<sub>3</sub> precipitate formation.....</b>	<b>152</b>
5-3-4-1- Formation of the precipitate and the crystallised areas	152
5-3-4-2- Determination of the second phase inside the precipitate	153
5-3-4-2- Hypothesis of Kirkendall effect	154
<b>5-4- Conclusion.....</b>	<b>154</b>
<b>5-5- References .....</b>	<b>158</b>

---

## Chapter V

# Suggested improvement of the critical diameter and of the lack of ductility on a well-known cast system for biomedical use

In the previous chapters, two new biocompatible compositions have been processed: Zr-based and Mg-based. However, besides the biocompatibility challenge, we have faced two main issues concerning the metallic glasses for biomedical use: the critical size effect and the lack of ductility. These two points could be very critical and should be improved. Therefore the next two chapters discuss remedial actions in order to prevent these two detrimental problems from occurring. Two main actions will be investigated on a well-known Ni-free, Al-free, Cu-Zr-Ti system: the first action on the cast system using Yttrium addition to increase the GFA and the ductility, developed in this chapter 5 and the other one, based on the modification of the process to elaborate bigger samples using Spark Plasma Sintering (SPS) technique, discussed in chapter 6. The advantage of this last technique is the possibility to process composite samples, which is very interesting in the biomedical field.

### 5-1- Improvement of mechanical, thermal, and corrosion properties of Ni- and Al-free Cu–Zr–Ti metallic glass with yttrium addition

This part is presented under the form of an article accepted in Materialia in June 2018.

### Article 3: Improvement of mechanical, thermal, and corrosion properties of Ni- and Al-free Cu–Zr–Ti metallic glass with yttrium addition

Oriane Baulin<sup>1\*</sup>, Matthieu Bugnet<sup>1</sup>, Damien Fabrègue<sup>1</sup>, Alexis Lenain<sup>2,3</sup>, Sébastien Gravier<sup>2,3</sup>, Sophie Cazottes<sup>1</sup>, Georges Kapelski<sup>2</sup>, Benoit Ter-Ovanessian<sup>1</sup>, Sandra Balvay<sup>1</sup>, Daniel J. Hartmann<sup>1</sup>, Jean-Marc Pelletier<sup>1</sup>

<sup>1</sup> Université de Lyon, INSA-Lyon, Université Claude Bernard Lyon 1, CNRS, Laboratoire MATEIS, 7 avenue Jean Capelle, 69621 Villeurbanne Cedex, France

<sup>2</sup> Science et Ingénierie des Matériaux et Procédés, Univ. Grenoble Alpes CNRS/Grenoble INP, 38302 Saint-Martin d'Hères, France

<sup>3</sup> VULKAM SAS, 101 rue de la Physique, 38400 Saint Martin d'Hères, France

\* Corresponding author: oriane.baulin@insa-lyon.fr

**Abstract** The development of biocompatible metallic glasses with enhanced ductility that are free of potentially toxic elements such as aluminium and nickel remains a challenge. Although Cu is associated with cytotoxicity levels above a safe threshold, the mechanical properties of Cu-rich metallic glasses are particularly attractive. Herein, the effect of minor additions of yttrium to the Cu–Zr–Ti system is studied. Rods of composition  $(\text{Cu}_{60}\text{Zr}_{30}\text{Ti}_{10})_{(100-x)}\text{Y}_x$  (with  $x = 0, 1, 2$ ) were prepared, and the critical diameter was improved from 2 to 3.5 mm with the addition of 1 at.% Y. The compressive fracture strength was greater than 2000 MPa for all of the compositions, and the plastic strain increased from 0.9% to 2% with the addition of 1 at.% Y. Transmission electron microscopy analysis revealed the presence of yttria precipitates surrounded by nanocrystallized areas, suggesting that the precipitates improved the plasticity. The addition of yttrium also led to the formation of a protective layer, which enhanced both the thermal stability and corrosion resistance of the metallic glass. Finally, the biocompatibility improved with minor additions of yttrium. Our findings demonstrate the wide range of beneficial properties of Cu-based metallic glasses, which may open the door for their potential application as biomaterials.

**Keywords** Metallic Glasses,  $\text{Y}_2\text{O}_3$  Precipitates, Yttrium, Mechanical Properties, Biomaterials

#### Introduction

Since the preparation of the first metallic glass in 1960 by Klement et al. [1], a wide variety of bulk metallic glasses (BMGs) have been prepared, including Zr-[2], Ti-[3], Fe-[4], Cu-[5]–[8], Ni-[9], Pt-[10], Pd-[11], Mg-[12], Co-[13], and Ca-based [14] metallic glasses. Metallic glasses exhibit appropriate mechanical properties, such as high fracture strength, hardness, and fracture toughness, for their use in biomedical applications [15]–[17] and are major constituents in dental implants, fixation screws, aneurysm clips, and bioresorbable materials. Their corrosion resistance is also higher than that of their crystalline counterparts because of the absence of microstructure and grain boundaries. In addition, their Young's modulus is

lower than that of crystalline alloys, which helps prevent stress-shielding problems and associated bone resorption [18].

Biocompatible metallic glasses have emerged in the past two decades and can be classified into two categories: biodegradable Mg-, Ca-, Zn-, and Sr-based metallic glasses [19], [20] and biocompatible and more resistant glassy alloys, including Zr-[21], Ti-[22], Cu-, and Pt-based glasses. One of the main drawbacks of metallic glasses is their lack of ductility. The most ductile systems often contain elements that promote plasticity, such as Al [23], [24], Be, or Ni [25]. However, these elements are potentially toxic once released into the human body [23]. Ti-6Al-4V (TA6V) is the conventional alloy used for this type of biomedical application, although it also contains the potentially harmful elements Al and V.

Cu-based metallic glasses possess excellent glass-forming ability, high fracture toughness, and good initial plasticity without the inclusion of additional harmful elements. Although there is general agreement that Cu above a safe threshold is not the best option for biomedical applications [26] [27], its place in the ranking of pure metal cytotoxicity is controversial. Nevertheless, the mechanical properties of Cu-based metallic glasses are exceptional compared with those of fully biocompatible and other brittle glassy alloys. Cu-based alloys, such as Cu-Hf-Ti and Cu-Zr-Ti, have been largely studied [8], [28], [29], and the composition  $\text{Cu}_{60}\text{Zr}_{30}\text{Ti}_{10}$  exhibits the highest glass-forming ability [8]. This system has been intensively studied, especially for use as an active brazing filler metal [30]. The effect of In, Y, Nb, Mo, and Ta as alloying elements on the corrosion resistance has been investigated [31]; however, the biocompatible potential of these elements has not yet been evaluated. Micro alloying with rare-earth elements, including Y and Sc, has been largely investigated in different systems [32]–[34]. For example, Y, Sc, Yb, Gd, and Er have been shown to have beneficial effects on the glass-forming ability, even as minor additions. Among these elements, Y exhibits unique properties such as oxygen scavenging. The oxygen content is critical for manufacturing metallic glasses, and Y removes impurities from the solution to create innocuous oxides, which decrease heterogeneous nucleation. Y also has a large atomic radius; therefore, the atomic mismatch and compact density of the liquid are increased, and the liquid phase is more stable. Finally, the addition of Y decreases the liquidus temperature, causing the composition to move closer to the eutectic composition and thereby facilitating the formation of an amorphous alloy [35].

In this study, the Cu-Ti-Zr-(Y) system was considered, and its biocompatibility was assessed. Compositions  $(\text{Cu}_{60}\text{Zr}_{30}\text{Ti}_{10})_{(100-x)}\text{Y}_x$  (with  $x=0, 1, \text{ and } 2$ ) were prepared, and the glass-forming ability was systematically evaluated. The relevant properties for the application of metallic glasses as biomaterials, including the thermal stability, mechanical properties, corrosion resistance, and cytotoxicity were experimentally investigated.

## 2 Experimental Procedure

### 2.1 Sample preparation

BMGs of composition  $(\text{Cu}_{60}\text{Zr}_{30}\text{Ti}_{10})_{(100-x)}\text{Y}_x$  (with  $x = 0, 1, \text{ and } 2$ ) were prepared from pure Cu (99.9%), Ti (99.9%), Zr (99.9%), and Y (99.99%) powders using arc melting under a Zr-gettered Ar atmosphere. The ingots were melted six times to improve the compositional homogeneity. To evaluate the available critical diameter, conical-shaped samples were prepared from the master alloy. Then, 2-mm-diameter rods were prepared using copper mould suction casting; the laminar liquid flow during suction casting was controlled using the pressure difference between the crucible and mould to avoid Ar trapping within the rods. The

rods were cut into 1-mm-long cylinders for the cytotoxicity tests, X-ray diffraction (XRD) analysis, and differential scanning calorimetry (DSC) measurements and into 3.5-mm-long cylinders for the mechanical tests. Given that the low concentration of yttrium (1 at. %) is close to the detection limit for scanning electron microscopy–energy-dispersive X-ray spectroscopy (SEM–EDX) analysis, the measured chemical compositions were equivalent with and without yttrium. The measured composition (Cu: 61.2%, Zr: 29.1%, Ti: 9.7%) was determined using a ZEISS Supra55 VP SEM equipped with an EDX detector (Oxford Instruments) operated at an acceleration voltage of 10 kV.

## 2.2 Experimental methods

The amorphous character of the bulk sample at room temperature (RT) was evaluated using XRD (D8 Advance, Bruker) with Cu K $\alpha$  radiation. To improve the signal, three 1-mm-thick plates were arranged side by side and placed on a Si support, which gives no parasite X-ray peak. The working conditions were 40 kV and 40 mA for the X-ray tube in the  $2\theta$  range of 30°–50°. The diffraction patterns were analysed using EVA software [36]. The crystallization kinetics were investigated using high-temperature XRD with the same apparatus equipped with a high-temperature furnace under vacuum. The non-isothermal treatment was performed from RT to 540 °C. The process is summarized in Fig. 1. From RT to 400 °C, the heating rate was 20 °C/min; then, the data was collected between 400 °C to 540 °C every 5 °C. Between each measurement, a heating rate of 20 °C/min was applied, leading to an average heating rate of 0.7 °C/min, considering the ramp and XRD measurement duration.

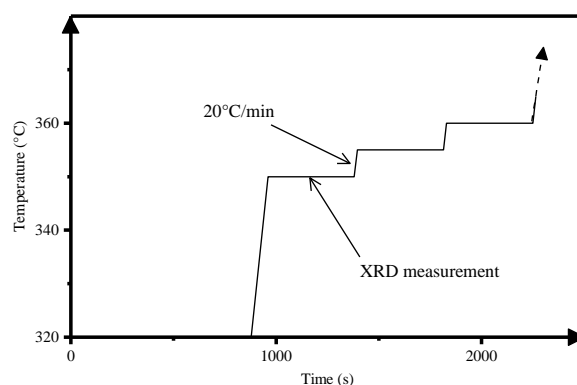


Figure 1: Schematic representation of the non-isothermal treatment during the high-temperature XRD experiments.

The isothermal measurements were conducted at 460 °C, and the spectrum was acquired every 5 min. The characteristic temperatures,  $T_g$  and  $T_x$ , and the width of the supercooled liquid region ( $\Delta T = T_x - T_g$ ) were determined using DSC. A Perkin Elmer DSC 7 apparatus was used under high-purity dry nitrogen at a flow rate of 20 ml/min, with a heating rate of 20 °C/min. The sample was sealed in an aluminium can, and an empty can was used as a reference. The samples considered for this characterization were the same size as those used for the XRD measurements.

To evaluate the mechanical properties of the alloy, the Young's modulus was measured using an ultrasonic technique based on the propagation velocity of the waves. Compressive tests were performed using an INSTRON 5967 apparatus equipped with a video extensometer to precisely determine the deformation. The samples for the compressive tests were 2 mm in

diameter and 3.5 mm long. The initial strain rate applied was  $1.2 \times 10^{-4} \text{ s}^{-1}$ . Nanoindentation tests were performed using a Buehler MicroMet 5104 nanoindenter over the range of 10 g to 1 kg. The high-load hardness was measured using a Future Tech FV-700 device for loads between 1 and 30 kg. The fracture toughness ( $K_{1c}$ ) was evaluated from SEM examination of the fracture topology.

Transmission electron microscopy (TEM) was employed to determine the effect of yttrium on the microstructure and mechanical properties. Scanning TEM–annular dark field (STEM-ADF) imaging, providing a Z-contrast, was performed using a JEOL 2010F (S)TEM operating at an accelerating voltage of 200 kV. Further chemical analyses were performed using electron energy-loss spectroscopy (EELS) and energy-dispersive X-ray spectroscopy (EDX) in a FEI Titan ETEM G2 80-300 operated at 300 kV.

Corrosion tests were performed using a thermostated three-electrode glass cell and a Gamry Reference 600+ potentiostat. The metallic glass studied constituted the working electrode, and a graphite pin and Ag/AgCl saturated electrode were used as the auxiliary and reference electrodes, respectively. The samples were embedded in a heat-shrinkable and adhesive tube before grinding down using 1200 SiC paper. The exposed area was a circular cross section of  $0.0314 \text{ cm}^2$ . Two solutions were used: a classical 0.9 M NaCl saline solution and a solution of 0.9 M NaCl and 4 g/L of bovine serum albumin (BSA >98.5%, fraction V, lyophilized, Sigma Aldrich). All the tests were performed in naturally aerated solutions at 37°C. First, the open-circuit potential (OCP) was measured for 1 h for the samples immersed in NaCl and for 3 h for the that immersed in NaCl with albumin to reach the stationary state of the system. Before the acquisition of the polarization curves, the stabilized values of the potential were  $-0.396 \text{ V}$  without albumin and  $-0.339 \text{ V}$  with albumin. Then, polarization curves were obtained during different ranges of the potential with and without albumin between  $-0.6 \text{ V}$  and  $0.2 \text{ V}$  and between  $-0.6 \text{ V}$  and  $-0.2 \text{ V}$ , respectively. The scan rate was  $1.6 \times 10^{-1} \text{ mV/s}$ . The sample surface was examined after 5 h at OCP using X-ray photoelectron spectroscopy (XPS) analysis. XPS experiments were performed using a PHI Quantera SXM spectrometer (Physical Electronics, Chanhassen, USA) equipped with a  $180^\circ$  hemispherical electron energy analyser and a monochromatized Al  $K\alpha$  X-ray ( $1486.6 \text{ eV}$ ) source operating at 15 kV and 4 mA.

The cytotoxicity tests were conducted with SaOS-2 cultured in 24-well cell culture plates (Corning, NY, USA, ref 3524) with RPMI 1640 medium (Dutscher, France, ref L0498-500) (containing stable L-glutamine and phenol red) supplemented with 10% fetal bovine serum (FBS, Dutscher, ref P040637100) and 5% antibiotic/antimycotic solution (Dutscher, Ref SV30079.01) at 37 °C in a humidified atmosphere of 5%  $\text{CO}_2$ . The samples were approximately 1-mm thick disks. The metallic disks were sterilized by UV irradiation for 20 min. A cellular suspension at 5000 cells was prepared using a cell counter (Millipore Scepter purchased at Dutscher, ref: 053750). The samples were placed in the 24-well cell culture plates (one sample in each well). Then, 50  $\mu\text{L}$  of cellular suspension containing 5000 cells was deposited in each well, and the cell culture plates were incubated for 2 h at 37 °C under a humidified atmosphere of 5%  $\text{CO}_2$  to allow cell adhesion. After the addition of 2 mL of culture medium, the cells were incubated for 22 h. The Prestoblue assay (Invitrogen, Carlsbad, CA, USA) was used to measure the cell viability [37]. The resazurin, which is blue and non-fluorescent, is reduced by the metabolic mitochondrial activity of the cells in resorufin, a pink and fluorescent product, detectable by fluorometry. The cellular proliferation was evaluated after 24 h. The culture medium was discarded and replaced by 1 mL of the culture medium without FBS, antibiotics,

and phenol red but with 10% Prestoblue added to each well. The samples were incubated for 1.5 h at 37°C under a humidified atmosphere of 5% CO<sub>2</sub>. Then, the plate was stirred, and 100 µL of the suspension from each well was transferred to a 96 black-well plate, and the fluorescence was measured using an INFINITE PRO 200 fluorimeter (Tecan) with a wavelength of 535 nm for excitation and 615 nm for emission. After each measurement, the cells were rinsed twice with RPMI; then, 2 mL of medium was added, and the plate was incubated until the next measurement. Each assay was performed in triplicate. For each sample, a plastic control (cell-culture-treated polystyrene) was included to verify the normal behaviour of the cells, and it was referred to as the “plastic control” of 1000 cells per 50 µL. Then, the samples were placed in a stove at 37 °C, and the measurements were performed after 1 day using the Prestoblue assay.

### 3 Results and Discussion

#### 3.1. XRD analysis and glass-forming ability

XRD patterns of the as-prepared metallic glasses are presented in Fig. 2. The broad peak observed for all three compositions, with and without yttrium, is typical of an amorphous structure. The critical diameters ( $D_c$ ) measured from the conical-shaped samples of all the compositions are reported in Fig. 2. Besides for the broad feature centred near 40°, no other peaks were detected, indicating that the three samples were fully amorphous. The addition of 1 at.% Y resulted in an increase of  $D_c$  from 2 to 3.5 mm. Further addition of Y (2 at.%) led to a decrease of  $D_c$ , which was the first indication that 1 at. % appears to be an optimal value.

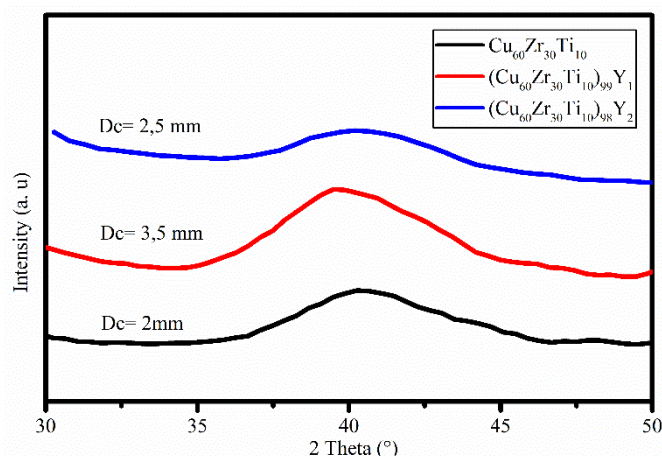


Figure 2: XRD patterns showing the amorphous feature of the prepared BMGs

#### 3.2 Thermal stability and resistance to crystallization

DSC experiments were performed to determine the range of the supercooled liquid region of the BMGs based on the glass transition temperature and crystallization temperature (see Fig. 3a). The DSC experiments were also performed using various heating rates to determine the apparent activation energy for the crystallization process, as shown in Fig. 3b.

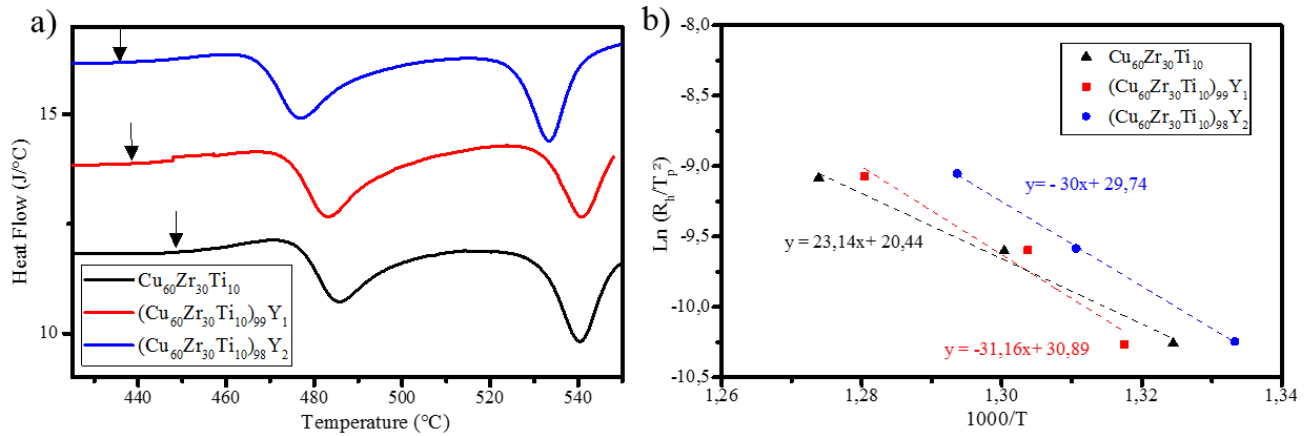


Figure 3: a) DSC patterns of Cu-based BMGs at heating rate of 20 K/min. The glass transition temperatures are indicated by the black arrows. b) Kissinger plots used to obtain the activation energy for the crystallization process.

The crystallization temperatures ( $T_x$ ), glass transition temperatures ( $T_g$ ), and values of  $\Delta T = T_x - T_g$  are summarized in Table 1. The crystallization process occurred in two steps, as shown in Fig. 3a; the crystallized volume fraction was dependent on the temperature.

Table 1: Characteristic parameters of the three compositions of the Cu–Ti–Zr–(Y) system

Samples	$T_g$ (°C)	$T_x$ (°C)	$\Delta T$ (°C)	$E_a$ (eV)
Cu–Zr–Ti	448	475	27	$2.1 \pm 0.2$
Cu–Zr–Ti–1Y	438	472	34	$2.7 \pm 0.6$
Cu–Zr–Ti–2Y	436	466	30	$2.6 \pm 0.1$

These results are consistent with the critical diameter determined from the XRD patterns. The yttrium addition led to a decrease of  $T_g$  and increase of the width of the supercooled liquid region. In the literature, for the Cu–Zr–Ti system, the width of the supercooled liquid region is evaluated to be  $\Delta T = 37$  °C [48] or 36 °C [8] and can reach 55 °C for the same system containing 40 at.% Zr [8].

Using non-isothermal DSC experiments, it was possible to evaluate the activation energy of this system and obtain more information about the effect of yttrium on the resistance to crystallization. Several experiments with different heating rates (20 °C/min, 40 °C/min, and 70 °C/min) are required to use the Kissinger or Flynn–Wall–Ozawa laws [38]–[41]. The plots are presented in Fig. 3b.

The activation energy for the first crystallization peak (in K) was determined using the slope of the curves and Kissinger's equation:

$$\ln \left( \frac{R_h}{T_p^2} \right) = - \frac{E_a}{RT_p} + C \quad (1)$$

where  $R_h$  is the heating rate,  $T_p$  is the temperature of the crystallization peak,  $E_a$  is the activation energy for the primary crystallization,  $R$  is the gas constant, and  $C$  is a constant.

The extracted values for the activation energy for the crystallization of the three compositions are summarized in Table 2. The activation energy of crystallization is a suitable parameter to evaluate the resistance to crystallization, with higher activation energy indicating higher resistance to crystallization [42]. Comparison with other Cu-based alloys, such as  $\text{Cu}_{50}\text{Zr}_{50}$ , which has an activation energy of crystallization ranging between 1 and 2.5 eV, [43] indicates that this Cu-Zr-Ti-(Y) alloy is crystallization resistant. However, taking into account the uncertainties, no real conclusion can be drawn on the influence of the yttrium content, even if it would seem that 1 at. % is the optimal value to improve corrosion resistance.

High-temperature XRD measurements were conducted to obtain information about the time available before crystallization, which is important to conduct the sterilization process. The average heating rate in this experiment and in the DSC analysis were not identical, hence resulting in slightly different  $T_g$  and  $T_x$  results. Therefore, non-isothermal measurements were performed to evaluate the crystallization temperature. The system containing 1 at. % Y had a lower  $T_x$  than that without yttrium ( $T_x = 465^\circ\text{C}$  and  $480^\circ\text{C}$ , respectively). Fig. 4a and 4b present 2D coloured maps of the crystallization for each system, and Fig. 4c shows the evolution of the crystallinity rate for both systems as a function of temperature. Yttrium has been shown to lower  $T_x$  [44], which offers the advantage of a chemical composition closer to the eutectic composition, hence increasing the glass-forming ability (GFA). However, the temperatures are sufficiently high that no modification of the structure may occur during the sterilization process.

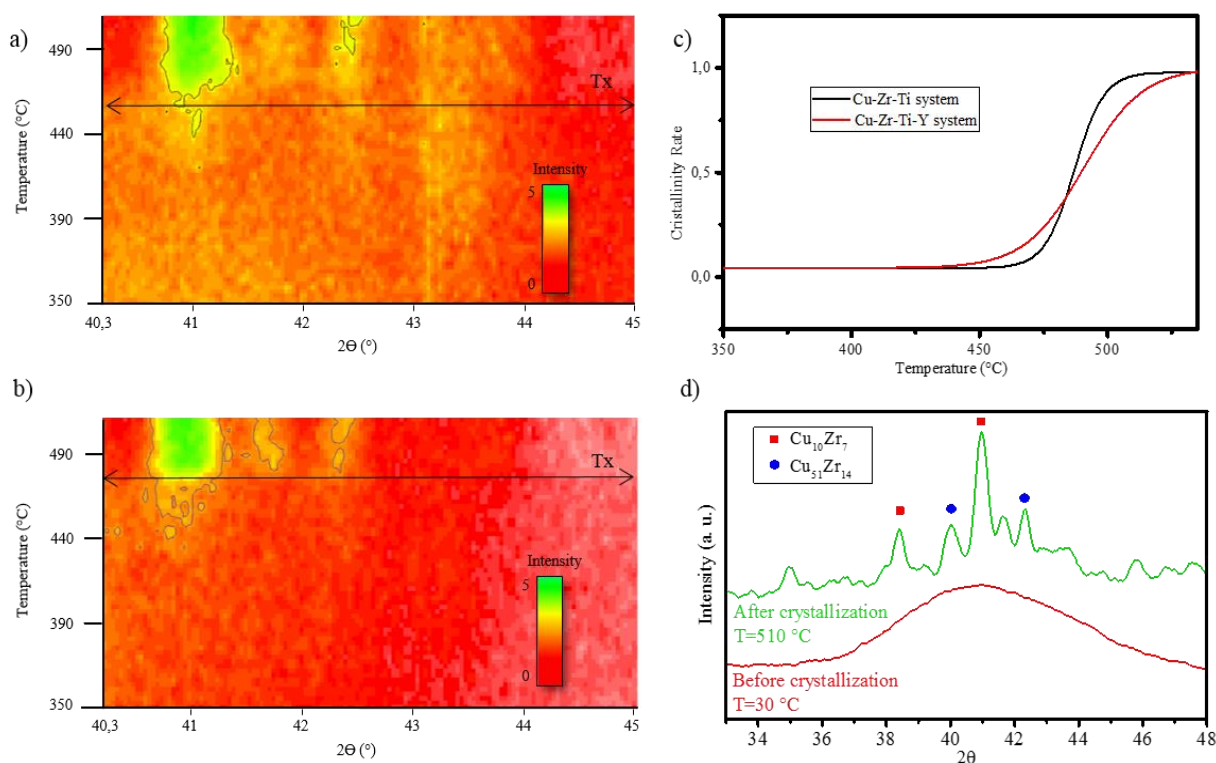


Figure 4: Non-isothermal high-temperature XRD measurement at an average heating rate of  $0.7^\circ\text{C}/\text{min}$  in a) Cu-Zr-Ti-Y system and b) Cu-Zr-Ti system. c) Evolution of the crystallinity rate of both systems during high-temperature XRD experiments. d) Initial and final XRD patterns for Cu-Zr-Ti system.

As shown in Fig. 4a and 4b, the crystallization temperature was lower for Cu–Zr–Ti–Y (465 °C) than for Cu–Zr–Ti (480 °C). However, the evolution of the crystallinity rate of both systems (Fig. 4c) indicates a slower crystallization for the sample containing yttrium. The Y addition appears to retard the crystallization and increase the crystallization resistance of the sample.

Isothermal tests were conducted at 460 °C, and the results are presented in Fig. 5. For both systems, the crystallization started at the same time, ~150 min. The main peak (40.8°) is less intense and larger for the Cu–Zr–Ti–Y system, which is confirmed in Fig. 5c, which shows the evolution of the full width at half maximum of the peak.

The size of the crystallites was calculated using the Scherrer equation (Eq. 2) [45]:

$$L = \frac{K\lambda}{\beta \cos\left(\frac{2\theta}{2}\right)} \quad (2)$$

where K is equal to 0.9,  $\lambda$  is the wavelength,  $\theta$  is the Bragg angle, and  $\beta$  is the full width at half maximum of the diffraction peak.

The crystallite size was smaller with the Y addition than without Y (4 and 10 nm, respectively), confirming the conclusions drawn from XRD regarding the crystallization delay when Y is present.

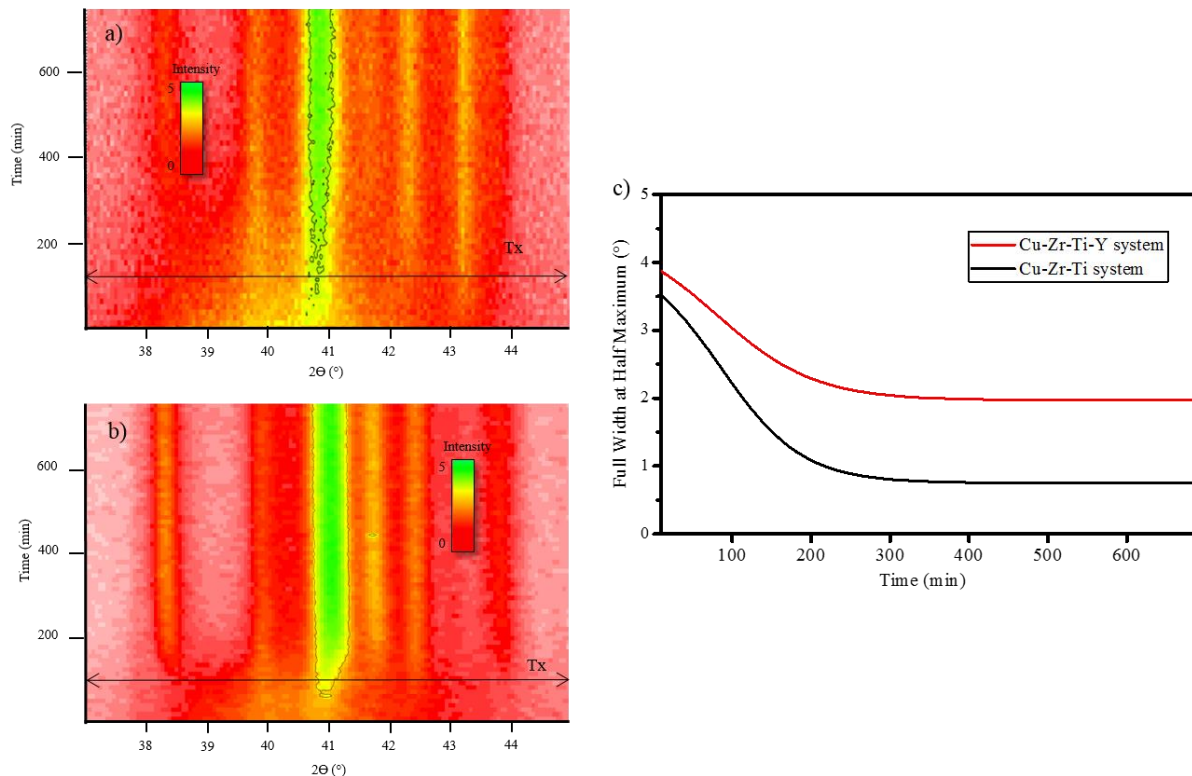


Figure 5: Isothermal high-temperature XRD measurements conducted at 460 °C for a) Cu–Zr–Ti–Y and b) Cu–Zr–Ti. c) Evolution of the full width at half maximum as a function of time for the two systems.

### 3.3 Effect of yttrium on plasticity

Fig. 6 a) presents compressive stress–strain curves for the Cu–Zr–Ti–Y system containing 0, 1, and 2 at. % Y. Each composition was tested three times, and the same

conclusions can be drawn. The fracture strength of all three compositions was over 2000 MPa. Compared with conventional Ti-based alloys used as biomaterials, such as Ti–6Al–4V, which exhibits a fracture strength of approximately 1000 MPa, these metallic glasses exhibit very promising mechanical behaviour. The plastic strain of the alloy containing 1 at. % Y was approximately 2%, which is quite remarkable for a metallic glass without Ni or Al. The gain in yield strength makes this glass much more promising than Ti–6Al–4V in terms of mechanical properties for biomedical applications. With the addition of 2 at. % Y, the fracture strength increased to the detriment of the plastic strain, which is less attractive for biomaterials.

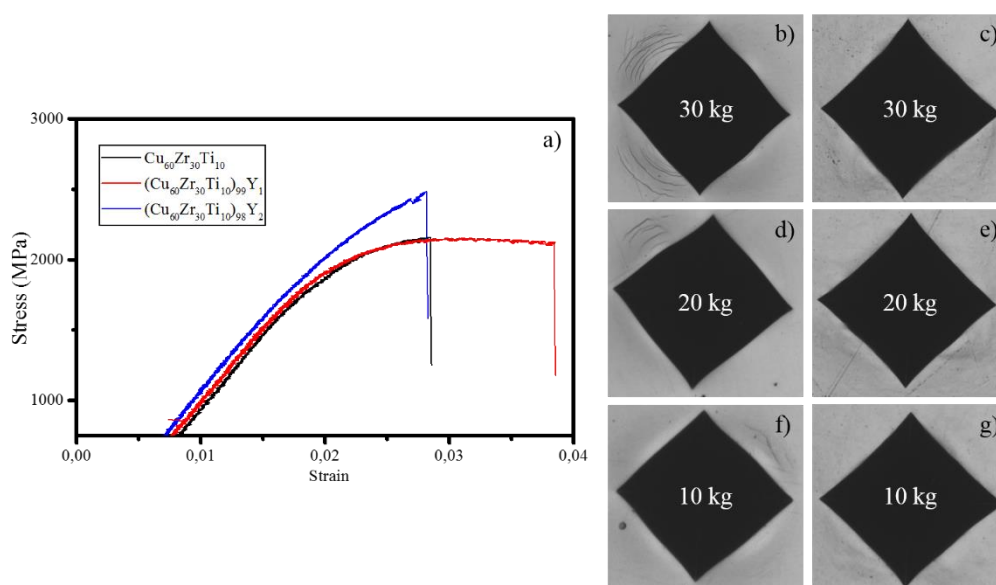


Figure 6: Compressive stress–strain curves for the Cu-based samples a) and micrographs showing hardness indents for three loads (10, 20 kg, 30 kg) of b), d) and f)  $\text{Cu}_{60}\text{Zr}_{30}\text{Ti}_{10}$ , c), e) and g)  $(\text{Cu}_{60}\text{Zr}_{30}\text{Ti}_{10})_{99}\text{Y}_1$ ,

Ultrasonic measurements were performed to evaluate the Young moduli of the samples. However, only the  $(\text{Cu}_{60}\text{Zr}_{30}\text{Ti}_{10})_{99}\text{Y}_1$  sample was tested because of the limited size of the sensors. Indeed, only the 3-mm rods could be tested, and this critical diameter could not be reached without the yttrium addition. Using the velocity of transversal and longitudinal waves, the measured Young modulus was 111 GPa and the Poisson's ratio 0.47, which are close to the properties of Ti–6Al–4V.

High-load hardness measurements were also conducted using 10- and 30-kg loads on the polished surface of the sample. Fig. 6 b) to f) shows the surface deformation of the alloy under the three loads. It is apparent that even under 30 kg, no cracks appeared, with only the appearance shear bands, suggesting that the samples exhibit local plasticity. This finding is a good indication of the high toughness of the metallic glasses evaluated in this study.

The toughness ( $K_C$ ) was evaluated based on the size of the vein pattern appearing on the fracture surface of the compression samples using the formula given by Xi et al. [46]:

$$K_C = \sigma_y \sqrt{\omega 6\pi} \quad (3)$$

where  $\sigma_y$  is the yield strength and  $w$  is the size of the vein pattern.

The size of the vein pattern was heterogeneous, and size measurements of the fracture surface were performed in multiple directions of several SEM micrographs to improve the accuracy.  $K_{IC}$  values of 38, 42, and 35 MPa  $\sqrt{m}$  were obtained for  $Cu_{60}Zr_{30}Ti_{10}$ ,  $(Cu_{60}Zr_{30}Ti_{10})_{99}Y_1$ , and  $(Cu_{60}Zr_{30}Ti_{10})_{98}Y_2$ , respectively. This toughness measurement is relevant from a comparative viewpoint. The optimal quantity of yttrium necessary to increase the toughness of the system appears to be 1 at.%, as indicated by the lower  $K_{IC}$  for 0 at.% and 2 at.% Y. These values are consistent with the notch toughness of approximately 36 MPa  $\sqrt{m}$  for a Cu–Zr–Y–Al metallic glass measured by Shen et al. [47]. More in-depth investigations of the microstructure should be conducted to understand the mechanisms explaining the improvement of plasticity for the 1 at. % Y addition.

### 3.4 Structural and Chemical Analyses

TEM analysis of the 1 at.% Y sample revealed the presence of numerous rectangular crystalline precipitates with lengths of 100–200 nm (Fig. 7a) surrounded by nanosized crystallized domains (Fig. 7b) arranged in a dendrite-like shape. The position of the rectangular precipitate within the dendrite-like structure suggests that the crystallization starts from the precipitate.

Selected area electron diffraction (SAED) patterns were used to determine the nature of the rectangular precipitates. Fig. 7c presents a STEM ADF image of the rectangular precipitate shown in Fig. 7a, with the corresponding diffraction pattern presented in Fig. 7d. The rectangular precipitate is composed of two phases, one in the  $200 \times 200 \times 160 \text{ nm}^3$  rectangular box containing a 60-nm large cuboid second phase, shown in bright contrast. The same diffraction pattern was obtained at positions A and B, which indicates that the 60-nm cuboid is either a second phase with similar lattice structure and orientation as the rectangular precipitate or a void. The diffraction pattern was indexed as the  $\langle 001 \rangle$  orientation of a cubic phase. As the matrix contains titanium, two types of cubic oxides can be expected: yttria  $Y_2O_3$  (bcc  $a = 10.5 \text{ \AA}$  or fcc  $a = 5.2 \text{ \AA}$ ) or pyrochlore  $Y_2Ti_2O_7$  (fcc,  $a = 10.1 \text{ \AA}$ ). Chemical analysis was performed to determine if Ti was present in the precipitates.

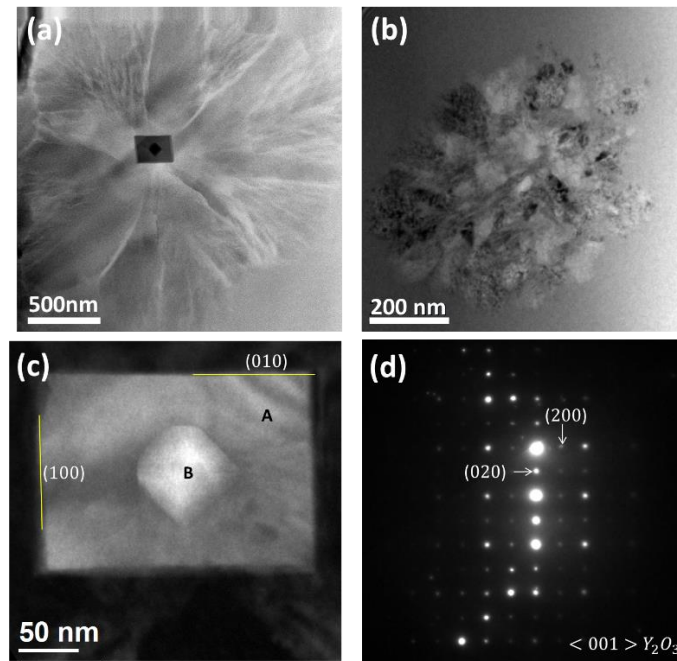


Figure 7: a) TEM image of the precipitate surrounded by the crystallized area. b) Crystallized area of Cu–Zr–Ti–Y. c) TEM image of the precipitate, showing the central phase. d) Diffraction pattern of the precipitate.

EDX analysis indicated that the most abundant elements within the rectangular precipitates were yttrium and oxygen, as shown in Fig. 8a. The presence of titanium in the precipitate was unclear from the EDX analysis, as the apparent Ti signal in the precipitate might originate from the matrix in projection.

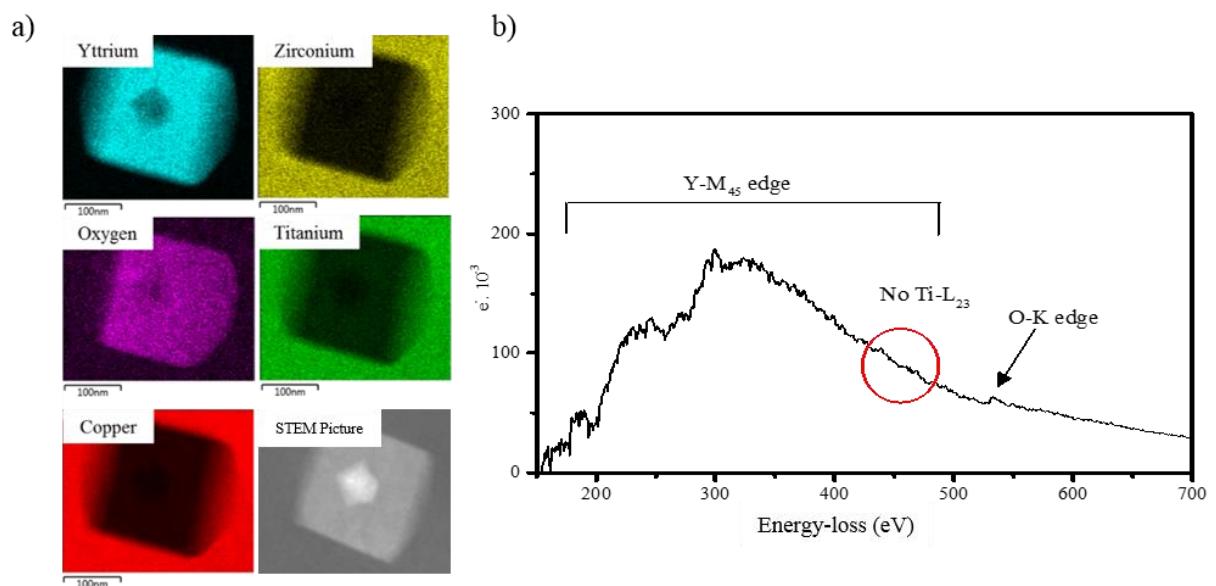


Figure 8: a) EDX analysis of precipitate. b) Typical example of the core-loss EELS spectrum of a single precipitate. The background was extracted using a conventional power-law model.

From the EDX maps, no additional elements other than titanium and oxygen were detected in the 60-nm cuboid, and all the maps were dark at the position of the cube, indicating that the rectangular precipitate likely contains a faceted hole at its centre. This observation was confirmed for multiple other precipitates (data not shown). The rationale behind the presence of this hole in the precipitates is beyond the scope of this work.

Fig. 8 b) presents a typical core-loss EELS spectrum of a precipitate. The shape of the Y-M<sub>45</sub> edge is affected by small amounts of carbon contamination starting at ~285 eV. The spectrum corresponds to a precipitate whose top and bottom surfaces were not covered by the matrix, as opposed to the one in Fig. 8 a) for EDX analysis. Nevertheless, the presence of the Y-M<sub>45</sub> edge and the O-K edge at ~530 eV but not the Ti-L<sub>23</sub> edge at ~455 eV indicates that the precipitates contain only oxygen and yttrium and are pure Y<sub>2</sub>O<sub>3</sub>. Further confirmation by fine structure analysis of the O-K edge was prevented by the carbon contamination and thickness of the precipitates. It is worth noting that the white lines of the Ti-L<sub>23</sub> edge in Y<sub>2</sub>Ti<sub>2</sub>O<sub>7</sub> are very intense and would have been detectable even in small amounts. From the EDX analysis and EELS measurements, we can conclude that the precipitates correspond to Y<sub>2</sub>O<sub>3</sub>. According to Ribis et al. [48], the morphology of this compound changes from spherical to cubical as a function of the lattice misfit with the matrix. In our case, no real lattice misfit can exist because the matrix is amorphous.

As the effect of yttrium on mechanical properties has been previously demonstrated [2], [49], its effect on other properties such as corrosion resistance and biocompatibility were also investigated.

### 3.5 Effect of yttrium on the corrosion resistance

The ductility was improved with the yttrium addition; however, evaluation of the corrosion resistance was needed before these alloys can be applied as biomaterials. For this purpose, OCP measurements and polarization curves were obtained.

The presence of proteins aims to mimic the conditions of the human body. The obtained representative polarization curves are presented in Fig. 9 for both Cu<sub>60</sub>Zr<sub>30</sub>Ti<sub>10</sub> and (Cu<sub>60</sub>Zr<sub>30</sub>Ti<sub>10</sub>)<sub>99</sub>Y<sub>1</sub> in NaCl electrolyte and NaCl with albumin.

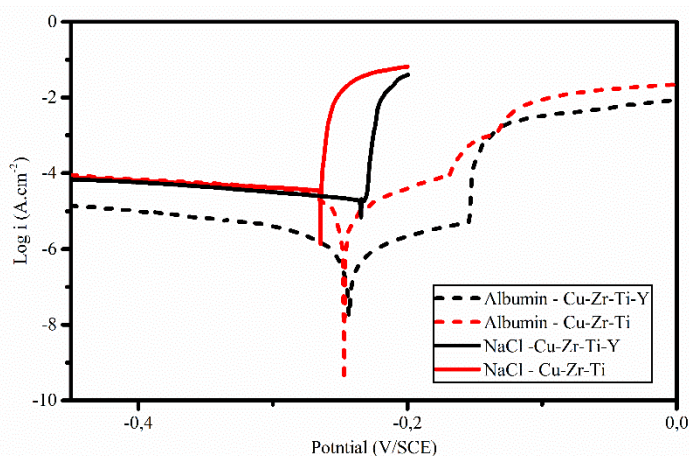


Figure 9: Polarization curves of Cu<sub>60</sub>Zr<sub>30</sub>Ti<sub>10</sub> and (Cu<sub>60</sub>Zr<sub>30</sub>Ti<sub>10</sub>)<sub>99</sub>Y<sub>1</sub> in NaCl electrolyte and NaCl with albumin

For all the experiments, the measured corrosion potential was close to that of the Ti-based alloys conventionally used as biomaterials, which is equal to  $-0.22$  V. This result indicates that the oxide layer at the surface of the sample may consist of Ti-rich oxides. In saline solution, the curves for both materials exhibited a cathodic current density plateau, and after the corrosion potential, the large current density increase suggests a fast corrosion rate. The corrosion potential shifted towards anodic potential with the addition of yttrium, suggesting a nobler material. However, the corrosion in the NaCl solution was instantaneous. The large amount of Cu, inducing immediate dissolution of the metallic glass, is a major drawback for the use of this system as a biomaterial. No passivation layer is assumed to grow on the sample surface in this NaCl medium. Nevertheless, the addition of 4 g/L of proteins from bovine serum in the medium induced modification of the anodic branch of the polarization curves. The slight increase and anodic plateau indicate that a blocking effect occurs for both materials, delaying the dissolution. Therefore, the proteins have a beneficial effect on the corrosion rate of the sample, which is a crucial advantage for applications in real conditions.

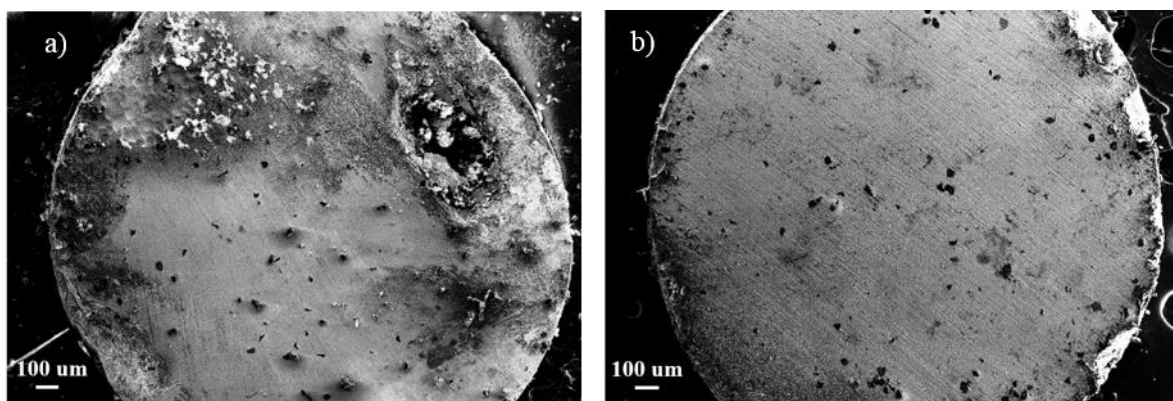


Figure 10: SEM images after the linear polarization of  $(\text{Cu}_{60}\text{Zr}_{30}\text{Ti}_{10})_{99}\text{Y}_1$  in a) NaCl without albumin and b) NaCl with 4 g/L of albumin.

Fig. 10 shows the difference between a sample after linear polarization in the electrolyte with and without albumin. Large and small pits are visible on the sample exposed to saline solution, whereas much less corrosion products were observed in the presence of BSA. This observation suggests that the albumin protects the sample surface. Several conclusions about the role of albumin are possible. The first one is that albumin is attracted to the surface of the sample because of the polarity of the molecules and creates an adsorbed protective barrier. The second conclusion is that albumin generates insoluble complexes with one of the elements on the sample and then impedes the interaction of  $\text{Cl}^-$  ions, reducing the dissolution of the sample and pitting susceptibility.

Released ion tests are necessary to evaluate the quantity of released  $\text{Cu}^{2+}$ , and complementary investigations are needed to confirm the absence of cytotoxicity. XPS analysis was conducted to understand the degradation of the material and to analyse the corrosion products on the surface. The oxide layer thickness was measured to be a maximum of 10 nm.

Table 2: Different components of the carbon peak on the surface of the samples (% of the element form) determined using XPS

	C-C/C-H	C-O/C-N	O-C-O/C=O	O-C=O	Metallic Oxides	Adsorbed H <sub>2</sub> O
Cu-Zr-Ti NaCl	83	9	4	4	39	14
Cu-Zr-Ti albumin	68	17	13	2	30	10
Cu-Zr-Ti-1Y NaCl	86	8	3	3	29	22
Cu-Zr-Ti-1Y albumin	74	14	10	2	25	13

Table 2 summarizes the amounts of the different chemical forms of carbon on the surfaces of the four samples. Several chemical bonds were present, and the corresponding quantities were measured. The presence of carbon at the surface of the sample is correlated to atmosphere contamination and the presence of molecular compounds adsorbed at the surface. More C-O, C-N, O-C-O, and C=O bonds were present on the surface sample immersed in the electrolyte containing albumin, which supports the speculation that the albumin is adsorbed on the surface and protects the sample.

Less metallic oxides were present on the surface of the samples containing yttrium because the degradation is less important for these samples. A second explanation is that the corrosion products are thinner and more compact in the presence of yttrium, leading to a more noble material. Moreover, it appears that albumin prevents the adsorption of water molecules at the surface of the sample, which contributes to increasing the corrosion resistance.

### 3.6 Effect of yttrium on biocompatibility

Cytotoxicity tests were conducted to evaluate the potential toxic character of (Cu<sub>60</sub>Zr<sub>30</sub>Ti<sub>10</sub>)<sub>99</sub>Y<sub>1</sub> and Cu<sub>60</sub>Zr<sub>30</sub>Ti<sub>10</sub>. After 1 day at 37°C, the cell proliferation was measured for both compositions. The results are summarized in Fig. 11.

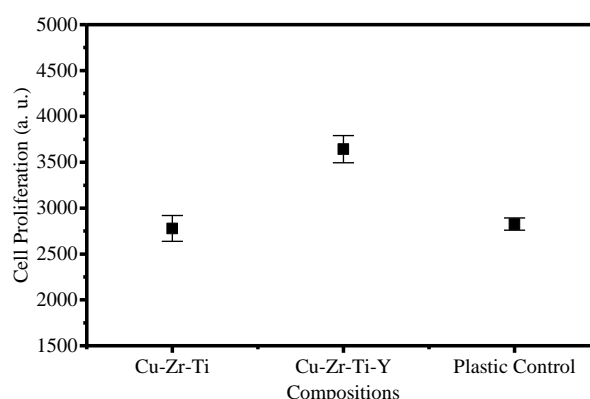


Figure 11: Evolution of the cell proliferation for plastic control, Cu-Zr-Ti-Y, and Cu-Zr-Ti

The cell proliferation results for the systems without Y and with 1 at.% Y are compared in Fig. 11. The plastic control was specially designed for cell adhesion and used to control the experiment. However, the most important point is the significant difference between the two compositions,  $\text{Cu}_{60}\text{Zr}_{30}\text{Ti}_{10}$  and  $(\text{Cu}_{60}\text{Zr}_{30}\text{Ti}_{10})_{99}\text{Y}_1$ . These preliminary results indicate that this system appears to be not harmful for the human body and that the addition of Y appears to improve the biocompatibility. However, longer tests are needed to provide more details on the full biocompatibility.

Further investigations on the cytotoxicity of this material should be conducted for a longer time to evaluate the effect of the copper degradation, the modification of the sample surface, and the released ions. However, based on this preliminary investigation, the absence of cytotoxicity of this material is clear after 1 day. The addition of yttrium appears to be beneficial for cell proliferation, offering a major improvement towards the applicability of metallic glasses as biomaterials.

## Conclusions

Cu-based BMGs were studied for their potential biomedical applications, and the effect of a minor Y addition in the system Cu–Zr–Ti was analysed.

After observing that the minor addition of 1 at.% Y induces an increase of the critical diameter, several additional effects of this addition were highlighted:

- Increase of the glass-forming ability.
- Improvement of the crystallization resistance.
- Improvement of the corrosion resistance. Very different behaviour was observed depending on whether proteins were present in the tested medium (the proteins were adsorbed on the surface and protected the sample). The corrosion potential of the Cu-based sample was close to that for TA6V (–0.25V/SCE and –0.2V/SCE, respectively).
- Improvement of the biocompatibility.
- Increase of the ductility and toughness of the material, with the same high yield strength of Cu–Zr–Ti maintained.

All these changes can be explained by the presence of nanoprecipitates of yttria inducing the formation of nanocrystallized areas. This combination of excellent mechanical properties has not been achieved in any other well-known fully biocompatible systems. In addition, this Cu-based system appears to be harmless to the human body. Further investigations are underway to further decrease the copper content and determine the biocompatibility of the material.

## Acknowledgements

Part of this research was financially supported by the GPM2 group at the SIMAP Laboratory, in Grenoble, France.

## References

- [1] W. Klement, R. H. Willens, et P. Duwez, « Non-crystalline structure in solidified Gold-Silicon alloys », *Nature*, vol. 187, n° 4740, p. 869-870, 1960.
- [2] W. Peng et Y. Zhang, « Micro-alloying of yttrium in Zr-based bulk metallic glasses », *Prog. Nat. Sci. Mater. Int.*, vol. 21, n° 1, p. 46-52, 2010.
- [3] M. Calin, A. Gebert, A. Cosmina *et al.*, « Designing biocompatible Ti-based metallic glasses for implant applications », *Mater. Sci. Eng. C*, vol. 33, n° 2, p. 875-883, 2013.
- [4] Y. B. Wang, H. F. Li, Y. F. Zheng, et M. Li, « Corrosion performances in simulated body fluids and cytotoxicity evaluation of Fe-based bulk metallic glasses », *Mater. Sci. Eng. C*, vol. 32, p. 599-606, 2012.
- [5] T. Zhang, K. Kurosaka, et A. Inoue, « Thermal and Mechanical Properties of Cu-Based Cu-Zr-Ti-Y Bulk Glassy Alloys », *Mater. Trans.*, vol. 42, n° 10, p. 2042-2045, 2001.
- [6] K. J. Laws, K. F. Shamlaye, B. Gun, et M. Ferry, « Synthesis of copper-based bulk metallic glasses in the ternary Cu-Mg-Ca system », *J. Alloys Compd.*, vol. 486, n° 1-2, p. L27-L29, nov. 2009.
- [7] P. Jia, H. Guo, Y. Li, J. Xu, et E. Ma, « A new Cu-Hf-Al ternary bulk metallic glass with high glass forming ability and ductility », *Scr. Mater.*, vol. 54, n° 12, p. 2165-2168, juin 2006.
- [8] A. Inoue, W. Zhang, T. Zhang, et K. Kurosaka, « High-strength Cu-based bulk glassy alloys in Cu-Zr-Ti and Cu-Hf-Ti ternary systems », *Acta Mater.*, vol. 49, n° 14, p. 2645-2652, 2001.
- [9] X. Ma, Q. Li, L. Chang, C. Chang, H. Li, et Y. Sun, « Enhancement on GFA and mechanical properties of Ni-based bulk metallic glasses through Fe addition », *Intermetallics*, vol. 90, p. 58-62, nov. 2017.
- [10] H. Kazemi, C. Cattin, M. Blank, et L. Weber, « Development of a new family of phosphorous-free Pt-based bulk metallic glasses », *J. Alloys Compd.*, vol. 695, p. 3419-3428, févr. 2017.
- [11] K. Takenaka, T. Wada, N. Nishiyama, H. Kimura, et A. Inoue, « New Pd-based bulk glassy alloys with high glass-forming ability and large supercooled liquid region », *Mater. Trans.*, vol. 46, n° 7, p. 1720-1724, 2005.
- [12] H. Li, S. Pang, Y. Liu, P. K. Liaw, et T. Zhang, « In vitro investigation of Mg-Zn-Ca-Ag bulk metallic glasses for biomedical applications », *J. Non-Cryst. Solids*, vol. 427, p. 134-138, 2015.
- [13] Z. Zhou, Q. Wei, Q. Li, B. Jiang, Y. Chen, et Y. Sun, « Development of Co-based bulk metallic glasses as potential biomaterials », *Mater. Sci. Eng. C*, vol. 69, p. 46-51, déc. 2016.
- [14] J. Dahlman, O. N. Senkov, J. M. Scott, et D. B. Miracle, « Corrosion Properties of Ca Based Bulk Metallic Glasses », *Mater. Trans.*, vol. 48, n° 7, p. 1850-1854, 2007.
- [15] P. Meagher, E. D. O’Cearbhaill, J. H. Byrne, et D. J. Browne, « Bulk Metallic Glasses for Implantable Medical Devices and Surgical Tools », *Adv. Mater.*, vol. 28, n° 27, p. 5755-5762, juill. 2016.
- [16] M. D. Demetriou, A. Wiest, D. Hofman *et al.*, « Amorphous metals for hard-tissue prosthesis », *JOM*, vol. 62, n° 2, p. 83-91, 2010.
- [17] S. Li, Q. Wei, Q. Li, B. Jiang, Y. Chen, et Y. Sun, « Development of Fe-based bulk metallic glasses as potential biomaterials », *Mater. Sci. Eng. C*, vol. 52, p. 235-241, juill. 2015.
- [18] A. Blanquer, E. Pellicer, A. Hynowska *et al.*, « In vitro biocompatibility assessment of Ti<sub>40</sub>Cu<sub>38</sub>Zr<sub>10</sub>Pd<sub>12</sub> bulk metallic glass », *J. Mater. Sci. Mater. Med.*, vol. 25, n° 1, p. 163-172, janv. 2014.
- [19] H. F. Li, K. Zhao, Y. B. Wang, Y. F. Zheng, et W. H. Wang, « Study on bio-corrosion and cytotoxicity of a Sr-based bulk metallic glass as potential biodegradable metal », *J. Biomed. Mater. Res. B Appl. Biomater.*, vol. 100B, n° 2, p. 368-377, 2012.
- [20] K. Zhao, J. F. Li, D. Q. Zhao, M. X. Pan, et W. H. Wang, « Degradable Sr-based bulk metallic glasses », *Scr. Mater.*, vol. 61, n° 11, p. 1091-1094, déc. 2009.
- [21] N. Hua, R. Li, H. Wang, J. Wang, Y. Li, et T. Zhang, « Formation and mechanical properties of Ni-free Zr-based bulk metallic glasses », *J. Alloys Compd.*, vol. 509, p. S175-S178, juin 2011.
- [22] S. Pang, Y. Liu, H. Li, L. Sun, Y. Li, et T. Zhang, « New Ti-based Ti-Cu-Zr-Fe-Sn-Si-Ag bulk metallic glass for biomedical applications », *J. Alloys Compd.*, vol. 625, p. 323-327, mars 2015.

- [23] A. P. Reis, C. Patinha, Y. Noack, S. Robert, et A. C. Dias, « Assessing human exposure to aluminum, chromium and vanadium through outdoor dust ingestion in the Bassin Minier de Provence, France », *Environ. Geochem. Health*, vol. 36, n° 2, p. 303-317, avr. 2014.
- [24] Tomljenovic Lucija, « Aluminum and Alzheimer's Disease: After a Century of Controversy, Is there a Plausible Link? », *J. Alzheimer's Dis.*, vol. 23, p. 567-598, 2011.
- [25] A. Duda-Chodak et U. Blaszczyk, « The effect of Nickel on human health », *J. Elem.*, vol. 13, n° 4, p. 685-696, 2008.
- [26] C. Pan, H. Liu, T. Liu, et S. Zhou, « A metal coating of copper-titanium as potential biomaterials », *Integr. Ferroelectr.*, vol. 179, n° 1, p. 56-62, mars 2017.
- [27] D. Wojcieszak, D. Kaczmarek, A. Antosiak *et al.*, « Influence of Cu-Ti thin film surface properties on antimicrobial activity and viability of living cells », *Mater. Sci. Eng. C*, vol. 56, p. 48-56, nov. 2015.
- [28] M. A. El-Hadek et M. Kassem, « Failure behavior of Cu-Ti-Zr-based bulk metallic glass alloys », *J. Mater. Sci.*, vol. 44, n° 4, p. 1127-1136, févr. 2009.
- [29] C. Dai, H. Guo, Y. Shen *et al.*, « A new centimeter-diameter Cu-based bulk metallic glass », *Scr. Mater.*, vol. 54, n° 7, p. 1403-1408, avr. 2006.
- [30] U. E. Klotz, C. Liu, P. J. Uggowitzer, et J. F. Löffler, « Experimental investigation of the Cu-Ti-Zr system at 800 °C », *Intermetallics*, vol. 15, n° 12, p. 1666-1671, 2007.
- [31] K. Asami, C.-L. Qin, T. Zhang, et A. Inoue, « Effect of additional elements on the corrosion behavior of a Cu-Zr-Ti bulk metallic glass », *Mater. Sci. Eng. A*, vol. 375-377, p. 235-239, juill. 2004.
- [32] Z. Xie, Y. Zhang, Y. Yang, X. Chen, et P. Tao, « Effects of rare-earth elements on the glass-forming ability and mechanical properties of  $\text{Cu}_{46}\text{Zr}_{47-x}\text{Al}_7\text{M}_x$  (M = Ce, Pr, Tb, and Gd) bulk metallic glasses », *Rare Met.*, vol. 29, n° 5, p. 444-450, oct. 2010.
- [33] L. Deng, B. Zhou, H. Yang, X. Jiang, B. Jiang, et X. Zhang, « Roles of minor rare-earth elements addition in formation and properties of Cu-Zr-Al bulk metallic glasses », *J. Alloys Compd.*, vol. 632, p. 429-434, mai 2015.
- [34] Y. F. Wang, L. Li, C. Sun, Q. L. Lu, et Z. Q. Shi, « Rare Earth Elements on Glass-Forming Ability and Thermal Stability of Cu-Zr-Al Metallic Glass », *Mater. Sci. Forum*, vol. 688, p. 426-430, juin 2011.
- [35] W. Wang, « Roles of minor additions in formation and properties of bulk metallic glasses », *Prog. Mater. Sci.*, vol. 52, n° 4, p. 540-596, mai 2007.
- [36] P. Berg, J. Nielsen, et M. K. Sørensen, « EVA: realized and predicted optimal genetic contributions », in *Proceedings of the 8th World Congress on Genetics Applied to Livestock Production, Belo Horizonte, Minas Gerais, Brazil, 2006*.
- [37] G. Vergnol, N. Ginsac, P. Rivory *et al.*, « *In vitro* and *in vivo* evaluation of a polylactic acid-bioactive glass composite for bone fixation devices », *J. Biomed. Mater. Res. B Appl. Biomater.*, vol. 104, n° 1, p. 180-191, janv. 2016.
- [38] H. E. Kissinger, « Reaction Kinetics in Differential Thermal Analysis », *Anal. Chem.*, vol. 29, n° 11, p. 1702-1706, 1957.
- [39] J. H. Flynn et L. A. Wall, « General treatment of the thermogravimetry of polymers », *J. Res. Natl. Bur. Stand. Sect. Phys. Chem.*, vol. 70A, n° 6, p. 487, nov. 1966.
- [40] J. H. Flynn et L. A. Wall, « A rapid, direct method for the determination of activation energy from thermogravimetric data », *J. Polym. Sci. [B]*, vol. 4, n° 5, p. 323-328, 1966.
- [41] T. Ozawa, « A New Method of Analyzing Thermogravimetric Data », *Bull. Chem. Soc. Jpn.*, vol. 38, n° 11, p. 1881-1886, nov. 1965.
- [42] X. Wang, M. Zeng, N. Nollmann, G. Wilde, J. Wang, et C. Tang, « Thermal stability and non-isothermal crystallization kinetics of  $\text{Pd}_{82}\text{Si}_{18}$  amorphous ribbon », *AIP Adv.*, vol. 7, n° 6, p. 065206, juin 2017.
- [43] D. Lee, B. Zhao, E. Perim *et al.*, « Crystallization behavior upon heating and cooling in  $\text{Cu}_{50}\text{Zr}_{50}$  metallic glass thin films », *Acta Mater.*, vol. 121, p. 68-77, 2016.

- [44] W. H. Wang, « Roles of minor additions in formation and properties of bulk metallic glasses », *Prog. Mater. Sci.*, vol. 52, p. 540-596, 2007.
- [45] P. Scherrer, « Bestimmung der inneren Struktur und der Größe von Kolloidteilchen mittels Röntgenstrahlen », in *Kolloidchemie Ein Lehrbuch*, vol. 277, n° 1916, Berlin, Heidelberg: Springer Berlin Heidelberg, 1912, p. 387-409.
- [46] X. K. Xi, D. Q. Zhao, M. X. Pan, W. H. Wang, Y. Wu, et J. J. Lewandowski, « Fracture of Brittle Metallic Glasses: Brittleness or Plasticity », *Phys. Rev. Lett.*, vol. 94, n° 12, p. 125510, avr. 2005.
- [47] Y. Shen et J. Xu, « Improving plasticity and toughness of Cu-Zr-Y-Al bulk metallic glasses via compositional tuning toward the CuZr », *J. Mater. Res.*, vol. 25, n° 2, p. 375-382, 2010.
- [48] J. Ribis et Y. De Carlan, « Interfacial strained structure and orientation relationships of the nanosized oxide particles deduced from elasticity-driven morphology in oxide dispersion strengthened materials », *Acta Mater.*, vol. 60, n° 1, p. 238-252, 2012.
- [49] J. Luo, H. Duan, C. Ma, S. Pang, et T. Zhang, « Effects of Yttrium and Erbium Additions on Glass-Forming Ability and Mechanical Properties of Bulk Glassy Zr-Al-Ni-Cu Alloys », *Mater. Trans.*, vol. 47, n° 2, p. 450-453, 2006.

In this work, it has been shown that the corrosion behaviour is different according to the different media used and the potential presence of proteins. Another experiment has been done, not included in the paper, closer to the human conditions because it uses the RPMI medium, as described below. The corrosion of the alloy in this medium is still poor and mechanisms need to be understood.

## 5-2- Corrosion resistance in RPMI medium

RPMI 1640 medium (Roswell Park Memorial Institute) is used to culture human leukemic cells suspension. This medium does not contain any proteins, lipids or growth factors. It can be supplemented using antibiotics and foetal bovine serum (FBS), depending on the targeted experiments.

A non-supplemented RPMI medium was used in order to investigate the corrosion resistance of the Cu-Zr-Ti-Y system. Figure 5-1 shows these results, comparing the corrosion behaviour in NaCl, NaCl + Albumin and RPMI electrolytes.

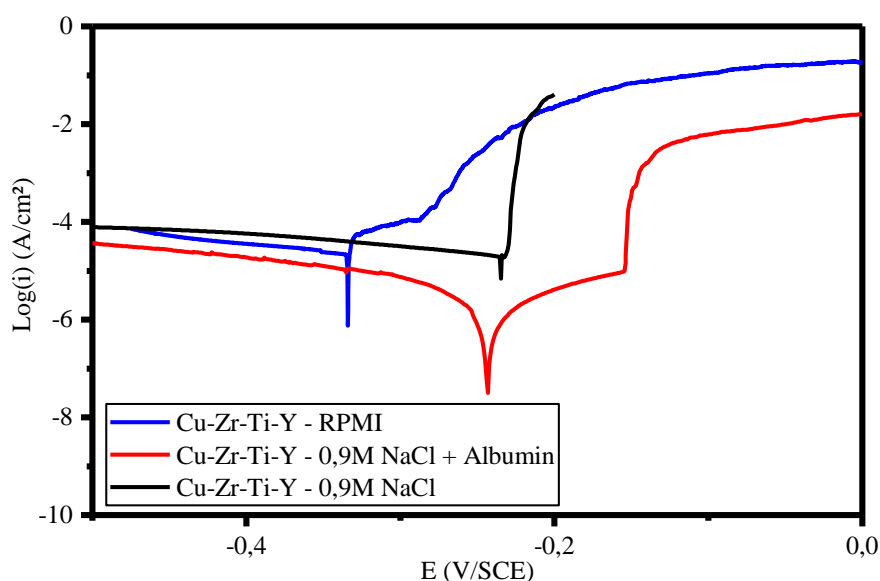


Figure 5-1: Polarization curves for the Cu-Zr-Ti-Y system in different electrolyte solutions: NaCl, NaCl+Albumin, RPMI

It has already been seen that albumin creates a protective layer on the sample surface. Indeed, albumin is an electronegative molecule and is adsorbed on the sample surface. The reason why adsorption mechanism is preferred compared to a complexation mechanism is that, if albumin created complexes, the latter will be dissolved quickly, and the degradation of the sample will be worse. Because of the apparent benefit of the albumin, we can conclude that albumin is adsorbed on the surface, creating a protective layer, preventing from the attack of the chloride ions (which is consistent with XPS analysis). However, the albumin is not the only compound to be beneficial to avoid the dissolution of the sample.

According to the results, corrosion potential of the experiments in RPMI medium is much lower than in the two other electrolytes, which means that the alloy is less resistant in the RPMI medium. However, a passivation plateau is noticeable on the polarization curve, without any proteins in the medium. In the human body, the conditions are closer to RPMI containing proteins, and the behaviour of the sample is not catastrophic even if the glassy alloy is mainly composed of Cu. It is possible to think that for in-vivo conditions, the behaviour of the sample will be more stable and a potential use as biomaterial could be practicable.

As corrosion resistance has been precisely analysed to understand the protective character of proteins, we will now focus on a further investigation of structural properties of the yttria precipitates.

### 5-3- Structural investigations into the $Y_2O_3$ precipitates

The part 5-1, explained the determination of the precipitate nature, as  $Y_2O_3$ , using the EDX and EELS measurements. In this part, further investigations have been conducted to precisely analyse their surrounding crystalline areas and understand their formation mechanisms. For this purpose, Transmission Electron Microscopy (TEM) experiment coupled

with Focused Ion Beam (FIB) technique have been used to reconstruct the precipitates distribution in the volume and highlight the link between the crystallized areas and the  $Y_2O_3$  box-shaped precipitates. The ultimate goal of this experiment should be the determination of the cubical phase in the middle of the precipitates and its formation.

### 5-3-1- Experimental methods

First of all, after checking the amorphous character of the metallic glass using XRD measurements (Bruker D8 Advance, Cu  $K\alpha$ , working conditions were 40 kV and 40 mA for the X-ray tube, while  $2\theta$  was in  $20^\circ$ – $70^\circ$  angular range.) TEM experiments were conducted.

Part of the previous Transmission Electron Microscopy (TEM) analyses has been also used in this analysis, conducted with a TEM-high angle annular dark field (STEM-HAADF) imaging, Z contrast (JEOL 2010F at 200 kV) and a FEI Titan ETEM G2 80–300 kV for SEM-EDX analysis. All these studies were coupled with a FIB/SEM workstation (NVision 40; Carl Zeiss Microscopy GmbH, Oberkochen, Germany) combining a SIINT zeta FIB column (Seiko Instruments Inc. NanoTechnology, Japan) with a Gemini I column has been employed to analyse the structure of the yttria precipitate and build a 3D distribution of the precipitates and the surrounding volumes, using a voxel size of  $5 \times 5 \times 5 \text{ nm}^3$ .

The protocol used for the FIB analysis is described in Figure 5-2. Before the serial sectioning, a trench was milled with a coarse ion beam current of 27 nA with an accelerating voltage of 30 keV. Then, carbon deposit has been done to protect and identify the interest area. Then five marks have been milled with Ga Focused Ion Beam. This helps to maintain a good autofocus and to limit the drift during the experiment, which could be long. In a second time, the serial sectioning has been done with a current 700 pA at 30 keV. Two detectors have been used to conduct the SEM imaging at the accelerating voltage of 1.5 keV: Everhart-Thornley and In-Lens detector. The analysis has been performed on a  $4.9 \times 4.75 \times 4.1 \mu\text{m}^3$  volume, after data cropping. NanoPatterning and Visualization Engine (NPVE)-FIBICS has been used to conduct the acquisition. All the image treatment has been processed with the software FIJI, an open source image processing package based on ImageJ software.

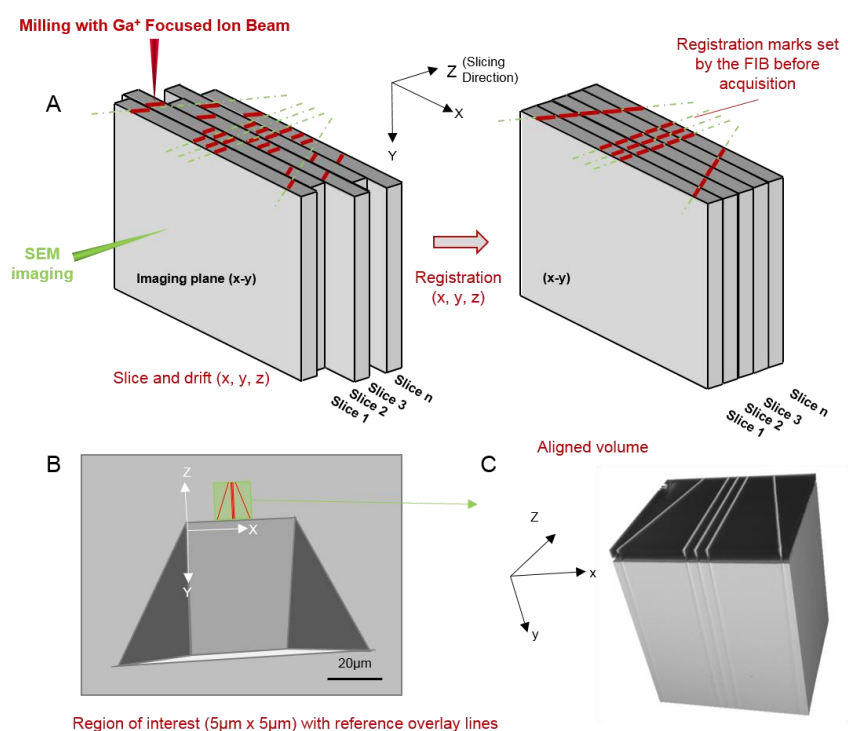


Figure 5-2: Schematic representation of the FIB experiment

### 5-3-2- Structural and chemical analysis of the precipitates surroundings

First, based on the TEM observations, two types of precipitates are noticed: the 200 nm length box shaped precipitates with a 60 nm long second feature inside, inducing nano-crystallized areas, and the 50 nm length precipitates, without any other feature inside or crystallized area around (Fig. 5-3). This difference of structure and size lead to the conclusion that the second feature formation only occurs beyond a size threshold.

According to the microscopy contrasts, two different phases in the crystallized area seem to be highlighted. EDX measurements confirm the existence of these two different phases: one Cu-rich and the other one is Ti-rich, as it is shown in Fig. 5-4. This finding is reinforced with the DSC curves obtained in the previous work in this chapter, showing a two-step crystallization.

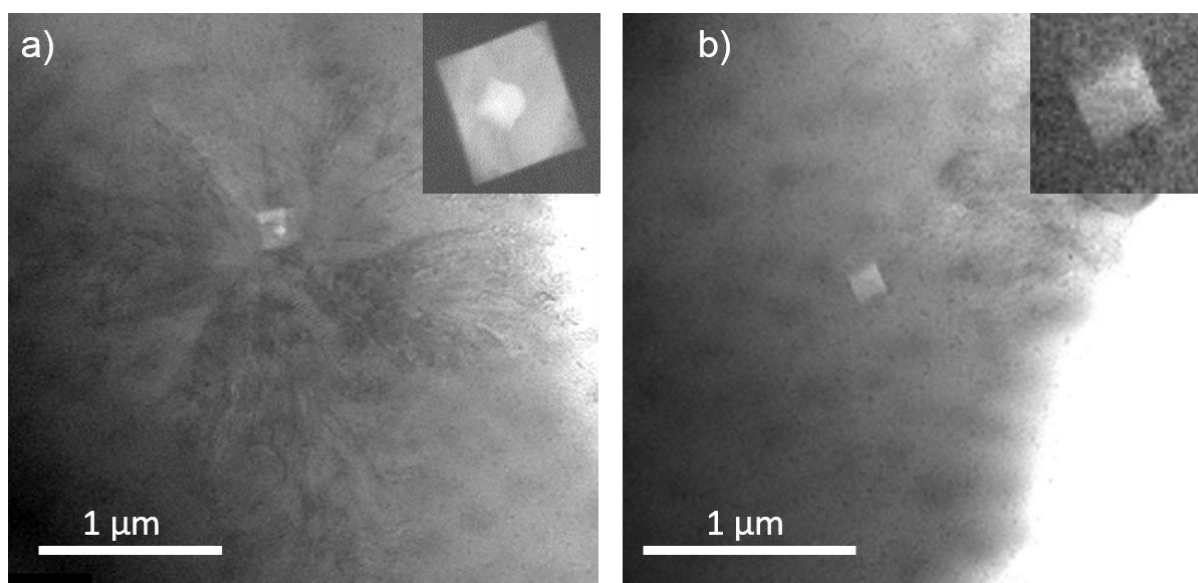


Figure 5-3: a), b) TEM micrograph of the two kinds of precipitates, with and without the surrounding crystalline areas.

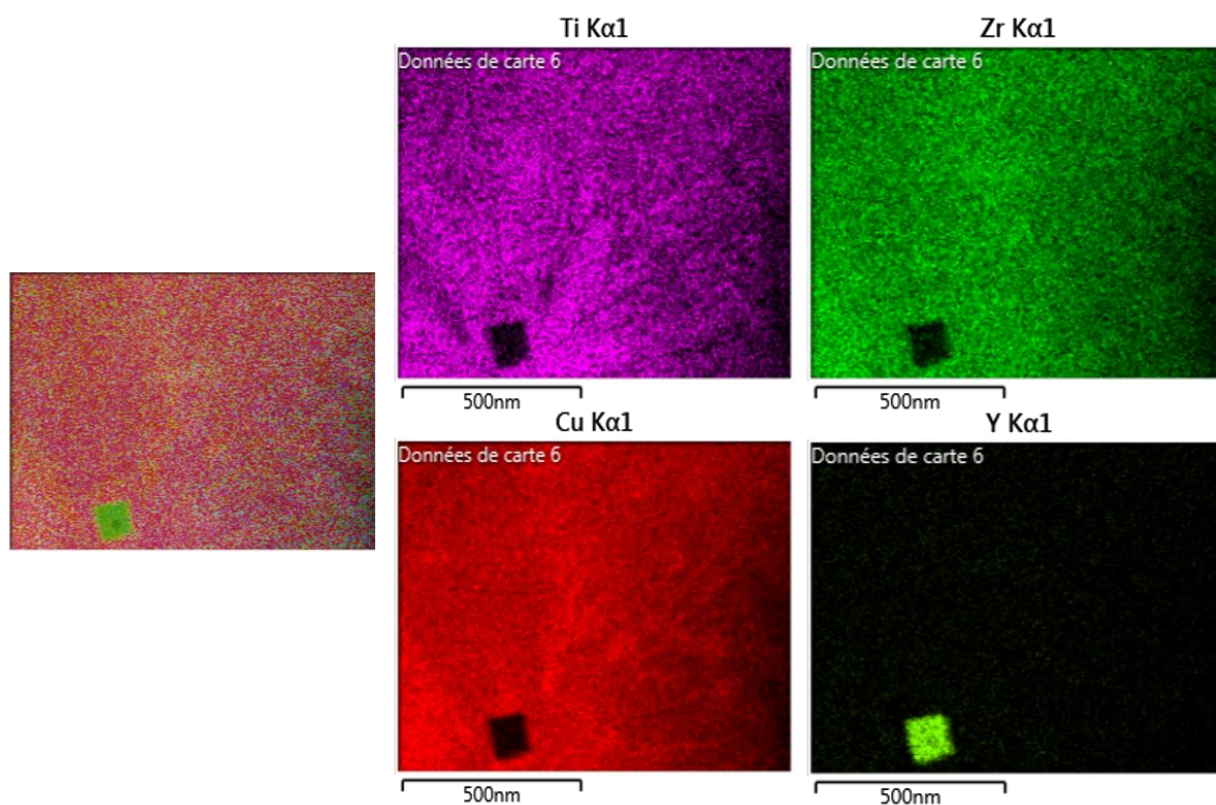


Figure 5-4: EDX maps of the precipitate and the surrounding crystallized area

### 5-3-3- 3D distribution of the precipitates and crystallized phases in the volume

Thanks to the TEM experiments, the presence of two kinds of precipitates has been highlighted. Moreover, information about their spatial organization can help to understand their formation mechanisms. In order to obtain information about the spatial distribution of the precipitates, FIB experiments are conducted. First, SEM (Scanning Electron Microscopy) and SIM (Scanning Ion Microscopy) characterizations of the polished  $(\text{Cu}_{60}\text{Zr}_{30}\text{Ti}_{10})_{99}\text{Y}_1$  sample have been conducted. SEM images depend on the signals produced from the interaction between the electron beam and the sample. Then, secondary electrons and backscattered electrons are used to obtain images. Using a low voltage SEM on a flat surface allows to obtain contrasts providing interesting structural or physical information. The second advantage of using a low-beam-energy operation is the increase in the secondary electrons produced to improve the signal.

SIM imaging is possible can be employed during FIB experiment. This ion-matter interaction induces secondary ions with an intensity dependent of the nature of the excited atoms (ISI: ion induced secondary ions). Once collected by the detector, the ISI signal shows the chemical contrast of the region of interest. Several crystalline areas have been identified in Fig. 5-5, using different magnification and detectors.

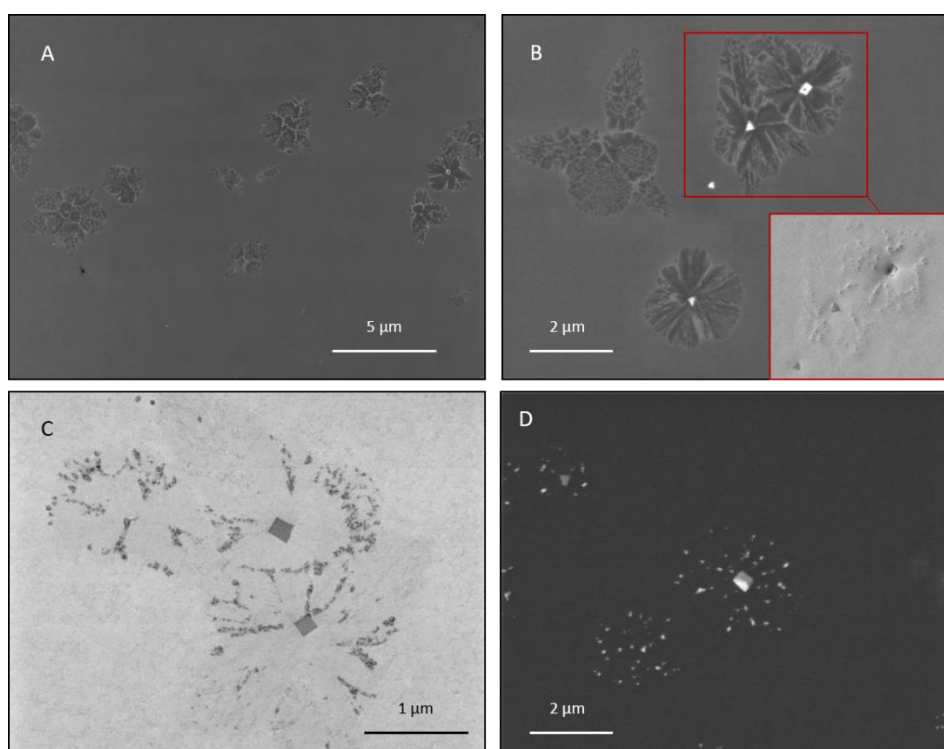


Figure 5-5: (A) Distribution of the large crystalline areas (In-Lens low voltage, SE imaging), (B) Visualization of a few crystalline areas with a few  $\text{Y}_2\text{O}_3$  precipitates (In-Lens low voltage SE imaging). The triangular shape is induced by the random cross-section. Insert is a standard Everhart-Thornley SE imaging of a selected area which shows more punctual elements (small dark contrasts) within the dendrite (C) Low loss in-Lens BS imaging of crystalline area. (D) ISI-SIM imaging of a few crystalline area and a precipitate.

According to the shape of the crystalline areas, Fig. 5-5 indicates that they are induced by the precipitates. In picture (A), a higher magnification is used to observe the distribution of the crystalline zones in a larger area of the sample. These objects are randomly distributed in the sample and usually contain a precipitate.

Using the Focused Ion Beam (FIB) technique, a small region of interest of the sample can be investigated and 3D reconstructed (Fig.5-6). The proportion of small precipitates  $Y_2O_3$  (yellow particles on Fig. 5-6) is evaluated to 0.01% of the analysed volume. This fraction is significant for an amorphous material, as the one of the apparent fraction of crystallized areas. However, the analysed volume is limited and chosen to analyse one interesting precipitate. Thus, the volume is not exactly representative of the entire sample, and the crystallised area volume is probably overestimated. Indeed, the sample is X-rays fully amorphous and some large areas appear to be also fully amorphous on the Fig. 5-5 (A). Nevertheless, the crystallised areas seems to play a key role on the ductility, but the differentiation of the role for the large crystalline areas and the smaller ones are not well defined yet.

Fig. 5-6 shows the 3D reconstruction of the region of interest and confirms the observation made by SEM imaging. The position of the box-shaped precipitate within the 'dendrite-like' structure indicates that the crystallization seems to start from the precipitate. The precipitates act like a heterogeneous site for the nucleation of crystallites. The crystalline areas are composed of two phases (red and green) or only one (red). Most part of the crystallized areas contain a precipitate. In the largest area, small additional precipitates are also contained.

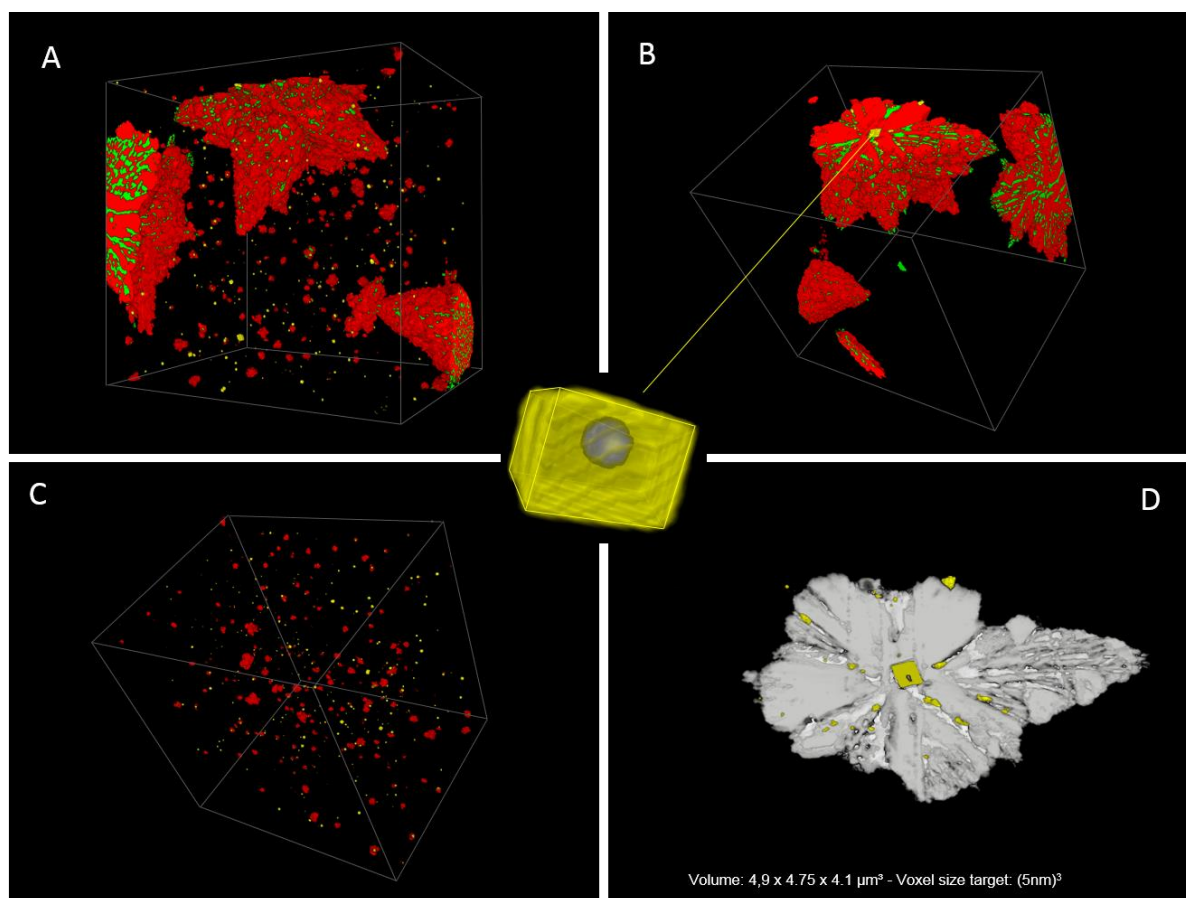


Figure 5-6: 3D FIB/SEM reconstructed views of (A) Crystallized area in the volume (red and green) and yttria precipitates (yellow), (B) Extracted dendrite-like structures detected in 2D by surface observations in SEM (7.6%vol here). Within a significant crystallized area, a cuboid precipitate (220nm x 140 nm x 215nm) in yellow contain a nanometric pore. (C) Extracted small crystallized volumes and cuboid precipitates less than 50 μm width. (D) Reconstructed view of a crystalline area with a large precipitate.

### 5-3-4- Discussion about hollow $Y_2O_3$ precipitate formation

#### 5-3-5-1- Formation of the precipitate and the crystallised areas

As the cooling is too fast to make the formation of the precipitate possible, the precipitation most probably takes place in the liquid phase, during the melting. Regarding the strong affinity between yttrium and oxygen, using the free energy of formation ( $\Delta H_f = -1932$  kJ/mol, compared to  $-950$  kJ/mol and  $-1097$  kJ/mol for  $TiO_2$  and  $ZrO_2$  respectively), the precipitate formation happens very quickly during the melting.

Then during the cooling, the precipitates act as nucleation sites for the crystallised areas formation, with an assumed size effect, as the small precipitate seems to induce small crystallized areas and large precipitates seem to induce large crystallized areas.

### 5-3-5-2- Determination of the second phase inside the precipitate

The main remaining question is the nature of the second feature in the middle of the largest precipitates. According to the STEM and TEM contrasts, this object could correspond to a void. Moreover, regarding the SEM-EDX analysis, no additional elements were detected in this small cube. The maps were very dark revealing that the largest box-shaped precipitates exhibit a hole in their middle part.

The analysis on the Figure 5-7 a) shows a dark contrast which can also be explained by the presence of a void. This conclusion is reinforced by the Fig. 5-7 c) and d) where the cavity is noticeable, varying the acceleration voltage or detector.

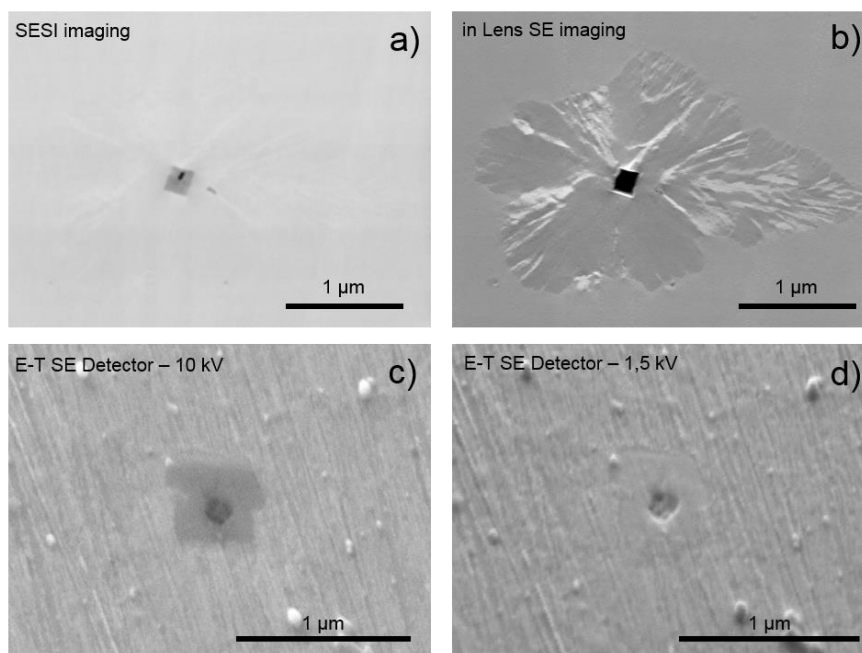


Figure 5-7: Analyse of the second phase in the middle of the precipitates, using different acceleration voltage or detector

Several large precipitates containing a void inside were investigated and Fig. 5-8 shows the different possible morphologies of void. It can be very different, from a spherical shape to a cubical one.

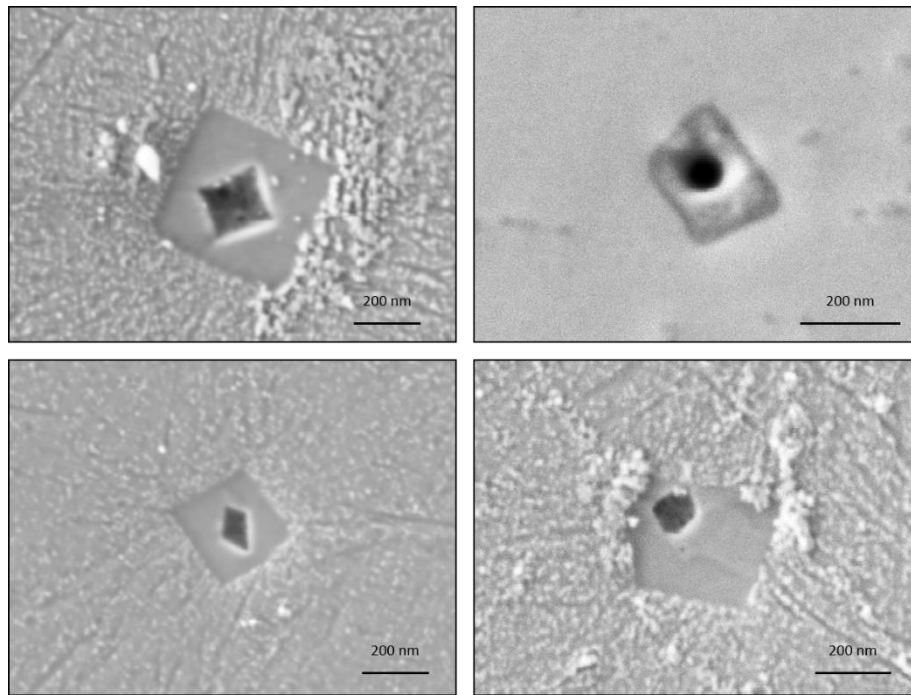


Figure 5-8: Low voltage Everhart-Thornley SE imaging of 4 hollow yttria precipitates. Several morphologies are visible from spherical to cubical. (White particules are colloidal silica particles used for polishing)

Two possible explanations can be used for the void formation in the middle of the precipitate, based on diffusion theory.

- First possibility is that an initiator particle can be produced, due to the oxygen impurities, as  $\text{TiO}_2$ . Then, addition of yttrium break the oxides to form a new one between Y and O, which is a promoted reaction according to the mixing enthalpy values. During this reaction Ti is ejected outside the precipitate while yttrium diffuses from the matrix to the precipitate.
- Second possibility is the same mechanism without the  $\text{TiO}_2$  formation. Only vacancies, due to the amorphous structure and free volume presence, and yttrium atoms diffuse in and outside the precipitate, respectively. The vacancies are then clustered, in the middle if the precipitate is larger than a threshold size, or eliminated outside for smallest precipitates.

#### 5-3-5-3- Hypothesis of Kirkendall effect

As, no  $\text{TiO}_2$  has been observed, the second scenario is promoted. The formation of the cavity is assumed to be based on the Kirkendall effect. This comes from the difference of diffusion rates between two species, namely yttrium and oxygen. Kirkendall effect was first highlighted observing CuZn diffusion couple<sup>1</sup>. Nowadays, a wide range of works uses this effect to obtain hollow nanostructures, modifying the process temperature to obtain different hollow shapes<sup>2</sup>. Based on previous works on hollow oxides formed by Kirkendall effect,

metallic atoms seem to diffuse faster than the oxygen in the oxide layer<sup>3</sup>. The unbalanced atomic fluxes are balanced by a vacancies flux:  $J_V = J_Y - J_O$ .

In our case, we assume to start with a Y-rich area. O diffuses inwards with a vacancies flux, as yttrium diffuses outwards (Fig. 5-9). An oxide layer is formed because of the strong affinity of the oxygen and the yttrium, which react immediately to form  $Y_2O_3$ . This phenomenon leads to the formation of a void, within the Y-rich particle, where all the vacancies are clustered. For the smaller precipitates, the vacancies are ejected outside.

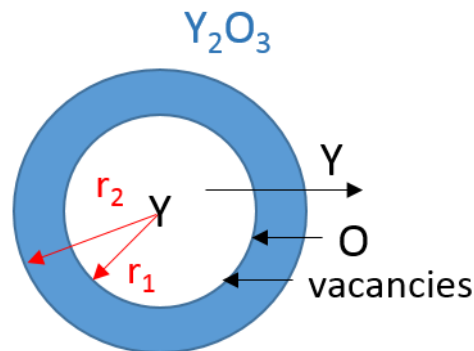


Figure 5-9: Schematic representation of Kirkendall effect in these samples

To confirm this scenario with our elaboration process parameters, a very simple diffusion model has been implemented. A lot of hypothesis have been used to simplify the model: first, a spherical shape has been studied. Then, we assume a stationary state. We also assume that yttrium diffuses faster than oxygen, as shown in some works in the literature dealing with hollow oxides particles formation, using Kirkendall effect<sup>4</sup>. The flux evolution is represented in Fig.5-10.

Assuming a diffusion-controlled process, let's consider the Fick's law to govern the layer thickening rate: the flux in O is proportional to the gradient of concentration in oxygen:

$$J_O(r_1) = - D_O \frac{\partial C_O}{\partial x} \quad (1)$$

and the same equation yields for Y:

$$J_Y(r_2) = - D_O \frac{\partial C_O}{\partial x} \quad (2)$$

The two interfaces move as following,  $r_1$  decreases and  $r_2$  increases, as shown on Fig. 5-10.

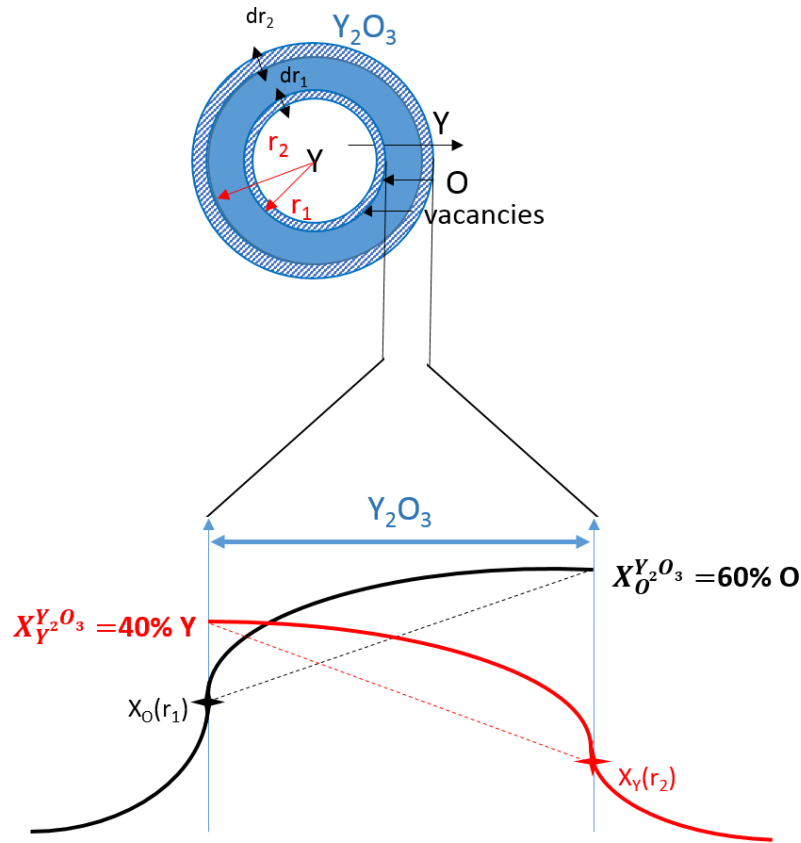


Figure 5-10: Evolution of the concentration in Y and O in the oxide layer

Assuming an affine gradient in the oxide layer, between the two interfaces, the flow of oxygen atoms and yttrium atoms can also be expressed as:

$$J_O(r_1) = -\frac{X_O^{Y_2O_3} - X_O(r_1)}{r_2 - r_1} D_O^{Y_2O_3} \quad (3)$$

$$J_Y(r_2) = -\frac{X_Y^{Y_2O_3} - X_Y(r_1)}{r_2 - r_1} D_Y^{Y_2O_3} \quad (4)$$

With  $X_O^{Y_2O_3}$  is equal to 60% and  $X_Y^{Y_2O_3}$  is equal to 40%.

The variation of  $r_1$  and  $r_2$  is expressed, from a mass balance as follow:

$$\frac{dr_1}{dt} = \frac{J_O(r_1)}{X_O(r_1)} \quad (5)$$

$$\frac{dr_2}{dt} = \frac{J_Y(r_2)}{X_Y(r_2)} \quad (6)$$

As the value of some parameters are missing with this kind of elements, as  $D_Y^{Y_2O_3}$  or  $D_O^{Y_2O_3}$  and the initial size of  $r_1$ , set to  $10^{-9}$ m. The purpose of this model is to adjust the two diffusion coefficients in order to obtain the final experimental values:  $r_2$  equal to 100 nm and  $a$ , the edge of the cube equal to 60 nm. To obtain these two values, the diffusion coefficient have been set to  $D_Y^{Y_2O_3} = 1.5 \times 10^{-16}$  m<sup>2</sup>/s and  $D_O^{Y_2O_3} = 1.5 \times 10^{-18}$  m<sup>2</sup>/s respectively. Gaboriaud *et al.* established a diffusion coefficient for the yttrium self-diffusion in  $Y_2O_3$ , with large uncertainties<sup>5</sup>, equal to:

$$D = 3.5 \times 10^{-9} \exp\left(\frac{-72}{RT}\right) \left(\frac{\text{kcal}}{\text{mole}}\right) m^2 \text{sec}^{-1} \quad (7)$$

This expression gives us the same diffusion coefficient for yttrium, for a temperature equal to  $T=1450^\circ\text{C}$ , which is consistent with the temperature reached during arc melting.

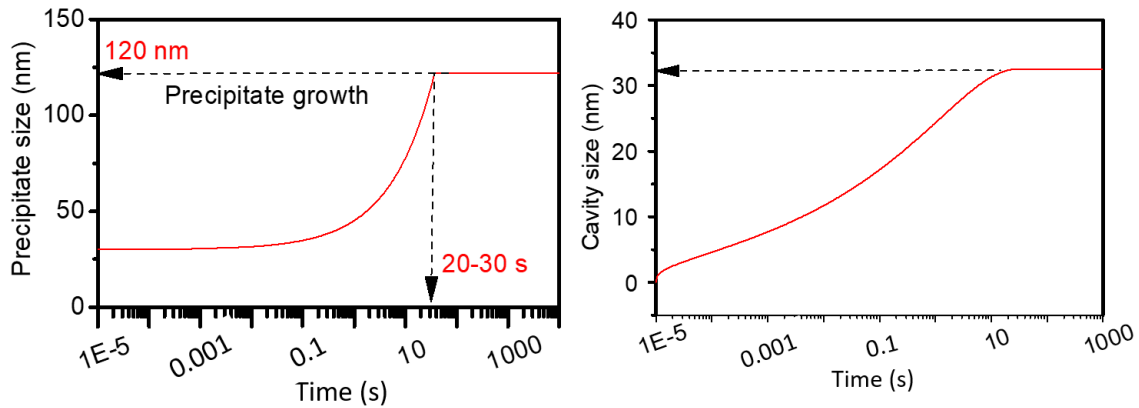


Figure 5-11: Evolution of a) the size of the precipitate ( $r_2$ ) and b) of the size of the cavity, a.

The time to form the precipitate and the cavity at this temperature corresponds to a time between 20 to seconds (Fig 5-11), according to the model, which is consistent with the process during the melting. The hypothesis about the formation of the precipitate and the cavity in the liquid phase, is then possible.

This effect has already been used to process hollow nanostructures of  $\text{Fe}_2\text{O}_3$ , nanorods and nanospheres. The morphology of the particles depends on the thermal treatment of diffusion. At high temperatures, the shape is spherical and at lower temperature the final shape is a rod<sup>2</sup>. This effect has also been used for the processing of hollow spheres of  $\text{SnO}_2$  via Spray Drying System<sup>6</sup>.

The coherence between the experimental work and the simple model based on Kirkendall effect do not constitute a proof. However, it indicates that this scenario is possible and allow to explain these hollow precipitates.

## 5-4- Conclusion

A well-known system has been studied in a purpose of use as biomaterials. Addition of yttrium has also been studied in order to increase the GFA and the plasticity of the sample, which were critical. This micro-alloying is really interesting to improve all the properties. It leads to an increase of the GFA, thermal stability, plasticity, corrosion resistance, and biocompatibility. Even if the alloy contains a large content of copper, in human body fluid, in presence of proteins, the degradation is slowed down and the corrosion potential is not far from the one of the Ti-6Al-4V. Moreover, a passivation plateau appears thanks to the presence of albumin in the electrolyte solution, which is close to the human body fluid conditions.

However, there is an optimum composition beyond which the properties are decreased. This new material can find a potential biomedical application as intrauterine contraceptive device, where a high amount of copper is needed for a spermicide effect and a micro irritation of the uterine wall, avoiding the implantation. Moreover, the amorphous character exhibits a better corrosion resistance, which allow to avoid the silver presence, usually used to delay to copper degradation.

Nevertheless, yttrium exhibits a strong affinity with oxygen and the increase of mechanical properties and corrosion resistance is due to the yttria precipitates formation during the melting, inducing surrounding crystalline areas, observed during TEM experiments. At the beginning of the process, raw materials as titanium and zirconium contain oxygen impurities, which helps the precipitates formation. Small precipitates and larger ones induce either sparse large crystallized areas or numerous smaller ones. But the differentiation of their role on the ductility is not clearly established yet.

However, yttrium may not show a beneficial effect in a system containing less oxygen impurities in the beginning of the process. Indeed, if yttrium can play the role of oxygen sink, it can form the precipitates, increasing the mechanical properties. Nevertheless, the action of yttrium in a system with less oxygen impurities remains uncertain.

## 5-5- References

1. Kirkendall, E., Thomassen, L., Upthegrove, C., Rate of diffusion of copper and zinc in alpha brass, *Trans. AIME* **133**, 1-18 (1938)
2. Cho, J. S., Ju, H. S., Kang, Y. C., Preparation of Hollow Fe<sub>2</sub>O<sub>3</sub> nanorods and nanospheres by nanoscale Kirkendall diffusion, and their electro-chemical properties for use in lithium-ion batteries, *Scientific Report* **6**, 38933 (2016)
3. Tu, K.N., Gösele, U., Hollow nanostructures based on Kirkendall effect: Design and stability considerations, *Applied Physics Letters* **86**, 093111 (2005)
4. Nakamura, R., Tokozakura, D., Nakajima, H., et al. Hollow oxide formation by oxidation of Al and Cu nanoparticles. *Journal of Applied Physics* **101**, 074303 (2007)
5. Gaboriaud, R.J., Self-Diffusion of yttrium in monocrystalline yttrium oxide: Y<sub>2</sub>O<sub>3</sub>, *Journal of Solid State Chemistry* **35**, 252-261 (1980)
6. Cho, J. S., Ju, H. S., Kang, Y. C., Applying nanoscale Kirkendall diffusion for template-free, kilogram-scale production of SnO<sub>2</sub> hollow nanospheres via spray drying system, *Scientific Report* **6**, 23915 (2016)



# Chapter 6

## Manufacturing of metallic glasses and composites by Spark Plasma Sintering

---

<b>SINTERED METALLIC GLASSES AND COMPOSITES BY SPARK PLASMA SINTERING .....</b>	<b>162</b>
<b>6-1- Reminders of powder metallurgy .....</b>	<b>162</b>
6-1-1- Powders processing .....	163
6-1-2- Densification of the samples .....	164
<b>6-2- Sintered samples and optimization of the process .....</b>	<b>168</b>
6-2-1- Manufacturing and characteristics of the powders .....	168
6-2-2- Optimization of the sintering process .....	170
6-2-2-1- Processing of sintered samples .....	170
6-2-2-2- Characterization of the sintered samples .....	175
<b>6-3- Improvement of the system by composite samples processing .....</b>	<b>179</b>
6-3-1- Processing of the composites samples .....	179
6-3-2- Characterization of the composites samples .....	182
6-3-2-1- Thermal Stability .....	182
6-3-2-2- Corrosion resistance .....	183
6-3-2-3- Mechanical Tests .....	183
<b>6-4- Conclusions .....</b>	<b>189</b>
<b>6-5- References .....</b>	<b>190</b>

---

## Chapter VI

# Sintered metallic glasses and composites by Plasma Sintering

In the previous chapter, a way to improve the critical diameter and the ductility using micro alloying with a rare earth element has been discussed. However, the highest reachable diameter was 3 mm for the cast-improved sample, which is still limited. Thus, another method has been tried in order to obtain larger-sized samples with the same system. For this purpose, in this part, a new process is developed based on the powder metallurgy. After a quick review of the different existing techniques to process the powder and the samples, the processing of powder using gas atomization and the densification using Spark Plasma Sintering (SPS) are explained and discussed. Due to the small size of the particles, fully amorphous powder is easy to obtain. Moreover, composite samples can be produced using a mixture of amorphous and crystalline powders to increase the ductility of the sample.

### 6-1- Reminders of powder metallurgy

Metallic glasses can be obtained using two routes: casting and through powder consolidation. The casting technique has been mainly discussed in the previous chapters with other systems. In this part, another process to obtain amorphous powders and get consolidated samples is discussed. Powder metallurgy<sup>1</sup> is a very interesting process because of the larger size of the metallic glass samples obtained, especially considering the biocompatibility limitations in terms of compositions. Using this technique, fully amorphous small particles can be processed, even for low GFA compositions, thanks to very high cooling rates<sup>2-6</sup>. Then, with a proper consolidation treatment, amorphous large samples with complex shapes can be obtained<sup>7</sup>. Composite samples can also be produced to improve the ductility, by mixing amorphous powders and crystalline powders<sup>8-11</sup>. The microstructure can be tailored by changing the volume fraction or the size of the particles for each powder. Moreover the temperature can be controlled to avoid crystallization.

First of all, let us give some details about the wide range of techniques suited to process the powder:

#### 6-1-1- Powders processing

- Gas atomization:

This is one of the most well-known techniques to process metallic powders<sup>9,12-14</sup>. A high pressure of inert gas jets (Helium or Argon) is applied to the molten alloy and the fine droplets are quickly ejected through a nozzle and cooled down during their fall. This technique

allows the formation of spherical particles during a highly clean process. The particles exhibit a good homogeneity in terms of composition and geometry.

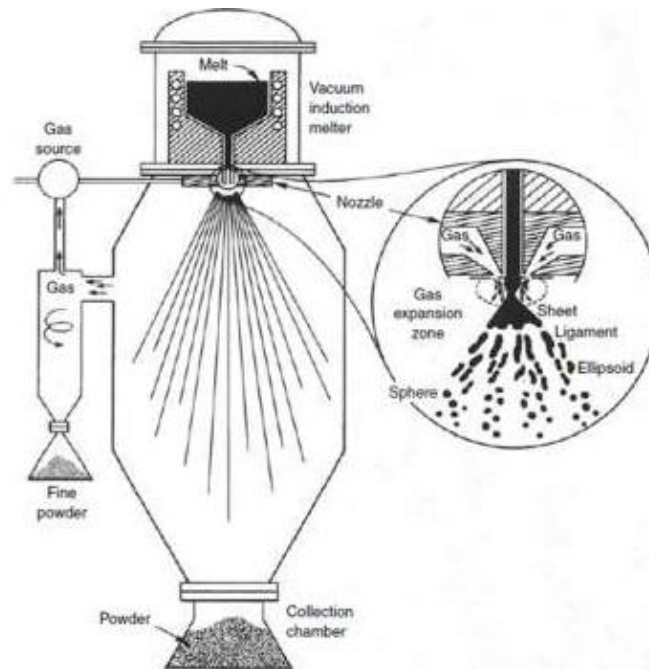


Figure 6-1: Schematic representation of the gas atomization technique <sup>15</sup>

- Milling/Grinding:

Solid pieces of the alloys are put in a mill and by grinding, crushing or cutting, the alloys break into smaller pieces <sup>16–18</sup>. For example, in a ball mill, stone or metal tumbling balls are contained in the device and rotates. Their movements and impacts break the alloy in smaller particles. The distorted geometry of the particles increases the compactness of the densified sample.

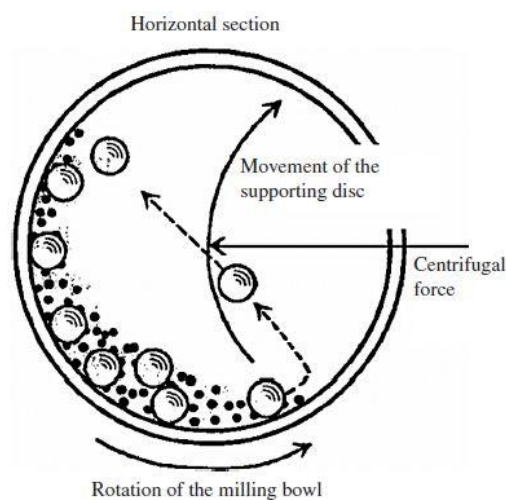


Figure 6-2: Principle of the milling/grinding technique <sup>19</sup>

- Electrolysis:

This technique uses an electrolyte cell operation for the deposition of the powder, as it is shown on the Figure 6-3. The raw materials dissolve at the anode, and the powder is deposited at the cathode. The deposition is driven by an external voltage. Then the powder is washed and dried <sup>1</sup>.

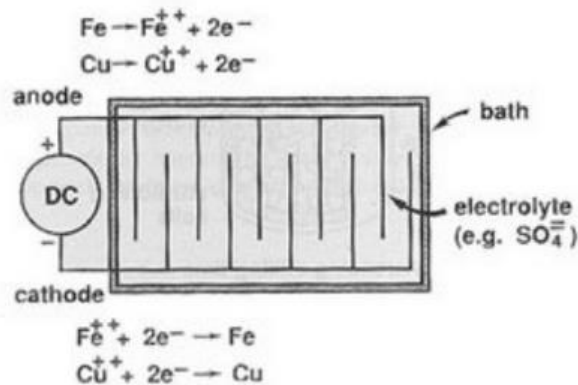


Figure 6-3: Processing of powder by electrolysis <sup>20</sup>

After the processing of the powder, the densification step is crucial to obtain good quality samples. Several techniques can be used for this purpose.

### 6-1-2- Densification of the samples

- Spark Plasma Sintering:

The association of a pulse electric current which directly passes in the graphite die then in the powder to heat it, coupled to a high pressure applied to the powder usually allows a dense sample. The process quality depends on several parameters, including time, heating rate or cooling rate. Once the parameters have been tested to find the optimal conditions, i.e. limited temperature and sintering time to avoid crystallization but keeping a good densification, the samples can be processed. On the Figure 6-4, the current path in the powder is represented as well as the temperature evolution in the powder particles <sup>6,18,21-24</sup>.

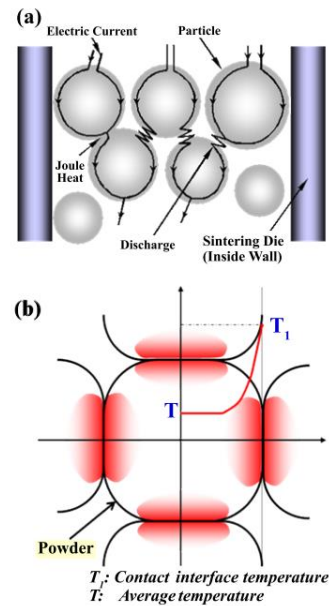


Figure 6-4: Current and heat repartition in the metallic powder and in the die during the SPS <sup>7</sup>

Figure 6-5 shows the schematic representation of the SPS device. As it is possible to notice on Figures 6-4 and 6-5, the current path is extremely hard to control in the powder particles so the densification can be inhomogeneous in the sample. However, the main drawback of the SPS, is the complexity of the device; the operating costs are higher than for other techniques.

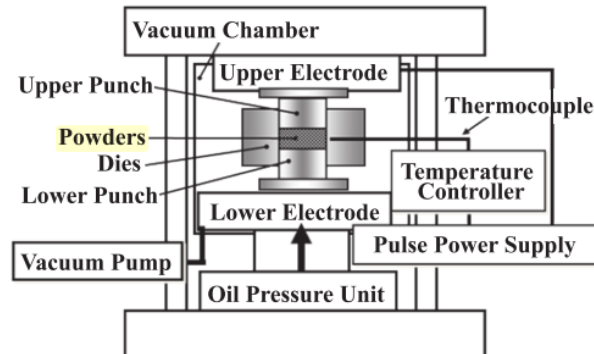
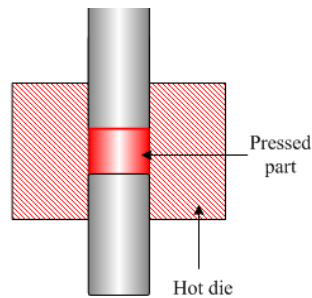


Figure 6-5: Schematic representation of the device used for the sintering of the sample <sup>21</sup>

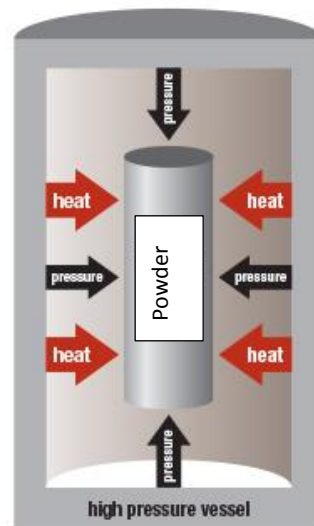
- Hot Pressing:

The Hot Pressing technique shows the same principle as the Spark Plasma Sintering, except that the heating takes place in a conventional furnace. There is no influence of any current in this case.

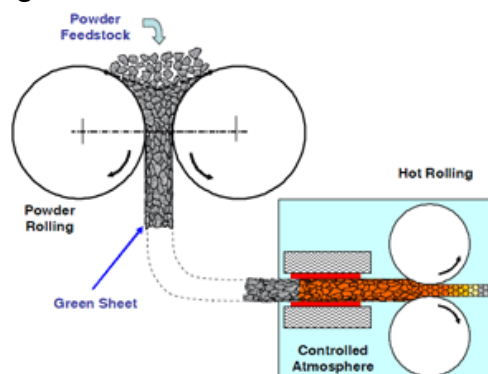
Figure 6-6: Hot Pressing schematic representation <sup>25</sup>

- Hot Isostatic Pressing:

In this technique, an elevated temperature associated with an isostatic gas pressure, are used in order to reduce the porosity and to densify the metals. An inert gas is used to avoid any reaction with the powder. Pressure is applied in all directions of the sample (Figure 6-7), thus the densification is more uniform <sup>14,26,27</sup>.

Figure 6-7: Picture of the Hot Isostatic Pressing (HIP) <sup>28</sup>

- Powder Rolling

Figure 6-8: Picture of the Powder Rolling process to obtain consolidated samples <sup>29</sup>

The powder is inserted in a roll gap, then a pair of high-rolling mills at room or high temperature compresses the powder in the form of a strip. Then the strip goes through a furnace to be sintered. This step achieves the mechanical bonding by diffusion of the atoms <sup>1</sup>.

- Powder extrusion:

The last technique presented in this part is the powder extrusion. The metal powder is encapsulated in a container and then extruded <sup>30</sup>. This process takes place at room or high temperature.

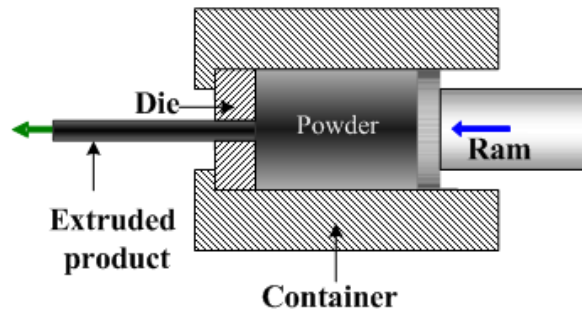


Figure 6-9: Picture of the extrusion process <sup>25</sup>

Table 1: Summarizing of the advantages/drawbacks of the densification techniques

	Homogeneity	T° control	High cooling/heating rate	Geometry	Costs	All materials	Low T°
<i>SPS</i>	-	-	+	+	-	+	+
<i>HP</i>	-	+	-	+	+	+	-
<i>HIP</i>	+	+	-	+	+	+	-
<i>Powder rolling</i>	+	+	-	-	+	-	-
<i>Powder extrusion</i>	+	+	-	-	+	-	-

A brief review of the main techniques has been done in this part. For this study, the powder was processed by gas atomization and the densification was operated using the Spark Plasma Sintering technique. This technique allows a short sintering time and a rapid decrease in temperature, thus avoiding crystallization. The high cooling rate and the low temperature are the main key parameters to process metallic glasses. Moreover, we have a long-time experience for this process dealing with metallic glasses for several years in the laboratory. Several works by Cardinal, Pelletier et al., have been done before on the sintering of metallic glass powders <sup>6,11</sup>.

## 6-2- Sintered samples and optimization of the process

### 6-2-1- Manufacturing and characteristics of the powders

For this study a well-known system has been chosen, the same as the one studied in the previous chapter:  $\text{Cu}_{60}\text{Zr}_{30}\text{Ti}_{10}$ . Because the maximal diameter for a cast sample has been reported to be 2 mm in chapter 5, this critical diameter and the ductility of this material should be improved. For this purpose, gas atomization powder and densification using SPS technique were conducted; sintered samples were characterized.

First, master alloys with the nominal composition were obtained from the base elements Cu (99, 9%), Ti (99, 9%) and Zr (99, 9%). The ingots were prepared using arc melting under Ar atmosphere, and purified by a Zr-getter, in Tohoku University, at IMR, in Sendai, Japan. The ingots were then cut in small pieces and inserted in a quartz tube followed by a rectangular nozzle, less than 1 mm wide, in order to use the high-pressure argon gas atomization method. Ingots pieces were melted using an induction heating coil. The liquid metal was ejected through a nozzle. The atomization by high pressure argon gas with dynamic pressure about 10 MPa was conducted on the liquid alloy, transformed into droplets.

Once the particles were cooled down, the powder was collected and analyzed. First, the particles distribution was investigated to check the shape of the grains (Figure 6-10) and then the calibration thanks to three sieves has been realized to keep all the particles with a diameter lower than 75  $\mu\text{m}$ .

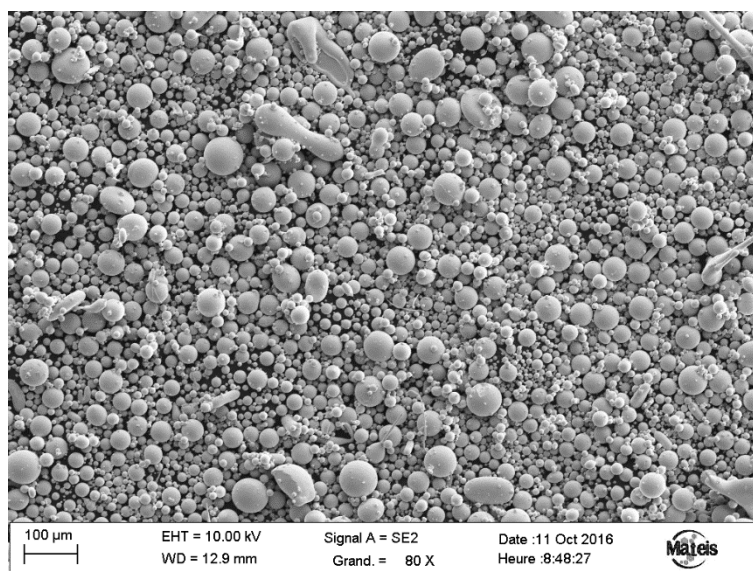


Figure 6-10: Amorphous powder  $\text{Cu}_{60}\text{Zr}_{30}\text{Ti}_{10}$  before calibration

Powder composition was controlled using EDX measurements. As presented in Table 2, the composition is very close to the nominal composition and the cast composition:

Table 2: EDX Results of the processed sample

<i>Elements</i>	<i>Quantity (at. %)</i>
<i>Cu</i>	60.8
<i>Zr</i>	28
<i>Ti</i>	11.2

The amorphous characteristics and the thermal parameters, such as the glass transition temperature ( $T_g$ ) and the crystallization temperature ( $T_x$ ) were determined using DSC experiments.

Figure 6-11 a) presents the amorphous shape of the XRD diffractogram with the absence of crystalline peaks, which proves the fully amorphous characteristic of the powder. Figure 6-11 b) shows the DSC curve with  $T_g$ , marked with the black arrow, equal to 445°C. The crystallization temperature is equal to 473°C, which is consistent with the previous results concerning the cast sample ( $T_g = 448$  °C and  $T_x = 475$  °C). The  $\Delta T$ , equal to 28°C, is low, which can cause some issues during the process of sintering to get a full densification avoiding crystallization.

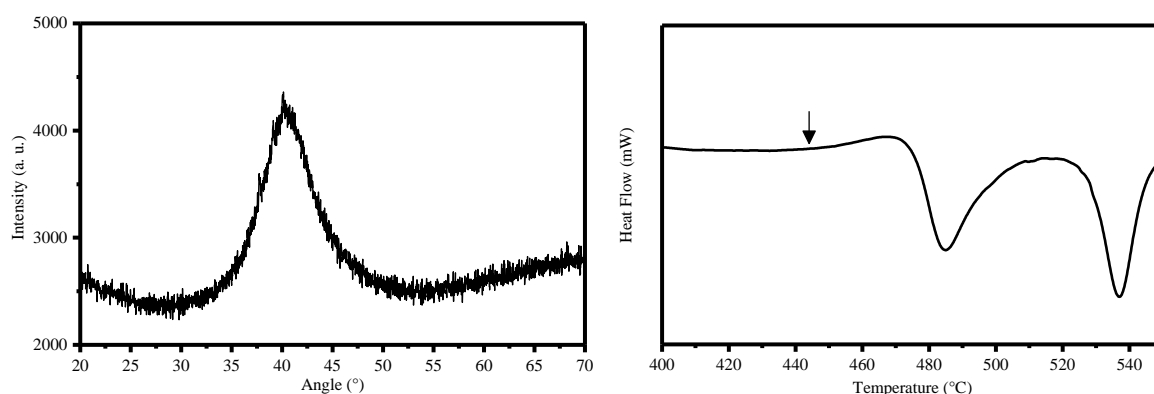


Figure 6-11: a) XRD spectrum of the Cu-Zr-Ti powder, b) DSC curve of the elaborated powder, with the black arrow for  $T_g$

The glass transition temperature and the crystallization temperature are important to check in order to optimize the sintering temperature in the SPS process to avoid crystallization.

### 6-2-2- Optimization of the sintering process

Several parameters have a key role in the sintering process and have to be optimized: the sintering temperature ( $T_s$ ), the sintering time ( $t_s$ ) and the applied pressure ( $P$ ). The choice of these parameters have a drastic influence on the mechanical behaviour or corrosion properties of samples. First of all, these parameters have to be studied in order to find the optimal sintering process.

## 6-2-2-1- Processing of sintered samples

The size of the graphite die was chosen equal to 10 mm diameter and was not changed during the different experiments. The applied pressure is maintained at the maximum using the graphite mould:  $P$  is equal to 90 MPa. The heating rate was set to 100 K/min and slowed down 20°C below  $T_s$  (Sintering temperature), in order to prevent potential overshoots from occurring. Figure 6-12 shows the process conducted during sintering.

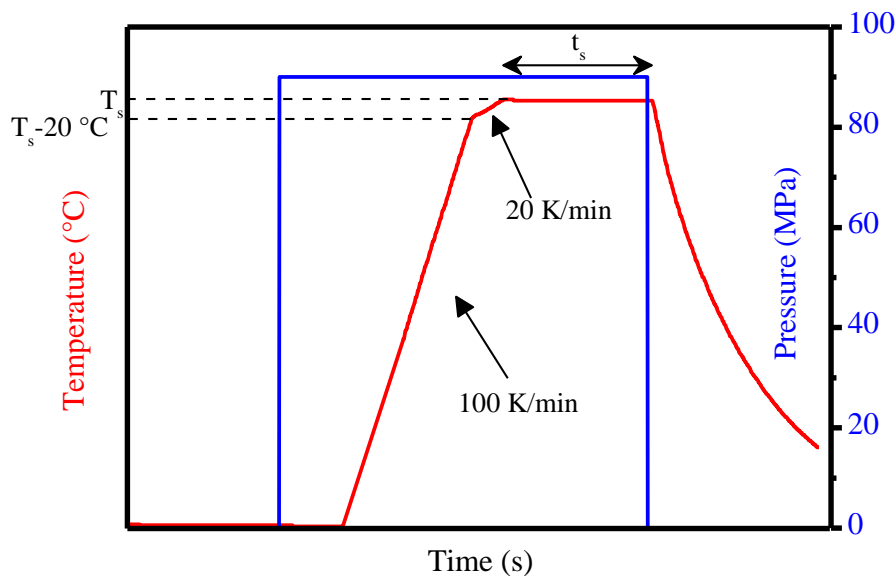


Figure 6-12: Schematic representation of the sintering process

The first parameter to be investigated was the sintering temperature, keeping the sintering time to 5 min. The choice of this parameter is crucial to avoid the crystallization from occurring. XRD measurements were conducted to check the amorphous character and to determine the limit temperature  $T_s$ , beyond which crystallization occurs. Figure 6-13 shows the XRD diffractograms for all sintering temperatures tested.

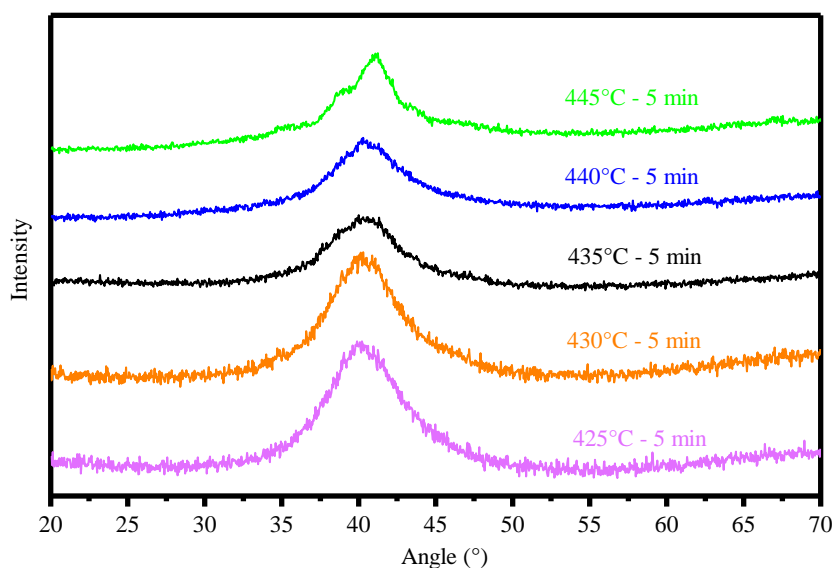


Figure 6-13: XRD diffractograms of the samples sintered at different temperatures

As a result, the sintering temperature should not exceed 435 or 440 °C. A treatment at 445°C seems to be too high because some crystalline peaks start to be observed. For the processing of this system, 435°C or 440 °C seems to be a good compromise to avoid crystallization and obtain a good densification of the sample (cf density measurements), therefore  $T_g - 10^\circ\text{C}$  or  $T_g - 5^\circ\text{C}$ , respectively.

However, once the sintering temperature is fixed, the sintering time has to be defined. To do this, 2 times for each of the selected temperature have been tested. Moreover a lower temperature (425°C) process during a longer time has also been tried for the sake of comparison.

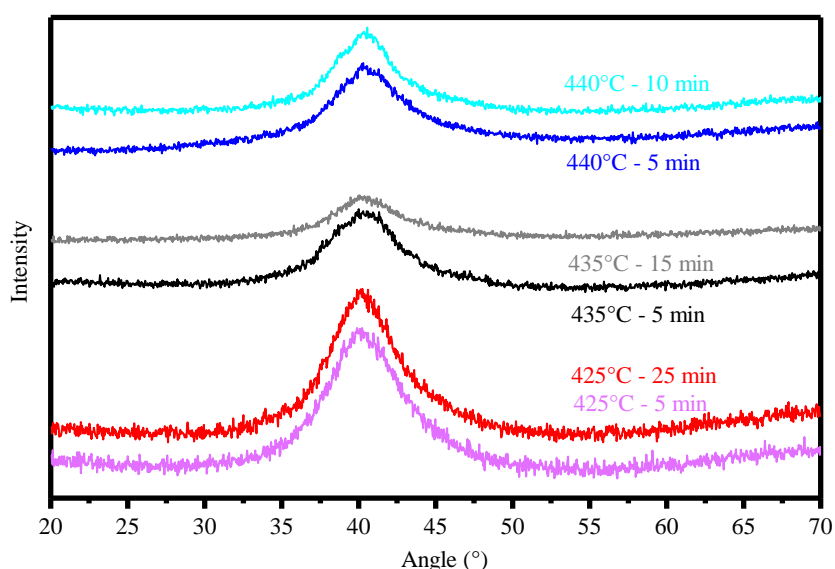


Figure 6-14: Influence of the sintering time on the amorphous characteristic of the sintered samples

Figures 6-14 shows the XRD diffractograms of the six sintered samples in the conditions defined. For the temperatures 425°C and 435°C, the two durations do not cause any crystallization. However, at 440°C, 10 min of processing is too long and crystallization occurs.

By now, the samples are fully amorphous but the quality of the sintering should be estimated. The risk is, avoiding the crystallization, to use a temperature process too low or a duration not long enough to obtain fully densified bulk samples, which will impact the mechanical properties.

The first basic tests to obtain information about the densification and the crystallinity of the samples are hardness and density measurements. Hardness measurements were done using Buehler MicroMet 5104 hardness tester. The density was measured using Archimedes's method. Table 3 summarized the measurements of all these samples.

Table 3: Characteristics of the sintered samples depending on the time

<i>Process</i>	$\rho_{\text{sample}} \text{ (g.cm}^3\text{)}$	Hardness (Hv <sub>1kg</sub> )	Sample
440 °C – 10 min	7.63	569	
440 °C – 5 min	7.54	550	
435 °C – 15 min	7.59	590	
435 °C – 5 min	7.55	545	
425 °C – 25 min	7.48	548	
425 °C – 5 min	7.45	545	

It should be noted that the cast sample exhibits a density of 7,54 g.cm<sup>3</sup> and a hardness of 545. All the values above these values may indicate the presence of a crystalline phase and all the values below can indicate a not fully densified sample. According to the Table 2, the density of the sample is very high for the sample processed at 440°C during 10 min. The same conclusion can be drawn in the view of the results for the sample 435°C during 15 min. For the sample at 425°C during 5 min, the densification is clearly not completed. However, the sample at the same temperature during 25 min seems to be fully amorphous and densified. But during the polishing, the sample breaks, indicating a heterogeneous densification and poor

mechanical resistance. The best samples from an amorphous and density point of view seem to be the two samples made at 435°C and 440°C for 5 minutes.

High-load hardness measurements were carried out using a Future Tech FV-700 device, over the load range from 1 to 30 kg, for two different selected samples. As no cracks appear, the samples seem to exhibit a local plasticity. However, the result is uncertain for the sample 440 °C – 5 min, as a small crack is already visible at 10 kg.

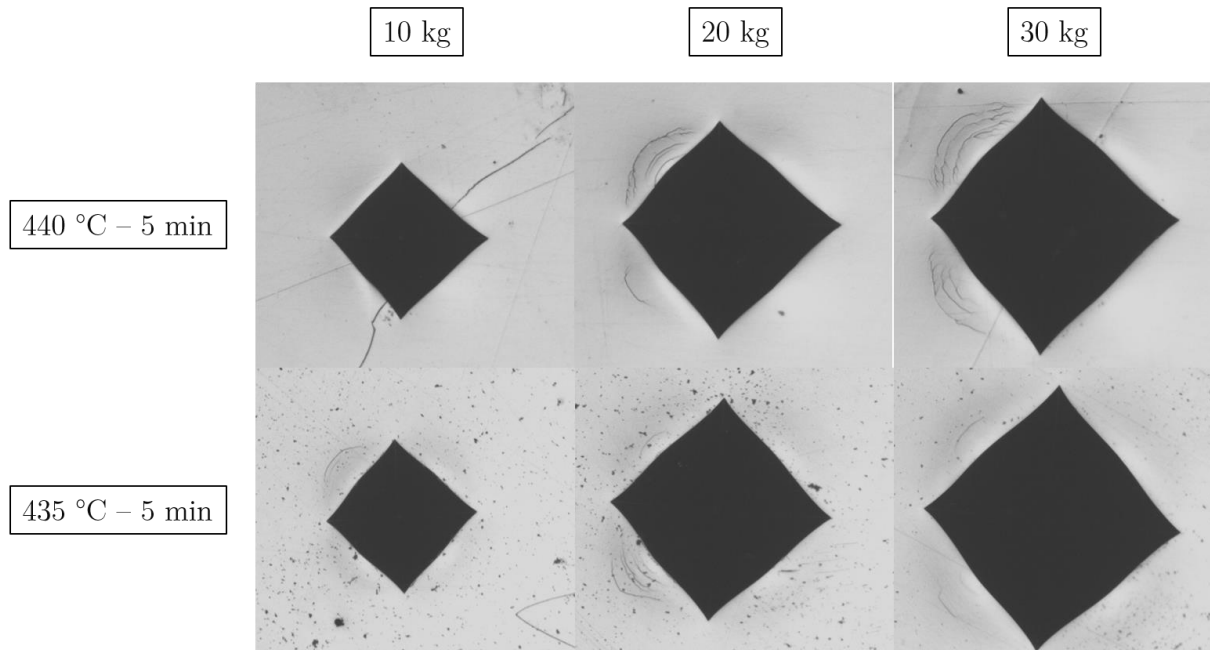


Figure 6-15: High load hardness measurements. The black points noticed on the picture of the 435 °C-5min sample are due to the polishing. It doesn't correspond to porosities.

Using SEM observations, it appears that the two samples are fully densified. No particle interfaces of the powder seem to be seen.

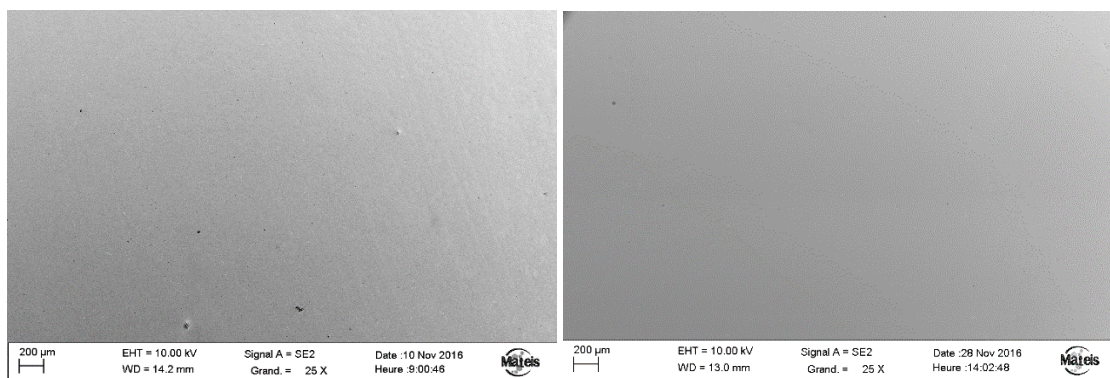


Figure 6-16: SEM micrographs after sintering process a) 435°C during 5 min, b) 440°C during 3 min

In conclusion of this part, the chosen processing conditions are 5 min at 435°C, to be sure to avoid the crystallization and thus being able to process composite samples.

### 6-2-2-2- Characterization of the sintered samples

After processing of the samples, characterization has been conducted. The change of process can impact several properties for this system. In this part the thermal stability, the mechanical properties and the corrosion resistance will be investigated.

#### 6-2-2-2-1- Thermal Stability

First of all, the thermal stability was investigated using DSC measurements (Figure 6-17) and high temperature XRD experiments, described in chapter 5.

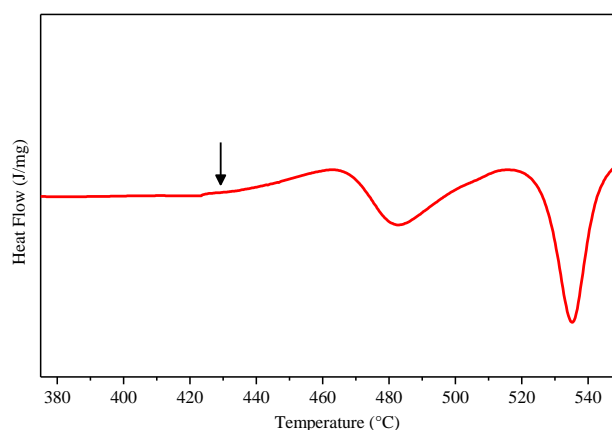


Figure 6-17: DSC curves of the sintered sample  $\text{Cu}_{60}\text{Zr}_{30}\text{Ti}_{10}$  (20 K/min)

DSC curves show characteristic temperatures lower than for the raw powder and the cast sample but the  $\Delta T$  is about the same value ( $T_g=430^\circ\text{C}$ ,  $T_x=463^\circ\text{C}$  and  $\Delta T=33^\circ\text{C}$ ). High temperature XRD measurements are conducted and the results are shown in Figure 6-18.

As shown in the Figure 6-18, the crystallization temperature of the SPS sample is lower than for the cast sample, with  $T_x=460^\circ\text{C}$  and  $T_x=480^\circ\text{C}$  respectively (in agreement with DSC). At the end of the experiment, the peaks seem to be a bit narrower in the SPS sample, which means that crystallites size is larger. The crystallization seems to be easier in the sintered sample, even if the crystallization temperature is still very high.

Moreover, to get information about the time available before crystallization, which is a key parameter for sterilization process, isothermal measurements have been performed. The same tests have been conducted as in Chapter 5. The Figure 6-19 shows the results for the two samples: cast and sintered samples. The isothermal temperature was  $460^\circ\text{C}$ .

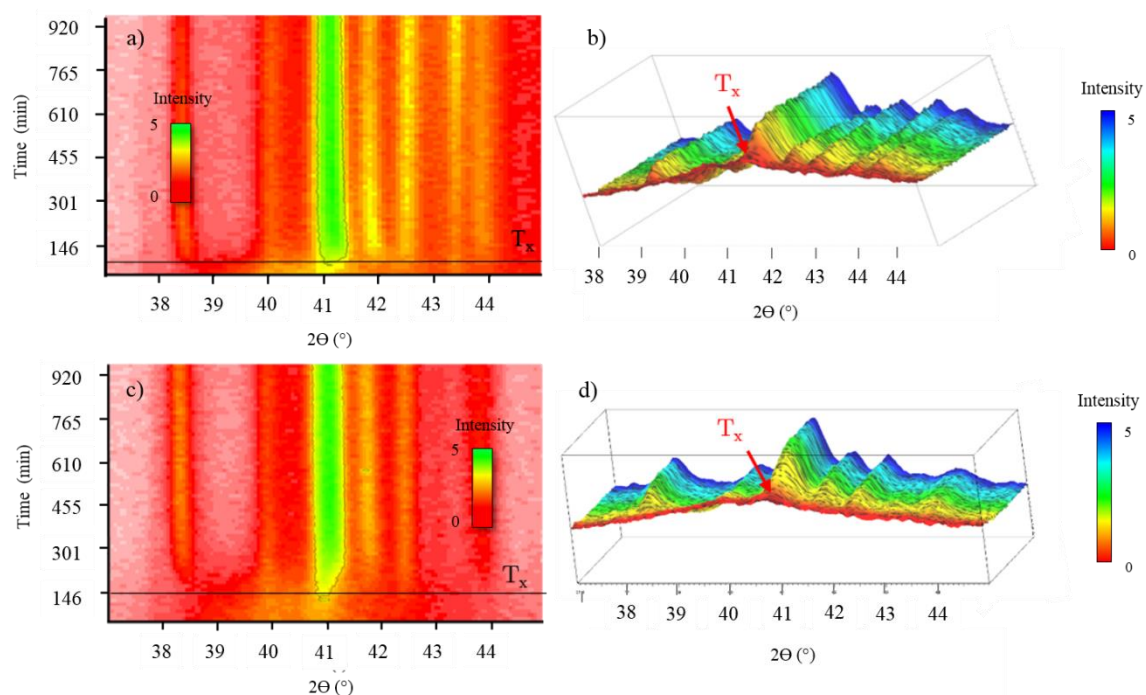
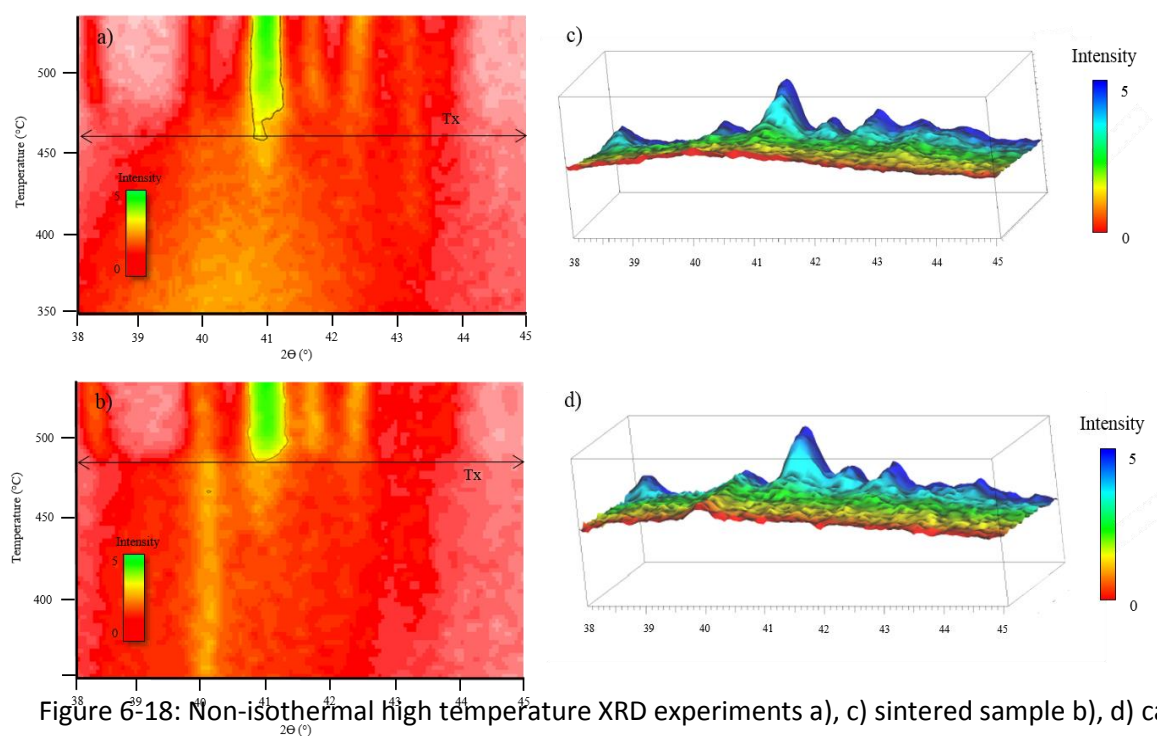


Figure 6-19: Isothermal high temperature XRD measurements a), c) sintered sample, b), d) cast sample

The crystallization time appears to be equal to 140 min for the cast sample and 75 min for the sintered sample, so the sintering process decreases the crystallization resistance. However, despite this phenomenon, the crystallization time is still consequent for such a high temperature. This same result is shown Figure 6-20. The crystallized fraction can also be calculated using the following equation:

$$X_C = \frac{I_X - I_{FC}}{I_{FA} - I_{FC}} \quad (2)$$

With  $I_X$  the intensity of the sample,  $I_{FC}$ , the intensity of a fully crystallized sample, and  $I_{FA}$ , the intensity of a fully amorphous sample.

The crystallized fraction in the sample becomes equal to unity faster than in the case of the cast sample.

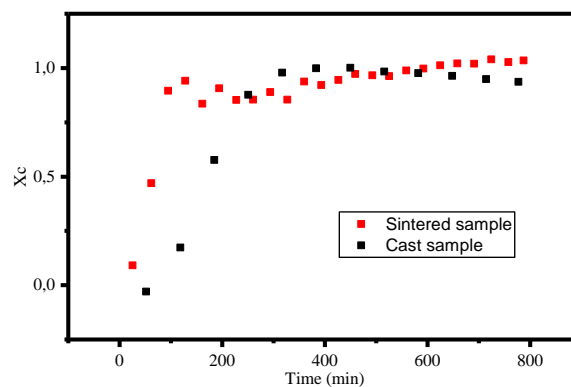


Figure 6-20: Evolution of the crystallized fraction in the cast and the sintered samples

#### 6-2-2-2-2- Corrosion Resistance

To assure potential biomedical applications, the sintering process should not affect the corrosion resistance, for example by creating more initiation sites for the corrosion phenomenon. Because of sintering, particle interfaces could be present and the advantage of having an amorphous structure could be impacted.

In order to verify this property, corrosion tests have been conducted in 0.9M NaCl solution. As for the cast sample, firstly Open-Circuit Potential (OCP) was measured for one hour. It appears that the potential reaches a stationary state very quickly, which could happen if the sample is sensitive to corrosion. After 1 hour of OCP, linear polarization curves were registered during different ranges of potential, as described in Chapter 2. The results are shown in Figure 6-21. The corrosion potential of the sintered sample is much lower than the cast one. However, the degradation seems to be slower. The anodic part increases drastically for the sample after corrosion potential is reached. Nevertheless, for the sintered sample even if the corrosion occurs at lower E, the degradation seems to evolve slower.

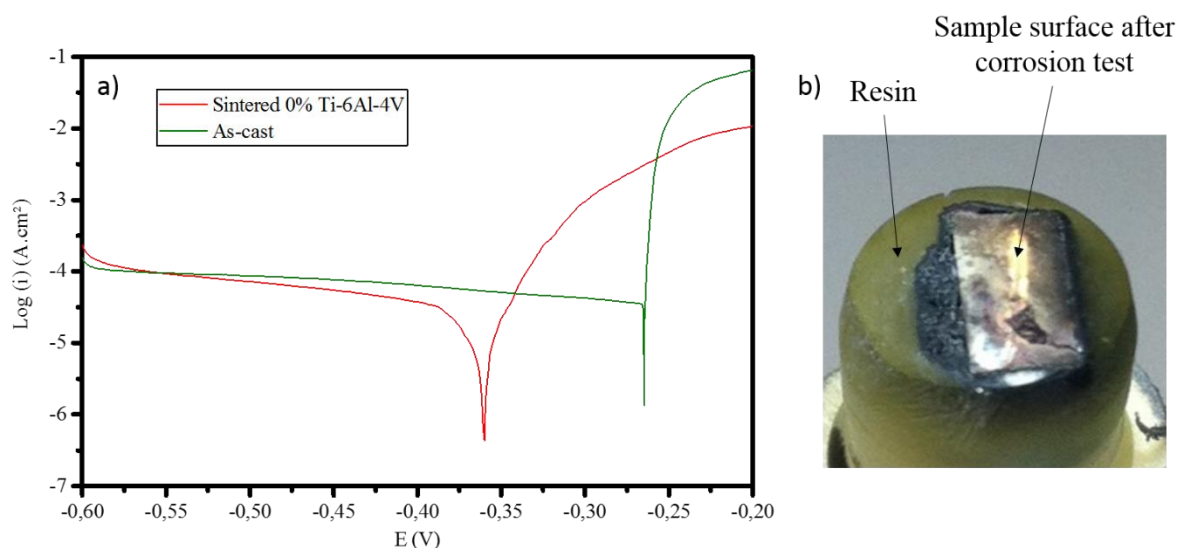


Figure 6-21: a) Polarization curves comparing two samples: sintered and cast. b) Photograph of the sample surface after the corrosion test.

The decrease in terms of corrosion resistance on the sintered samples can be explained by poor densified interfaces between particles leading to the presence of preferential sites for corrosion. This is proved by the broken surface of the sample after corrosion test.

#### 6-2-2-2-3- Mechanical Properties

In the 1 centimetre diameter sample after SPS process, three or four samples of 3 millimetres in diameter have been processed using electrical discharge machining (EDM). The samples for mechanical testing were, therefore, 4 millimetres high and 3 millimetres diameter. The mechanical tests for this part was done exactly with the same protocol as that used for all the other tests using an initial strain rate of about  $1.2 \times 10^{-4} \text{ s}^{-1}$ .

The results are shown in Figure 6-22.

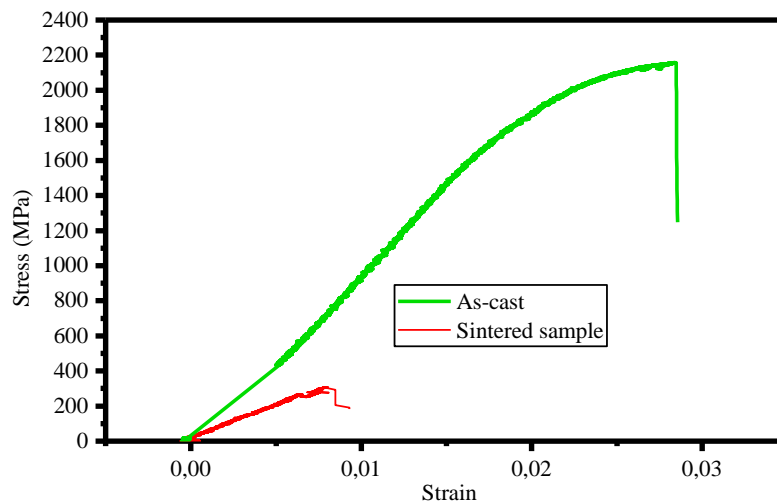


Figure 6-22: Compressive tests of the cast sample (green) and sintered sample (red) at  $1.2 \times 10^{-4} \text{ s}^{-1}$

First of all, the samples are very hard to process because of an apparent brittleness. Indeed, only 3 samples among 7 were correctly machined to undergo the compressive test. This fact contributes to confirm that this sample, as it is, will not resist to a high compressive load. Figure 6-22, shows that with this sample, the mechanical properties are far from the ones of a cast sample and the sintering process has to be improved.

## 6-3- Improvement of the system by composite samples processing

Because the sintered samples are too brittle, we decided to elaborate ex-situ composite, using crystalline particles to increase the ductility.

### 6-3-1- Processing of the composites samples

The chosen crystalline particles to add in the amorphous matrix are Ti-6Al-4V ones, which is the usual alloy used in biomedical applications. The characterization of the powder should be done before additions.

Figure 6-23 presents the Ti-6Al-4V powder, exhibiting a spherical shape. The size is distributed with an average of  $50 \mu\text{m}$  diameter and a maximum size about  $100 \mu\text{m}$ .

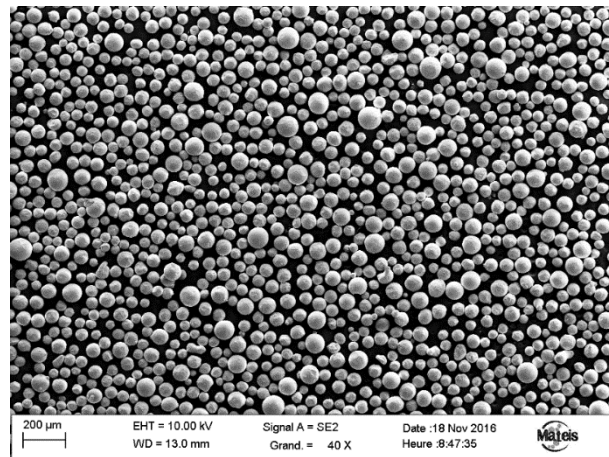


Figure 6-23: SEM Micrograph of the Ti-6Al-4V powder

The added mass fractions of crystalline particles tested are 10% and 30%. Higher volume fractions have not been addressed due to the loss of strength expected in that case.

Before setting up the powder in the graphite mould in order to carry out the sintering, the two powders, amorphous and crystalline, should be mixed together. They are placed in a closed bottle and manually mixed for five minutes. Then, the mixing was placed in the graphite mould and the proper pressure and temperature were applied to obtain composite samples.

The sintering conditions were the same as for the optimized sample without crystalline particles ( $T_s = 435^\circ\text{C}$ ,  $t_s = 5$  min).

After the processing, the density was measured and summarized in Table 4. In order to compare to the theoretical values of the density, the mixing law was applied to the system using the Eq. 2, to obtain the “theoretical density” values.

$$M_f \% = \frac{M_f \%}{M_f \% + \left(\frac{\rho_f}{\rho_m}\right)(1 - M_f \%)} \quad (3)$$

With  $M_f$ , the mass of the crystalline particles,  $M_f$ , the mass of the matrix,  $\rho_f$ , the mass fraction of the crystalline particles, and  $\rho_m$ , the mass fraction of the matrix.

Table 4: Characteristics of the elaborated composites samples

<b>Composition</b>	<b>Sintered density (g.cm<sup>-3</sup>)</b>	<b>Theoretical density (g.cm<sup>-3</sup>)</b>
0 % Ti-6Al-4V (0%)	7.5	7.54 (cast density)
10 % Ti-6Al-4V (10%)	7.08	7.22
30 % Ti-6Al-4V (30%)	6.21	6.59

The difference between the theoretical and the experimental values is significant. This could indicate a low densification of the samples in some areas or a small change in the composition during the process.

To observe the distribution of the crystalline particle in the matrix, SEM was conducted on the three compositions of the sintered samples. Figure 6-24 presents the micrographs.

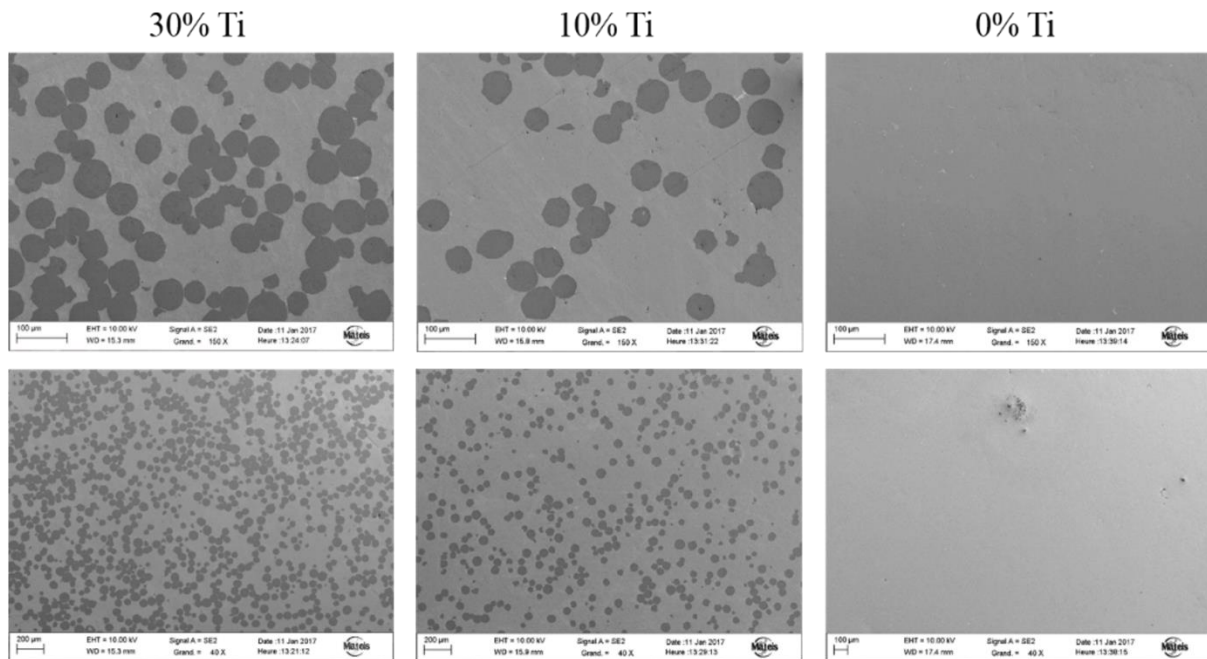


Figure 6-24: SEM micrographs of the crystalline particles distribution and surface observations

Using these results, the conclusion is that the sintered samples exhibit a good quality and seem to be fully densified. Moreover the particles are not homogeneously distributed in the sample. In some parts, the number of crystalline particles (dark grey) is more important. Several kinds of interfaces can be found: between two crystalline particles, between crystalline and amorphous particles or between two amorphous particles. All these differences cause more or less strong interfaces which will have an influence during mechanical tests.

XRD measurements were done in order to check the amorphous and semi-crystalline nature of the sample to be sure that the addition of crystalline particles does not disturb the sintering process (Figure 6-25).

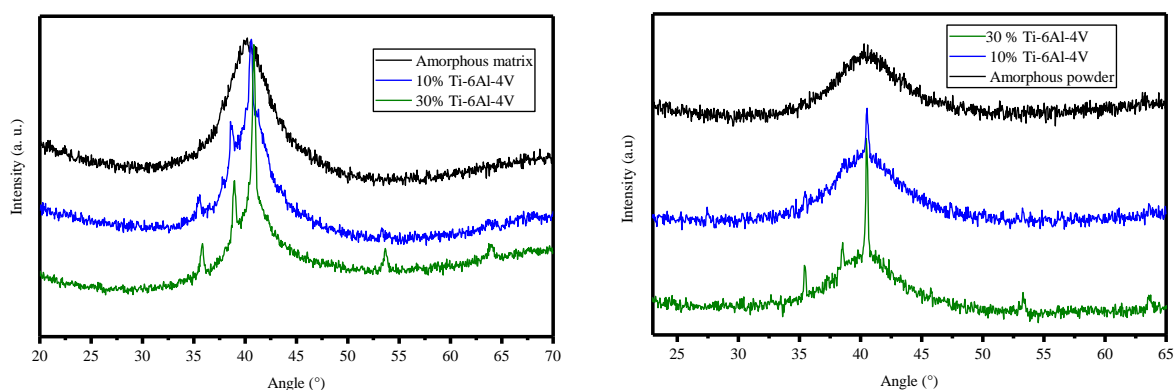


Figure 6-25: (Left) XRD diffractograms of the three samples: 0%, 10% and 30% Ti-6Al-4V, (Right) Comparison with the powder before sintering process.

The three curves exhibit the superposition of an amorphous shape and the crystalline peaks corresponding to Ti-6Al-4V particles, with an increase of the intensity depending on the added crystalline particles fraction.

At this stage, the sintering of the composite samples seems to have been conducted with a good compactness and no disturbance of the amorphous character of the matrix.

## 6-3-2- Characterization of the composites samples

### 6-3-2-1- Thermal Stability

Investigations have been made using high temperature XRD experiments, to ensure that the presence of crystalline particles does not affect the thermal stability of the sample. The results are exactly the same as for the fully amorphous sintered samples, except the readability of the results because of the presence of the crystalline peak, initially present. The crystallization temperature of the amorphous phase is about 460 °C for the non-isothermal treatment and the time of crystallization about 95 min for the isothermal treatment at this temperature.

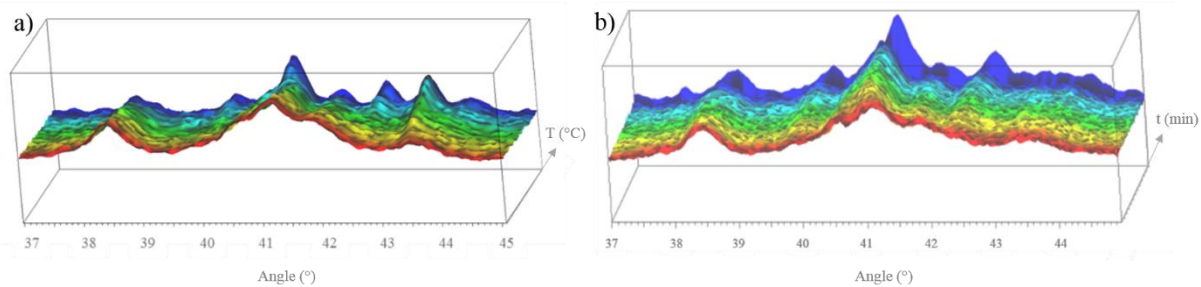


Figure 6-26: High temperature XRD 3D-spectra for the sample with 10% Ti-6Al-4V, a) isochronal measurement, b) isothermal measurement at  $T=460$  °C

The thermal stability of the sample is not affected by the presence of the crystalline particles. The amorphous phase in the composite samples exhibits the same resistance to crystallization during heat treatment.

### 6-3-2-2- Corrosion resistance

The corrosion resistance of the three samples was investigated using the same experimental procedure than previously, as shown in the Figure 6-27. The corrosion potential of all the sintered samples is lower than that of the cast sample, which is a predictable result because the sintering process does not fully suppress interfaces between powder grains. This constitutes preferential sites for the corrosion. Moreover, as it has been said, different interfaces exist: crystalline-crystalline, crystalline-amorphous, or amorphous-amorphous. Some of them are probably weaker than the other against corrosion and contribute to decrease the corrosion resistance. It makes the samples more sensitive to corrosion, whatever the medium used during the experiment.

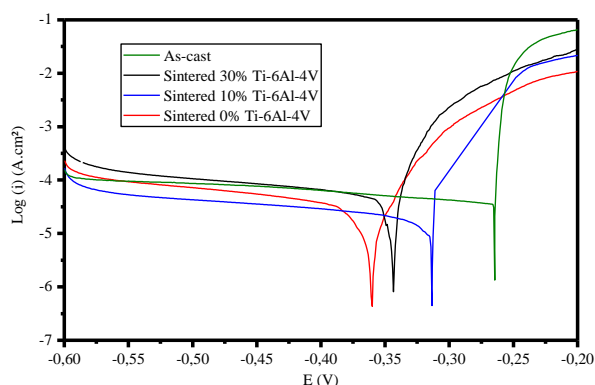


Figure 6-27: Polarization curves of all the samples: cast, 0%, 10% and 30% Ti-6Al-4V

However, another interesting result is that the sample containing 30% of Ti-6Al-4V exhibits lower corrosion potential than 10% of Ti-6Al-4V, which is in contrast with the expected results. Indeed, as the Ti-6Al-4V is resistant to corrosion, the higher the Ti-6Al-4V volume fraction, the better the sample should resist to corrosion. This could indicate an optimal fraction of Ti-6Al-4V to obtain a good sintering and keeping a low number of interfaces, to increase the corrosion resistance. However, the sample with 30% of crystalline particles seems to exhibit too many interfaces and thus, the corrosion resistance is lowered.

### 6-3-2-3- Mechanical Tests

As shown in Figure 6-28, compression tests have been conducted, three times for each composition. The sample without and with only 10% of crystalline particles exhibit a very low yield strength compared to the cast sample. The sample containing 30% of Ti-6Al-4V can reach higher yield strength, much closer to the cast sample. However, the sintering has to be improved to obtain mechanical properties similar to those of the cast sample because the ductility of this sample is still low.

The yield strength is supposed to be decreased by the addition of the Ti-6Al-4V particles. Calculating the theoretical yield strength values of the samples using a mixing law, we obtain 1680 MPa and 1880 MPa for the 30% and the 10% samples respectively. The experimental yield strength observed on Fig. 6-28 correspond to 98% and 32% of the theoretical value respectively. The conclusion of this is that the consolidation is good for the sample with 30 % of crystalline particles, but the sintering process is not optimal for the one with 10% and for the sample without any crystalline particles.

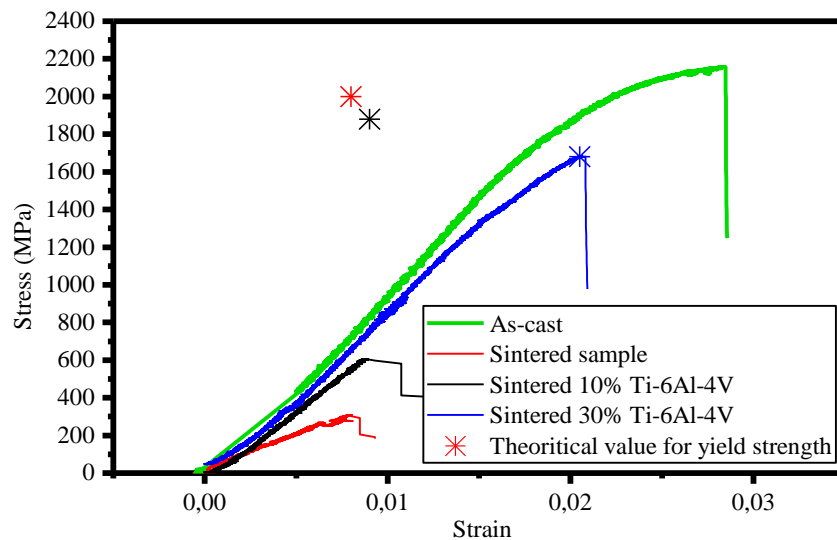


Figure 6-28: Compression tests of all the elaborated sintered composite samples compared to the cast sample

To investigate the reason of the poor ductility, SEM observations of the fracture surfaces have been realized. The fracture surfaces of the three different samples are shown in Figure 6-29.

In this figure, the particles are not distinguished, so the sintering seems to be strong. The sample after fracture does not exhibit only two pieces with a plane at  $45^\circ$ , as for the cast samples, but several pieces, indicating a fragmentation fracture mode and a poor adhesion between particles. Some parts of the fracture surface are at  $45^\circ$ , but some others are oriented along the sollicitation directions.

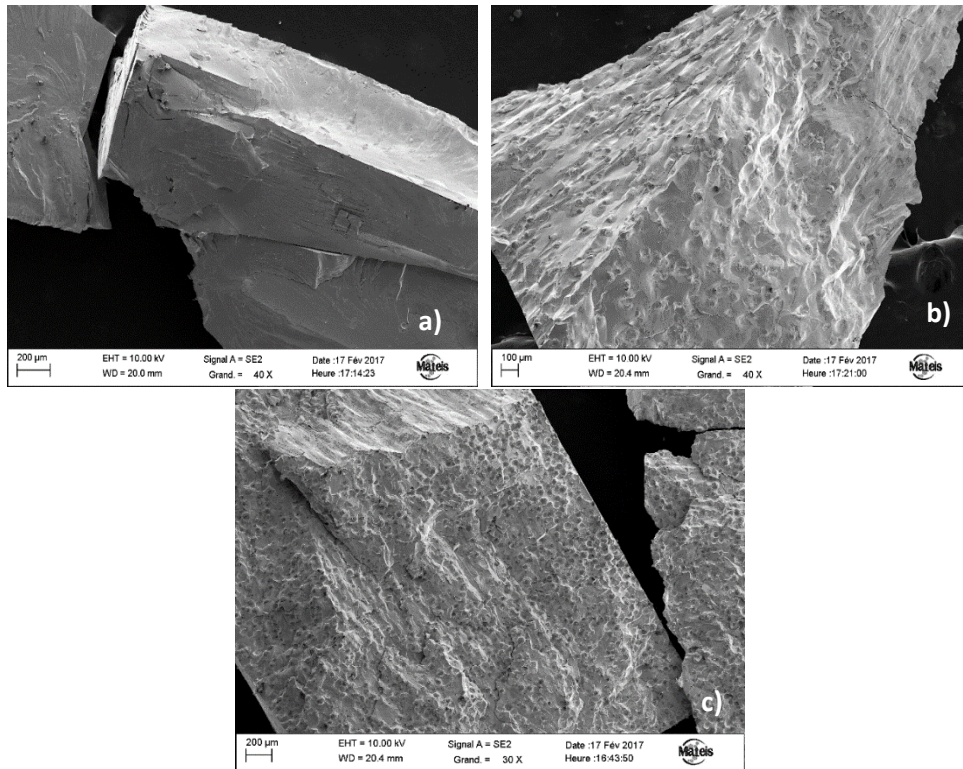


Figure 6-29: SEM micrographs of the fracture pieces of the sintered samples: a) 0% particles, b) 10% particles, c) 30% particles

In order to understand the fracture mechanisms, especially around the crystalline particles, SEM observations with higher magnification could be used. For example, it could provide information in case of the detachment at the interface between crystalline particles and amorphous matrix. Or if the crystalline particles are broken along the fracture plane. An observation of the pattern on the surface could also be a good indicator of the ductility.

Figure 6-30 shows the micrographs for all three samples.

The 0% sample exhibits a very brittle fracture, with no vein pattern, the entire sample suffered from a fracture mode by fragmentation, where the sample splits into fine particles. The surface exhibits many small pits corresponding to the fracture sites. The fracture surfaces are smooth without a vein or other pattern.

The fracture surface consists of a high number of small fracture zones, breaking the sample into many small parts. In the work of Zhang et al. <sup>36</sup>, a comparison of the mechanism in a pure shear fracture and a fragmentation fracture has been developed. To compare the brittleness, a fragmentation coefficient has been implemented:

$$F_n = \frac{A_n}{A_0} = 2^n - 1 \quad (4)$$

With  $A_n$ , the new surface area,  $A_0$  the original surface area for a sample broken into  $n$  pieces.

$F_n$  increases with the increase of pieces number after fracture. This coefficient determines the degree of brittleness of a sample. In the work of Zhang et al. <sup>36</sup>, a demonstration showed that a pure shear mode induces a special fragmentation mode with  $F_n=0.28$ , which is the lowest possible value of this coefficient. In this work, the number of particles after fracture was too high to be accurately evaluated. However, the pieces number for a sample without any crystalline particles was higher than for a composite.

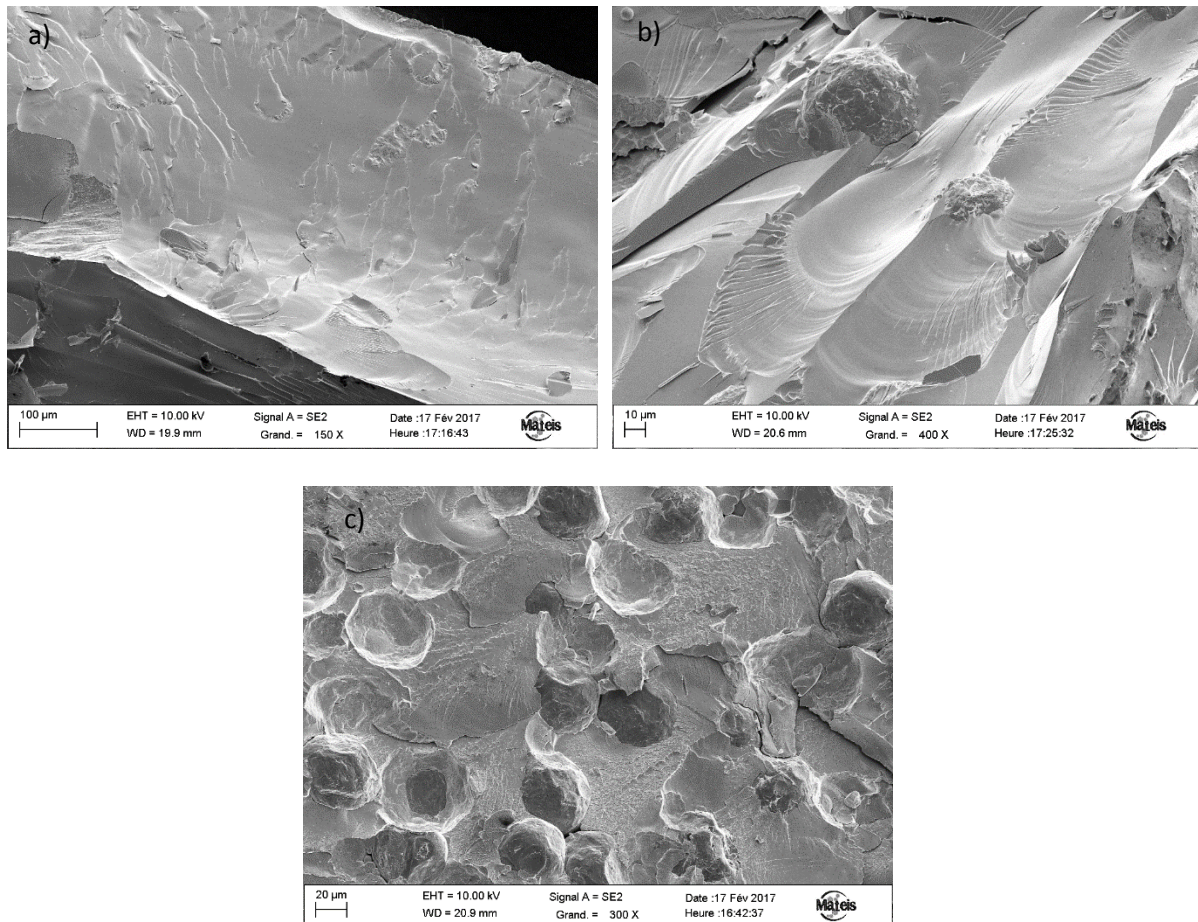


Figure 6-30: Higher magnification on the fracture topology a) 0% of crystalline particles, b) 10% and c) 30% Ti-6Al-4V

Concerning the sample with 10% and 30% Ti-6Al-4V, the fracture topology is more complex. In the interface between the crystalline particles and the amorphous matrix, two mechanisms are observed (Figure 6-30 c) and 6-31 a)). Some Ti-6Al-4V particles are peeled off from the matrix, because of a weak adhesion and some others are sheared and finally broken by the shear action. Two kinds of fracture morphologies are also presented in Figure 6-31 a): Mirror-like areas, meaning a brittle fracture and also vein patterns, meaning a local ductility. The same topology has been observed in the work of Hsieh et al. <sup>37</sup>. Vein patterns are only present on the cut particles because of a spreading of the amorphous part. Crystalline particles act like sites where the stress and shear band concentrations are increased, because of the difference in materials behaviour. Indeed, there exists a difference of Young modulus and of yield strength between the matrix and the particles. This leads to higher stresses at the interfaces. Vein patterns are the consequence of a large amount of strain along a shear band, then leading to a localized melting. The stress is also more concentrated in the interfaces areas

and when the stress concentration reaches the shears yielding level of the amorphous matrix, shear bands start to arise and slip<sup>38</sup>. The particles are like a network which separates and restricts the shear band in order to avoid the catastrophic failure. However, the particles in the two images do not present a deformed shape, which means that the energy of the shear band has not been absorbed by the ductile crystalline particles, in contrary to the work of Kinaka et al.<sup>38</sup>. In the work of Jang et al., which is based on a Mg-based, the minimum fraction to observe ductility on the stress-strain curves is 30 wt. % of Ti particles<sup>39</sup>.

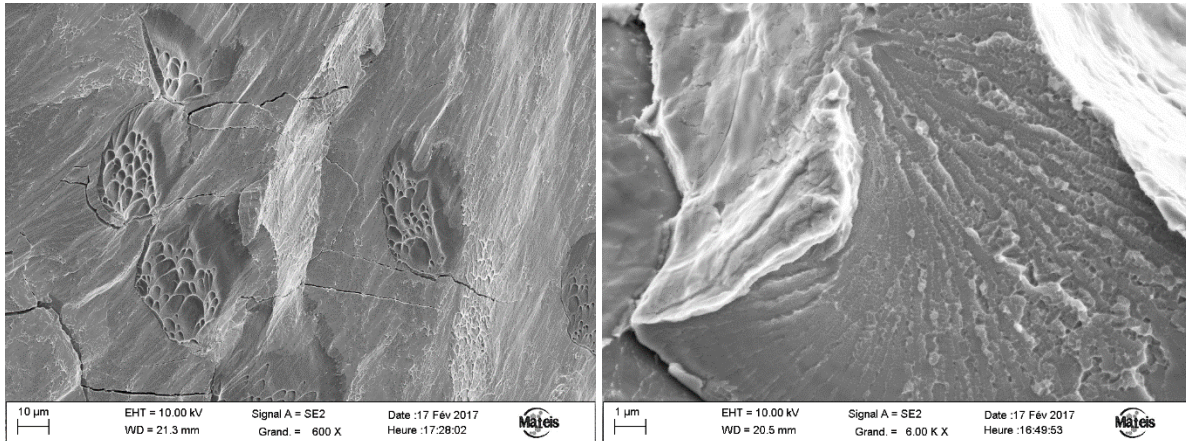


Figure 6-31: SEM micrographs of vein patterns of the composites fracture topology samples a) 10% and b) 30%

Some sintering issues have been found in the 30% Ti-6Al-4V samples, at the bottom of the sample (see Figure 6-31). The sintering has not been completed and this may be a cause of the poor mechanical properties and an early brittle fracture.

Another parameter could be noticed on the Figure 6-30, during the process, the high temperature used allows the deformation of the amorphous particles but not the crystalline particles. Ti-6Al-4V particles remain spherical after sintering and no change of shape appears, indicating that the crystalline particles are more difficult to deform. Indeed, the yield value is much higher for the amorphous powder than the crystalline one at ambient temperature. However, at a higher temperature, because of the glassy structure, once the glass transition is reached, the yield value of the amorphous powder is lower than the one of the crystalline particles. Thus, they are easier to deform.

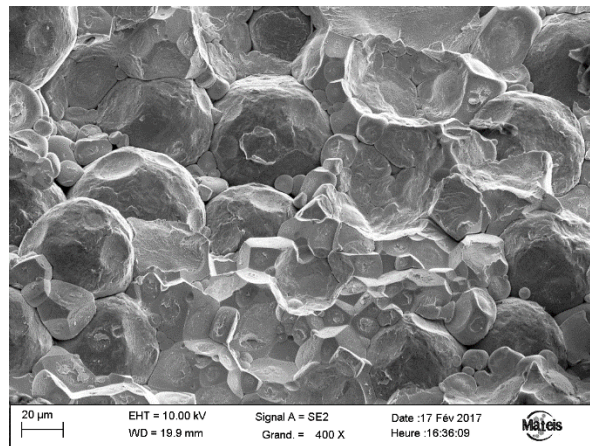


Figure 6-32: SEM picture of the bad quality of densification at the bottom of the 30% Ti-6Al-4V sample

Observing the Figure 6-31 a), the vein patterns are located in a small surrounding area. The crystalline particles seem to be broken during the fracture and a part of the amorphous matrix is lying on the particles. This part of the amorphous matrix exhibits vein patterns. It is like a spreading of the amorphous matrix of the crystalline particles. EDX experiments are conducted and given in Figure 6-33.

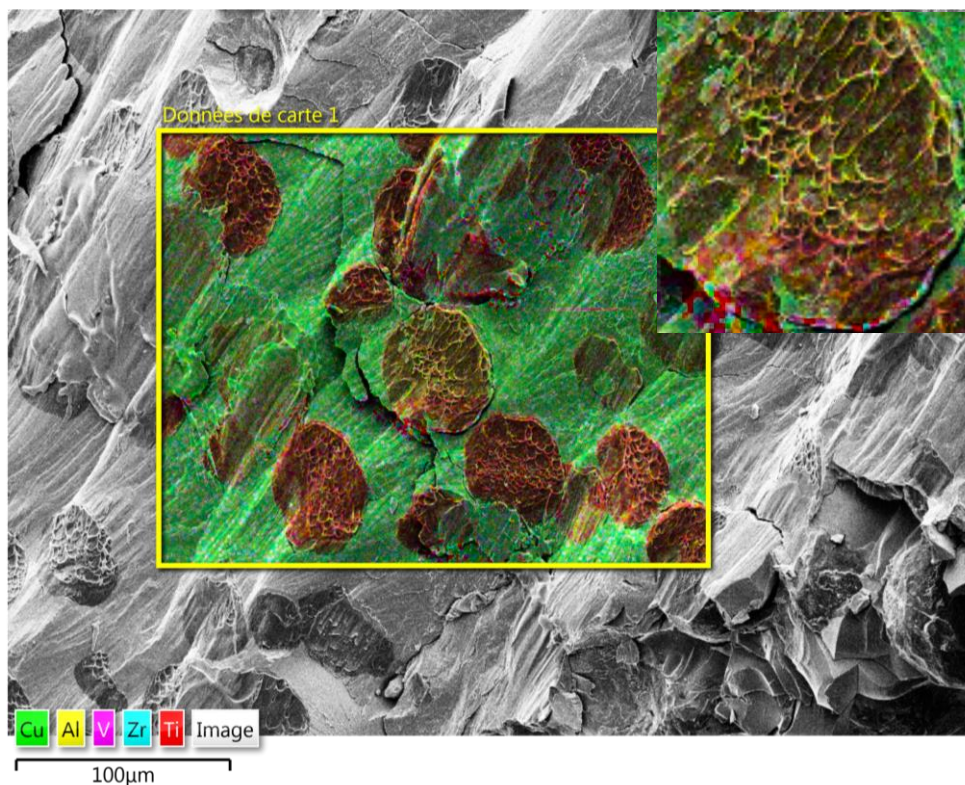


Figure 6-33: EDX map analysis of the fracture topology of the 30% sample

The vein patterns come from the amorphous matrix. However, they are located only on the Ti-6Al-4V particles by a spreading effect. At the interface between the matrix and the crystalline particles, the fracture seems to be more ductile and leads to vein pattern of the

amorphous phase in this area, contrary to the interface constituted of only amorphous particles, leading to a brittle fracture.

When particles are present in the sample, two kinds of fractures appear, either detachment of particles or fracture of the particles and spreading of the amorphous part in vein patterns on the particles.

## 6-4- Conclusion

A new process of manufacturing for metallic glasses has been conducted and optimized: the spark plasma sintering. The first step of the study is to investigate the influence of two parameters: sintering duration and sintering temperature to obtain good quality of samples for the characterization. The studies lead to choose a high temperature during a short time (435 °C during 5 min for a sample with a  $T_g = 445$  °C). The elaborated sample exhibits a size of one centimetre, which is a significant improvement compared to the cast sample. However, the corrosion resistance, the thermal stability and the mechanical properties, as the yield strength and the ductility, are all decreased. To obtain properties closest to the ones of the cast samples, introduction of crystalline particles in the amorphous matrix is needed. In this part, 30 wt % was a good fraction to obtain good mechanical properties, which is already an important fraction. The sintering process also could be improved to reach properties closed to those for a cast sample.

One possible outlook would be, and this has already been studied in other works, to use another BMG system or non-spherical particles of this material. The sample will exhibit higher compactness after the process because of the irregularities of the particles, as it is shown by the work of Cardinal et al.<sup>11</sup>, or in Zheng et al. work<sup>18</sup>. The sintering process can also be conducted in a controlled atmosphere containing Ar and 5% H in order to eliminate a potential oxide layer on the surface. Another way to process without the critical sintering quality criteria is to process in situ composites by precipitation of a crystalline phase using proper thermal treatment, as in the work of Song et al.<sup>40</sup>. However only few alloys are able to obtain improvement of mechanical properties by formation of in-situ composites. For example, the Cu-Zr-Al system, exhibits work hardening by the phase transformation between austenite CuZr B2 in martensite B19'<sup>44,45</sup>. The same phenomenon as in TRIP steels takes place and usually a compromise between the TRIP effect and the GFA is needed. Most part of time, the first phase to be formed is an intermetallic, which contributes to the brittleness of the alloy. The effect is the same as by particles additions, but the brittleness issues are prevented because the interfaces between the two phases are better.

The last outlook of this study is the processing of the possible porous bulk metallic glasses without losing mechanical properties<sup>22,436</sup>, which could be an advantage for the cellular growth.

## 6-5- References

1. Tsukerman, S. A. *Powder Metallurgy*. Pergamon Pres (1965).
2. Xie, G., Louzguine-Luzgin, D. V., Kimura, H. & Inoue, A. Nearly full density Ni<sub>52.5</sub>Nb<sub>10</sub>Zr<sub>15</sub>Ti<sub>15</sub>Pt<sub>7.5</sub> bulk metallic glass obtained by spark plasma sintering of gas atomized powders. *Applied Physics Letters* **90**, 241902 (2007).
3. Liu, L. H., Yang, C., Yao, Y. *et al.* Densification mechanism of Ti-based metallic glass powders during spark plasma sintering process. *Intermetallics* **66**, 1–7 (2015).
4. Scudino, S., Liu, G., Prashanth, K. *et al.* Mechanical properties of Al-based metal matrix composites reinforced with Zr-based glassy particles produced by powder metallurgy. *Acta Materialia* **57**, 2029–2039 (2009).
5. Lee, P. Y., Kao, M. C., Lin, C. K. & Huang, J. C. Mg–Y–Cu bulk metallic glass prepared by mechanical alloying and vacuum hot-pressing. *Intermetallics* **14**, 994–999 (2006).
6. Cardinal, S., Pelletier, J. M., Qiao, J. C., Bonnefont, G. & Xie, G. Influence of spark plasma sintering parameters on the mechanical properties of Cu<sub>50</sub>Zr<sub>45</sub>Al<sub>5</sub> bulk metallic glass obtained using metallic glass powder. *Materials Science and Engineering: A* **677**, 116–124 (2016).
7. Xie, G. Powder Metallurgy & Mining Spark Plasma Sintering: A Useful Technique to Develop Large-Sized Bulk Metallic Glasses. *Xie. J Powder Metall Min* **2**, (2013).
8. Bae, D. H., Lee, M. H., Kim, D. H. & Sordellet, D. J. Plasticity in Ni<sub>59</sub>Zr<sub>20</sub>Ti<sub>16</sub>Si<sub>2</sub>Sn<sub>3</sub> metallic glass matrix composites containing brass fibers synthesized by warm extrusion of powders. *Applied Physics Letters* **83**, 2312–2314 (2003).
9. Xie, G., Louzguine-Luzgin, D. V., Song, L., Kimura, H. & Inoue, A. Dual phase metallic glassy composites with large-size and ultra-high strength fabricated by spark plasma sintering. *Intermetallics* **17**, 512–516 (2009).
10. Drescher, P., Witte, K., Yang, B. *et al.* Composites of amorphous and nanocrystalline Zr–Cu–Al–Nb bulk materials synthesized by spark plasma sintering. *Journal of Alloys and Compounds* **667**, 109–114 (2016).
11. Cardinal, S., Pelletier, J. M., Xie, G. Q. & Mercier, F. Manufacturing of Cu-based metallic glasses matrix composites by spark plasma sintering. *Materials Science and Engineering: A* **711**, 405–414 (2018).
12. Yang, C.-C., Hang Chau, J. L., Weng, C.-J., Chen, C.-S. & Chou, Y.-H. Preparation of high-entropy AlCoCrCuFeNiSi alloy powders by gas atomization process. *Materials Chemistry and Physics* **202**, 151–158 (2017).
13. Yan, M., Yu, P., Kim, K. *et al.* The surface structure of gas-atomized metallic glass powders. *Scripta Materialia* **62**, 266–269 (2010).
14. Itoi, T., Takamizawa, T., Kawamura, Y. & Inoue, A. Fabrication of Co<sub>40</sub>Fe<sub>22</sub>Nb<sub>8</sub>B<sub>30</sub> bulk metallic glasses by consolidation of gas-atomized powders and their soft-magnetic properties. *Scripta Materialia* **45**, 1131–1137 (2001).
15. Al-Mangour, B. *Powder Metallurgy of Stainless Steel: State-of-the Art, Challenges, and Development*. *Stainless Steel* (2015).
16. Ramasamy, P., Shahid, R. N., Scudino, S., Eckert, J. & Stoica, M. Influencing the crystallization of Fe<sub>80</sub>Nb<sub>10</sub>B<sub>10</sub> metallic glass by ball milling. *Journal of Alloys and Compounds* **725**, 227–236 (2017).

17. Ramya, M., Karthika, M., Selvakumar, R., Raj, B. & Ravi, K. R. A facile and efficient single step ball milling process for synthesis of partially amorphous Mg-Zn-Ca alloy powders for dye degradation. *Journal of Alloys and Compounds* **696**, 185–192 (2017).
18. Zheng, B. *et al.* Influence of mechanically milled powder and high pressure on spark plasma sintering of Mg–Cu–Gd metallic glasses. *Acta Materialia* **61**, 4414–4428 (2013).
19. Cao, W. Synthesis of Nanomaterials by High Energy Ball Milling. *Skyspring Nanomaterials, Inc.* (2016). Available at: <http://www.understandingnano.com/nanomaterial-synthesis-ball-milling.html>. (Accessed: 17th June 2018)
20. Parekh, K. Basic Processes of Powder Metallurgy. *Technology* (2016). Available at: <https://www.slideshare.net/KedarParekh1/basic-processes-of-powder-metallurgy>. (Accessed: 17th April 2018)
21. Xie, G. Spark Plasma Sintering: A Useful Technique to Develop Large-Sized Bulk Metallic Glasses. *Journal of Powder Metallurgy & Mining* **02**, (2013).
22. Xie, G., Zhang, W., Louzguine-Luzgin, D. V., Kimura, H. & Inoue, A. Fabrication of porous Zr–Cu–Al–Ni bulk metallic glass by spark plasma sintering process. *Scripta Materialia* **55**, 687–690 (2006).
23. Perrière, L., Thai, M., Tusseau-Nenez, S. *et al.* Spark plasma sintering for metallic glasses processing. *Revue de Métallurgie* **109**, 5–10 (2012).
24. Nowak, S., Perrière, L., Dembinski, L., Tusseau-Nenez, S. & Champion, Y. Approach of the spark plasma sintering mechanism in Zr<sub>57</sub>Cu<sub>20</sub>Al<sub>10</sub>Ni<sub>8</sub>Ti<sub>5</sub> metallic glass. *Journal of Alloys and Compounds* **509**, 1011–1019 (2011).
25. Kopeliovich, D. Graphite manufacturing process. (2013). Available at: [http://www.substech.com/dokuwiki/doku.php?id=graphite\\_manufacturing\\_process](http://www.substech.com/dokuwiki/doku.php?id=graphite_manufacturing_process). (Accessed: 17th April 2018)
26. Wang, Z., Scudino, S., Prashanth, K. G. & Eckert, J. Corrosion properties of high-strength nanocrystalline Al<sub>84</sub>Ni<sub>7</sub>Gd<sub>6</sub>Co<sub>3</sub> alloy produced by hot pressing of metallic glass. *Journal of Alloys and Compounds* **707**, 63–67 (2017).
27. Srivastava, A. P., Tong, M., Ştefanov, T. & Browne, D. J. Elimination of porosity in bulk metallic glass castings using hot isostatic pressing. *Journal of Non-Crystalline Solids* **468**, 5–11 (2017).
28. Deloro Wear Solutions. Hot Isostatic Pressing. (2016). Available at: <https://www.deloro.com/hot-isostatic-pressing/>. (Accessed: 17th April 2018)
29. Whittaker, D. Australian titanium: A new continuous process for the direct production of CP Ti powder developed at CSIRO. (2012). Available at: <http://beta.ipmd.net/articles/001587.html>. (Accessed: 17th April 2018)
30. Kawamura, Y., Kato, H., Inoue, A. & Masumoto, T. Full strength compacts by extrusion of glassy metal powder at the supercooled liquid state. *Applied Physics Letters* **67**, 2008–2010 (1995).
31. Dai, C. L., Deng, J. W., Zhang, Z. X. & Xu, J. Cu-Zr-Ti ternary bulk metallic glasses correlated with (L → Cu<sub>8</sub>Zr<sub>3</sub>+ Cu<sub>10</sub>Zr<sub>7</sub>) univariant eutectic reaction. *Journal of Materials Research* **23**, 1249–1257 (2008).
32. Dai, C.-L., Guo, H., Li, Y. & Xu, J. A new composition zone of bulk metallic glass formation in the Cu–Zr–Ti ternary system and its correlation with the eutectic reaction. *Journal of Non-Crystalline Solids* **354**, 3659–3665 (2008).
33. Jia, P., Guo, H., Li, Y., Xu, J. & Ma, E. A new Cu–Hf–Al ternary bulk metallic glass with high glass forming ability and ductility. *Scripta Materialia* **54**, 2165–2168 (2006).

34. Wesseling, P., Nieh, T. G., Wang, W. H. & Lewandowski, J. J. Preliminary assessment of flow, notch toughness, and high temperature behavior of  $\text{Cu}_{60}\text{Zr}_{20}\text{Hf}_{10}\text{Ti}_{10}$  bulk metallic glass. *Scripta Materialia* **51**, 151–154 (2004).
35. Inoue, A., Zhang, W., Zhang, T. & Kurosaka, K. Cu-based bulk glassy alloys with high tensile strength of over 2000 MPa. *Journal of Non-Crystalline Solids* **304**, 200–209 (2002).
36. Zhang, Z. F., Zhangy, H., Shenz, B. L., Inouez, A. & Eckertx, J. Shear fracture and fragmentation mechanisms of bulk metallic glasses. *Philosophical Magazine Letters* **86**, 643–650 (2006).
37. Hsieh, P. J., Yang, L. C., Su, H. C., Lu, C. C. & Jang, J. S. C. Improvement of mechanical properties in  $\text{MgCuYNdAg}$  bulk metallic glasses with adding Mo particles. *Journal of Alloys and Compounds* **504**, S98–S101 (2010).
38. Kinaka, M., Kato, H., Hasegawa, M. & Inoue, A. High specific strength Mg-based bulk metallic glass matrix composite highly ductilized by Ti dispersoid. *Materials Science and Engineering: A* **494**, 299–303 (2008).
39. Jang, J. S. C., Chang, Y., Li, T. *et al.* Plasticity enhancement of  $\text{Mg}_{58}\text{Cu}_{28.5}\text{Gd}_{11}\text{Ag}_{2.5}$  based bulk metallic glass composites dispersion strengthened by Ti particles. *Journal of Alloys and Compounds* **504**, S102–S105 (2010).
40. Song, K. K., Han, X., Pauly, S. *et al.* Rapid and partial crystallization to design ductile CuZr-based bulk metallic glass composites. *Materials & Design* **139**, 132–140 (2018).
41. Sarac, B., Söpu, D., Park, E. *et al.* Mechanical and Structural Investigation of Porous Bulk Metallic Glasses. *Metals* **5**, 920–933 (2015)



# Chapter 7

## Influence of the rejuvenation mechanisms on ductility of BMGs

---

<b>CHAPTER VII</b> .....	<b>196</b>
<b>INFLUENCE OF THE REJUVENATION MECHANISMS ON THE DUCTILITY OF BMGS</b> .....	<b>197</b>
<b>7-1- Rejuvenation in metallic glasses</b> .....	<b>197</b>
7-1-1- What is rejuvenation? .....	197
7-1-1- How to obtain rejuvenation? .....	198
<b>7-2- Methods</b> .....	<b>202</b>
7-2-1- Experimental compressive tests .....	202
7-2-2- Simulation methods .....	204
<b>7-3- Results</b> .....	<b>205</b>
7-3-1- Mechanical properties of pre-cycled Cu-Zr metallic glass: experimental results .....	206
7-3-2- Mechanical properties of pre-cycled Cu-Zr metallic glass: molecular dynamics simulations .....	207

<b>7-4- Discussion about elementary deformation processes responsible for the ductility increase .....</b>	<b>209</b>
<b>7-4-1- Fracture plane topology analysis .....</b>	<b>210</b>
7-4-1-1- Vein pattern size analysis	210
7-4-1-2- Discussion about the toughness evaluation	212
7-4-1-3- Differences on the amplitude of pre-cycling	213
<b>7-4-2- Verification using molecular dynamics &amp; complementary experimental analysis .....</b>	<b>214</b>
7-4-2-1- Complete study of N and $\sigma_c$ using molecular dynamic	214
7-4-2-1- Adaptation to the strain rates influence	215
<b>7-5- Conclusion.....</b>	<b>217</b>
<b>7-6- References .....</b>	<b>217</b>

---

## Chapter VII

# Influence of the rejuvenation mechanisms on the ductility of BMGs

(This work has been done in collaboration with Jonathan Amodeo and David Rodney)

In the Cu-Zr-Ti system, several mechanisms were investigated to improve the critical size and ductility. In Chapter 5, we dealt with microalloying of rare earth elements, while Chapter 6 was devoted to another processing route based on powder metallurgy. In this chapter, a recent method developed to improve ductility is investigated. This process, called “rejuvenation” is the opposite of structural relaxation. Rejuvenation knows an increasing interest since 2010 and the work of Dmowski et al.<sup>1</sup>. First, the different methods allowing to reach this state will be explained, and our work on the influence of the pre-cycling compressive tests will be developed.

## 7-1- Rejuvenation in metallic glasses

### 7-1-1- What is rejuvenation?

It has already been mentioned that mechanical properties of metallic glasses strongly depend on their structural stability and their atomic packing density<sup>2</sup>. At room temperature, the deformation of metallic glasses is heterogeneous, ruled by the dilatation and softening in some areas due to the free volume difference. This free volume induces difference of compactness in the samples and the lowest compact zones act as preferential site to initiate the shear transformation zones (STZs) first, and then the shear bands.

It has been presented in Chapter 1 that, after the quench, the system can evolve towards a lower energy state, keeping its amorphous character. This is the so-called, structural relaxation. For example, annealing can cause structural relaxation in a metallic glass. During this step, the free volume decreases and the density increases. Moreover, because of the structural heterogeneities drop, the material becomes more brittle, the strain is strongly localized and the shear bands are supposed to be larger with a higher offset between each other<sup>3</sup>.

In the opposite, the system can also evolve towards a higher energy state with a lower density. Thus, the plastic deformation is enhanced and the ductility is increased. This mechanism is called “rejuvenation”.

In order to obtain a rejuvenated metallic glass samples, several methods described in the next part have been developed for ten years: plastic deformation, thermal ageing, irradiation...

These two different mechanisms (structural relaxation and rejuvenation) are illustrated in Fig. 7-1.

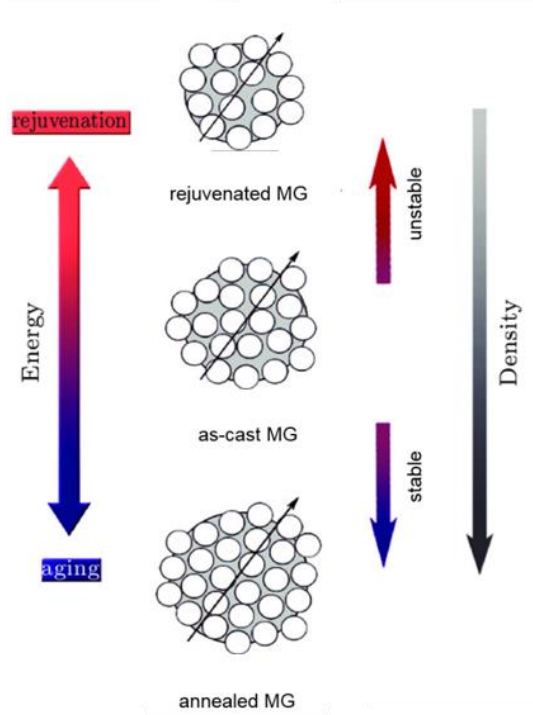


Figure 7-1: Schematic representation amorphous structures differences between structural relaxation and rejuvenation <sup>4</sup>

### 7-1-2- How to obtain rejuvenation?

To conduct rejuvenation in a metallic glass sample, several ways can be employed to increase the energy level, depending on the targeted applications.

- Severe Plastic Deformation (SPD)

Energy is brought to the sample with a high level deformation and a fraction of this energy is stored leading to higher energy states. This technique causes a change in the shape of the sample. However, after the deformation, the samples could exhibit higher ductility.

Several means can be used to conduct SPD, such as cold-rolling <sup>5</sup>, high-pressure torsion (HPT), as shown in Fig. 7-2 <sup>1,6</sup>, or surface treatment as shot-peening <sup>7-9</sup>. Dmowski et al. used the atomic pair distribution function (PDF) to show that not only free volume is

created during SPD but more extensive atomic rearrangements take place. To perform these technique, the samples need to exhibit a bit of ductility at room temperature.

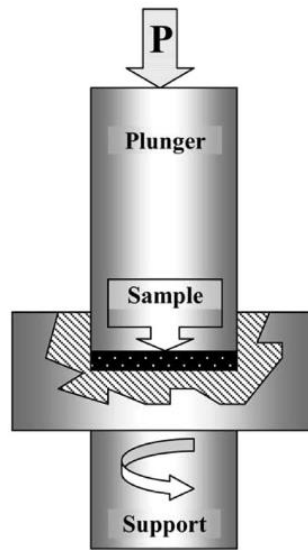


Figure 7-2: Schematic representation of the High-Pressure Torsion (HPT) technique <sup>10</sup>

Lee et al. show that the enhancement of free volume makes the creation of STZs easier<sup>2</sup>. Moreover, it lowers the atomic bonding. Multiple shear bands can be initiated in many local areas and the plastic deformation appears at a lower stress.

Concerning the shot-peening, Concustell et al. demonstrated that it can introduce defects where shear bands are initiated<sup>9</sup>. However, it also anneals them in the matrix between the bands. This effect depends on the initial state of the sample.

Qiao et al. also study the effect of the thermal annealing and cold rolling on the atomic mobility<sup>11</sup>. They conclude that atomic mobility is reduced by ageing but enhanced by cold rolling and explain it using the quasi-point defect model. They evaluate the atomic mobility of a BMGs in different states using dynamic mechanical analysis (DMA)<sup>12</sup>.

- Thermal cycling

For a few years, a wide range of works deal with this technique <sup>3,13-17</sup>. Due to the structural heterogeneities of this kind of material, thermal expansion during a temperature change will not be the same in the entire samples, creating expansion or contraction. Local stresses will induce internal strains. This internal defect introduction leads to rejuvenate the sample and increase the ductility. However, to avoid crystallization or structural relaxation, the range of temperature used is cryogenic (77 K). This technique is adapted to all the sample shapes, and it is also non-destructive, isotropic and generates no change in geometry. However, this is not permanent, as it disappears after a relaxation time at room temperature <sup>13</sup>. Bian et al. try to explain the enhancement of the mechanical properties with the decrease of the temperature by a structural approach, using the Varshni expression <sup>17</sup>.

- Irradiation

Irradiation is a surface treatment technique, which can be conducted using different means, as for example ions or neutrons<sup>18-21</sup>. Laser technique used to tune the mechanical properties of metallic glasses is a very recent technique investigated for only few years. For example, in the work of Huang et al.<sup>22</sup>, nanosecond pulsed laser irradiation is used to soften some areas. They also showed that it enhances the serrated flow in the load depth.

In the work of Bian et al.<sup>20</sup>, the Xe-ions are used to control the free volume fraction and homogenize it by a low dose of ion irradiation.

However, this technique exhibits a drawback due to the limited penetration depth of the primary knock-on damage, it can thus, be used only on the nanoscale sample.

- Elastostatic loading

Lee et al. highlighted that even compressive tests in the elastic range of the system can lead to rejuvenation of the material, even at room temperature<sup>23</sup>. They conducted a compressive test of a Cu-Zr sample between 50% and 90% of the yield strength for 12h. Then, after subsequent tests, they concluded that the elastostatic compression for a long time leads to the formation of viscoelastic strain, inducing irreversible deformations. However, the induced deformation is homogeneous and causes no shear bands formation. They also reported that free volume increases with the level of compression, leading to an increase of plasticity but a decrease of the yield strength. Several other works have drawn the same conclusion<sup>24-27</sup>.

- Heating above glass  $T_g$  followed by fast cooling

Wakeda et al. report a recipe to obtain a controlled degree of rejuvenation by annealing the sample above  $1.1 T_g$ , followed by a fast quench, with a rate exceeding the previous one<sup>28</sup>. They also designed out a rejuvenation map providing the temperature-cooling rate conditions to obtain the targeted degree of rejuvenation. This theory has been proved by experiments on a Zr-based sample.

Based on the stored energy, which is related to the rejuvenation degree, Greer and Sun highlighted that the stored energy is similar between the different techniques: thermal cycling, elastostatic compressing and severe plastic deformation<sup>3</sup>. They focused their work on thermal cycling and elastostatic compressing and report a study investigating the origins of stored energy, which should be different from those operating in energetic processes (as SPD).

All these techniques are based on the addition of structural changes. Due to the heterogeneities in the structure of this kind of material, excess free volume and anti-free volume are generated, inducing local strains and stresses. The atomic packing density becomes lower and shear bands can be initiated at lower stresses. This leads to the homogenization of the deformation and a plasticity increase. However, mechanisms are not fully clear yet, and none of the techniques listed above proposes a permanent mechanism without any geometry modification. Cyclic loading with a few number of cycles (between 5 and 40 maximum) has already been used to investigate the hardening by nanoindentation<sup>29,30</sup> associated with molecular dynamic. The hypothesis to explain this phenomenon was first, a structural change creating stiffened region carrying higher stresses, or secondly the formation of harder areas, deviating the shear bands path and increasing the stress to create a new path<sup>31</sup>. However, no compressive cycling tests have been conducted yet to investigate the plastic deformation process.

This work proposes an investigation using both experimental compressive tests in the elastic range using a statistical analysis of the fracture plane and atomistic simulation by molecular dynamics, to understand the shear band nucleation and the influence of pre-cycling tests on the plasticity. This way exhibits the advantage to be non-destructive and permanent.

## 7-2- Methods

In this part, experimental compressive tests and atomistic simulation by molecular dynamics will be described.

### 7-2-1- Experimental compressive tests

In order to find a new way to increase the plasticity of a metallic glass sample, pre-loading compressive tests have been conducted. The preliminary results carried out in this study were first done using Cu-Zr-Ti-Y samples, as in other chapters. However, due to the low critical diameter (3 mm), and the targeted experiments with successive loading and unloading compressive tests, we used a system with a higher GFA to conduct reliable and reproductive tests. Thus, another system (close to the one investigated in the previous chapters) has been chosen: Vitreloy 105 ( $Zr_{52.5}Cu_{17.9}Ni_{14.6}Al_{10}Ti_5$ ). The main advantage is the large glass forming ability of this alloy. The 3 mm diameter samples of metallic glass will be isotropic, homogeneous and exhibit a higher reproducibility for compressive tests with successive loading steps.

First, master ingots have been melted using arc melting technique, under Ar-gas and Zr-gettered atmosphere. The raw materials used, have been Zr (99.99%), Cu (99.99%), Ni (99.9%), Al (99.98%) Ti (99.99%). Then, by suction casting technique, 3 mm diameter rods have been processed. This processing has been conducted in SIMAP laboratory. The compressive

test samples were cylinders cut in 4 mm long with a wire saw then polished with SiC 1200 to obtain plane and parallel surfaces. The cylindrical surface has also been polished using the same way to observe potential shear bands formation after compressive tests.

The tests have been conducted using an INSTRON 5967 apparatus, equipped with a video extensometer to precisely determine the deformation. First, in order to study pre-cycling effect, the lowest strain rate has been chosen,  $1.2 \times 10^{-4} \text{ s}^{-1}$ . Several number of cycles (N) have been conducted: 0, 2, 4 and 6. Also the effect of the compressive load amplitude ( $\sigma_c$ ) has been investigated with the following value of amplitude: 400 MPa (22% of the yield strength), 700 MPa (39% of the yield strength) and 1200 MPa (66% of the yield strength). Then, to enlarge the investigation about the strain rate influence, three strain rates in the quasi-static range have been tried:  $1.2 \times 10^{-4} \text{ s}^{-1}$ ,  $1.2 \times 10^{-3} \text{ s}^{-1}$  and  $1.2 \times 10^{-2} \text{ s}^{-1}$ . Ten tests for each strain rate have been conducted.

Fig. 7-3 shows the setting up of the compressive test.

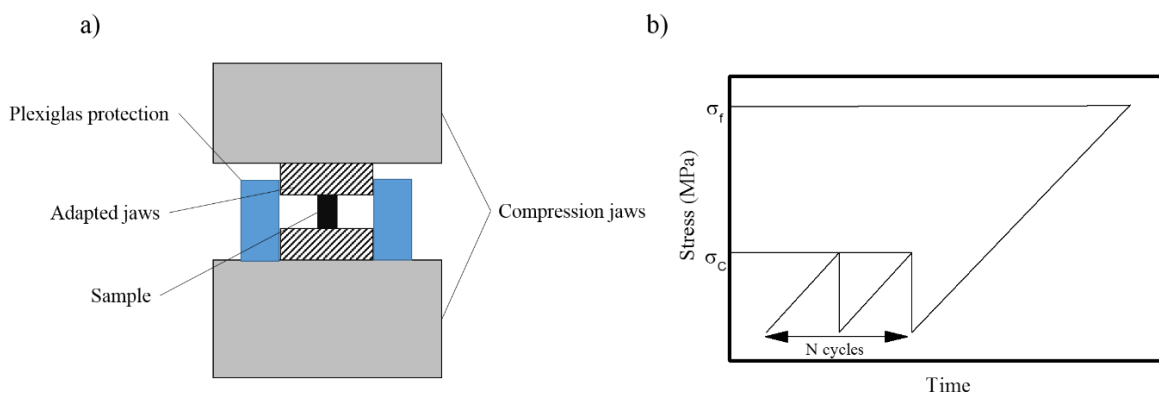


Figure 7-3: a) Picture of the compressive apparatus, b) schematic representation of the sample setting up.

To relate the macroscopic behaviour to the fracture plane microstructure and to evaluate the influence of the strain rate or of pre-cycling, SEM micrographs have been carried out using ZEISS Supra 55 VP at 10 kV. The measurement of the vein pattern areas have been performed using the Fiji software<sup>32</sup>. Fig. 7-4 summarizes the measurement process: three pictures for each tested sample have been taken, then between 330 and 340 measurements for each picture have been realized. In total, 1000 measurements for a test have been performed. To enlarge the investigation on the strain rate evaluation, ten tests for each strain rate have been conducted to increase the measurements number about to 3000 for each strain rate value.

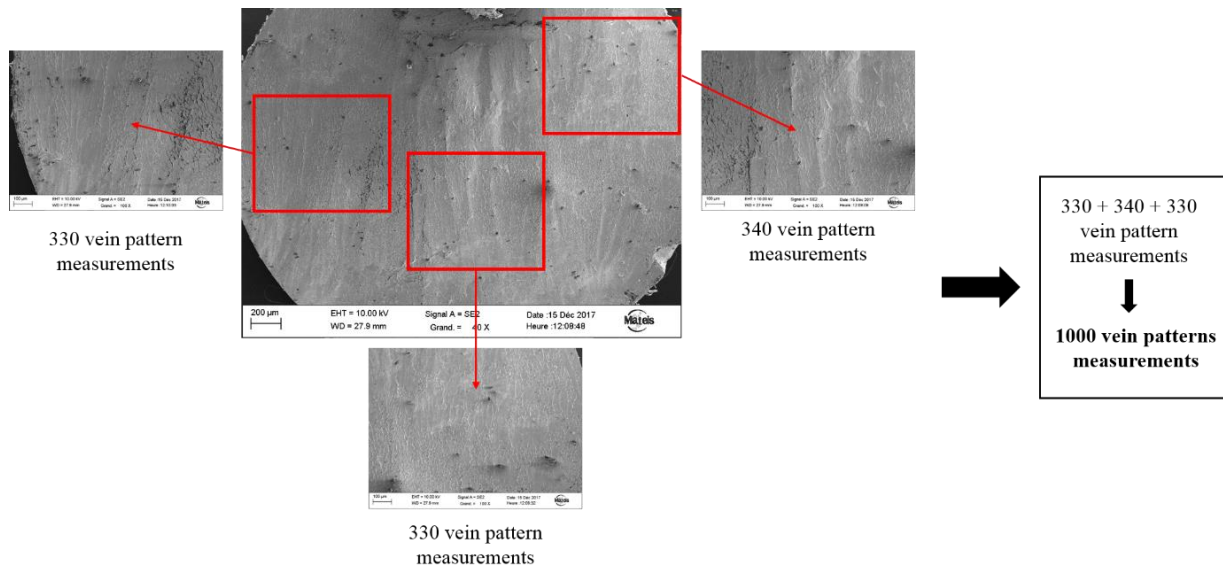


Figure 7-4: Picture of the measurement method to determine the vein pattern area in order to study the pre-cycling influence. The measurement number increases to 3000 for the strain rate influence study.

Coupled with experimental technique based on statistical data, atomistic simulation has been used to confirm or explain the conclusion of the experiments. The technique employed was the molecular dynamic (MD), as described below.

### 7-2-2- Simulation methods

MD simulations were performed using the Mendeleev EAM potential<sup>31</sup>, which is regularly used to model the deformation of Cu-Zr metallic glasses. Besides the system (which is a simple binary) and the deformation rate, which are widely different than from the experiments, molecular dynamics simulation are known to provide a qualitative framework to investigate Cu-Zr glass elementary deformation processes and discuss experimental studies.

The composition used in the simulation is  $\text{Cu}_{64.5}\text{Zr}_{35.5}$ . The fabrication method is similar to the one of Cao et al.<sup>31</sup> which is commonly used in the literature. First, a small  $\text{Cu}_{64.5}\text{Zr}_{35.5}$  simulation box containing 13 500 atoms ( $6.3 \times 6.3 \times 6.3 \text{ nm}^3$  cell, fcc positions) The amorphous alloy is then constructed using a typical melting-quenching technique i. e. the system first equilibrated at 2000 K (beyond the melting temperature) for 2 ns ( $dt=1 \text{ fs}$ ) using the NPT ensemble and then, the system is quenched down to 50 K. Several cooling rates of 10 K/ns, 1000 K/ns, and  $10^5 \text{ K/ns}$  were tested to investigate different relaxation states. Before compression, the system is replicate, up to  $39.2 \times 6.3 \times 45.8 \text{ nm}^3$  (675 000 atoms), and equilibrated for another 0.5 ns at 800 K to relax interfaces between replicas (Fig.7-5).

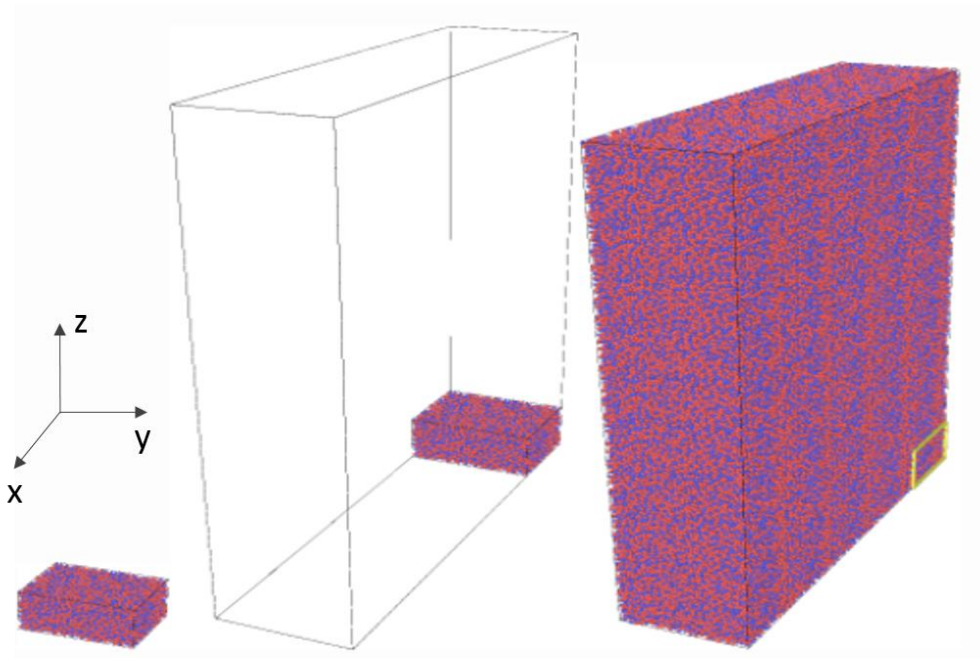


Figure 7-5: Illustration of the Cu-Zr sample before and after replication

The mechanical behaviour of the final quasi-2D sample cooled down at 10 K/ns is probed using a simulated uniaxial compressive test, as commonly conducted in laboratory experiments. The uniaxial compressive force is along z-direction while free space is introduced between the box and the sample, along the x direction, to generate artificial free surfaces. Different strain rates of:  $10^8 \text{ s}^{-1}$ ,  $10^9 \text{ s}^{-1}$  and  $10^{10} \text{ s}^{-1}$  are tested. Compressive simulations are performed at  $T=50\text{K}$ .

Pre-cycling is applied up to equivalent stresses from 200 MPa up to 3000 MPa.

In the following, plastic shear events are identified using the non-affine squared displacement ( $D^2_{\min}$ ) as defined by Falk and Langer<sup>33</sup> and implemented within the Ovito software.  $D^2$  is the mean-square difference between neighbouring atoms relatively to a central one and the one they would have under uniform strain. Indeed, only atoms with  $D^2_{\min} > 100$  are shown.

### 7-3- Results

First, the results of the experimental work on the role of pre-cycling on the macroscopic mechanical response are described. Then, atomic scale deformation mechanisms are investigated by means of molecular dynamics simulations.

### 7-3-1- Mechanical properties of pre-cycled Cu-Zr metallic glass: experimental results

Yield strengths and strains obtained after compressing pre-cycled samples with various number of cycles (0, 2, 4 and 6) and pre-cycle stress amplitude (400, 700 and 1200 MPa) are presented in Fig. 7-7. Compressive tests are shown in Fig. 7-6.

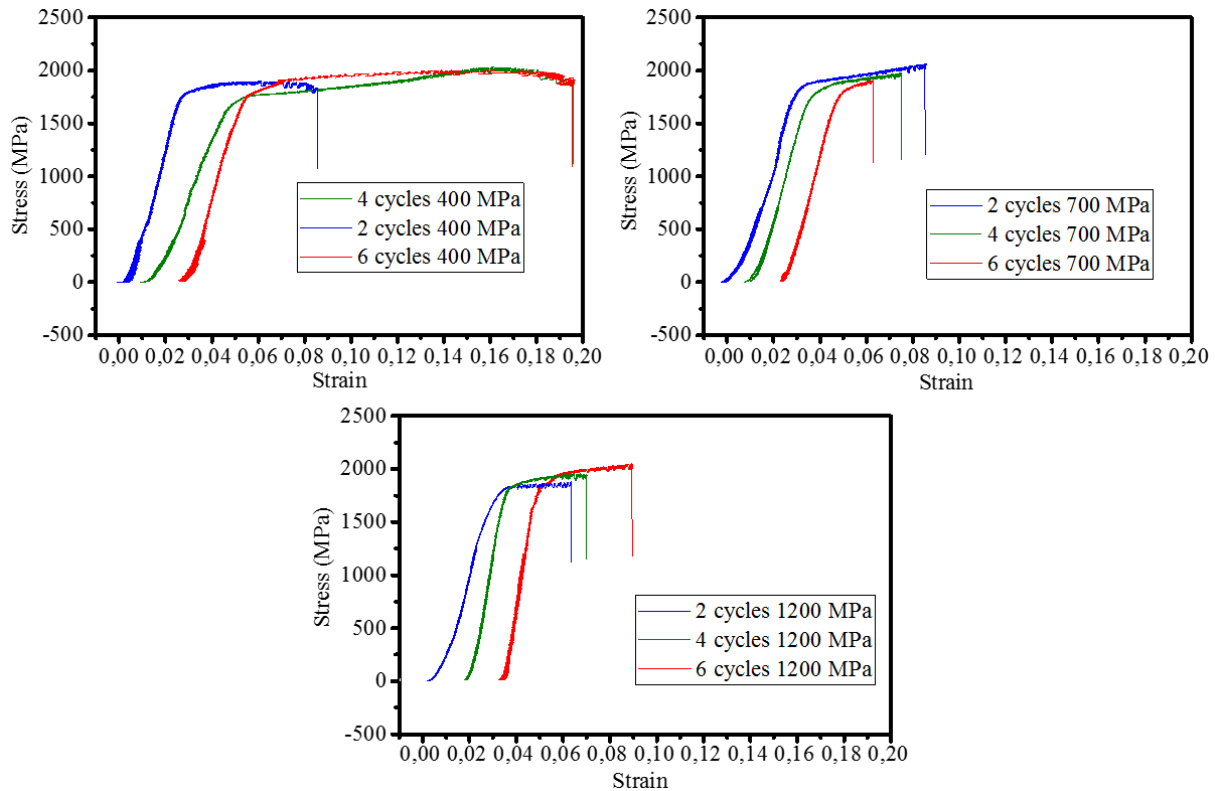


Figure 7-6: Stress-Strain curve for pre-cycled samples, at 400 MPa, 700 MPa and 1200 MPa, 2, 4 and 6 cycles

The as-cast sample ( $N=0$ ) exhibits a yield strength of about 1843 MPa and a plastic strain of about 3%. This last value is lower when compared to the plastic strain for pre-cycled samples (between 3 and 15 %). A strong beneficial effect on the plastic strain is clear between 2 and 4 cycles at 400 MPa pre-cycle stress amplitude, while no real difference between 4 and 6 cycles have been observed. For the pre-cycling at 700 MPa, a strong effect is noticed between 0 and 2 cycles, but then the ductility of the sample decreases (Fig. 7-7b). At least, concerning the pre-cycling at 1200 MPa, no clear beneficial or detrimental action on the plastic strain of the sample appears.

On the other hand, no real quantitative effect is noticed or perhaps a slight trend to decrease on the yield strengths (Fig. 7-7a).

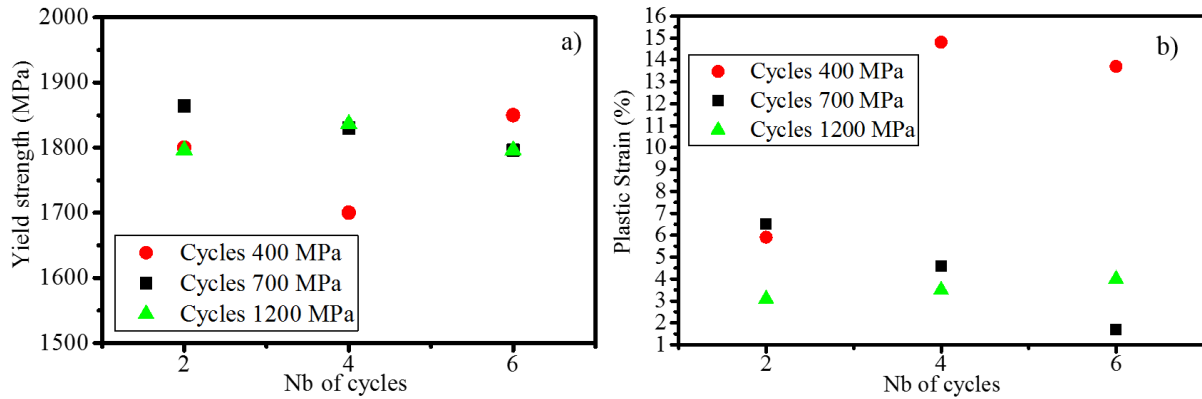


Figure 7-7: Yield strength values a) and plastic strain values b) obtained from the stress-strain curves of the pre-cycled samples

To better investigate the pre-cycling influence on the plastic strain and to understand the mechanisms explaining these results we chose to compare these results to those obtained using molecular dynamic simulation.

### 7-3-2- Mechanical properties of pre-cycled Cu-Zr metallic glass: molecular dynamics simulations

The influences of strain rate and of cooling rate on the deformation mechanisms have been investigated, in order to choose the conditions of the pre-cycling. In a first step, the strain rate was fixed equal to  $10^8 \text{ s}^{-1}$  (Fig. 7-8 a), and different cooling rates (10 K/ns, 1000 K/ns and  $10^5$  K/ns) were set. A cooling rate equal to 10 K/ns corresponds to a high level of relaxation and a lower energy state (The potential energy is  $-3.010 \times 10^6$  eV,  $-3.0048 \times 10^6$  eV and  $-3.0042 \times 10^6$  eV for the samples cooled at 10 K/ns, 1000 K/ns and  $10^5$  K/ns respectively). In contrary, a very high cooling rate of  $10^5$  K/ns corresponds to low relaxation level and to a higher energy state sample.

According to the results of the Fig. 7-8, the well-relaxed system exhibits a strongly localized deformation in the main shear band, while the sample with a higher quantity of structural defect (less relaxed) exhibits a more homogeneous deformation.

Then, the cooling rate has been fixed equal to 10 K/ns, and the three strain rates have been tested ( $10^8 \text{ s}^{-1}$ ,  $10^9 \text{ s}^{-1}$ , and  $10^{10} \text{ s}^{-1}$ ), as shown in Fig. 7-8 b. The same observation between the two different mechanisms can be done i.e. a strongly localized deformation for the sample deformed at low strain rate and a more homogeneous deformation at high strain rate.

The sample deformed at the lowest strain rate exhibits a strong heterogeneous deformation, concentrated in one shear band. In opposite to this result, the sample deformed using the highest strain rate exhibits a more homogeneous deformation, without any shear band formation at this stage.

The deformation mechanisms seem to be very different depending on the initial state of the sample and mechanical conditions. However, according to the stress-strain curves, the stress level reaches a stationary level.

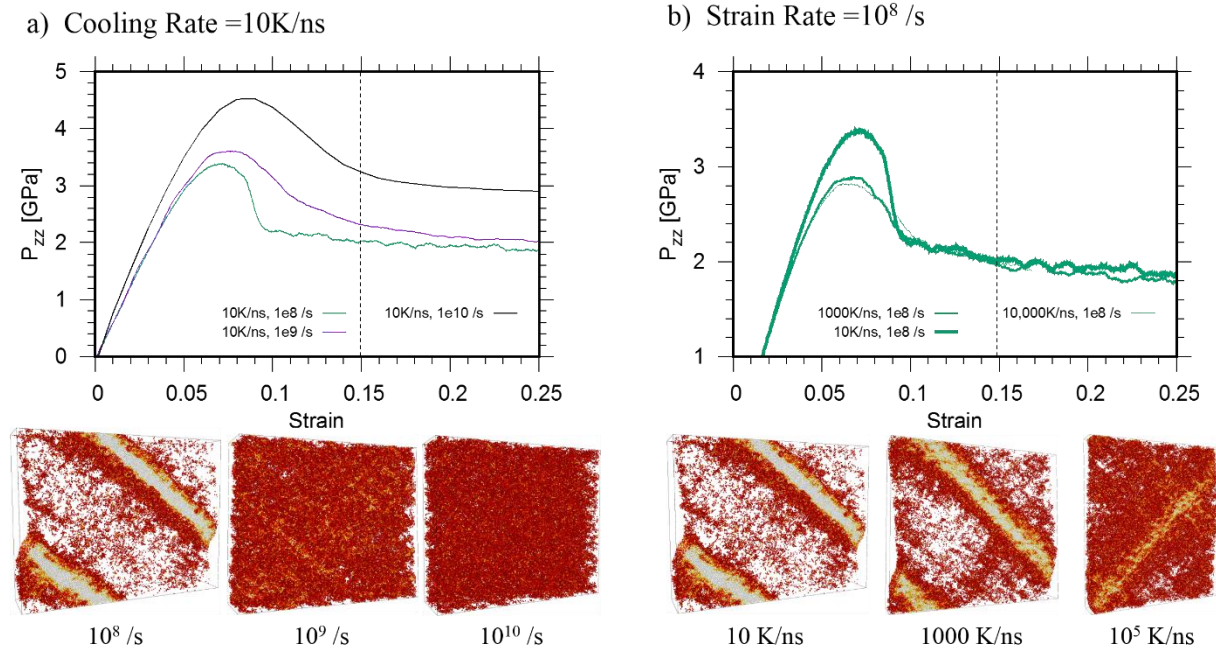


Figure 7-8: a) Illustration of the deformation mechanisms for different cooling rates, b) for different strain rates. Only atoms with  $D^2 > 100$  are shown with yellow atoms corresponding to higher values of  $D^2$ .

To study the influence of pre-cycling on the deformation mechanisms, a cooling rate of 10 K/ns and a strain rate of  $10^8 \text{ s}^{-1}$  were set. A comparison between an as-quenched sample and a pre-cycled sample with 6 cycles at 2000 MPa is shown in Fig. 7-8. Fig. 7-8a shows a localized deformation in the primary shear band for the as-quenched sample whereas Fig. 7-8b exhibits a more homogeneous deformation for the pre-cycled sample, with the secondary shear bands formation.

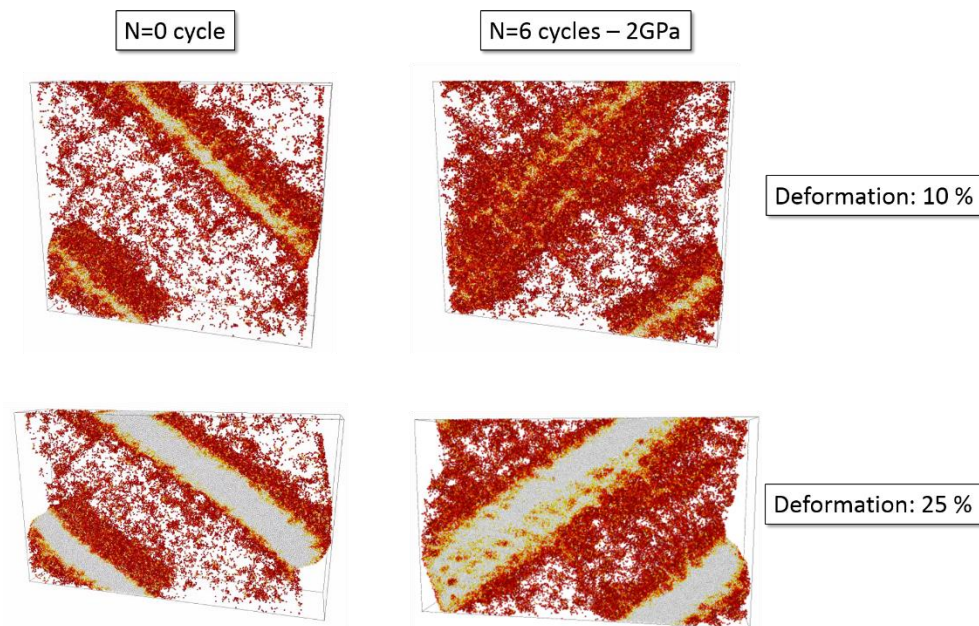


Figure 7-9: Results of the deformation for two compressed samples: no pre-cycling (Left), 6 cycles at 2000 GPa (Right)

As a conclusion, the experimental work shows an influence of the pre-cycling on the plastic strain. At the meantime, deformation mechanisms have been investigated using molecular dynamic simulations to understand this result. Two different mechanisms have been highlighted, between a non-pre-cycled sample, showing a localized strain events, strongly heterogeneous, with a single promoted shear band, and a pre-cycled with a more homogeneous deformation featuring several initiated shear bands (primary and secondary). The pre-cycling could cause a multiplication of the structural defects in the sample, acting as preferential sites for simultaneous shear bands nucleation, permitting the homogenization of the deformation and leading to an increase of the ductility. The strain rate influence and the use of a less-relaxed sample seems to induce the same effect, as shown in Fig. 7-8: a high strain rate allows the creation of several simultaneous nucleation site for shear band, and the deformation becomes more homogeneous. In the case of a less-relaxed sample, the structural heterogeneities are more numerous and then, several nucleation site of shear bands can be activated simultaneously.

## 7-4- Discussion about elementary deformation processes responsible for the ductility increase

In the previous section, two different deformation processes were highlighted. The increase of the ductility could be due to the multiplication of shear bands nucleation sites, because of the introduction of irreversible structural defects by pre-cycling. This theory is mainly used in the literature to explain the plasticity increase of rejuvenated samples. However, no statistical analysis based on quantitative experimental data can be found in the literature. Here we propose to investigate the vein pattern areas to correlate fracture plane

topology and the apparent localization of the deformation. The influence of the pre-cycling stress amplitude is also discussed.

## 7-4-1- Fracture plane topology analysis

### 7-4-1-1- Vein pattern size analysis

During ductile fracture, the sample fracture plane exhibits a particular pattern called vein pattern (see e.g. Chapter1), which has been described and investigated in the previous chapters.

As it has been said previously, while the plastic deformation depends on the shear localization/homogenization within the sample, one can ask if the fracture surfaces can be used to rationalize such differences. However, based on simple analyses, no clear evidence can be made for an unaided eye.

Thus, we implemented a statistical analysis method based on the measurements of the vein pattern areas, using SEM micrographs, Fiji software <sup>32</sup>, and the method described above. The purpose was to determine a difference in the distribution of the vein pattern areas, reflecting the existence of these two mechanisms. The assumptions are as follow: for a pre-cycled sample, the shear bands nucleation sites are more numerous. Several shear bands are initiated simultaneously and the plastic strain is enhanced. Thus, the fracture surface should exhibit a larger proportion of small vein patterns. However, for a non-pre-cycled sample, the size of the defect is increased and thus, the size of the vein pattern on the fracture surface should be larger.

Fig. 7-10 shows the statistical analysis with (a) the distribution of the 1000 areas measurements, and b) the box-plot analysis) obtained for an as-cast sample, a pre-cycled sample with 4 cycles at 400 MPa and another pre-cycled with 4 cycles at 1200 MPa.

According to this figure, the as-cast sample exhibits a spread distribution with a low fraction of small vein pattern and some very large ones (up to 9000  $\mu\text{m}^2$ ). Pre-cycling leads to a higher fraction of small vein patterns and reduces the largest ones. Moreover, for the most beneficial pre-cycling (i.e. 400 MPa), no vein pattern over 3000  $\mu\text{m}^2$  are observed. This conclusion confirms the hypothesis of a more homogenized deformation in the sample, leading to an increase of the small vein patterns fraction and a less spread distribution.

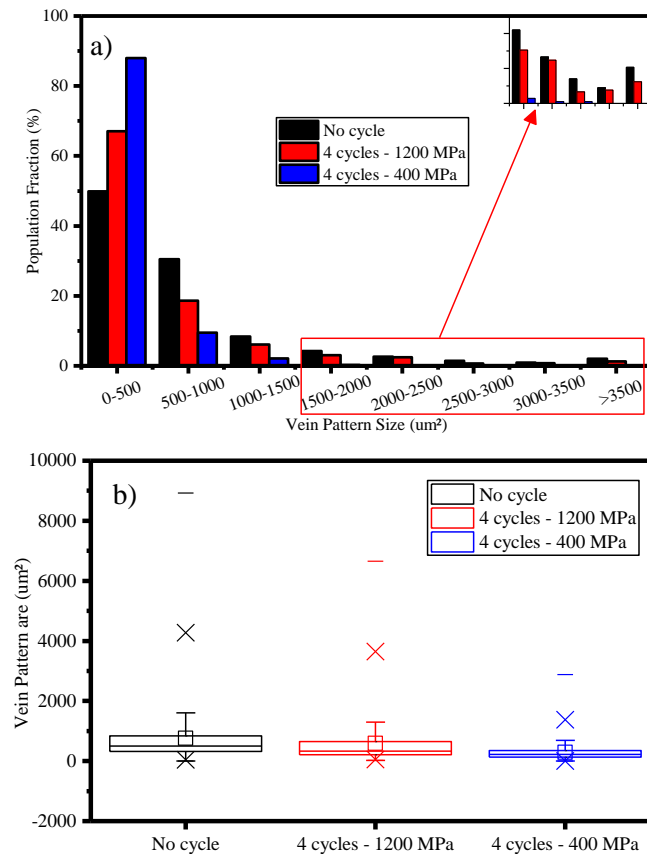


Figure 7-10: a) Distribution of the vein pattern areas for an as-cast sample, a pre-cycled sample at 400 MPa and another one at 1200 MPa (1000 measurements for each sample), b) Box-plot of the distribution of the vein pattern areas. The dash shows the maximum value, the cross whiskers indicate the 5<sup>th</sup> and the 95<sup>th</sup> percentiles, the box shows the interquartile range between the 25<sup>th</sup> and 75<sup>th</sup> percentile, the medium line indicates the median of the distribution.

Then, a comparison between the 400 MPa cycling, which increases the ductility and the 1200 MPa cycling which exhibits no effect, has been performed to characterize the stress amplitude influence on the fracture topology. Even if pre-cycling at 1200 MPa reduces the number of large vein patterns, it still exhibits a significant proportion of it. We believe this could explain why 1200 MPa pre-cycled samples do not exhibit improved mechanical properties, when compared to the 400 MPa pre-cycled sample. The stress amplitude at 1200 MPa for pre-cycling is such a high stress that the defects have already started to grow. The compressive stress behind will therefore focus on these defects. This assumption could lead to the conclusion that deformation relocalization could happen for a too high pre-cycling stress amplitude ( $\sigma_y$ ) or a too high cycles number ( $N$ ). Moreover, the localization of the deformation induces a decrease of ductility in the sample and cause the presence of large vein patterns. These latter can be the most critical ones for the fracture.

## 7-4-1-2- Discussion about the toughness evaluation

The results show a relationship between the homogeneity of the plastic strain and the fracture surface. However, for several years it is established that the following equation relate the characteristic size of the vein pattern and the toughness using the expression of Xi et al.<sup>34</sup>

$$K_C = \sigma_y \sqrt{\omega 6\pi} \quad (1)$$

With  $K_C$ , the stress intensity factor,  $\omega$ , the size of the vein pattern,  $\sigma_y$ , the yield strength.

According to this equation, if the size of the vein pattern is increased, the toughness is also enhanced, which is not going in the same direction than the results above. However, this relationship must be taken with care because the distribution of the vein pattern areas is widely spread on the fracture plane and the value used in the equation can be the mean, the maximum or the minimum, and we expected that the most critical defect inducing the fracture is the largest one. Moreover, this relationship has been, first, implemented for a bending fracture of a notched sample<sup>34</sup>. The  $K_C$  seems to be a mix of the modes I and II, and larger than the true  $K_{IC}$ <sup>35</sup>. In addition, the macroscopic yield strength of a bulk metallic is not relevant, as pre-cycling at 400 MPa already induces residual strain. Moreover, the analysis on the fracture surface is done after fracture and the strain level reached for a sample pre-cycled at 1200 MPa and at 400 MPa is very different.

Another way to evaluate the toughness rather than using the fracture surface topology is using the notch toughness. It allows to estimate the  $K_{IC}$ , but even for this method, the results can be spread. For example, Kim et al. estimated a value equal to 27 MPa.m<sup>1/2</sup> and 80 MPa<sup>1/2</sup> for Zr<sub>44</sub>Ti<sub>11</sub>Ni<sub>10.2</sub>Cu<sub>9.3</sub>Be<sub>25</sub>Fe<sub>0.5</sub> and Zr<sub>33.5</sub>Ti<sub>24</sub>Cu<sub>15</sub>Be<sub>27.5</sub>.<sup>36</sup> The notch toughness is often higher than the true  $K_{IC}$ . The latter depends on a lot of parameter, as for example, the sample size<sup>37</sup>, the state of relaxation<sup>38</sup>, the composition<sup>36</sup> or the compressive residual stresses<sup>38</sup>. For example, Lewandowski et al. measured a  $K_C$  for a fatigue pre-cracked sample about 17.8 MPa.m<sup>1/2</sup><sup>39</sup>, as Gilbert measured a  $K_C$  equal to 55 MPa.m<sup>1/2</sup><sup>40</sup> for the same materials. For the same purpose, Kim et al. estimated the  $K_C$  of four types of Vitreloy samples<sup>36</sup>, with the same elastic properties, and similar yield strength. However, the  $K_C$  varies from 25 to 85 MPa.m<sup>1/2</sup>.

As an example, if we calculated the  $K_C$  with different kind of size value, using the equation (1) the values of  $K_C$  would be very different:

Table 1: Variability of  $K_C$  depending on the chosen size of the vein pattern for an un-pre-strained sample, a sample cycled with 4 cycles at 1200 MPa and another one with 4 cycles at 400 MPa.

	$K_C^0$ (MPa.m <sup>1/2</sup> )	$K_C^{1200 \text{ MPa}}$ (MPa.m <sup>1/2</sup> )	$K_C^{400 \text{ MPa}}$ (MPa.m <sup>1/2</sup> )
<i>Maximum Size</i>	76	70	57
<i>Arithmetical Mean</i>	41	38	32
<i>Median</i>	37	33	30
<i>Volume-weighted mean size</i>	41	38	33

The distribution of  $K_C$  can also be investigated using each size measurements of the vein pattern for each sample: no pre-cycled, pre-cycled at 400 MPa and at 1200 MPa, shown in Fig. 7-11.

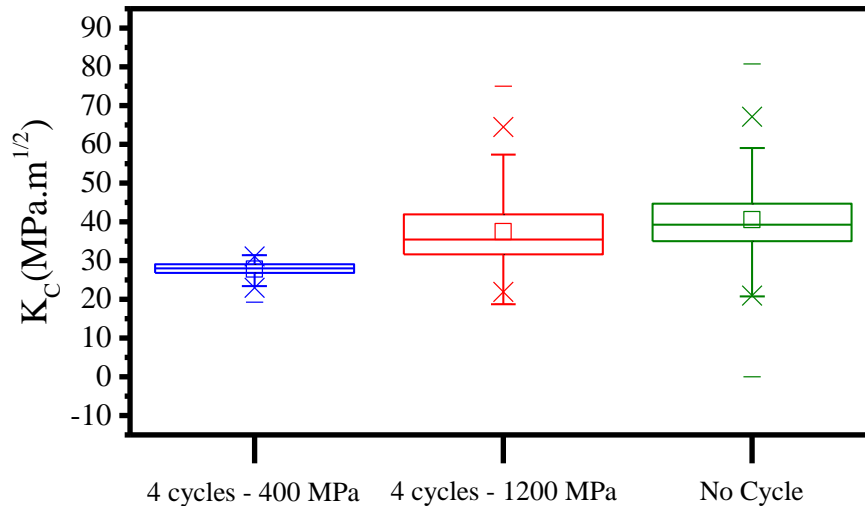


Figure 7-11:  $K_C$  distribution calculated from the size of the vein pattern measured for the three samples: pre-cycled at 400 MPa, 1200 MPa and no pre-cycled. See Fig. 7-10 for more details on the box-plot.

According to the Fig. 7-11, it is difficult to conclude on a comparison of  $K_C$ , taking into account the spread distribution, no conclusion can be drawn to compare the  $K_C$  between the different samples. The main result using this figure is the homogeneity of the value for a pre-cycling at 400 MPa, due to the more homogeneous vein pattern size.

#### 7-4-1-3- Differences on the pre-cycling amplitude

To understand further the role and differences induced by the two different stress amplitudes, (400 MPa and 1200 MPa), SEM observations were performed after the pre-loading and before the subsequent test. Fig. 7-12 shows the different micrographs of these two samples.

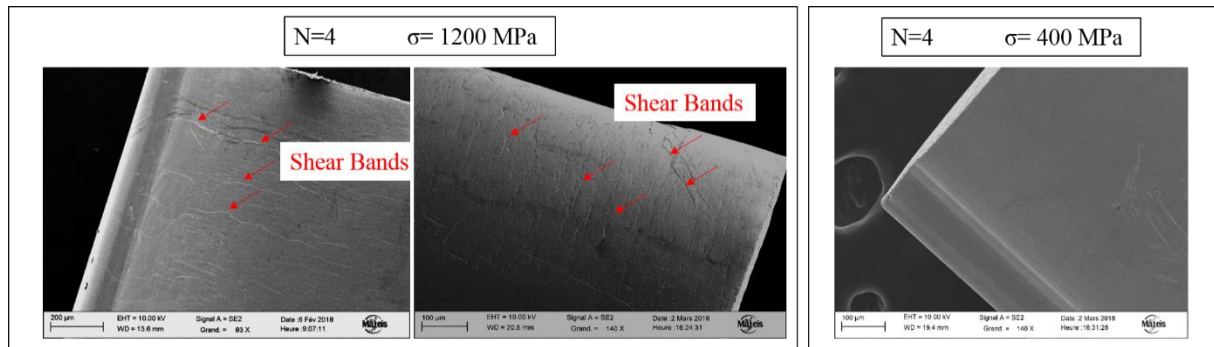


Figure 7-12: SEM pictures of the samples  $N=4$ ,  $\sigma_c= 1200$  MPa (left), and the sample  $N=4$ ,  $\sigma_c= 400$  MPa (right)

On the sample preloaded at 1200 MPa, a large number of shear bands at  $45^\circ$  and perpendicular to the solicitation direction are visible on the sample surface. The surface is very rugged compared to the sample pre-cycled at 400 MPa where no crack and no shear bands are visible. The surface is very smooth.

This result leads to the conclusion that cycling at 400 MPa is enough to introduce structural defects and observe a strong influence on plastic deformation. However, cycling at 1200 MPa is above a threshold in stress amplitude and the localization of the deformation has already been performed, which can be observed on Fig. 7-12. For this reason the benefit of a 1200 MPa stress amplitude for pre-cycling is cancelled, so does the one at 700 MPa. To reach this threshold at 400 MPa, the number of cycles should be very high. It seems to have a correlation between the number of cycles ( $N$ ), stress amplitude ( $\sigma_c$ ) and above a particular number of cycles or a limit stress amplitude, re-localization appears.

## 7-4-2- Verification using molecular dynamics and complementary experimental analysis

### 7-4-2-1- Complete study of $N$ and $\sigma_c$ using molecular dynamic

A three steps deformation mechanism has been highlighted for the rejuvenation by pre-cycling in the elastic domain for limited stresses. Figure 7-13 summarizes it. First, the cycling exhibits a beneficial effect due to the numerous structural heterogeneities created. The number of sources of shear bands nucleation is increased and thus, the ductility is enhanced. This effect is observed below a critical value of cycle's number or stress cycling amplitude.

However, once the critical stress amplitude or cycles number are reached, the heterogeneities, acting as structural defects, are already irreversible and may coalesce to promote a single shear band. The deformation localization is induced.

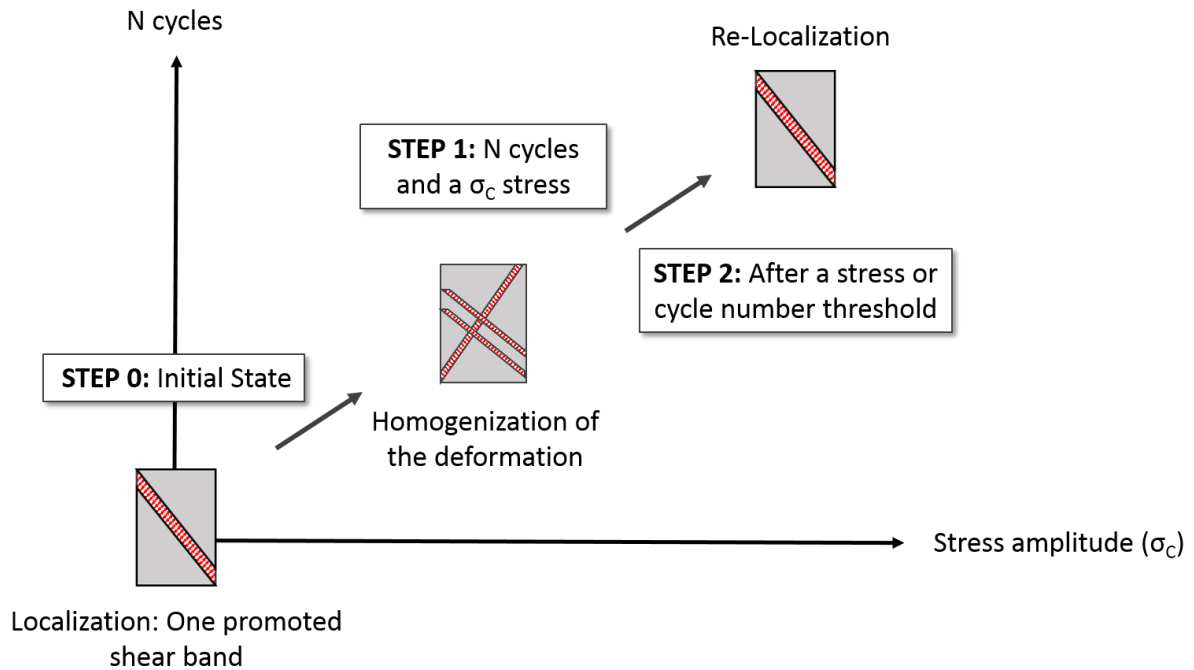


Figure 7-13: Schematic representation of the three steps mechanisms observed during experimental tests and atomistic simulation

The first mechanism, i.e. homogenization by introduction of new defects sources has been observed during compressive tests and experimental results, but also as a result of the atomistic simulations. All the pre-cycled samples exhibit a more homogeneous deformation. However, the localization beyond a critical stress has been shown only during experimental work for now, on the sample surface. Further investigation to observe this result using molecular dynamics are needed and maybe the limit of the molecular dynamics simulation is reached in this case. This may be due to the experimental apparition of macroscopic defects at the surface, which could not be taken into account in the simulation.

#### 7-4-2-2- Adaptation to the strain rates influence

This study based on compressive tests and statistical analysis of the fracture plane topology can be transposed to the strain rate influence on the mechanical response. Stress-strain curves were recorded for 10 samples at each strain rate. However, no clear influence on the mechanical response can be observed, even if some more ductility has been observed on some samples.

Nevertheless, statistical analysis were conducted on fracture surfaces using 3000 measurements for each strain rate. The distribution and the box-plot analysis are presented in Fig. 7-14.

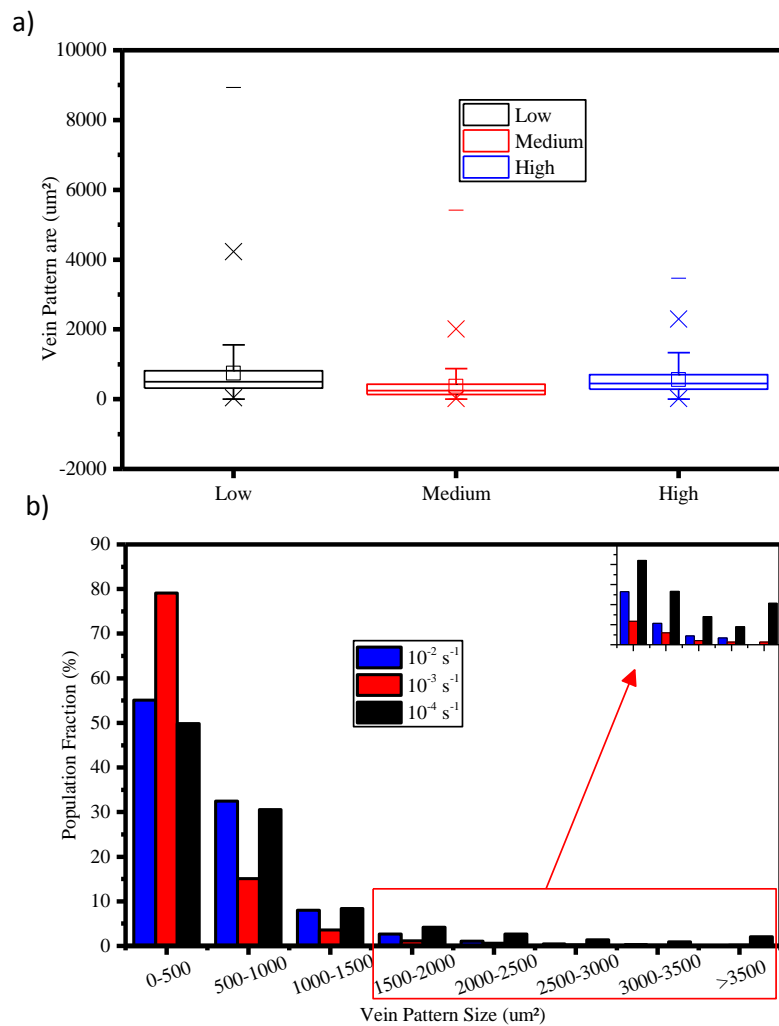


Figure 7-14: a) Distribution of the vein pattern area for different strain rates, b) Box-plot analysis of the distribution

The distribution for the lowest strain rate exhibits some really significant vein patterns, while the fraction of small vein pattern is increased for a high strain rate (the biggest vein pattern does not exceed 3700 um<sup>2</sup>). We conclude that increasing the strain rate promotes the development of isolated shear events of small amplitude (characterized by small vein patterns), unlike the original shear banding process that is rather correlated to largest shear patterns. These results are confirmed by MD simulation presented shown Fig. 7-15 that emphasizes the occurrence of homogeneous shear events increasing the strain rate.

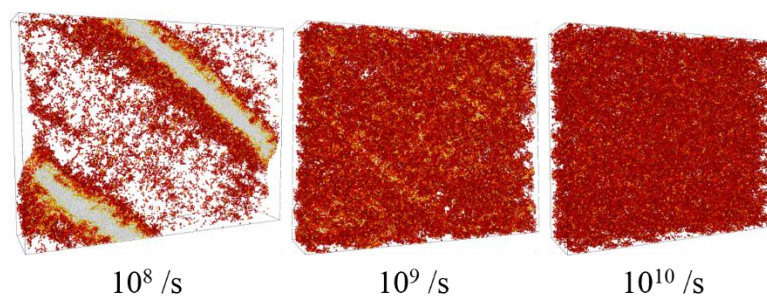


Figure 7-15: Evolution of the deformation mechanisms depending on the compressive strain rate (Snapshots refer to the same accumulated strain)

Even if the experimental evidence are not so clear (partially due to the small number of sample and also to the limited range of strain rates investigated), the MD simulation are in line with the trends observed.

## 7-5- Conclusion

To conclude, rejuvenation has been investigated with the Vit105 system for the experimental work, while the atomistic simulation used a Cu-Zr BMG, since potential for a more sophisticated system is difficult to implement. Both techniques compared the influence of the pre-cycling (with a number of cycles  $N$  equal to 2, 4 and 6 and a stress amplitude  $\sigma_c$  equal to 400, 700 and 1200 MPa). The role of rejuvenation on BMGs ductility and deformation mechanisms that justify its beneficial effect were explored using molecular dynamics simulations and compressive tests analyses. Two different processes were highlighted i.e. i) a strong localization of the deformation for as-cast samples, ii) a more homogeneous deformation for pre-cycled sample. The pre-cycling introduces some structural defects which act as simultaneous nucleation sites for the shear bands. Thus, the ductility is increased. All these results are confirmed both by molecular dynamic simulations and by statistical analyses of the vein patterns.

However, beyond a critical pre-cycling stress amplitude (between 400 and 700 MPa in this case) this process seems to be reversed and the new regime of localized deformation is promoted. However this latter has only been observed in the experimental work and needs to be confirmed by the atomistic simulation.

## 7-6- References

1. Dmowski, W., Yokoyama, Y., Chuang, A. *et al.* Structural rejuvenation in a bulk metallic glass induced by severe plastic deformation. *Acta Materialia* **58**, 429-438 (2010).
2. Lee, S.-C., Lee, C.-M., Yang, J.-W. & Lee, J.-C. Microstructural evolution of an elastostatically compressed amorphous alloy and its influence on the mechanical properties. *Scripta Materialia* **58**, 591–594 (2008).
3. Greer, A. L. & Sun, Y. H. Stored energy in metallic glasses due to strains within the elastic limit. *Philosophical Magazine* **96**, 1643–1663 (2016).
4. Ri, M.C., Sohrabi S., Ding, D. *et al.* Serrated magnetic properties in metallic glass by thermal cycle. *Chinese Physics B* **26**, 066101 (2017).
5. Liu, J. W., Cao, Q. P., Chen, L. Y., Wang, X. D. & Jiang, J. Z. Shear band evolution and hardness change in cold-rolled bulk metallic glasses. *Acta Materialia* **58**, 4827–4840 (2010).
6. Meng, F., Tsuchiya, K., Seiichiro & Yokoyama, Y. Reversible transition of deformation mode by structural rejuvenation and relaxation in bulk metallic glass. *Applied Physics Letters* **101**, 121914 (2012).

7. Wang, L., Bei, H., Gao, Y. F., Lu, Z. P. & Nieh, T. G. Effect of residual stresses on the hardness of bulk metallic glasses. *Acta Materialia* **59**, 2858–2864 (2011).
8. Fornell, J., Concustell, A., Greer, A. L. *et al.* Effects of shot peening on the nanoindentation response of Cu<sub>47.5</sub>Zr<sub>47.5</sub>Al<sub>5</sub> metallic glass. *Journal of Alloys and Compounds* **586**, S36–S40 (2014).
9. Concustell, A., Méar, F. O., Suriñach, S., Baró, M. D. & Greer, A. L. Structural relaxation and rejuvenation in a metallic glass induced by shot-peening. *Philosophical Magazine Letters* **89**, 831–840 (2009).
10. Zhilyaev, A., Nurislamova G. V., Kim, B. K. *et al.* Experimental parameters influencing grain refinement and microstructural evolution during high-pressure torsion. *Acta Materialia* **51**, 753–765 (2003).
11. Qiao, J.C., Pelletier, J.M., Esnouf, C., Liu, Y., Kato, H., Impact of the structural state on the mechanical properties in a Zr-Co-Al bulk metallic glass, *Journal of Alloys and Compounds* **607**, 139-149, (2014).
12. Qiao, J.C., Pelletier, Kou, H.C., Zhou, X., Modification of atomic mobility in a Ti-based bulk metallic glass by plastic deformation or thermal annealing, *Intermetallics* **28**, 128-137, (2012).
13. Ketov, S. V., Trifonov, A., Ivanov, Y. *et al.* On cryothermal cycling as a method for inducing structural changes in metallic glasses. *NPG Asia Materials* **10**, 137-145 (2018).
14. Saida, J., Yamada, R., Wakeda, M. & Ogata, S. Thermal rejuvenation in metallic glasses. *Science and Technology of advanced Materials* **18**, 152–162 (2017).
15. Lübke, J. & Wilde, A. G. Cryogenic Rejuvenation of Metallic Glasses, Westfälische Wilhelms Universität Münster. (2014).
16. Guo, W., Yamada, R. & Saida, J. Rejuvenation and plasticization of metallic glass by deep cryogenic cycling treatment. *Intermetallics* **93**, 141–147 (2018).
17. Bian, X. L., Wang, G., Yi, J. *et al.* Atomic origin for rejuvenation of a Zr-based metallic glass at cryogenic temperature. *Journal of Alloys and Compounds* **718**, 254–259 (2017).
18. Baumer, R. E. & Demkowicz, M. J. Radiation response of amorphous metal alloys: Subcascades, thermal spikes and super-quenched zones. *Acta Materialia* **83**, 419–430 (2015).
19. Huang, Y., Fan, H., Zhou, X. *et al.* Structure and mechanical property modification of a Ti-based metallic glass by ion irradiation. *Scripta Materialia* **103**, 41–44 (2015).
20. Bian, X. L., Wang, G., Chen, H. C. *et al.* Manipulation of free volumes in a metallic glass through Xe-ion irradiation. *Acta Materialia* **106**, 66–77 (2016).
21. Magagnosc, D. J., Kumar, G., Schroers, J *et al.* Effect of ion irradiation on tensile ductility, strength and fictive temperature in metallic glass nanowires. *Acta Materialia* **74**, 165–182 (2014).
22. Huang, H., Jiang, M. & Yan, J. Softening of Zr-based metallic glass induced by nanosecond pulsed laser irradiation. *Journal of Alloys and Compounds* **754**, 215–221 (2018).
23. Lee, P. Y., Kao, M. C., Lin, C. K. & Huang, J. C. Mg–Y–Cu bulk metallic glass prepared by mechanical alloying and vacuum hot-pressing. *Intermetallics* **14**, 994–999 (2006).
24. Wang, Y. M., Zhang, M. & Liu, L. Mechanical annealing in the homogeneous deformation of bulk metallic glass under elastostatic compression. *Scripta Materialia* **102**, 67–70 (2015).
25. Lee, J.-C. & Fleury, E. Structural disordering process of an amorphous alloy driven by the elastostatic compression at room temperature. *Applied Physics Letters* **92**, 151906 (2008).
26. Park, K. W., Lee, C. M., Wakeda, M. *et al.* Homogeneous deformation of bulk amorphous alloys during elastostatic compression and its packing density dependence. *Scripta Materialia* **59**, 710–713 (2008).

27. Park, K. W., Lee, C. M., Lee, M. R. *et al.* Paradoxical phenomena between the homogeneous and inhomogeneous deformations of metallic glasses. *Applied Physics Letters* **94**, 021907 (2009).
28. Wakeda, M., Saida, J., Li, J. & Ogata, S. Controlled Rejuvenation of Amorphous Metals with Thermal Processing. *Scientific Reports* **5**, 10545 (2015)
29. Packard, C. E., Homer, E. R., Al-Aqeeli, N. & Schuh, C. A. Cyclic hardening of metallic glasses under Hertzian contacts: Experiments and STZ dynamics simulations. *Philosophical Magazine* **90**, 1373–1390 (2010).
30. Packard, C. E., Witmer, L. M. & Schuh, C. A. Hardening of a metallic glass during cyclic loading in the elastic range. *Applied Physics Letters* **92**, 171911 (2008).
31. Cao, R., Deng, Y. & Deng, C. Hardening and crystallization in monatomic metallic glass during elastic cycling. *Journal of Materials Research* **30**, 1820–1826 (2015).
32. Schindelin, J. *et al.* Fiji: an open-source platform for biological-image analysis. *Nature Methods* **9**, 676–682 (2012).
33. Cheng, Y. Q. & Ma, E. Atomic-level structure and structure–property relationship in metallic glasses. *Progress in Materials Science* **56**, 379–473 (2011).
34. Falk, M. L. & Langer, J. S. Dynamics of viscoplastic deformation in amorphous solids. *Physical Review E* **57**, 7192–7205 (1998)
34. Xi, X. K., Zhao, D. Q., Pan, M. X. *et al.* Fracture of Brittle Metallic Glasses : Brittleness or Plasticity. *Physical Review Letters* **94**, 125510 (2005)
35. Varadarajan, R.; Thurston, A.K.; Lewandowski, J.J. Increased toughness of zirconium-based bulk metallic glasses tested under mixed mode conditions. *Metall. Mater. Trans. A* **2010**, *41*, 149–158
36. Kim, C.P.; Suh, J.Y.; Wiest, A.; Lind, M.L.; Conner, R.D.; Johnson, W.L. Fracture toughness study of new Zr-based Be-bearing bulk metallic glasses. *Scr. Mater.* **2009**, *60*, 80–83.
37. Gludovatz, B.; Naleway, S.E.; Ritchie, R.O.; Kruzic, J.J. Size-dependent fracture toughness of bulk metallic glasses. *Acta Mater.* **2014**, *70*, 198–207.
38. Launey, M.E.; Busch, R.; Kruzic, J.J. Effects of free volume changes and residual stresses on the fatigue and fracture behavior of a Zr–Ti–Ni–Cu–Be bulk metallic glass. *Acta Mater.* **2008**, *56*, 500–510.
39. Lowhaphandu, P.; Lewandowski, J.J. Fracture toughness and notched toughness of bulk amorphous alloy: Zr–Ti–Cu–Ni–Be. *Scr. Mater.* **1998**, *38*, 1811–1817
40. Gilbert, C.J.; Schroeder, V.; Ritchie, R.O. Mechanisms for fracture and fatigue-crack propagation in a bulk metallic glass. *Metall. Mater. Trans. A* **1999**, *30*, 1739–1753.

# Conclusion & Outlooks

---

# Conclusion

This work dealt with the processing and the characterization of new metallic glass compositions for biomedical applications. At the present time, there is a real lack of fully biocompatible compositions for this kind of material. Some small atoms as beryllium or aluminium are added due to their ability to increase the glass forming ability and the ductility. As they could be harmful to the human body, many researches attempt to replace such elements, keeping good mechanical properties and good glass forming ability. It has to be based on the understanding of new biocompatible composition processing, to choose proper elements and improve it, but also through an understanding of the deformation mechanisms.

The state of art, firstly conducted, allows us to obtain an overview of the attractive properties of the metallic glasses compared to their crystalline counterparts. The different techniques to process these materials have been also detailed depending on the thickness of the sample and their constituents. The existing glassy systems appropriated for biomedical applications and their main particularities have been presented. This has enabled us to choose and process two different systems: a Mg-based system for bioresorbable applications, as bones void fillers, and a Zr-based system for reinforcement biomaterials, as for example, screws or dental implants. Then, different ways to improve the ductility or critical diameter, such as microalloying and manufacturing of composites using powder metallurgy, have been discussed. These two techniques have been investigated in this work, based on a known Cu-based system to find a way to increase the ductility and the size of the sample. Finally, the mechanical behaviour has been explained depending on the temperature or stress level. A new method to improve the ductility has been determined based on the deformation mechanisms, involving rejuvenation by pre-cycling.

In the second chapter, all the experimental techniques used in this PhD work have been described. First, the two-step elaboration process has been presented: (i) the master ingots have been processed using different techniques as induction or arc melting depending on the vaporization temperature of the constituents. (ii) Then, the sample shaping has been conducted using melt-spinning or suction casting, depending on the sample thickness and the GFA of the samples. The second part of this chapter is dedicated to the presentation of the characterization techniques. First, the structure is investigated using density measurement, XRD, TEM and the composition is checked using EDX experiments. No vaporization of any constituents has been measured. Then, thermal stability is a key parameter for biomaterials and the characterization through DSC or high-temperature XRD have been performed. All the samples were resistant enough to avoid crystallization during the sterilization process. Mechanical properties have been evaluated using nanoindentation for ribbon samples and compressive tests for bulk samples. During compressive tests, Cu-BMGs show a high yield strength (over 2 GPa) and a low ductility which may be increased by microalloying of rare earth elements. Hardness measurements have also been conducted and even for high loads, no crack initiation has been noticed, indicating a local plasticity for all the samples. Then, corrosion resistance has been examined through immersion tests in simulated body fluids for ribbon samples and corrosion tests in different media. Ribbon samples show a higher

corrosion resistance with microalloying of Si and Sn while bulk samples also exhibit a higher corrosion potential with microalloying of yttrium. Moreover, a different behaviour due to the introduction of proteins in the medium has been illustrated: the immediate dissolution of the Cu-based samples has been prevented by the formation of a passive layer when proteins are present. At last, cytotoxicity tests have been performed on some ribbon and bulk samples with osteoblast-like cells and none of the composition shows cytotoxicity.

The third chapter highlighted the processing and the characterization of a potential ribbon Mg-based metallic glass sample as bioresorbable materials. The use of the induction melting associated to the melt-spinning lead to shiny ribbon samples with no vaporization of any element, checked by EDX measurements. The thermal stability has been shown to be high enough to resist the sterilization process. The sample has also been immersed in simulated body fluid and its resistance to immersion is still very low. Addition of Yb has been tried to increase the diameter and the resistance to the immersion. However, only the thermal stability of the system has been enhanced.

Another promising reinforcement biomaterial has been obtained in chapter 4 with the Zr-Co-Ga system, replacing aluminium by gallium. The samples are under ribbon form because of its low GFA. However, micro alloying of Si and Sn have been tried and their first beneficial action is to increase the GFA. They also improve the resistance to immersion in simulated body fluid after 10 and 20 days. Using the nanoindentation experiment, the Young modulus has been evaluated to be of the same order of magnitude as the pure zirconium. Then, an experimental design has been implemented to obtain a bulk sample adding titanium atoms in the system to have substitutions and try to increase the GFA. Because no bulk sample has been processed yet, only potential applications as coating can be considered.

In the Chapter 5, a Ni-, Be-, Al- free system has been used to try improvement techniques to increase the ductility or the critical size. The chosen system was Cu-Zr-Ti and addition of 1 and 2 at. % of Y have been tested. A thermal stability increase, but also an increase of corrosion resistance, biocompatibility and ductility have been observed for 1 at. % Y. In order to determine the causes of the increase in ductility, TEM experiments associated with EDX and EELS measurements have been carried out. This revealed the presence of box-shape precipitates of yttria, which induces crystallized areas above a size threshold. The precipitates seem to exhibit a cubic hole in the middle of it, probably created by diffusion phenomena.

Chapter 6 highlights the possibility to use another processing technique to form larger bulk metallic glass samples, based on the powder metallurgy. After a reminder about the technique to obtain powders and to perform densification, gas atomization for the powder and SPS technique to densify the sample have been chosen. The same system, Cu-Zr-Ti has been used in order to compare the results and the characteristics of those samples from the casting technique. The process has been optimized to define the best parameters to obtain a fully densified sample without any crystallization. The processed sample exhibits a diameter of 10 mm. The densification quality has been checked by Archimedes density measurements, SEM observation and hardness measurements. Even if no crack appears under hardness measurements (indicating a local ductility), the mechanical response under compressive tests

was very poor. Indeed, the sample reaches a very low yield strength and exhibits a brittle fracture. Moreover, the thermal stability and the corrosion resistance are also lowered by this technique.

Then composites samples have been processed, introducing 10 and 30 wt. % of Ti-6Al-4V crystalline particles in the system. Even if the yield strength of the sample containing 30 wt.% of crystalline particles is very close to the one expected, the ductility has to be improved. The corrosion potential has also been enhanced by the crystalline particles additions.

In the last chapter, a description of the rejuvenation mechanisms inducing more ductility has been conducted first. The different techniques to induce rejuvenation have been presented. In this chapter, we developed a simple way to induce a rejuvenated state without any geometry change by pre-cycling the sample. The influence of this mechanism has been investigated studying the mechanical response and implementing a statistical analysis of the vein pattern size on the fracture plane. Molecular dynamics have also been used to determine the elementary deformation caused by the pre-cycling. A three steps mechanisms has been highlighted: first the deformation is strongly localized in the shear band. Then, thanks to the pre-cycling deformation, irreversible defects are introduced acting as nucleation sites for shear bands and multiple shear bands are created simultaneously, inducing a more homogeneous deformation and an increase of the ductility. At last, for too high stresses or for too high a number of cycles, the deformation is already localized again in promoted shear bands.

This work offers new perspectives on the following points:

- The first one, concerns an outlook on the processing of the Zr-Co-Ga. This system is promising as biomaterials because Al is avoided and the experimental design showed that Y additions can be very helpful to increase the glass-forming ability and the diameter of the sample. Moreover, it could also enhance the mechanical properties of a system, especially in a system with other constituents rich in oxygen impurities, as Ti or Zr. In a system such as Zr-Ti-Co-Ga, yttrium additions can improve the GFA and may allow to obtain bulk samples.  
Powder of Zr-Co-Ga-Ti can also be easily produced thanks to the very high cooling rate of gas atomization. Then densification stage may allow to obtain a large bulk samples of this composition without any glass forming ability issue.
- The second outlook to develop concerns the Y additions. It has been shown that yttrium improvement comes from the formation of precipitates. However, the precipitation can also be understood, using accurate models, and the distribution of the precipitates and the crystallized areas could be potentially predicted to optimize the properties of the materials. Nevertheless, the yttrium beneficial effect should be investigated for systems containing less oxygen impurities. A size threshold to create the void can also be estimated, using models.

Moreover, the role of the different crystalline areas on the ductility should be investigated depending on their size, varying the cooling rate to change the proportion of large and small areas, the mechanical responses can be studied.

- Concerning the composites processing, the properties of those elaborated in this work are not good enough yet, even if the size of the sample has been largely increased and mechanical properties of a sample containing 30% of crystalline particles are close to those of a cast sample. However, trying to use milled powder could increase the compactness and could lead to better properties. The process can also be modified using an atmosphere composed of Ar and H in order to avoid an oxide layer on the powder surface. The Ti-6Al-4V could also be not appropriate to add in the matrix and the choice of other particles could induce better properties.
- At last, the rejuvenation effect has been briefly investigated and discussed. This effect should be proved on other compositions. A purpose for the experimental work could be the implementation of a model curve of the number of cycles (N) depending on the stress amplitude ( $\sigma_c$ ), as shown in Fig. ii, to predict the homogeneous or heterogeneous deformation. As only three amplitude stresses have been tested, other experimental data should be interesting for a better understanding of the plasticity and fracture mechanisms on the pre-cycled samples. Moreover, a program to automate the fracture plane analysis could be interesting. A potential stress threshold to obtain rejuvenation can be highlighted and maybe an optimum cycle number can be determined in order to get the targeted properties, especially plastic strain. The plastic strain seems to stabilize after 4 cycles, a higher cycle's number could confirm this trend. Then, the relationship between toughness and fracture topography still remains unclear and should be further investigated to help the understanding of the fracture mechanisms.

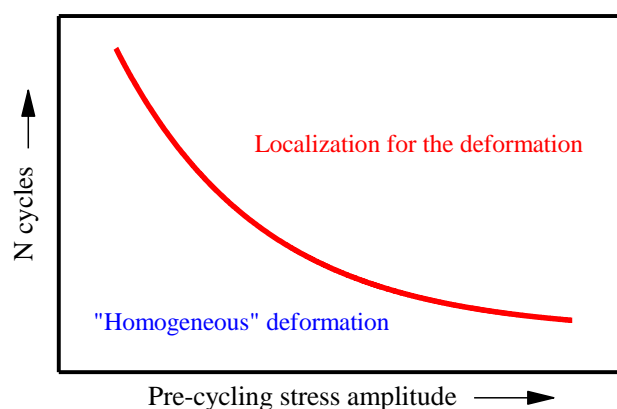


Figure ii: Cycles number depending on the localization of the deformation

- The preliminary results about the influence of the strain rate on the localization of the deformation should also be deeper investigated. The number of tests was not enough to obtain a real relevant statistical analysis of the mechanical response.



## FOLIO ADMINISTRATIF

### THESE DE L'UNIVERSITE DE LYON OPEREE AU SEIN DE L'INSA LYON

NOM : Baulin

DATE de SOUTENANCE : 12 octobre 2018

Prénoms: Oriane

TITRE: Development of amorphous metallic alloys for biomedical applications and understanding of the plasticity phenomena.

NATURE : Doctorat

Numéro d'ordre : 2018LYSEI073

Ecole doctorale : ED 34 – Matériaux de Lyon

Spécialité : Matériaux

#### RESUME :

L'objectif de cette thèse est de développer et de caractériser des alliages métalliques amorphes biocompatibles. De par la nature amorphe de ces alliages et leur absence de microstructure, les propriétés mécaniques et la résistance à la corrosion sont plus élevées que dans le cas de matériaux cristallins. Toutefois, la taille et la déformation plastique de ces matériaux sont extrêmement limitées.

Dans ce but, une première phase a permis de développer deux compositions de verres métalliques biocompatibles sous forme de rubans et de les caractériser.

Dans un second temps, nous nous sommes intéressés à l'amélioration de la ductilité et de la taille critique en nous basant sur un système connu, Cu-Zr-Ti. Il a donc été démontré que le micro-alliage de terre-rares comme l'yttrium pouvait avoir un impact considérable sur la cytotoxicité, la résistance à la corrosion mais aussi sur la ductilité des matériaux. Ceci intervient grâce à la formation de précipités d' $Y_2O_3$  provoquant la formation de zones nano-cristallisées, ceci ayant pour but d'augmenter la ductilité. De plus, le changement de procédé de fabrication en se basant sur la métallurgie des poudres, a aussi permis de réaliser des pièces d'un diamètre de 10 mm, pouvant être renforcées par l'insertion de particules cristallines, créant ainsi un matériau composite ex-situ.

Enfin, puisque la déformation des verres métalliques passe avant tout par la compréhension des mécanismes de déformation, une étude couplant simulations par dynamique moléculaire et une analyse statistique des faciès de rupture en compression, a permis de mettre en évidence une homogénéisation de la déformation par l'introduction de défauts dans le matériau pendant le phénomène de rajeunissement. Le rajeunissement a été réalisé par pré-cyclage quasi-statique en compression. Cette technique a pour effet d'améliorer grandement la ductilité du matériau.

MOTS-CLÉS : Metallic Glasses, Biomaterials, Micro-alloying, Rejuvenation, Molecular dynamics

Laboratoire (s) de recherche

MATEIS –UMR CNRS 5510

INSA de Lyon

25 avenue Jean Capelle

69621 Villeurbanne Cedex

Directeur de thèse: Damien Fabrègue

President de jury: A. Lindsay Greer

Composition du jury : Mariana Calin, Jean-Jacques Blandin, Anne Tanguy, Jean-Marc Pelletier, Damien Fabrègue, Sébastien Gravier, David Rodney